Investigation of crystalline silicon solar cells at the nano-scale using scanning probe microscopy techniques

Paul Narchi

NNT : 2016SACLX085

THESE DE DOCTORAT
DE
L'UNIVERSITE PARIS-SACLAY
PREPAREE A
L'ECOLE POLYTECHNIQUE

ECOLE DOCTORALE N° 573 Interfaces
Approches interdisciplinaires : fondements, applications et innovation

Spécialité : Physique

Par

M. Paul Narchi

Investigation of crystalline silicon solar cells at the nano-scale using scanning probe microscopy techniques

Thèse présentée et soutenue à Palaiseau, le 12 décembre 2016 :

Composition du Jury :

Dr.	Kleider, Jean-Paul	GeePs	Président du jury
Dr.	Mélin, Thierry	IEMN	Rapporteur
Dr.	Seassal, Christian	INL	Rapporteur
Dr.	Fejfar, Antonín	Inst. Phys. ASCR	Examinateur
Dr.	Gordon, Ivan	IMEC	Examinateur
Dr.	Betremieux, Isabelle	Total	Examinatrice
Dr.	Prod'homme, Patricia	Total	Encadrante
Dr.	Foldyna, Martin	LPICM	Encadrant
Prof.	Roca i Cabarrocas, Pere	LPICM	Directeur de thèse

“C’est avec la logique que nous prouvons,
et avec l’intuition que nous trouvons.”

Henri Poincaré

à mes parents, Patrick et Blandine

Remerciements

Cette thèse est le fruit d'une collaboration entre le Laboratoire de Physique des Interfaces et Couches Minces – LPICM, ayant pour tutelle l'Ecole Polytechnique et le CNRS, et Total, à travers sa branche Total Energies Nouvelles. Elle s'inscrit dans le cadre de la construction de l'Institut Photovoltaïque d'Ile de France (IPVF) dans lequel participent le LPICM et Total ainsi que d'autres partenaires industriels et académiques.

J'aimerais donc commencer par remercier le LPICM, Total, l'IPVF et l'ANRT dont les financements et le soutien ont permis le développement de mes travaux de recherche. J'ai eu la chance d'évoluer dans un environnement multiculturel, très ouvert, plein d'opportunités, et extrêmement motivant. J'ai très rarement eu du mal à me lever le matin pour aller au laboratoire et certains vendredi soir, en rentrant en RER, il m'est arrivé d'avoir hâte d'être lundi pour poursuivre mes recherches et aller de l'avant.

Un doctorat c'est aussi des rencontres et des interactions humaines. Dans ma recherche, ces interactions ont été clés car elles m'ont inspiré, cadré, orienté et ouvert à de nouvelles perspectives. Je tiens donc naturellement à remercier mon équipe d'encadrement de thèse. Nos réunions mensuelles en salle 406 (souvent longues et parfois passionnées !) m'ont beaucoup aidées durant ces trois années et ont, selon moi, porté leurs fruits. Je commence par remercier mon directeur de thèse, *Pere Roca i Cabarrocas*. Son optimisme à toute épreuve, sa grande fiabilité, sa vision d'ensemble et son esprit d'innovation m'ont beaucoup inspiré. Cela a été une très grande joie de travailler trois ans sous sa direction. Un grand merci à *Patricia Prod'homme*, mon encadrante Total, qui a partagé mon enthousiasme pour la microscopie à sonde locale au pays des photovoltaïciens. Je suis reconnaissant pour son soutien et son encadrement tout au long de mon doctorat. Merci à *Martin Foldyna* pour son encadrement et sa générosité. Je garderai en mémoire les longues discussions (scientifiques et non-scientifiques) que nous avons eues entre Palaiseau, Lund, Göteborg et Prague. Merci également à *Gennaro Picardi* qui m'a permis de mettre le pied à l'étrier de la microscopie à sonde locale au début de mon doctorat, ainsi qu'à *Chiara Toccafondi*, pour ses idées et les discussions de microscopie que nous avons eues, à la fin de mon doctorat.

J'ai également eu le privilège de soutenir mon doctorat devant un jury de très grande qualité : *Thierry Mélin, Antonín Fejfar, Christian Seassal, Jean-Paul Kleider, Ivan Gordon, Isabelle Bertemieux* et *Jean-Paul Kleider*. Je souhaite les remercier pour leur présence et leurs questions lors de la soutenance ainsi que pour leur contribution au manuscrit de thèse.

J'ai passé trois superbes années au LPICM et les membres du laboratoire y sont pour beaucoup. L'atmosphère y est à la fois sérieuse et détendue et j'ai eu la chance d'interagir quotidiennement avec des chercheurs passionnés par leur travail. J'aimerais remercier en premier lieu, *Joaquim Nassar*, pour ses apports théoriques dans mon travail de recherche et pour la semaine d'enseignement que nous avons passée à Wuhan, en Chine. Grâce à lui, je me suis découvert un goût pour les cérémonies du thé et … le karaoké ! Ce voyage m'a réellement ouvert l'esprit sur la culture chinoise, que je connaissais peu. Je suis également reconnaissant à *Bernard Drévillon*, qui m'a suivi depuis le master REST. Au LPICM, je tiens également à remercier *Ileana Flora* (et pour les discussions de microscopistes), *Rym Boukhicha* (et sa bonne humeur !), *Enric Caurel Garcia* (et les aventures du SCOP), *Denis Tondelier* (et nos discussions dans le bus 91.06), *Wanghua Chen*, *Jean-Eric Bourree* (et ses anecdotes), *Jean-Luc Maurice*, *Yvan Bonnassieux*, *Erik Johnson*, *Pavel Bulkin*, *Dmitri Daineka*, *Bernard Geoffrey*, *Jacqueline Tran*, *Jean-Luc Moncel* et *Garry Rose*. Un merci tout particulier à l'équipe administrative, et en particulier à *Laurence Géro*t et *Gabriela Medina*, dont l'état d'esprit et l'efficacité sont remarquables. Un grand BIG UP à l'équipe du Beer (*Cyril Jadaud, Nacib Benmammar, François Silva, Jérôme Charliac* et *Frédéric Farci*) et à l'équipe informatique (*Eric Paillassa* et *Frédéric Liège*). Leur efficacité et leur sérieux font du LPICM un endroit où il fait bon être chercheur. Un merci particulier à *Frédéric Farci* pour son aide dans le développement d'accessoires de mesures (a.k.a Timon & Pumba Génération 5), qui m'ont rendu la vie beaucoup plus simple.

Je pense ensuite à l'équipe R&D de Total dans le solaire. Merci beaucoup à *Lars Oberbeck, Dominique Neerinck* et *Fabrice Devaux* de m'avoir fait confiance et de m'avoir permis de faire une thèse CIFRE au sein de leur équipe (dont je remercie tous les membres). En tant que doctorant, cela a été une grande opportunité d'évoluer et d'être impliqué dans une équipe industrielle de recherche, à travers les réunions, les formations, les séminaires, (les pauses café et les Magnans), … En particulier, je tiens à remercier les « expatriés de Palaiseau »: *Ludovic Hudanski*, *Gilles Poulain*, *Nada Habka*, *Sergej Filonovich*, *Etienne Drahi*, *Martin Sanders*, *Jara Fernandez*, *Jean-François Besnier* pour leur aide et leur bonne humeur. Mes remerciements ne se limitent

pas à la frontière hexagonale. Je tiens également à remercier les équipes Total à l'IMEC en Belgique et à SunPower en Californie, que j'ai eu l'occasion d'aller voir et avec qui j'ai pu intéragir.

Si je n'ai pas vu le temps passer durant ces trois années de thèse, c'est aussi grâce à l'interaction avec des stagiaires, thésards et postdocs. Je tiens à remercier *Mintae Chung*, le stagiaire que j'ai supervisé en troisième année de thèse. Son aide a été très précieuse dans le développement de nouvelles procédures de mesure microscopique. Parmi les stagiaires que j'ai rencontrés, je tiens à remercier *Tang Miao* et *Yu Jingwen* (pour leur hospitalité et leur accueil lors de mon voyage en Chine), *Christopher Griz* (pour son aide sur les mesures de sonde Kelvin) et *Mickaël* (pour son aide sur le polissage). Merci également aux postdocs que j'ai pu côtoyer : *Nicolas Vaissière* (Park Run !), *Céline Richard* et *Ahmed Ben Slimane*. Je finis par remercier les trois générations de thésards. Tout d'abord, les anciens pour leurs conseils et l'émulation dont j'ai pu bénéficier : *Romain Cariou* (#SunRun&Movember_buddy), *Bastien Bruneau* (#Rainbow_guy), *Igor Sobkowicz* (#Mister_20%), *Jean-Christophe Dornstetter* (#Le_Harry_Potter_du_SiF4), *Coralie Charpentier*, *Soumyadeep Misra*, *Dennis Lange* et *Guillaume Courtois* (mon premier co-bureau). Ensuite, je remercie mes « contemporains » : *Farah Haddad*, *Tang Jian* et en particulier *Ronan Léal*, mon co-bureau et camarade de misères durant ces trois années de thèse. Nos discussions existentielles à 22h dans les Algécos vides me manqueront ! Enfin, je tiens à remercier la nouvelle génération de thésards prometteurs, à commencer par ma co-bureau, et sparing partner de répétions, *Gwenaëlle W. Hamon*. Je n'oublie pas, *Fabien Lebreton* (#Fabulous_Fab), *Guillaume Fischer*, *Rafaël Peyronnet*, *Linda Assam* et *Amadeo Michaud*. Je compte sur vous pour faire (enfin) gagner le LPICM au tournoi de foot à l'X et fêter la victoire au bar de Lozère !

Mon travail de recherche m'a amené à travailler en collaboration avec quatre entités de recherche, ce qui a été très épanouissant pour moi. Je tiens donc à saluer les chercheurs de l'IEF (*Maria Tchernycheva*, *Valerio Piazza*, *Vladimir Neplokh*, *Fabien Bayle*), l'IEMN (*Didier Théron*, *Charlène Brillard*, *Fei Wang*), de l'IMEC (*Twan Bearda*), du GeePs (*José Alvarez*, *Abel Roige*, *Pascal Chrétien*, *Raphaël Lachaume*). Lors de ma thèse, j'ai également eu la chance de participer à deux projets de recherche: Nathisol et PhotoNvoltaics. Je tiens à remercier l'ensemble des membres des projets et en particulier, les coordinateurs, *Valérie Depauw* et *Emmanuel Drouard*.

Pour finir, cela fait 5 ans que je suis dans le domaine du photovoltaïque et j'aimerais remercier les gens qui m'ont donné envie de faire un doctorat dans ce domaine : *Riad Haidar* et son équipe à l'ONERA, *Alexandre Freundlich* et son équipe à University of Houston, les enseignants du master REST à l'Ecole Polytechnique et l'équipe prospective de Total Energies Nouvelles (en particulier mon encadrante *Véronique Jolivet*). Ces rencontres et expériences m'ont permis d'arriver avec un background suffisamment solide pour commencer mon doctorat dans de très bonnes conditions. Merci à eux.

Enfin, je suis évidemment très reconnaissant envers ma famille et mes amis, qui ont été d'un soutien sans faille tout au long de mon doctorat.

Paris, 30 Décembre 2016 P. N.

Contents

List of acronyms

Acronym	Definition
µ-PCD	Microwave PhotoConductance Decay
a-Si:H	Hydrogenated amorphous silicon
AFM	Atomic Force Microscopy
ALD	Atomic layer Deposition
AlO_x	Aluminum Oxide
AM	Amplitude Modulation
c-Si	Monocrystalline silicon
CAPEX	Capital Expanditures
CdTe	Cadmium Telluride
CIGS	Copper Indium Gallium Selenide
CP-AFM	Conducting Probe AFM
CPD	Contact Potential Difference
C-V	Capacitance Voltage
EBIC	Electron Beam Induced Current
E_F	Fermi level energy
E_g	Energy Bandgap
EFM	Electrostatic Force Microscopy
EM	Electron Microscopy
EM/SPM	Setup combining EM and SPM
EQE	External Quantum Efficiency
epi-Si	Epitaxial silicon
FIB	Focused Ion Beam
FF	Fill factor
FM	Frequency Modulation
FZ	Float Zone
HF	Hydrofluoric acid
IBC	Interdigitated Back Contact Solar Cells
IQE	Internal Quantum Efficiency
ITO	Indium Tin Oxide (Tin doped Indium Oxide)
IR	Infrared
J_{sc}	Short-circuit current
J(V)	Current density – voltage

Acronym	Definition
KPFM	Kelvin Probe Force Microscopy
LCOE	Levelized Cost Of Electricity
LED	Light Emitting Diode
OM	Optical Microscopy
NPV	Net Present Value
OM/SPM	Setup combining OM and SPM
OPEX	Operational Expanditures
PECVD	Plasma Enhanced Chemical Vapor Deposition
PL	Photoluminescence
Pt/Ir	Platinum Iridium
PV	Photovoltaics
RMS	Root Mean Square
SBB	Surface Band Bending
SE	Secondary Electrons
SEM	Scanning Electron Microscopy
SIMS	Secondary Ion Mass Spectroscopy
SiN_x	Silicon Nitride
SPM	Scanning Probe Microscopy
SP	Surface Potential
SSRM	Scanning Spreading Resistance Microscopy
STM	Scanning Tunneling Microscopy
TEM	Transmission Electron Microscopy
TIBB	Tip Induced Band Bending
TRMC	Time Resolved Microwave Conductivity
tr-EFM	Time Resolved Electrostatic Force Microscopy
tr-KPFM	Time Tesolved Kelvin Probe Force Microscopy
tr-PL	Time Resolved Photoluminescence
UPS	Ultraviolet Photoelectron Spectroscopy
UHV	Ultra High Vacuum
UV	Ultraviolet
V_b	Voltage Bias, Electrical Bias
V_{oc}	Open Circuit Voltage

Chapter 1 - Context

Contents

1.1 Crystalline silicon solar cells

1.1.1 Solar: A super-abundant source of green power

"The ultimate answer to humanity's energy problems rises every morning and sets every evening"
Editorial, Nature, 14th August 2008, A task of terawatts

As global population is increasing steadfastly and standards of living are improving worldwide, energy supply is undoubtedly one of the key 21st century challenges for humanity. Depending on scenarios, the world primary energy demand could increase between 12% and 45% by 2040 [1]. The answer to this challenge is all the more complicated that it is constrained by the evidence of the role of humanity on global warming. In 2007, the Fourth Assessment Report of the United Nations Intergovernmental Panel on Climate Change (IPCC) stressed that "warming of the climate is unequivocal" and that "most of the observed increase in global average temperature since the mid-20th century is very likely due to the observed increase in anthropogenic greenhouse gas concentrations." [2]. In 2014, the IPCC projections showed that temperature could increase up to 4°C in 2100 compared to its 2000 level [2]. In December 2015, the Conference of Parties (COP21) was held in Paris to tackle this issue and 185 countries agreed to commit to long-term greenhouse gas emission trajectories with long term targets to keep temperature increase below 2°C or even 1.5°C by the end of the century. In this perspective, abundant sources of energy with low global warming effect are required in order to meet global demand.

Within energy demand, electricity is expected to take up an increasing role. In 2013, electricity weighted 18% of global energy demand in total final consumption. The IEA expects this share to will reach 40% by 2040, driven by increasing use in industries, ongoing shift of population to urban centers and rising living standards [1], including the electrification of vehicles. In the following, we will provide insights on the problematic of supplying more electricity while reducing greenhouse emission gases.

To address this problematic, we can make a two steps reasoning. First, we list the different energies by availability of resources. Then, we list them by their impact on environment through greenhouse emissions. In order to assess the availability of final energy, we have to consider its potential resource, its energy efficiency and its load factor. Figure 1.1 shows the resources availability of each kind of energy source with respect to global annual energy consumption.

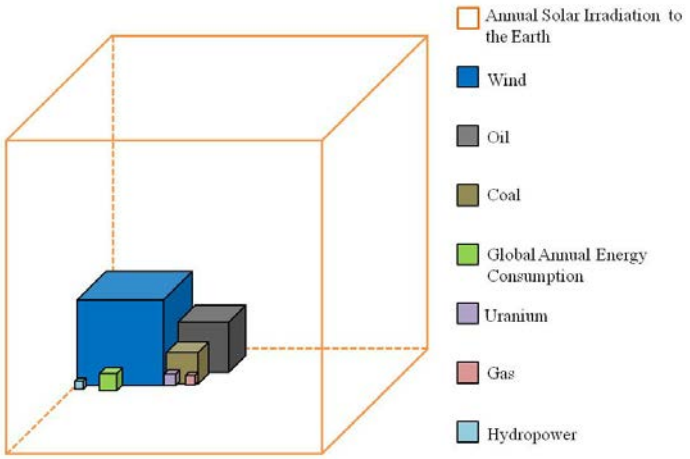

Fig. 1.1 – Fuel ressource per energy with respect to the global energy consumption. Fossils fuels are expressed with their total known reserves. Renewable energies are expressed with their yearly energy resource.

This figure shows that solar energy is by far the most abundant source of primary energy on earth. Calculations show that the annual incident solar energy on Earth is 10 000 times the annual consumption. To give an order of magnitude, covering India (~0.6% of Earth surface) with average solar panels (15% efficiency) and an average load factor of 10% would be enough to cover humanity energy needs. These panels could also be positioned on water areas thanks to the recent development of floating photovoltaics [3]. It can also be noticed that solar energy is much more abundant than other energy sources and that, most of the renewable abundant energy sources (e.g. wind, hydroelectricity and biomass) are indirectly linked to incident solar power.

Table 1.1 shows the greenhouse gases emission by energy source, according to Intergovernmental Panel on Climate Change (IPCC) [2]. For solar power, different ways of producing electricity can be considered such solar thermal energy and photovoltaics. For photovoltaics, the greenhouse emission gases level depends on the country of production, because the electricity is more carbonated in some countries than others. In any case, renewable energies are in median 4 to 20 times less polluting than conventional fossil fuels. It should also be noted that photovoltaics requires low water consumption during its operation compared to thermal energy sources (only for cleaning of modules). This strengthens its low environmental impact.

Table 1.1 – Greenhouse Emission Gases by Energy Source [2]

	Lifecycle Emissions (incl. albedo effect) (gCO_2eq/kWh)		
Technologies	**Min**	**Median**	**Max**
Coal – (Pulverized Coal)	740	820	910
Gas – Combined Cycle	410	490	650
Solar PV – utility scale	18	48	180
Solar PV – rooftop	26	41	60
Concentrated Solar Power	8.8	27	63
Nuclear	3.7	12	110
Wind Onshore	7	11	56

These elements highlight that renewable energies provide abundant and environment friendly solutions to meet the XXIst century energy challenge. Most of these energies (e.g. wind, hydropower) are either directly or indirectly coming from solar energy. The most straightforward way to produce electricity from solar energy is photovoltaics because no intermediate energy is used, which enables higher efficiency of energy conversion. However, it is not enough for photovoltaics to be an efficient, low carbon emission and unlimited resource. It also has to be cost competitive and reliable in time to be adopted worldwide. In the following part, we will detail how photovoltaics made it from a scientific curiosity to a bankable energy solution.

1.1.2 Photovoltaics: From a scientific curiosity to a bankable energy solution

The photovoltaic (PV) effect was discovered in 1839 by Antoine Cesar Becquerel and his son Alexandre Edmond Becquerel. The latter presented this effect in front of the French “Académie des Sciences”. Using this effect, the first solar cell was fabricated in 1883 by Charles Fritts who used very thin layers of gold on selenium. The efficiency reached was around 1% and the project was stopped because of the cost of materials [4].

More than 70 years passed before a technological breakthrough enabled to consider possible photovoltaics applications: in 1954, Gerald Pearson, Darryl Charpin and Calvin Fuller from Bell Laboratories presented a silicon solar panel reaching 6% efficiency and patented it as a “solar energy converting apparatus” [5]. They used silicon doping that was discovered just fifteen years before by Russell Ohl. First applications included PV powered dollar bill changers.

One of the first photovoltaics applications was energy provision in space. In 1958, the first solar cells were sent to space and were providing electricity to the radioelectric emitters of the satellite Vanguard 1. They were made of silicon and reached 9% efficiency.

In the 1970s, Dr Elliott Berman designed a less costly solar cell bringing down the cost from $100/W to $20/W [6]. This paved the way for terrestrial applications such as navigation warning lights and horns, lighthouses or railroad crossings. Photovoltaics started to be considered as an interesting energy source for remote off-grid locations.

In the beginning of the 1980s, solar modules were considered for building power stations. The first megawatt-scale power station was built in Hisperia, California in 1982[7]. That same year, the worldwide photovoltaic production exceeded 9 MW. Some rural areas in Tahiti, Kenya and Central America started to use PV as the main source of energy [7]. At this time people came to realize that solar energy could also be considered as a decentralized source of energy and the idea of rooftop applications came up. In 1985, Sunpower, the current technological leader of commercial crystalline silicon solar cells was founded by Dr. Richard Swanson [8].

In the 1990s, solar cells price continued to drop and efficiencies continued to rise. Solar proved to be a cost effective solution to small scale electrical demands located away from utility lines. Solar cells started to power bus shelters, street lamps and warning lights. The applications started to be visible inside the cities. However the prices were still too high to be competitive with traditional electrical sources (e.g. nuclear, gas and coal).

Since the beginning of the 2000s, the cost of solar panels started to be low enough to be considered as cost competitive solution on the electrical grid. Today, the capacity is about to hit 200 GW and the record commercial cell efficiency is 25% [9]. Figure 1.2 shows how the price of solar electricity was reduced compared to other energy sources in China. It can be noted that photovoltaics has the fastest declining cost and will soon be competitive with the onshore wind. The tendency makes some analysts believe that solar modules will soon become a commodity market [10]. The social acceptance of photovoltaics will increase thanks to decreasing energy paybacktime and improvement of solar modules recyclability which today already reaches over 90% [11].

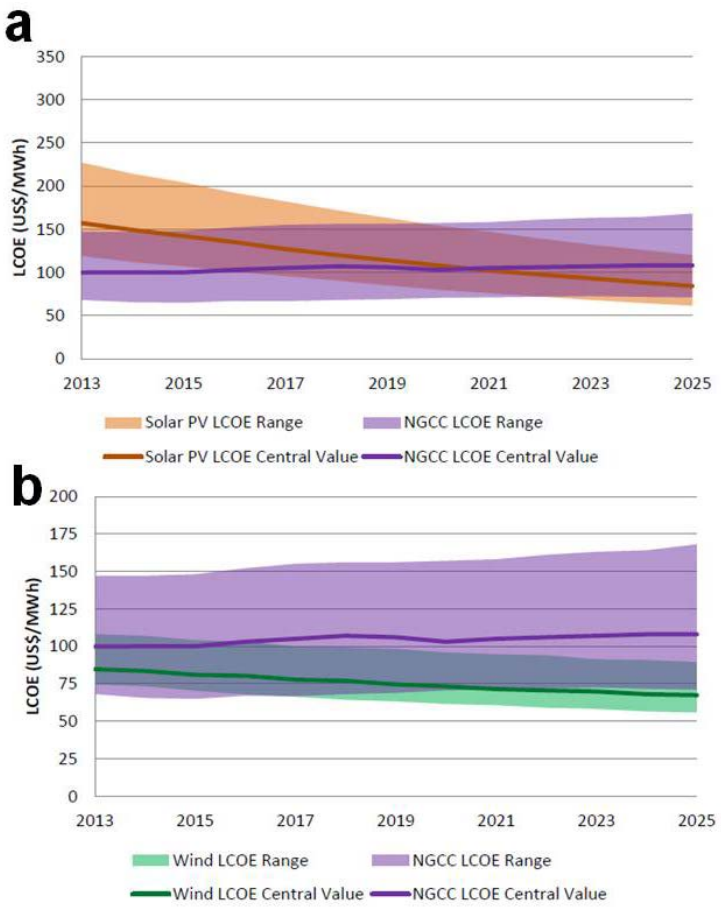

Fig. 1.2 – a) Evolution of China utility Solar PV Levelized Cost of Electricity (LCOE) compared to Natural Gas Combined Cycle (NGCC). b) Evolution of China Wind Levelized Cost of Electricity (LCOE) compared to Natural Gas Combined Cycle (NGCC) [12]

Solar modules are more competitive economically and this translates in terms of installed capacity. Even though, photovoltaics only represents 1% of global electricity mix worldwide, the tendency is shaping up, as Figure 1.3 shows. By 2040, the total capacity should grow by 500%. This trend should lead solar PV to reach 4% of the electricity generation by 2040, according to the new policies scenario of EIA [1].

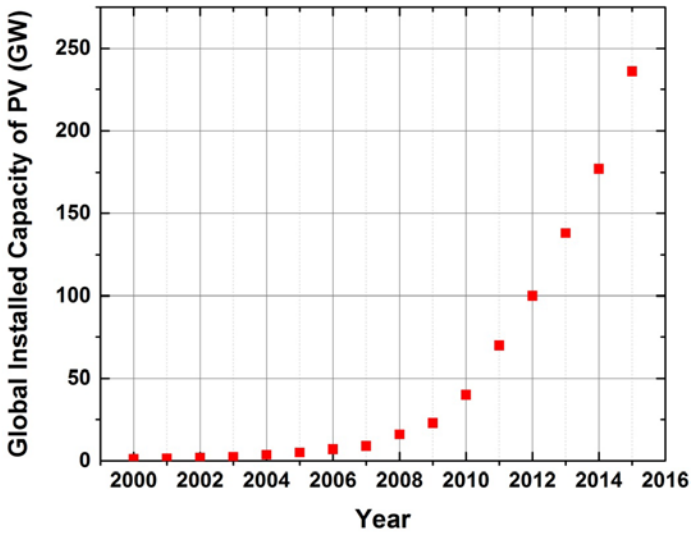

Fig. 1.3 – Evolution of global installed capacity of photovoltaics [13]

For the moment, the growth of photovoltaics is limited by three main hurdles:

- Solar energy is intermittent: low energy is produced during cloudy days and no energy is produced at night. The intermittency raises problems of stability on the electrical grid. This limitation can be mitigated with better weather forecast and electrical grid interconnections. It could be solved with cost competitive electrical storage solutions. The recent progresses in batteries make this perspective foreseeable at mid term. Batteries adapted for residential application, such as Powerwall by Tesla, start to be cost-competitive. The solution "solar panels + batteries" could lead to a competitive decentralized energy production that could significantly change the centralized conception of energy that has been promoted by utilities so far.
- Photovoltaics is a capital intensive energy. Compared to fossile fuel energies (e.g. coal or gas), a lot of capital expenditures (CAPEX) have to be spent first. Then, operational expenditures (OPEX) are very low because no fuel and low maintenance is required. The high CAPEX/OPEX ratio makes it a financially risky energy. This risk is all the more perceived by investors that in many countries, the regulatory framework has lately been unpredictable and unreliable for long term investments. A long term vision is required to make investments in photovoltaics trustworthy and to gain back the confidence of investors. To mitigate the financial risks, solar installers and module manufacturers now propose new financial solutions for rooftop applications. They will invest in a proportion of the capital expenditures.
- The global solar module capacity does not match the evergrowing demand and a lot of solar manufacturers are out of stock and planning capacity expansions. This capacity increase is also expected for raw material providers. For instance, polysilicon capacity is expected to rise from 376 kilometric tons in 2015 to 481 kilometric tones in 2018 [14].

None of these limitations are unadressable and solutions are already coming up to overcome them. That is why the future of solar PV looks bright. From a scientific curiosity in the middle of the XIXth century, it has become a competitive energy source, already reaching "grid parity" in many countries. All the trends show that its competitiveness will increase in the XXIst century to start gaining significant market shares worldwide [15].

The current and future technological progresses are at the heart of solar PV improvement. In particular, silicon solar modules have made spectacular progress in the last decades. Even though this technology is considered as the first generation [16], the evolution of market shares shows that crystalline silicon solar cells has always been dominant on the market and that its hegemony is going to last in the future decades.

1.1.3 Silicon Solar Cells : The unassailed first generation

"What makes competition between technologies interesting is that usually technologies become more attractive –more developed, more widespread, more useful – the more they are adopted" –

Arthur, 1988, "Competing technologies: an overview", in Dosi *et al.*, Technical Change and Economic Theory, Pinter Publishers.

Solar cell industry often is divided into three generations [16]. The first generation is the historic crystalline silicon (c-Si) technology. It benefits from a well developed understanding of the physics of silicon devices and the huge technology base developed by the microelectronics industry. This generation is divided in monocrystalline, multicrystalline and ribbon silicon solar cells. The second generation is called thin film solar technologies because the thickness of the cell (a few microns) is 10 to 100 times thinner than the first generation. The second generation is composed of amorphous silicon (a-Si:H) solar cells, copper indium gallium diselenide (CIGS) and cadmium telluride (CdTe) solar cells. Finally, the third generation of solar cells includes all the new concepts that include organic and inorganic solar cells and some concepts, such as multijunctions, that could enable to overcome some efficiency limitations of the first and second generation of solar cells. Despite the fact

that recent third generation of solar cells such as perovskite solar cells, have made considerable efficiency improvements, this generation of solar cells is not mature yet. In particular, the lifetimes of these cells are often lower than one year, compared to 25 to 35 years for the first and second generation.

Figure 1.4 shows the evolution of market shares of the three subfamilies of the first generation and the second generation. It can be seen that even though ribbon silicon has totally disappeared from the market, the share of the first generation (mono-Si and multi-Si) has always been above 65% and that in the last five years, it went from 80% to 90%. Two reasons can be given for this trend: first, crystalline silicon factories are cheaper to build than thin film factories. Then, the price of polysilicon decreased. It was divided by almost 5 since 2010 because there has been an increase in polysilicon production capacities over the past five years.

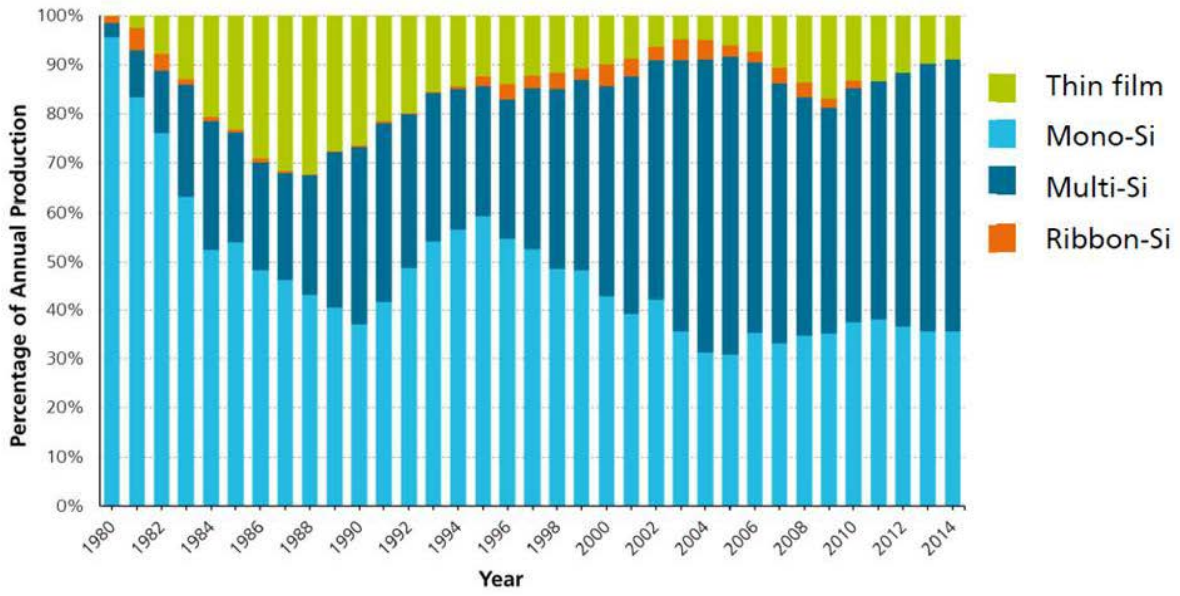

Fig. 1.4 – Market share of crystalline silicon in time [17]

In terms of $/W, the cost of the most competitive thin film solar modules (CdTe) is close to that of the most competitive c-Si solar cells (polysilicon solar module). According to PVInsight in March 2016, a polysilicon solar module was priced 0.54$/W in average compared to $0.57/W, the average price of a thin film solar module [18]. However, crystalline silicon solar modules present higher efficiencies. The record large c-Si solar module reaches 24.1% [19] whereas the record thin film solar modules is 17.5% [20]. When designing solar power plant projects, efficiency of modules is a key because, for the same capacity installed, less land, maintenance, and balance of system (wirings, racks, invertors) are required. Therefore, even though c-Si modules are more expensive, their efficiency can make the solar project less costly. In the case of rooftops, the area available for solar modules is limited. So, people will turn more easily to crystalline silicon solar modules to get the most energy out of their limited space. It also has to be added that crystalline silicon solar modules usually have a slightly lower degradation rate than thin film solar modules, which increases their competitiveness in the long run. The best crystalline silicon modules now reach below 0.5%/year degradation rates enabling 25 years commercial warranties, whereas best thin film modules are between 0.5%/year and 1%/year degradation rates [21].

Besides the toxicity of elements, such as cadmium, in certain technologies, one of the main limitations of thin film technologies is that most of the elements used are limited in reserves. Contrary to silicon which is one of the most abundant materials in the earth’s crust, tellurium, selenium and indium are not suitable for very large-scale deployment of solar photovoltaics. These materials have a crustal abundance seven to nine order of magnitudes lower than silicon and are only one to three order of magnitudes less material intensive [22].

Given the low price of polysilicon, it is very unlikely that crystalline silicon solar modules will be challenged by thin films in the short/midterm.

1.1.4 Solar cells: one of the many pieces of the photovoltaics puzzle

Photovoltaics has already reached grid parity in different parts of the world (e.g. Italy, California, Germany) but in order to widespread grid parity worldwide, photovoltaics (PV) has to keep getting more competitive with respect to other power sources.

Competitiveness is not only related to solar modules improvements. One has to keep in mind that the final aim of an investor is to get the highest net present value (NPV) possible out of a project. Net present value is the difference between the present value of revenues and the present value of costs. Therefore many strategies to increase the NPV without changing modules can be thought off. For instance, cost strategies may include a reduction of installation labor through an automation, a reduction of project balance of systems (wiring, invertors, racking systems,…), a reduction of maintenance costs, using robots to clean the panels for instance. Revenue strategies are closely linked to the way the solar energy is rewarded (e.g. auto consumption, feed-in tariffs). It is the energy (kWh) that is rewarded and not the power capacity (kW). Examples include installation of battery systems and smart grid systems when it is viable, improvement in cleaning of solar modules or positioning the panels in areas which are cooled down by wind because silicon solar panels produce more energy at lower temperatures and thus profit from cooling.

Nevertheless, solar module improvement remains the key in the competitiveness of solar energy projects. At this point, we can raise the question: What is a valuable solar panel?

Three main criteria can define a valuable solar panel: cost, efficiency and reliability. Cost is all the more important that solar projects are capital extensive. Some customers may limit their requirements because of budget limitations. Efficiency is the share of incident photon energy that can be transformed into electricity. This electrical energy produced will directly translate in terms of revenue. Since solar projects are rewarded on the energy produced over their lifetime (~25years), the efficiency of the solar modules has to be maintained during that time. This is why reliability of solar modules is the key. Nowadays, solar cell manufacturers guarantee that the efficiency of the solar panels after 25 years will be higher than 80% of their nominal efficiency. Other criteria of competitiveness should be mentioned. Aestethics for instance is a matter of interest for building integration. The thermal behavior and angular dependence of the cell efficiency are two parameters that can help produce more energy for a given nominal efficiency. Thermal behavior will help lose less energy when the temperature rises [23] and angular behavior will help produce more energy at sunrise, sunset and with diffuse light [24].

A crystalline silicon solar module is composed of solar cells, wirings, glass, encapsulant, frame and junction box. All these elements have to be optimized to make cost-competitive, efficient, long lasting solar modules. That is why the efficiency of solar modules is often lower than the solar cell efficiency. In that perspective, the improvement of solar cells is important but it is only one piece of the complex puzzle of photovoltaics competitiveness.

1.1.5 Silicon Solar Cells: How to be valuable when approaching the theoretical limit?

As for solar modules, the three main parameters of a solar cell are efficiency, cost and reliability.

In terms of reliability, the efforts to increase the lifetime of modules are often focused on the glass, the encapsulant, the by-pass diodes or the frame. Those items aim at protecting the solar cell from external degradation phenomena (e.g. mechanical, UV exposure, humidity). Despite these protections, the solar cell itself can degrade with time. The most common degradation of crystalline silicon cells is due to the UV exposure [25], cracking due to mechanical or thermal stresses [26], corrosion of electrical contacts [27] and hot spot heating [28]. The attention on solar cells reliability is

all the more important that the failure of a single cell leads for the whole module to fail because the poor cell will dissipate the extra power of the rest of the cells. Therefore, an homogeneity of solar cells behavior has to be achieved. In order to fully understand degradation phenomena, nano-scale characterization techniques can be valuable. For example, in the case of UV degradation, it has been shown that the nanometric antireflective layer SiN_x is affected and the interface with the crystalline silicon is degraded [25]. Nano-scale investigation techniques enable to analyze the interfaces and their homogeneity along the wafer cross-section. Metal/Semiconductor interfaces investigation would also be of interest in the case of the corrosion of contacts for instance.

Regarding the efficiency, the first and second generations are single junction solar cells. This means that only one kind of material is used to absorb the light. All the incident photons on a single junction solar cell cannot convey all their energy to the electrons because the low energy photons are not absorbed by the cell and high energy photons energy is transformed only partially into electric energy. In 1961, William Schockley and Hans Queisser demonstrated that the maximum achievable efficiency for a single junction solar cell is 33% [29]. In the case of silicon which bandgap is not optimal and presents inherent losses, the maximum achievable efficiency is estimated at 29%. In 2016, Kaneka announced a laboratory record of 26.33% with a single junction silicon solar cell (IBC heterojunctions) [30]. Thus, the gap between theory and experiments for single junctions is narrowing down to a mere 3.4%. These losses are composed of optical losses and electrical losses: resistive or recombination losses. For both kinds of losses, the improvements in the industry are expected in a near future. These improvements are well summed up in the ITRPV report [31]. For instance, to reduce optical losses, the trend toward putting the two contacts at the back of the cell (back contact solar cells) may increase from less than 5% of the market today to 20% in 2025. These cells sometimes face series resistance issues due to issues of contacting. In these cases of investigation, having a nano-scale resolution can be very useful. In order to reduce the electrical losses, different strategies include new processes for wafers (new crystallization [32] and new sawing techniques), new strategies for doping the wafers (decreasing sheet resistance of contacted parts and new doping techniques), new contacting techniques to achieve low recombination contacts and new passivation techniques to reduce the defects responsible for recombination on the two sides of the wafers. Even when using new processing techniques, some defects are still remaining. For instance, in n-type crystalline silicon wafers, some atomic dislocations have induced parasitic electrical effects [33]. These are all short to midterm strategies. At long term, the necessity to go beyond the Schockley Queisser limit while being cost competitive seems inevitable. To achieve this objective, the most likely way is to go toward a double junction with another material. Many materials, such as perovskites, CZTS or GaAs are under investigation worldwide but for the moment, no solution is mature enough in a midterm perspective. For these multi-junction technologies, nano-scale analysis of interfaces between materials is crucial to check the electrical properties and their homogeneity [34].

Given that efficiency improvements are limited to 3.4% at midterm perspective, cost improvements represent the main overall challenge for crystalline silicon solar cells. Different strategies of cost reduction are considered. The reduction of wafer thickness is one of the most important. According to ITRPV, the average wafer thickness in industry should decrease from 180 µm in 2015 to 120 µm in 2025 [31]. More aggressive strategies using bottom up epitaxial silicon aim at producing wafers 50 µm thick or below [35], [36]. At LPICM, an expertise on low temperature epitaxial silicon solar cells has been built [37], [38]. To increase the absorption of these cells, improvement on light trapping has to be achieved. This can be performed by using nanophotonics concepts, which was the ambition of the European project PhotoNvoltaics [39], [40] and French project Nathisol [41]. Light trapping can be obtained using photonic crystals [42] or nano-texturing. In the case of nano-texturing, the use of nano-scale characterization techniques is obvious. Nanostructuring techniques are sometimes aggressive and create nano-scale defects that have to be investigated. Other cost reduction strategies include the reduction of the costs of contacts. One example is the amount of silver per cell. A decrease from 0.10 g/cell in 2015 to 0.04 g/cell in 2025 is expected. Other materials such as copper are also considered to replace silver. Another example is the use of new metallization technologies and to reduce the contact fingers width [31]. Finally, improvements in the throughput of equipments at all solar cell process steps are expected, making

future cells more cost competitive. All the difficulty is to be able to reduce costs while preserving efficiency and reliability. Therefore, any change in the production line may induce new sources of performance or reliability drop. Investigation of these drops is crucial to start a new optimization of processes enabling to achieve a new efficiency-cost-reliability optimum.

While mapping the different perspectives for future crystalline silicon solar cells improvement, we concluded that nano-scale analysis could help understanding degradation phenomena and detect defects in new designs that aim at improving efficiency and reducing cost. The closer from the limit we get, the harder the implementation of novel solutions on crystalline silicon solar cells are. In that perspective, developing new nano-scale characterization techniques designed for specific photovoltaic problematic is important.

In the following part, we will discuss the recent evolution of a young family of microscopy techniques called scanning probe microscopy. It enables new nano-scale measurement on solar cells which were not possible with traditional optical and electronic microscopy techniques before.

1.2 Scanning probe microscopy

1.2.1 Scanning Probe Microscopy: “Feeling” the surface at the nano-scale.

“For scanning tunneling microscopy, we brought along some experience in tunneling and angstroms but none in microscopy or surface science. This probably gave us the courage and light-heartedness to start something which should “not have worked in principle” as we were so often told. “

Gerd Binnig and Heinrich Rohrer, Nobel Lecture, December 8th 1986 – Scanning Tunneling Microscopy from Birth to Adolescence.

In 1986, Gerd Binnig and Heinrich Rohrer received the Nobel Price for the invention of the scanning tunneling microscope (STM) which dazzled the world in 1981 with the first real-space images of the surface of silicon. Not only this invention enabled to perform surface measurements with a resolution which was unachievable at that time, but it also paved the way for a new family of microscopy techniques called “scanning probe microscopy” (SPM) which enables today to perform a broad range of measurements (e.g. electrical, chemical, thermal) at the nano-scale on the surface of all kinds of materials.

In nano-scale research, three families of microscopies are used: optical microscopy, electron microscopy and scanning probe microscopy. In optical and electron microscopies, a beam of carriers, either photons or electrons are focused on a spot of the surface to be analyzed. Because the wavelength of these carriers is below the micrometer, these techniques enable researchers to see at the nano-scale. The information on the surface is extracted from the reflected or transmitted carriers. This is exactly the mechanism used by the human eye to see an object by interpreting the intensity of detected photons. In the case of scanning probe microscopy, images of surfaces are performed using a physical nano-probe that scans the surface. Therefore, scanning probe microscopy is very similar to feeling or touching the surface at the nano-scale. For the three microscopy techniques, surface roughness can be seen. However, the way to get it is different. This induces pros and cons for each of these techniques.

Optical microscopy is the oldest family of microscopies. The development of modern optical microscopy took place in the middle of the 19th century. It is the only microscopy technique that enables real color imaging. It also has the advantage of being versatile, fast and to require no sample pre-treatment. However, its lateral resolution is limited by the diffraction limit to more than a hundred of nanometers. Recently, some progress has been made to go below the 100nm resolution using

holography or fluorescence for instance, but these techniques remain so far limited to niche applications.

In order to reach resolutions below 100nm, shorter wavelengths than the traditional one used in optical microscopy can also be used. High energy electrons can reach much shorter wavelengths that enable resolution below one Angstrom. For instance, using a 20 kV electron gun, the electron spot can reach down to 0.3 Angstroms. Electron Microscopy was invented in 1931 by two German scientists: Max Knott and Ernst Ruska [43]. Ernst Ruska was awarded the Nobel Prize in 1986, the same year as Gerd Binnig and Heinrich Rohrer. Transmission electron microscopy (TEM) was developed first because the resolution for scanning electron microscopy (SEM) was limited at that time to 100 µm [38]. The first transmission electron microscope was built in 1933 [43] and the first commercial TEM was available in 1939 for which a resolution of 2 nm was claimed [43]. Because it was difficult to compete with the resolution of TEM, it took a long time for the community to understand the interest of scanning electron microscopy. The first true SEM was developed by Zworykin in 1942 and reached a resolution of 50 nm. It took more than 20 years of resolution improvements to convince the scientific community of the interest of SEM. In 1965, the first commercial SEM was presented by Cambridge Scientifc Instruments [44] with a resolution of 10 nm. Since then, the number of publications using SEM has overcome that using TEM, as Figure 1.5 shows. SEM offers the advantage of analyzing all kind of samples: conductors, semiconductors or insulators (covered with stain coating). It does not require a major surface preparation step. However, its resolution is limited to a few nanometers which is one to two order of magnitudes better than optical microscopy but also one to two orders of magnitude worst than TEM and scanning probe microscopies. Indeed, TEM can reach resolutions close to the Angstrom (<0.2 nm) enabling direct imaging of crystalline lattices, which is used to delineate defects inside the sample for instance. However, the preparation of samples for TEM is complicated and time consuming because a long preparation is required to make the samples atomically thin.

Compared to optical and electron microscopies, scanning probe microscopy is not limited by any resolution limitation due to diffraction. It is only limited by the size of the probe-sample interaction volume. With ultra-sharp tips, resolution below the nanometer can be achieved [45]. The most striking example is the imaging of silicon atomic steps, with STM for instance [46]. This offers unparallel possibilities of height measurement. With the improvements of the scanning probes, resolutions in the angstrom range are now possible using SPM. Another advantage of SPMs is that they can perform measurements in a wide range of environments: ambient air, vacuum and also liquids. However, scanning probe microscopy is currently limited by its scan speed and the maximum measurable size which is close to 100 µm. Uncertainties due to the piezoelectric actuator and to the shape of the probe can also be problematic for accurate measurements. We will detail the advantages and limitations of scanning probe microscopies for solar cell investigation in part 3 and part 4 of the manuscript. Many of the SPM limitations are addressable and current trends show that serious progresses are coming up. One has to keep in mind that scanning probe microscopy is a relatively young family of microscopy techniques. It was developed in the 1980s-1990s. Considering the number of publications (Fig.1.5), SPM techniques are 50 years older than the first electron microscopy technique (TEM), and 25 years older than SEM. The historic SPM techniques like scanning tunneling microscopy (STM) and atomic force microscopy (AFM) have reached maturity and are now used on regular basis, offering complementary analysis to optical and electron microscopies. However, the new SPM techniques are still at maturation level and show great promises in different fields of application. In the following, we will come back on the history of SPMs and see how the STM gave birth to a wide family of SPM techniques.

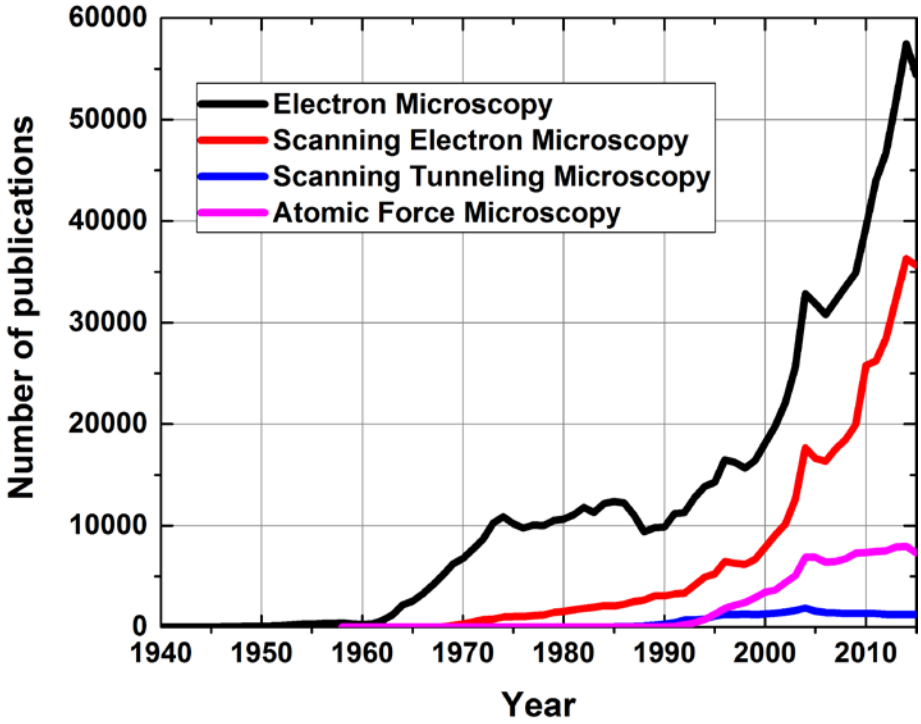

Figure 1.5 – Evolution of the number of publications in the SCOPUS database for the family of electron microscopy (SEM and TEM), scanning electron microscopy (SEM), scanning tunneling microscopy and atomic force microscopy

1.2.2 STM, AFM & the wide family of AFM extensions

The two main reasons behind the birth of scanning probe microscopy techniques at the beginning of the 1980s were the maturity of tunneling experiments and the availability of piezoelectric devices.

Even though the principle of tunneling effect was discovered in 1903, the acceptance of electron tunneling in solids happened in the late 1950s with the first studies on semiconductors. Vacuum tunneling spectroscopy measurements took time to develop because of experimental hurdles, mainly vibration problems. In 1981, G. Binnig *et al.* showed the feasibility of vacuum tunneling with modest means. The suppression of vibrations was achieved by soft suspension of a compact tunneling unit [47]. Given this result, mapping of tunneling signal was achieved with the use of a piezoelectric actuator which enables motions of the scanning tip below the nanometer.

Despite the fact that piezoelectricity found its first applications at the beginning of the 20th century, the spreading of piezo devices only happened in the 1970s when Japanese companies and universities formed a “competitively cooperative association” which aimed at developing knowledge, new applications, new processes, and new commercial markets for piezoelectric devices in a coherent and profitable way. This lead to the development of new piezoresistive families which were both competitive and free of patents. Those actuators were used in the first scanning probe microscopes.

In 1981, G. Binnig and H. Rohrer introduced the Scanning Tunneling Microscope (STM), which was the first instrument to generate real-space imaging of surfaces with atomic resolution. Their key success was to introduce a feedback loop to regulate the distance between the sample and the probe. STM was the first scanning probe microscopy technique and it paved the way for a wide family of scanning probe microscopy techniques, as Figure 1.6 shows.

Following the STM, two topographical scanning probe microscopies rose up: the scanning near field optical microscope (SNOM) and the atomic force microscope (AFM). The SNOM uses near

field optics below the scanning tip to perform optical images with a resolution lower than the wavelength λ, typically λ/20. The AFM uses the forces between the tip and the sample to make a 3D image of the surface at the nano-scale. The motion is monitored by the reflection of a laser beam on the tip which is recorded by a photodetector. The great advantage of AFM compared to STM is that it is not limited to electrically conductive surfaces to get a tunneling current. AFM is a material agnostic technique. It was invented in 1986 by G. Binnig, C. Gerber and C.F. Quate and became commercially available in 1988.

During an AFM scan, several kinds of interactions can be recorded along with the topographical image. For instance, electrostatic or magnetic forces can interact with the probe while scanning. An SPM extension is a manner of using these interactions to map a signal. Shortly after the invention of AFM, a wide range of SPM techniques was developed enabling nano-scale imaging of thermal, piezoelectric, mechanical, chemical, magnetic and electrical properties (see Figure 1.6). The principle of these techniques is the same: the AFM probe makes it possible to transfer an existing macro-scale technique to a nano-scale one. However, quantitative analysis at nano-scale is challenging to achieve because many additional artefacts take place, such as correlation of the measurement to the topography or local tip-induced oxidation. Therefore, interpretations of nano-scale SPM measurements are sometimes challenging and some SPM extensions remain qualitative. Improvements of SPM extensions are still underway with qualitative measurements at nano-scale already giving insightful information in several research fields.

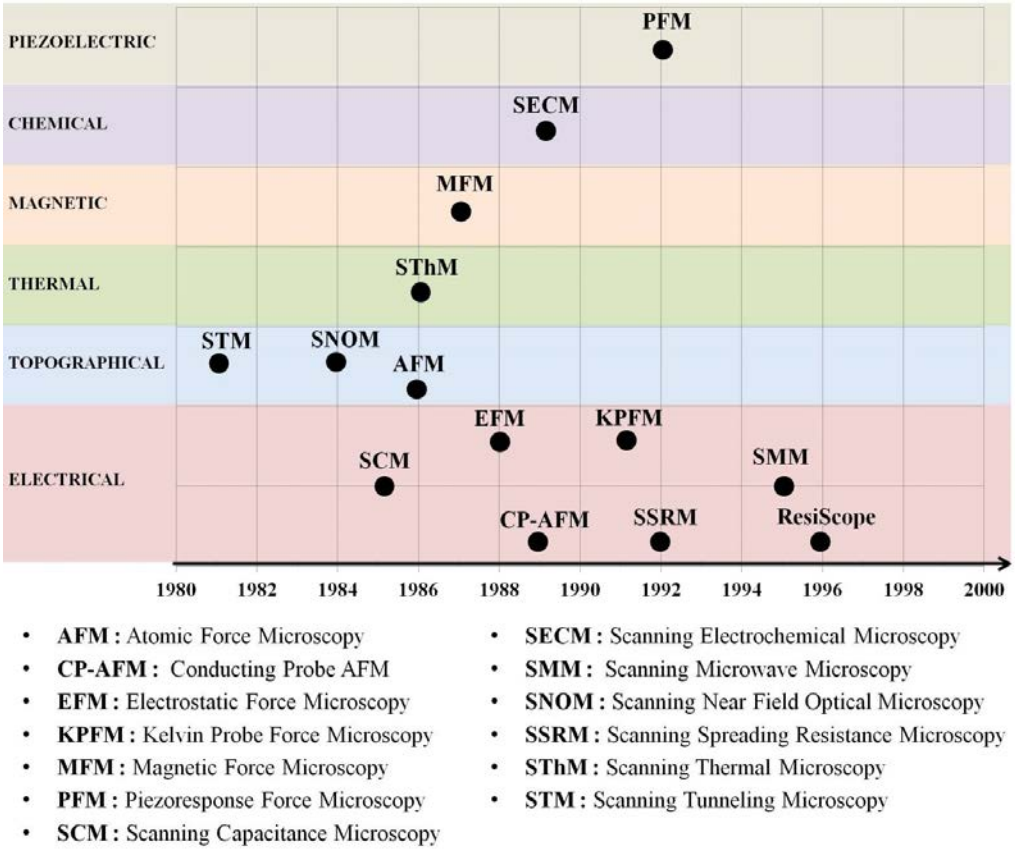

Figure 1.6 – Family tree of the main scanning probe microscopy techniques with their dates of invention

To investigate solar cells, several scanning probe techniques can be of interest. Topographical techniques for example are used routinely to investigate the roughness of wafers or devices that use micro and nanostructures to improve light trapping. This investigation can be performed both on the solar cell and on the covering glass that can be structured as well. Mechanical properties can also be

investigated at the nano-scale. For a failure analysis for instance, it is of the prime interest to investigate stress within solar materials and devices. Another measurement of interest can be thermal investigation at the nano-scale in solar cells. As we saw previously, hot spots are particularly detrimental for solar cells. Having the ability to investigate temperature changes at the nano-scale using scanning thermal microscopy can provide additional information on the reasons for different quality or failure of solar cells [48].

In this Ph.D. project, the aim was to use electrical AFM extensions to investigate silicon solar cells. The scope of SPM was narrowed down to these extensions which already constitute a broad field of investigation. In the following, we will detail the different electrical extensions and explain the three main electrical extension families.

1.2.3 Electrical Extensions: Putting on the right glasses for solar cell investigation

All electrical extensions perform electrical measurements at nano-scale using a conducting probe. From our analysis, we propose to divide electrical extensions in three main categories: the electrostratic extensions, the current/resistance extensions and the impedance extensions.

The current/resistance extensions measure current and resistance at nano-scale by applying a voltage bias difference between the probe and the sample. These extensions are performed with the tip always in contact with the surface (AFM contact mode). The recorded current can be a tunneling current on an insulating layer, as in the case of tunneling atomic force microscopy, or a contact current as in the case of conducting probe AFM (CP-AFM). To obtain a wider range of measurable currents, a logarithmic amplifier can be added to measure currents over several orders of magnitude. This is the case for Scanning Spreading Resistance Microscopy (SSRM) and Resiscope, which are very similar techniques.

The electrostatic extensions map the electrostatic force between the sample and the probe. It can be measured directly in Electrostatic Force Microscopy (EFM) or using a feedback loop monitoring the amplitude of the AFM cantilever in Kelvin Probe Force Microscopy (KPFM). Measurements are performed in AFM tapping mode which means that the tip is softly oscillating in front of the surface. Therefore, they are not destructive. However, the resolution of these techniques is not better than 10 nm because measurements are performed at a distance of the sample.

Finally, the impedance extensions perform local capacitance and impedance measurements operating in contact mode by forming a metal-insulator-semiconductor (MOS) structure between the tip and the sample. This impedance is measured with an ultra-high frequency detector and is varied from an applied AC+DC bias which aims at creating impedance variations through the accumulation and depletion of the surface layers. Impedance extensions include Scanning Capacitance Microscopy (SCM) which measures the capacitance, and Scanning Microwave Microscopy (SMM) which measures the total impedance at the nano-scale.

Figure 1.7 shows the evolution of the number of publications in the database SCOPUS related to three electric extension categories until 2015. The keywords used for each category are mentioned. Compared to the number of articles published in 2015 mentioning AFM (~8000), the number of articles published for each category remains quite small (50 to 300). However, the rise of publications started five to ten years later than the invention of AFM and the increase is linear for electrostatic extensions and current/resistance extensions. The impedance extensions seem to have reached a plateau since the beginning of the 2000s, even though these techniques are very promising. An explanation might be that in impedance extensions, the combination of microwave and scanning probe is complex and requires a lot of expertise to achieve interpretable results. Electrostatic and Resistance/Current extensions are more user friendly techniques. If we sum up the publications, impedance extensions represent less than a fifth (16%), resistance/current extensions represent more than a third (35%) and the electrostatic extensions represent almost half of the publications (49%). Kelvin Probe Force Microscopy itself represents one third of electrical extension publications.

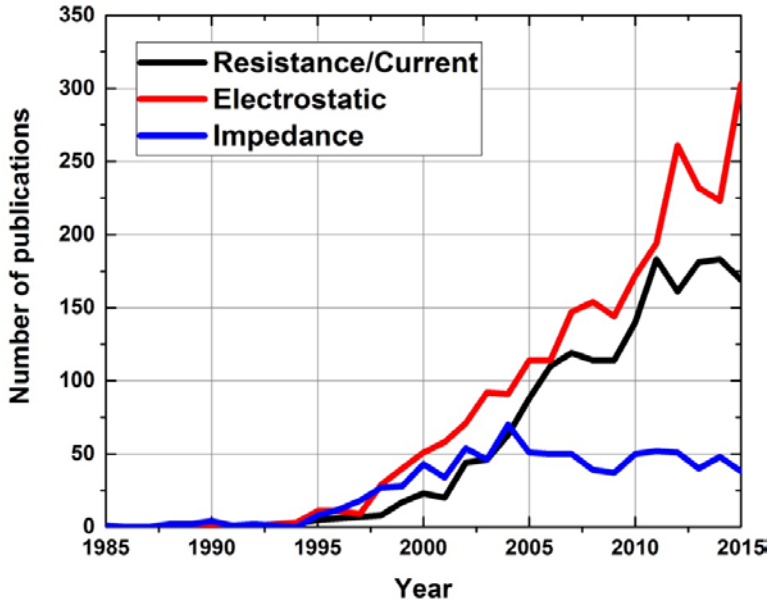

Keywords :

- **Resistance / Current Extensions :** "Conductive Atomic Force Microscopy", "Conducting Probe AFM", "CP-AFM", Resiscope", "SSRM", "Scanning Spreading Resistance Microscopy", "Resiscope", "Tunneling Atomic Force Microscopy"
- **Electrostatic Extensions :** "KPFM", "Kelvin Probe Microscopy", "Kelvin Probe Force Microscopy", "Scanning Kelvin Probe Force Microscopy", "Electrostatic Force Microscopy", Electric Force Microscopy"
- **Impedance Extensions:** "Microwave Microscopy", "Scanning Capacitance Microscopy", "Scanning Microwave Microscopy", "Scanning Microwave Impedance Microscopy"

Figure 1.7 – Repartition of the number of articles by year for the different electrical extension families

In this Ph.D. project, we chose to focus on the Kelvin Probe Force Microscopy and Resiscope, which is an advanced Conducting Probe AFM technique developed by LGEP (now GeePs), to investigate crystalline silicon solar cells. The reason for the choice of these extensions is that they are relatively user friendly and that in literature these techniques have already proven to be adapted for solar cell investigations at the nano-scale. Some measurements were also performed using electron microscopy techniques (SEM and EBIC) to compare with CP-AFM and KPFM measurements and assess how scanning probe microscopy and electron microscopy can be complementary for solar cells investigation. In the following, we will first explain in details the microscopy techniques used and the solar cells investigated (Chapter 2). Then, we will develop in details the challenges (Chapter 3) and the advantages (Chapter 4) of scanning probe microscopy techniques to investigate solar cells with respect to other nano-scale resolution techniques. In Chapter 5 and 6, we will detail respectively material and devices measurements of interest for solar cells using these techniques. In the conclusion, we will sum up our achievements, and propose an ideal SPM setup for nano-scale investigation of solar cells.

"The STM's "Years of Apprenticeship" have come to an end, the fundamentals have been laid, and the "Years of Travel" begin. We should not like to speculate where it will finally lead, but we sincerely trust that the beauty of atomic structures might be an inducement to apply the technique to those problems where it will be of greatest service solely to the benefit of mankind. Alfred Nobel's hope, our hope, everybody's hope. »

Gerd Binnig and Heinrich Rohrer, Nobel Lecture, December 8th 1986 – Scanning Tunneling Microscopy from Birth to Adolescence.

REFERENCES

[1] The International Energy Agency (IEA). The World Energy Outlook 2015, 2015

[2] IPCC. Climate Change 2014: Mitigation to Climate Change. Contribution of Working Group III to Fifth Assessment Report to the Intergovernmental Panel on Climate Change. *Cambridge University Press*. 2014

[3] K. Trapani, M. R. Santafé, "A review of floating installations: 2007-2013", *Prog. Photovolt. Res. Appl.*, vol. 23, no. 4, pp. 524–532, Apr. 2015.

[4] C. Fritts, “On a new form of selenium cell, and some electrical discoveries made by its use,” Am. J. Sci., vol. 26, pp. 465–472, Dec-1883.

[5] D. M. Chapin, C. S. Fuller, and G. L. Pearson, “Solar energy converting apparatus,” US2780765 A, 05-Feb-1957.

[6] E. Berman, “The Down-to-Earth Story of Photovoltaics,” *Science*, vol. 287, no. 5451, pp. 233–233, Jan. 2000.

[7] J. Perlin, “A History of Photovoltaics”, *Available at* (http://www.usc.edu/org/edisonchallenge/2008/ws1/A%20History%20of%20Photovoltaics.pdf) (accessed on 8 Oct. 2016)

[8] SunPower Corporation website, “SunPower History,” *Available at* (https://us.sunpower.com/company/history/) (accessed on 8 Oct. 2016)

[9] P. J. Cousins, D. D. Smith, H. C. Luan, J. Manning, T. D. Dennis, A. Waldhauer, K. E. Wilson, G. Harley, and W. P. Mulligan, “Generation 3: Improved performance at lower cost,” *35th IEEE Photovoltaic Specialists Conference (PVSC)*, 2010, pp. 000275–000278.

[10] H. K. Trabish, “Are PV Modules a Commodity?,” *Available at (*http://www.greentechmedia.com/articles/read/are-pv-modules-a-commodity.) (accessed on 8 Oct. 2016).

[11] J. Tao, S. Yu, "Review on feasible recycling pathways and technologies of solar photovoltaic modules", *Sol. Energy Mater. Sol. Cells*, vol. 141, pp. 108-124, October 2015

[12] C. Stark, J. Pless, J. Logan, E. Zhou, D. J. Arent, "Renewable Electricity: Insights for the coming decade", National Renewable Energy Laboratory, Feb. 2015

[13] REN21. Renewable energy policy network for the 21st century. *Renewables 2015 Global Status.* Jun. 2016.

[14] GTM Research, "Polysilicon 2015-2018: Supply, Demand, Cost and Princing", *Available at* (https://www.greentechmedia.com/research/report/polysilicon-2015-2018) (accessed on 8 Oct. 2016)

[15] A. Jäger-Waldau, “Photovoltaics: Status and Perspectives until 2020,” *Green*, vol. 1, no. 3, pp. 277–290, 2011.

[16] M. A. Green, “Third generation photovoltaics: solar cells for 2020 and beyond,” *Phys. E Low-Dimens. Syst. Nanostructures*, vol. 14, no. 1–2, pp. 65–70, Apr. 2002.

[17] Fraunhofer Institute for Solar Energy Systems, "Photovoltaics Report", Nov. 2015

[18] PV Insights: Solar Photovoltaic Prices and Research Reports. *Available at* (http://pvinsights.com/) (accessed on 8 Oct. 2016)

[19] D. D. Smith, G. Reich, M. Baldrias, M. Reich, N. Boitnott, and G. Bunea, “Silicon solar cells with total area efficiency above 25%,” *43rd IEEE Photovoltaic Specialists Conference (PVSC)*, 2016, pp. 3351–3355.

[20] M. A. Green, K. Emery, Y. Hishikawa, W. Warta, and E. D. Dunlop, “Solar cell efficiency tables (Version 45),” *Prog. Photovolt. Res. Appl.*, vol. 23, no. 1, pp. 1–9, Jan. 2015.

[21] D. C. Jordan and S. R. Kurtz, “Photovoltaic Degradation Rates—an Analytical Review,” *Prog. Photovolt. Res. Appl.*, vol. 21, no. 1, pp. 12–29, Jan. 2013.

[22] MIT Energy Iniatitve, “The Future of Solar Energy,” *Available at (*http://energy.mit.edu/publication/future-solar-energy/) (accessed on 8 Oct. 2016)

[23] P. K. Dash, “Effect of Temperature on Power Output from Different Commercially available Photovoltaic Modules,” *Int. J. Eng. Res. Appl.*, vol. 1, no. 5, pp. 148–151.

[24] M. Ebert, H. Stascheit, I. Hädrich, and U. Eitner, “The impact of angular dependent loss measurement on PV module energy yield prediction,” *29th EU PVSEC Proceedings*, no. 5CV.2.10, pp. 3244–3247, 2014.

[25] H. Kim, P. Choi, K. Kim, H. Kuh, D. Beak, J. Lee, J. Yi, and B. Choi, “Performance Degradation of c-Si Solar Cells Under UV Exposure,” *J. Nanosci. Nanotechnol.*, vol. 14, no. 5, pp. 3561–3563, 2014

[26] T.-K. Wen and C.-C. Yin, “Crack detection in photovoltaic cells by interferometric analysis of electronic speckle patterns,” *Sol. Energy Mater. Sol. Cells*, vol. 98, pp. 216–223, Mar. 2012.
[27] M. Abdelhamid, R. Singh, and M. Omar, “Review of Microcrack Detection Techniques for Silicon Solar Cells,” *IEEE J. Photovolt.*, vol. 4, no. 1, pp. 514–524, Jan. 2014.
[28] J. Bauer, J.-M. Wagner, A. Lotnyk, H. Blumtritt, B. Lim, J. Schmidt, and O. Breitenstein, “Hot spots in multicrystalline silicon solar cells: avalanche breakdown due to etch pits,” *Phys. Status Solidi RRL – Rapid Res. Lett.*, vol. 3, no. 2–3, pp. 40–42, Mar. 2009.
[29] W. Shockley and H. J. Queisser, “Detailed Balance Limit of Efficiency of p-n Junction Solar Cells,” *J. Appl. Phys.*, vol. 32, no. 3, pp. 510–519, Mar. 1961.
[30] S. Pothecary, “Kaneka achieves new efficiency record for a practical size crystalline silicon PV cell,” *PV Magazine*. Available at (http://www.pv-magazine.com/news/details/beitrag/kaneka-achieves-new-efficiency-record-for-a-practical-size-crystalline-silicon-pv-cell_100026182/). (accessed on 8 Oct. 2016)
[31] International Technology Roadmap for Photovoltaic (ITRPV), Results 2015, Seventh Edition, March 2016.
[32] I. Gordon, L. Carnel, D. Van Gestel, G. Beaucarne, and J. Poortmans, “8% Efficient thin-film polycrystalline-silicon solar cells based on aluminum- induced crystallization and thermal CVD,” *Prog. Photovolt. Res. Appl.*, vol. 15, no. 7, pp. 575–586, Nov. 2007.
[33] C. Park, J. Lee, D. Yang, N. Balaji, M. Ju, and J. Yi, “Dislocation and Saturation Current Density Analysis by Rear-Side Al Amount Variation for n-Type Al-p+ Emitter Crystalline Silicon Solar Cell,” *Sci. Adv. Mater.*, vol. 8, no. 3, pp. 563–568, Mar. 2016.
[34] M. Moczała, N. Sosa, A. Topol, and T. Gotszalk, “Investigation of multi-junction solar cells using electrostatic force microscopy methods,” *Ultramicroscopy*, vol. 141, pp. 1–8, Jun. 2014.
[35] I. Gordon *et al.*, “Three novel ways of making thin-film crystalline-silicon layers on glass for solar cell applications,” *Sol. Energy Mater. Sol. Cells*, vol. 95, Supplement 1, pp. S2–S7, May 2011.
[36] E. Wesoff, “Beamreach Unstealths (Again) With Lightweight PV Module for Commercial Roofs,” Available at: http://www.greentechmedia.com/articles/read/Beamreach-Unstealths-Again-With-Light-Weight-PV-Module-For-Commercial-Roo.
(accessed on 8 Oct. 2016)
[37] R. Cariou, “Epitaxial growth of Si(Ge) materials on Si and GaAs by low temperature PECVD: towards tandem devices,” phdthesis, Ecole Polytechnique, 2014.
[38] R. Cariou *et al.*, “Ultrathin PECVD epitaxial Si solar cells on glass via low-temperature transfer process,” *Prog. Photovolt. Res. Appl.*, vol. 24, no. 8, pp. 1075–1084, Aug. 2016.
[39] V. Depauw *et al.*, “Micrometer-Thin Crystalline-Silicon Solar Cells Integrating Numerically Optimized 2-D Photonic Crystals,” *IEEE J. Photovolt.*, vol. 4, no. 1, pp. 215–223, Jan. 2014.
[40] W. Chen *et al.*, “Nanophotonics-based low-temperature PECVD epitaxial crystalline silicon solar cells,” *J. Phys. Appl. Phys.*, vol. 49, no. 12, p. 125603, 2016.
[41] A. Gaucher *et al.*, “Ultrathin Epitaxial Silicon Solar Cells with Inverted Nanopyramid Arrays for Efficient Light Trapping,” *Nano Lett.*, vol. 16, no. 9, pp. 5358–5364, Sep. 2016.
[42] X. Meng *et al.*, “Design, fabrication and optical characterization of photonic crystal assisted thin film monocrystalline-silicon solar cells,” *Opt. Express*, vol. 20, no. S4, p. A465, Jul. 2012.
[43] F. Haguenau, P. W. Hawkes, J. L. Hutchison, B. Satiat–Jeunemaître, G. T. Simon, and D. B. Williams, “Key Events in the History of Electron Microscopy,” *Microsc. Microanal.*, vol. 9, no. 2, pp. 96–138, Apr. 2003.
[44] C. W. Oatley, W. C. Nixon, and R. F. W. Pease, “Scanning Electron Microscopy,” in *Advances in Electronics and Electron Physics*, vol. 21, L. Marton, Ed. Academic Press, 1966, pp. 181–247.
[45] F. Krok, K. Sajewicz, J. Konior, M. Goryl, P. Piatkowski, and M. Szymonski, “Lateral resolution and potential sensitivity in Kelvin probe force microscopy: Towards understanding of the sub-nanometer resolution,” *Phys. Rev. B*, vol. 77, no. 23, p. 235427, Jun. 2008.
[46] L. Oberbeck, N. J. Curson, T. Hallam, M. Y. Simmons, G. Bilger, and R. G. Clark, “Measurement of phosphorus segregation in silicon at the atomic scale using scanning tunneling microscopy,” *Appl. Phys. Lett.*, vol. 85, no. 8, pp. 1359–1361, Aug. 2004.
[47] G. Binnig, C. F. Quate, and C. Gerber, “Atomic Force Microscope,” *Phys. Rev. Lett.*, vol. 56, no. 9, pp. 930–933, Mar. 1986.
[48] P. Klapetek, I. Ohlídal, and J. Buršík, “Applications of scanning thermal microscopy in the analysis of the geometry of patterned structures,” *Surf. Interface Anal.*, vol. 38, no. 4, pp. 383–387, Apr. 2006.

Chapter 2 – Experimental Background

Contents

2.1 Atomic Force Microscopy

In this work, we investigate electrical measurements on solar cells performed with different extensions of atomic force microscopy (AFM). During the same scan, topographical image is obtained along with the electrical image and additional mechanical images (e.g. phase image). In this part, we will detail the principle of the Atomic Force Microscopy and the different AFM modes to measure topography at the nano-scale.

Atomic Force Microscopy is a near-field microscopy. Measurements are performed very on the very surface thanks to a tip with a nano-scale apex curvature that varies between 1 and 100 nm. The radius of the tip is of importance because it limits the lateral resolution of measurements. Figure 2.1 shows that this tip is at the extremity of a micro-scale probe. This micro-scale probe is at the end of a cantilever which is usually 200 µm long. The length of the cantilever defines its stiffness, which may be tuned depending on applications. Finally, the cantilever is the edge of a millimeter-scale chip, which is easy to handle by microscope users. Since the tip, the probe and the cantilever are fragile and wear off, they need to be changed regularly. The materials used for probes and cantilever are usually either silicon nitride or silicon. For electrical extensions, conducting tips have to be used to be sensitive to electrical properties of the sample. Therefore, tips are either covered with conducting materials (e.g. doped diamond, gold, titanium, iridium) or are composed of a bulk conducting material.

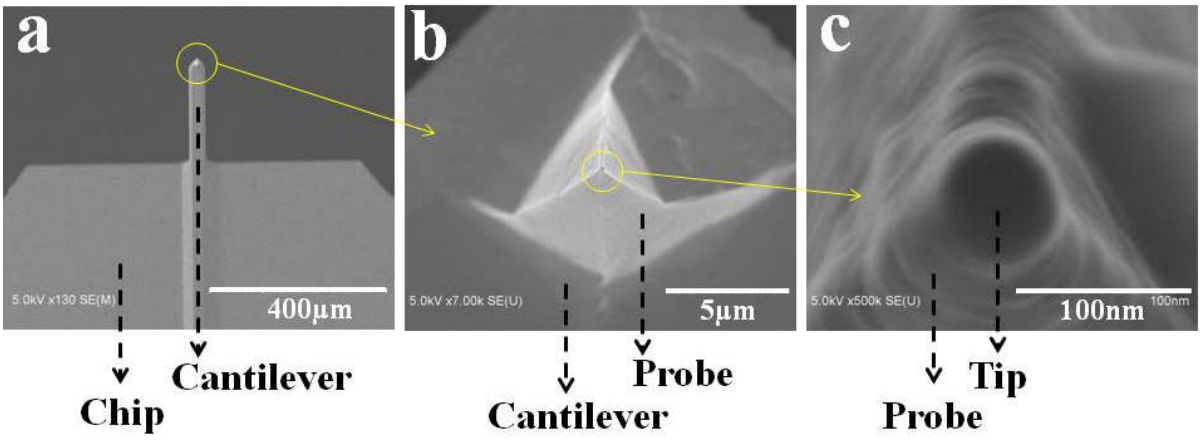

Fig. 2.1 – (a) SEM image of AFM chip and cantilever (b) SEM image zoomed on the cantilever showing the cantilever and the probe (c) SEM Image zoomed on the probe showing the probe and the tip

To perform measurements, the tip is brought at a nano-scale distance from the sample. Therefore, it is sensitive to forces which depend strongly on the distance at nano-scale. These forces can be either attractive or repulsive. Figure 2.2 shows the different forces the tip is sensitive to.

- At very small tip-sample distance (a few angstroms), the contact force is predominant. It is highly repulsive because of the overlap of the electronic orbitals at atomic distances.
- For distances between 1 nm and 10 nm, Van der Walls forces are predominant. It is a lowly attractive force that comes from interaction between molecules and groups of atoms.
- Between 10 and 200 nm, fluid surface tension leads to an attractive force. This force originates from the nano-scale water film at the surface of the sample leading to a water meniscus below the tip.
- Between 100 nm and 1 µm, electrostatic and magnetostatic forces between the tip and the sample lead to forces that can be either attractive or repulsive depending on the materials of the tip and the sample.
- For distances around 10 µm, fluid film damping forces can be taken under consideration.

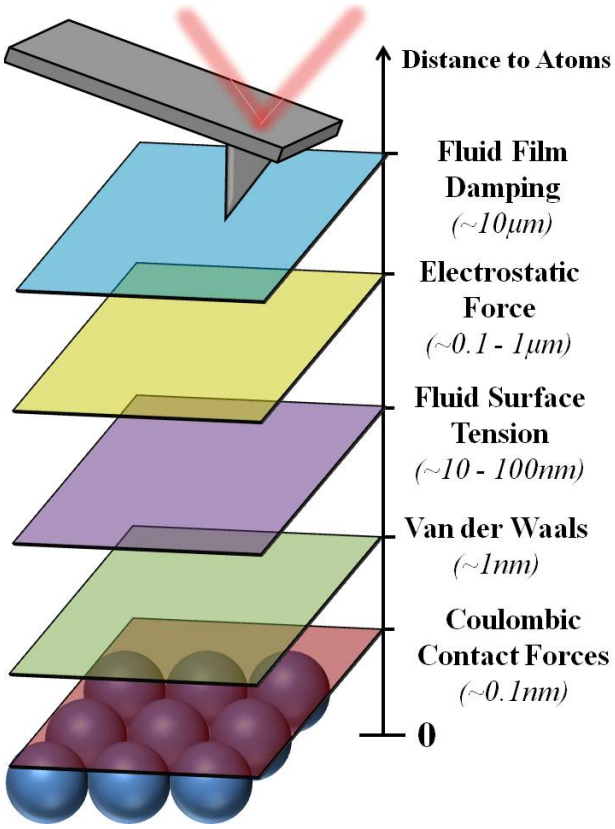

Fig. 2.2 – Different forces applied to the tip when approaching the surface and the typical distance to the surface at which these forces apply (not to scale).

The sum of the different forces defines an interaction between the tip and the sample, which leads to a mechanical bending of the cantilever. Therefore, we can monitor the interaction between the tip and the sample by analyzing the motion of the cantilever. In order to detect this motion, a laser is focused on the edge of the cantilever and is reflected on a four quadrants photo-detector. The position of the reflected laser amplifies 100,000 times the motion of the cantilever. Figure 2.3 details the AFM setup. In order to measure the height at the nano-scale, the AFM requires a feedback signal. It can be either the deflection of the cantilever (contact) or the amplitude/frequency of oscillation of the cantilever (tapping and non-contact mode). A value is given as a setpoint target for this signal and has to be maintained constant during the scans. If an error to the target is made, a vertcal piezoelectric actuator is in charge of correcting the error using a proportional-integral-derivative (PID) controller. The error made during the scan is also acquired. Therefore, the vertical piezoelectric actuator is the metrologist in AFM measurements. In order to scan the surface, either the tip or the sample are moved using lateral piezoelectric actuators in a micro-controller. This enables the image acquisition of the topography. It can be seen that the piezoelectric actuators are at the heart of the AFM spatial resolution because an important voltage is required to perform a small spatial motion. To give an order of magnitude, voltages between 250V and -250 V are used to achieve vertical displacements of about 50µm. In particular, AFM is an unchallenged technique for the vertical resolution.

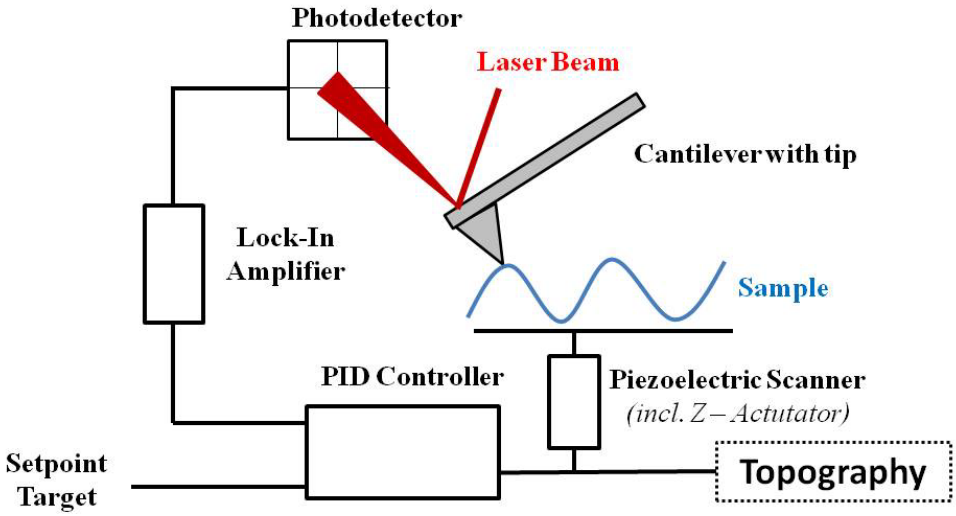

Fig. 2.3 – Atomic Force Microscopy Setup. The motion and the cantilever is monitored through the reflection of the laser beam on the photodetector. This motion is amplified by a lock-in amplifier and compared to the setpoint target. The error is corrected by adapting the Z position of the piezoelectric actuator through a PID controller.

Three AFM modes can be used to perform AFM measurements: a contact mode, a tapping mode and a non-contact mode. Figure 2.4 illustrates the three modes and the distance from the sample at which they operate.

- The contact mode was used in the first AFM in 1986 [1]. In this mode, the tip is always in contact with the sample. The feedback signal is the bending of the cantilever, also called deflection. The motion of the cantilever can be understood mechanically as that of a semi built-in beam and can be modeled using Hooke's law. If the force applied by the tip on the surface is too high, the surface can be nano-indented. This can be an advantage in certain cases (cf. Chapter 4), but it is a drawback to perform accurate topography measurements. Therefore, low stiffness cantilevers (0.01 N/m to 1 N/m) are usually used. The force applied on the surface can be estimated with approach/retreat curves. These curves also help quantify the adhesion and the capillarity of the surface locally. Many AFM extensions use AFM contact mode. This is the case for Lateral Force Microscopy (LFM) which measures the friction at the nano-scale, through the lateral motion of the cantilever. In electrical extensions, Conducting Probe AFM (CP-AFM) uses contact mode, as will be further discussed. Other examples of extensions include Scanning Capacitance Microscopy (SCM), Piezoresponse Force Microscopy (PFM) and Chemical Force Microscopy (CFM).

- The non-contact mode was invented in 1987 [2], shortly after the contact mode. In this mode, the cantilever is oscillating without touching the surface. It is about 10 nm above the surface and hence, the tip only interacts through Van der Walls forces. The cantilever is a harmonic oscillator. Its acceleration depends on the distance to the surface because of Van der Waals forces; modify both the amplitude and the frequency of oscillations. Therefore, both amplitude and frequency are dependent on the distance to the surface and can be used as feedback signals. Since the response time is usually very long for amplitude modulation mode, frequency modulation mode is normally used in non-contact mode. Non-contact mode offers the advantage of degrading neither the tip nor the sample and is very popular to investigate fragile materials. However, because of the low intensity of Van der Walls force and the sensitivity to the water adsorbed on the surface, non-contact mode is usually used

under ultra-high vacuum (UHV), making it a less versatile AFM mode. Under UHV, Kelvin Force Probe Microscopy can be used in non-contact mode.

- The tapping mode was invented in 1993 [3]. Tapping is at half distance between non-contact and contact modes because the tip is oscillating and touching the surface of the sample. The amplitude and the frequency of the signal can be used as feedback signals, as for non-contact mode. Compared to non-contact mode, it has the advantage of interacting with a strong contact force and not being sensitive to water meniscus, so it can be operated in ambient environment. Compared to contact mode, it has the advantage of being more stable on highly textured surfaces and of reducing the friction force, hence avoiding the degradation of the tip or the sample. Several AFM extensions can be coupled to AFM tapping mode such as Kelvin Probe Force Microscopy (KPFM), Electrostatic Force Microscopy (EFM) and Magnetic Force Microscopy (MFM). Besides, in amplitude modulation mode, the AFM records the phase signal, which is the phase shift between the oscillations of the piezoelectric actuator and the oscillations of the cantilever. This signal provides mechanical information about the softness of a material.

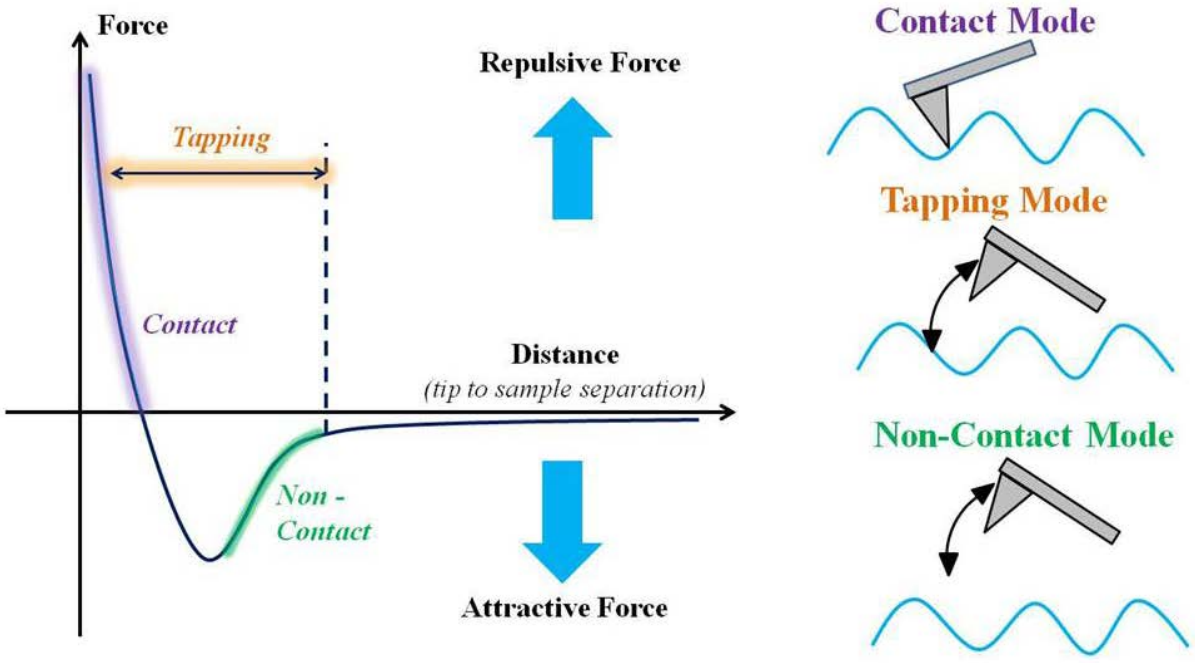

Fig. 2.4 – Force applied on the tip by the surface versus the tip-sample distance. The contact mode operates in the region close to the surface where the Coulomb forces are highly repulsive. The non-contact mode operates far from the sample and is sensitive to the attractive Van der Waals forces. The tapping mode oscillates between contact region and non-contact region.

In this manuscript, the AFM used for topography were an Agilent 5500 and an Agilent 5600. In these equipments, the tip is scanning and the sample is still. The wavelength of the AFM laser is 680nm. Since this wavelength is in the visible range and silicon absorbs in the visible range, it will be absorbed by silicon solar cells. This will be discussed in Chapter 3. Regarding topography measurements, we used AppNano AFM tips. The probe models were ACT and ACTA probes with a frequency of oscillation around 300kHz and a tip radius of 6 nm.

2.2 Kelvin Probe Force Microscopy

2.2.1 Basic Principles

Kelvin Probe Force Microscopy is an AFM electrical extension that enables to map the surface work function (or surface potential) at the nano-scale. It can be used either in tapping mode or non-contact mode.

Kelvin Probe Force Microscopy was first introduced in 1991 by Nonnenmacher *et al.* [4]. However, the principle of the Kelvin Probe measurement was stated almost one century earlier, by Lord Kelvin, in 1898 [5]. He showed that Coulomb forces cause repulsion within a gold leaf electroscope when he brought zinc and copper plates into proximity while the plates were electrically connected. In 1932, Zisman described a method for measuring contact potential differences between dissimilar metals [6]. The method was based on the response of the electrometer deflection as a function of the voltage applied to the tip V_{dc} to find the zero force on the tip, meaning that V_{dc} equals the potential difference between the probe and the sample. Zisman used a vibrating metal plate so as to have continuous measurements of the potential difference. This technique enabled measurement with a resolution down to mm size.

To understand the principle of Kelvin probe measurements, we can consider the energy diagrams of the sample and the probe, as shown in Figure 2.4. When the probe and the sample are far from each other, their Fermi levels are different but the vacuum level is the same. Both have a work function which is equal to the difference between Fermi level and the vacuum level. When the probe and the sample are connected, current flows from the sample to the tip. This results in alignment of the Fermi levels and distortion of the vacuum level by the contact potential difference V_{CPD}, equal to the difference between the work function of the tip and that of the sample.

Kelvin Probe measurements aim at introducing a voltage source in the electrical circuit to compensate the vacuum level distortion by applying an electrical bias equal to V_{CPD}. Since the work function of the probe is known, measuring V_{CPD} is equivalent to measuring the work function of the sample. To detect the alignment of vacuum level, a monitoring signal is required. In traditional Kelvin Probe setup, as that imagined by Zisman, the monitoring signal is the current flowing from the probe to the sample. When this current is equal to zero, the vacuum levels are aligned and the applied electrical bias is equal to V_{CPD}. In Kelvin Probe Force Microscopy, the monitoring signal is either the amplitude modulation (AM mode) or the frequency modulation (FM mode).

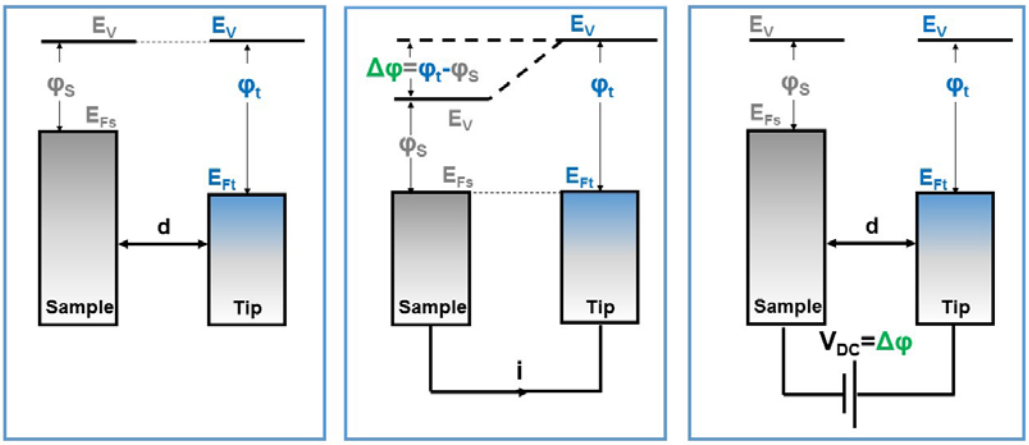

Fig. 2.4 – Principle of Kelvin Probe Measurement. When the tip and the sample are contacted, a DC voltage bias is applied to align the vacuum levels. The obtained value is equal to the difference of work function between the tip and the sample.

All KPFM measurements reported in this manuscript have been performed in AM mode. Therefore, we will explain how the amplitude can be used to monitor the alignment of vacuum levels between the tip and the sample.

In KPFM, a sinusoidal voltage is applied to the tip:

$$V_{tip} = V_{dc} + V_{ac}.\cos\omega t \tag{2.1}$$

To assess the electrostatic force acting on the cantilever, we need to consider the equations of a charge in a capacitor. We consider a capacitor between the tip and the sample as shown in Figure 2.5, for different distances between the tip and the sample.

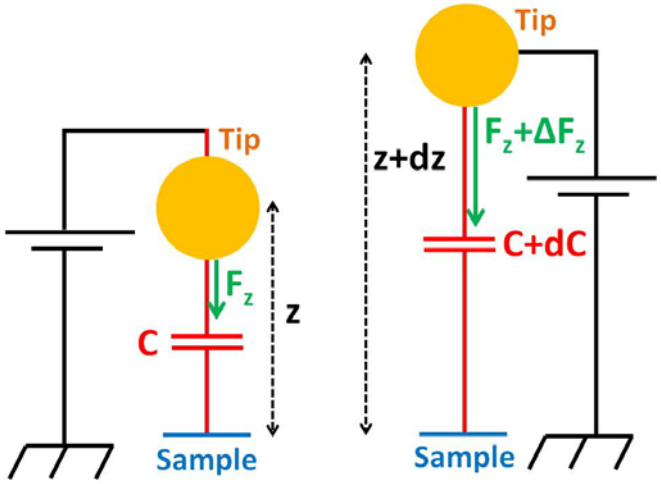

Fig. 2.5 – Capacitance between the tip and the sample is dependent on the distance, resulting in a force which depends on the distance.

The voltage V applied to this capacitor is:

$$V = V_{tip} - V_{sample} = V_{dc} + V_{ac}.cos\omega t - V_{CPD} \tag{2.2}$$

Where: V_{CPD} is the contact potential difference.

The energy stocked in a capacitor is:

$$E = \frac{1}{2}.C.V^2 \tag{2.3}$$

So if we introduce the work W_{el} done by the electrostatic force F_{el} which applies on the probe, W_{el} is defined as:

$$W_{el} = F_{el}.\partial z \tag{2.4}$$

And W_{el} is also equal to the variation of energy received by the capacitor :

$$W_{el} = \partial\left(\frac{1}{2}.C.V^2\right) = \frac{1}{2}\,\partial C.V^2 \tag{2.5}$$

Hence, the force F_{el} can be expressed as:

$$F_{el} = \frac{1}{2}.\frac{\partial C}{\partial z}.V^2 \tag{2.6}$$

$$where\ V = V_{dc} + V_{ac}.\cos(\omega t) - V_{CPD} \tag{2.7}$$

$$\text{Therefore, we can write}\ \ F_{el} = F_0 + F_\omega + F_{2\omega} \tag{2.8}$$

$$where \begin{cases} F_0 = \frac{1}{2} \cdot \frac{\partial C}{\partial z} \cdot \left[(V_{dc} - V_{CPD})^2 + \frac{{V_{ac}}^2}{2} \right] & (2.9) \\ F_\omega = \frac{\partial C}{\partial z} \cdot (V_{dc} - V_{CPD}) . V_{ac} . \cos(\omega t) & (2.10) \\ F_{2\omega} = \frac{1}{4} . \frac{\partial C}{\partial z} \cdot {V_{ac}}^2 . \cos(2\omega t) & (2.11) \end{cases}$$

In AM mode, KPFM uses oscillation amplitude as a feedback signal. The oscillation amplitude of the cantilever is proportional to the force applied to the cantilever. So, if the amplitude A_ω of the cantilever movement at the angular frequency ω is null, the force applied at the angular frequency ω, F_ω is also null.

Thereby, by properly adjusting V_{dc}, V_{CPD} is found when F_ω equals to 0 and thus when the feedback signal A_ω equals 0.

The $F_{2\omega}$ term can be used to measure $\frac{\partial C}{\partial z}$. Hence, capacitance gradient is a common measure carried out during KPFM measurements.

As it can be seen from these equations, the grounding of the sample is crucial to measure the surface potential of the sample. We observed important measurements difference when applying or not grounding to the sample. When performing a KPFM measurement, the grounding of the sample should be designed properly.

2.2.2 AM vs FM mode

We will not detail the equations for FM mode but we will detail the advnatages and disadvantages of AM mode and FM mode.

The AM mode presents the advantage of requiring a much lower sampling voltage than FM mode. Therefore, there is less chance of inducing tip-induced band bending for semiconducting samples [7]. Another advantage is that AM mode measures the surface potential directly from the resonance peak whereas the FM mode measures it through an FM demodulator. This additional electronics adds noise to the FM measurement. Hence, the signal to noise ratio in AM mode is higher than in the FM mode, thus enabling a better energy resolution in AM mode. Expected signal resolution in AM mode is 5meV, as opposed to 10-20 meV in FM mode [8].

FM mode also presents some advantages compared to AM mode. A key difference between AM-KPFM and FM-KPFM is that AM measures the force of the substrate on the tip while FM measures the gradient of this force. When increasing tip-sample distance, the gradient of the force dies off quicker than the force itself. Hence, FM-KPFM is less sensitive to averaging effects due to stray capacitances, such as cantilever capacitance. This artifact will be detailed in section 3.5. Therefore, FM-KPFM has a better lateral resolution [7][9] and is more accurate for measurement of energy differences [10].

Another difference is that FM-KPFM measurements prove to be much less sensitive to the tip-sample distance than AM-KPFM ones since a major part of the measured force gradient stems from the area beneath the tip [10][11][12]. As a consequence, FM-KPFM is less impacted by topography cross-talk on surface potential measurements. It means that FM-KPFM should be preferred for rough surfaces.

The Kelvin Probe Force Microscopy setup in AM mode is described in Figure 2.6. It is based on an AFM setup, as the one described in Figure 2.3. The bottom part (in black) shows the AFM topographic measurement components. The top part (in green) shows the components used to map the

surface potential, including the lock-in amplifier and the KPFM controller. The AC voltage is applied from the lock-in amplifier reference signal voltage output to the tip.

In AM mode, V_{ac} with a resonant frequency f_2 different from that of the resonant peak of tip oscillation f_1 is applied to the AFM tip to excite it with an electrical force. The amplitude of oscillation has two components: the mechanical frequency f_1 and the V_{ac} frequency f_2 used to measure the surface potential. A band-pass filter sorts out f_1 and f_2 signals. The f_2 signal feeds directly the lock-in amplifier and the KPFM controller measures the surface potential using f_2 component. The f_1 signal is used to scan the topography.

To perform KPFM measurements, a conducting tip is required. The tips can be either made of a bulk conducting material, such as heavily doped silicon cantilever; or a conducting layer can be coated on a regular silicon cantilever, such as Pt/Ir-coated cantilevers. These tips are less expensive but lead to lower spatial resolution. Other materials such as gold or chromium can be used as a coating to improve the spatial resolution.

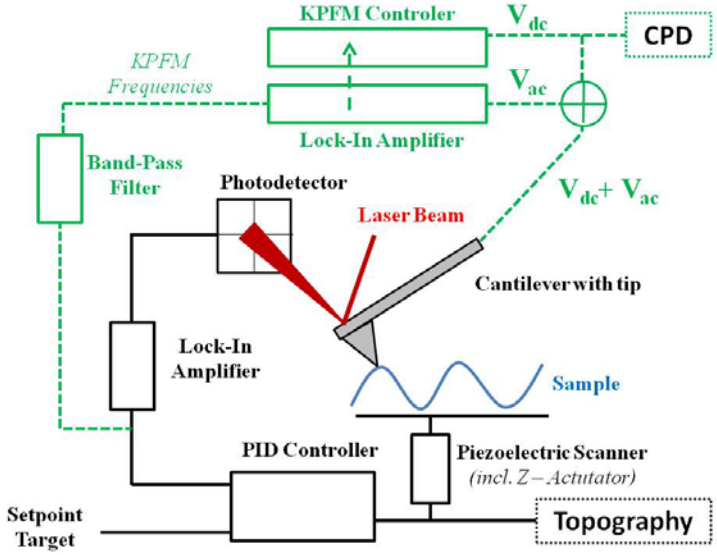

Fig. 2.6 – Kelvin Probe Force Microscopy Setup in AM mode. The bottom part in black represents the AFM topography measurement. The top part in green represents the KPFM surface potential measurement.

For our KPFM measurements, we used an Agilent 5500 setup. The AM mode was privileged to prevent band bending phenomena on semiconductors and because FM mode signal to noise ratio was too low. The probes used were App Nano's Pt-Ir coated tips, called ANSCM-PT. The resonance frequency is around 65 kHz, the spring constant around 3N/m, the tip radius around 30 nm and the length of the cantilever is 225 µm. Most of the measurements were performed under controlled nitrogen atomosphere to prevent tip-induced oxidation, as will be discussed in Chapter 3.

2.3 Conductive Probe AFM

In the end of the 1980s and beginning of the 1990s, the first local contact resistance measurements were carried out for different applications such as the local conductance of metal surfaces in air [13] or the link between mechanical and nano-electrical properties of gold [14]. In these approaches, the apparatus was homemade and designed for a specific application and the tip was fabricated from a metal wire.

Shortly after, in the middle of 1990s, first local resistivity cartographies appeared in the literature. These techniques were called conducting probe AFM (CP-AFM) and enabled topography

and resistivity topographies at the same time. Shafai *et al.* proposed a technique enabling the delineation of semiconductor doping with a lateral resolution better than 35 nm [15].

In 1996, a French team in Laboratoire de Génie Electrique de Paris (L.G.E.P), now named laboratoire de Génie électrique et électronique de Paris (GeePs) proposed a promising technique performing localized resistivity measurements with a conductive probe [16]. The originality of this technique is that it incorporates a logarithmic amplifier allowing resistance measurement over ten orders of magnitude: from $10^2\ \Omega$ to $10^{12}\ \Omega$. This technique was further developed by the LGEP team [17]. In the beginning of the 2000s, it eventually resulted in the commercialization of an AFM extension called "Resiscope" that can be implemented on commercial AFM to perform local resistance measurements. This equipment has been used for the characterization of different materials : thin magnetic cermet films [18], amorphous and microcrystalline silicon thin films [19], boron doped homoepitaxial diamond films for diodes [20], GaN nanowires [21] or oxide layers grown on stainless steel [22].

Simultaneously, in the 1990s, another CP-AFM technique using a logarithmic amplifier called "Scanning Spreading Resistance Microscopy" (SSRM) was developed at IMEC. Resiscope and SSRM techniques are very close to each other since the core principle is the same. The differences are technical particularities: Resiscope enables a slightly higher range of measurable resistivites than SSRM. Besides, SSRM also requires applying more strength and higher voltage/intensity on the tip. Finally, SSRM only outputs the resistance measured whereas Resiscope outputs both resistance and intensity measured at a particular voltage.

Among the Scanning Probe Microscopy techniques, confusion can be made between Scanning Tunneling Microscopy (STM) and Conductive AFM (CP-AFM) since both of them use the current to perform nano-scale measurements. The difference is that STM uses tunneling current as a feedback signal to measure topography whereas, in CP-AFM, topography is measured with contact mode and at the same time, current I is measured while a DC bias voltage V is applied between the sample and the conductive AFM tip. Hence CP-AFM measures the ratio I/V. In the case of SSRM and Resiscope, the IV measurement is performed through a logarithmic amplifier.

A schematic view of the Resiscope system is given in Figure 2.7. The tip and the cantilever are made either of a highly conducting material such as doped silicon and full diamond; or, of silicon nitride coated with metal film for conduction. Platinum iridium and diamond are two examples of coating materials for conductive AFM tips. The sample and the cantilever holders must be carefully insulated from the apparatus frame.

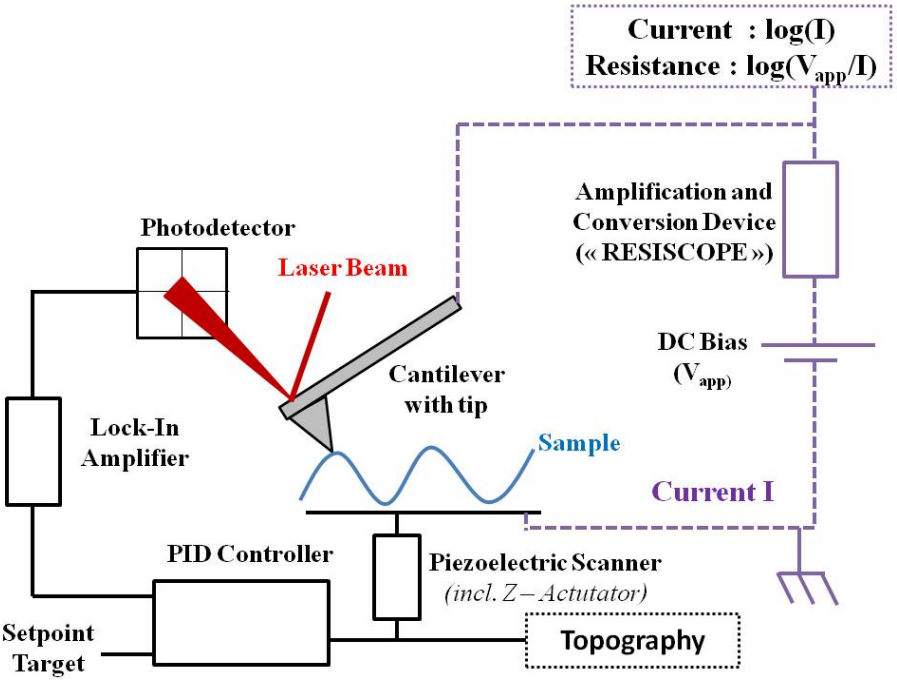

Fig. 2.7 – Resiscope Setup. The AFM is in contact mode and the current flow through the tip and the sample is amplified and measured through a logarithmic amplifier.

The resistance measured by Resiscope is actually the sum of several resistances in series: the resistance of the probe itself, the sample resistance (between the back contact and the probe), the back contact resistance and the tip-sample contact resistance [23]. In most cases, the tip-sample resistance is much higher than the other resistances because the area of contact is nano-metric. Therefore, the resistance measured by the Resiscope is equal to the tip-sample contact resistance because the other resistances are negligible. If the force applied is strong enough, the contact resistance reduces suddenly and can be measured by the Resiscope setup, if the resistance is not screened by the other parasitic resistances. This low tip-sample contact resistance is called spreading resistance.

In order to perform conductive AFM measurements, the contact between the tip and the sample should be ohmic. Otherwise, in the case of a Schottky contact, the tunneling term will be predominant. In this case, the spreading resistance is also called the Wexler resistance [24].

To express Wexler resistance, some assumptions about the contact and the sample have to be done:

- The contact is of elastic nature.
- The Hertz theory can be applied. It describes the deformation of solids that touch each other.
- The substrate is infinite on both sides of the constriction.
- The contact is ohmic between the tip and the sample.
- The doping of the sample is uniform.

Given these assumptions, the Wexler ressitance can be expressed as [24]:

$$R_{wexler} = \frac{\rho}{2a}\,\Gamma(K_n) + \frac{4\rho}{3\pi a}K_n \qquad (2.12)$$

Where:

- ρ *: the local resistivity*
- a *: the radius of the contact*
- K_n *: Knusden number defined as* $K_n = \frac{\lambda}{a}$
- λ *: mean free path of electrons*
- $\Gamma(K_n)\begin{cases} 1 & K_n \to 0 \\ \frac{9\pi^2}{128} & K_n \to \infty \end{cases}$

Two particular cases have to be distinguished here:

- ***Case 1 :*** $a << \lambda$ *(*$K_n \to \infty$*)*

$$R_{Wexler} \to R_{Sharvin} = \frac{4\rho\lambda}{3\pi a^2} \quad [25] \quad (2.13)$$

- ***Case 2 :*** $a >> \lambda$ *(*$K_n \to 0$*)*

$$R_{Wexler} \to R_{Maxwell} = \frac{\rho}{2a} \quad [26] \quad (2.14)$$

Therefore, CP-AFM can measure a local resistivity ρ at the nano-scale. This is of interest in the microelectronic and photovoltaic industries since the resistivity is linked to the doping carrier density and the doping levels, through the mobility:

$$\rho = \frac{1}{q\, n\, \mu(n)} \quad (2.15)$$

Where:

- q*: the charge of the electron*
- n*: the density of carriers*
- μ(n) *: the mobility of carriers*

For crystalline silicon, empiric expressions of the mobility versus the carrier density give [27]*:*

$$\mu(n) = \mu_{min} + \frac{\mu_{max} - \mu_{min}}{1 + \left(\frac{n}{n_r}\right)^{\alpha}} \quad (2.16)$$

Where μ_{min}, μ_{max}, *α and* n_r *are fitting parameters.*

We can notice that for high doping carrier densities n, it is harder to detect changes in resistivity. So the resolution of the conductive probe AFM is lower for high carrier densities. For instance, signal dynamics in SSRM becomes challenging for crystalline silicon doped above 10^{19} at. cm^{-3}.

For our CP-AFM measurements, we used a Resiscope coupled on different AFM setups: Agilent 5500, Agilent 5600 and Digital Instruments Nanoscope IIIa Multimode. Since the measured resistance is inversely proportional to the radius of contact if a<<λ (equation 2.13) or to the square of the radius of contact if a >>λ (equation 2.14), a strong force has to be applied on the tip to be sure to get a signal over the saturation limit. Therefore, we used high stiffness cantilevers (48 N/m). The probes were made of silicon and coated with conducting doped diamond. These commercial probes were bought from Nanosensors (CDT-FMR). The work on CP-AFM has mainly been done through a collaborative project with the laboratory GeePs, in the framework of the "Institut Photovoltaïque d'Ile de France" (IPVF).

2.4 Electron Microscopy: SEM and EBIC

Some electron microscopy techniques enable to access electrical properties at the nano-scale and are therefore of interest to compare with the electrical extensions of Atomic Force Microscopy. This is particularly the case for two electron microscopy techniques: scanning electron microscopy (SEM) and Electron Beam Induced Current (EBIC). In the following, we will explain the principle of electron microscopy and the setup used, and we will detail the principles of SEM and EBIC.

In electron microscopy, a nanometric beam of electrons with a size of around 2nm is focused on the surface of the sample. The incident electrons interact with the coulomb field of both the atoms nucleus and electrons which result in two kinds of events:

- **Elastic events:** The electron interacts with the electric field of the atom without losing a significant amount of energy but changing its direction. If the elastically scattered

electron is deflected back from the specimen, it is called **backscattered electron (BSE)**. Since light elements backscatter electrons less than heavy elements, backscattered electrons signal can be used to analyze chemical composition of the sample.

- **Inelastic events:** The incident electron interacts with the electric field of the atom and loses a significant amount of energy to the atom. The extra energy can be dissipated in different ways by the atom:

  - An electron can be expulsed from the low orbital of the atom and emitted outside the sample. This electron has low energy (<50 eV) and is called **secondary electron (SE).** Secondary electrons are collected with a scintillator-photomultiplier detector to obtain the SEM image.
  - If the device is contacted, an electron can be expulsed from the low orbital of the atom and collected in the circuit. The value of current is recorded for each point to obtain the EBIC image.
  - An electron can be expulsed from the low orbital of the atom. An electron from a higher orbital will take its place and lose energy through **X-Ray emission**.
  - An electron can be expulsed from a high orbital of the atom. This electron has high energy and is called **Auger electron.** Both X-Ray emission and Auger electrons are used to perform elemental composition analysis, but they have different sensitivity and work for different material thicknesses.
  - An electron can be expulsed from an orbital of the atom and recombine inside the sample leading to an emission of photon. The emitted photons can be collected to obtain a cathodoluminescence image.

These different responses of the sample to the incident beam come from different depths in the sample. Figure 2.8 shows the depth of the different responses. The combined effect of inelastic and elastic interactions distributes the primary beam of electrons over a three dimensional interaction volume. The area of reemission of the different responses, also called escape depth, can vary. For example, electrons do not need a lot of energy to be backscattered, therefore the escape depth of BSE is one to two orders of magnitude higher than secondary electrons escape depth. Interaction volume and escape depths can be simulated using Monte Carlo method.

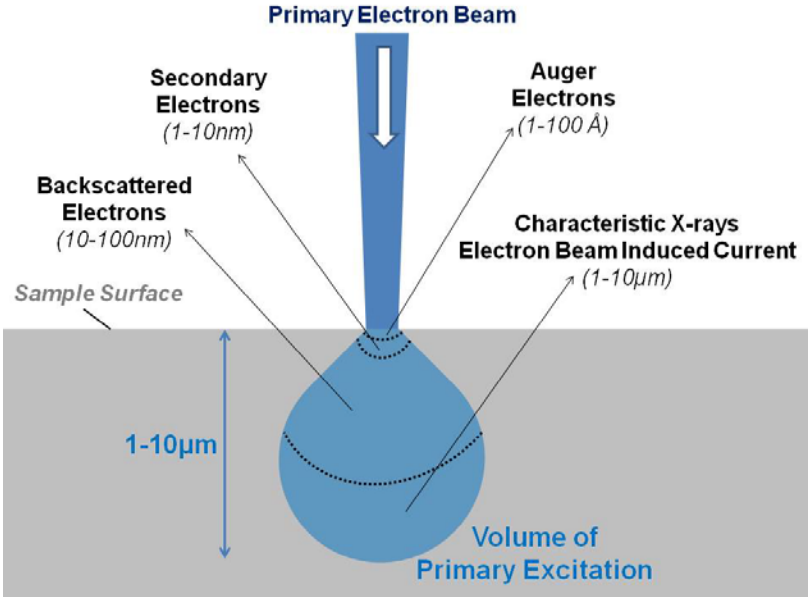

Fig. 2.8 – Scheme of electron microscopy principle. A primary electron beam is focused on the sample surface and creates a volume of primary excitation. From this volume, different responses are collected from different escape depths. Among them secondary electrons which are reemitted from a few nanometers below the surface.

In the following, we discuss the electrical properties that can be measured using SEM and EBIC.

SEM collects either secondary electrons or both secondary and backscattered electrons. The contrast mechanism is due to many factors and not fully understood, but three main contrast factors can be highlighted:

- **Topographical Contrast:** Secondary electrons (SE) are re-emitted from the surface of the sample. Thus, the emission of SE is much higher when the electron beam hits the surface obliquely than when it hits it perpendicularly. Therefore, the intensity of the electron beam is highly dependent on the orientation of the features of the sample. As a consequence, SEM is routinely used to image the size, shape, texture of three dimensional objects.

- **Composition Contrast:** Both backscattered and secondary electrons are sensitive to the material composition of the sample. Backscattered electrons are sensitive to the atomic number of the atoms. The secondary electron yield is also material dependent. Therefore SEM contrast can help detect different kinds of materials.

- **Surface Potential Contrast:** Since secondary electrons have a small energy, they are very sensitive to the electrostatic potential from the sample. Several authors have reported the influence of surface potential on SE collection [28][29][30]. In particular, the SE contrast of PN junctions has been extensively studied [31][32]. This makes comparison between KPFM and SEM straightforward. In particular, the SEM and KPFM investigation on an IBC solar cell under varying electrical bias will be presented in Chapter 6.

EBIC also enables to investigate electrical properties at the nano-scale. In this technique, the sample has to be contacted in order to collect a current. This current originates from the carriers excited by the incident electron beam. Figure 2.9 shows the two microprobes used on our setup to contact the IBC solar cell. These probes are also used to apply an electrical bias and monitor its influence on SEM and EBIC. EBIC technique is often used to identify buried junctions or defects in semiconductors and to examine minority carrier properties. When the electron beam is directed on the space charge region (SCR) of a junction, the separation of carriers is effective and the EBIC signal is high. If the electron beam spots out of the SCR, the EBIC signal will depend on the distance to the SCR and on the diffusion length of the material. For high diffusion length materials such as lowly doped crystalline silicon, the EBIC signal is strongly convoluted with the diffusion length, making interpretations harder than for low diffusion length materials.

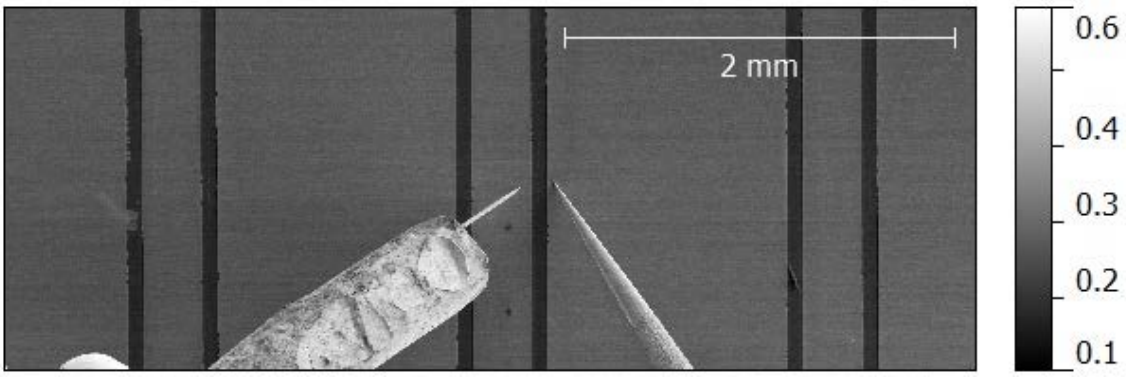

Fig.2.9 – SEM image of an IBC solar cell contacted with the microprobes within the SEM/EBIC chamber.

Our SEM and EBIC images were collected in a Hitachi SU-8000 UHR cold-emission FE-SEM setup at room temperature. Measurements were performed at Institut d'Electronique Fondamentale (IEF) with the great help of their team. The vacuum level inside the chamber is around 10^{-5} Pa.

2.5 Investigated Samples and Solar Cells

In this part, we will detail the samples and devices investigated by scanning probe microscopy techniques (CP-AFM and KPFM) and electron microscopy. Samples go from simple passivated crystalline silicon wafers to complex interdigitated back contact solar cell devices. The objective was to compare the techniques for both material and devices investigation, in order to determine the advantages and limitations of each technique.

2.5.1 Passivated Crystalline Silicon Wafers

The simplest samples investigated are crystalline silicon wafers. We studied both p-type and n-type doped Float Zone (FZ) silicon wafers with a resistivity of 1-5 Ω.cm and a thickness of 280 μm. In particular, we studied the effect of passivation on these wafers. Passivation consists in depositing layers on both sides of the wafer to reduce the number of defects at their surfaces (chemical passivation) and/or to create an electric field to repel carriers away from the surface (field-effect passivation). Using passivation, the carriers can travel a longer path without recombining. Both diffusion lengths and carrier lifetimes are increased. In our case, the layers used are a passivation layer of aluminum oxide (AlO_x) with a thicknesss of 7nm and a capping layer of silicon nitride with a thickness of 70 nm.

The AlO_x layer was deposited using thermal Atomic Layer Deposition (ALD) from trimethylaluminium (TMA) and water (H_2O). Deposition temperature was 250°C, 60 cycles have been done resulting in a layer of about 10 nm.

The SiN_x layer was used to cap the passivated wafers. This layer was deposited on both sides by radio-frequency capacitive coupled plasma (RF-CCP) plasma enhanced chemical vapor deposition (PECVD) in a MVS reactor. Deposition temperature was 300°C, SiH_4 and NH_3 (9.9/90.1) were used at a chamber pressure of 100Pa, an electrode distance of 20 mm and a power density of 36 mW/cm^2 (13.56 MHz).

Annealing under a forming gas was carried out in a furnace after the deposition of the two layers on both sides. Passivation activation of AlO_x has been carried out at different temperatures for different durations. This explains the different lifetimes (τ) observed on the samples. Finally, samples undergo a final annealing of 20min at 380°C, mimicking the metallization process developed at Institut Photovoltaïque d'Ile de France (IPVF).

Figure 2.10 shows photoluminescence (PL) calibrated by microwave photoconductance decay (μ-PCD) images of two wafers: one is poorly passivated (τ ~0.5 ms) and one is well passivated (τ ~6.9 ms). Using Kelvin Probe Force Microscopy, we tried to determine the lifetime at the nano-scale using surface potential decays. We also aim at investigating nano-defects on the cross-section of passivated crystalline silicon wafers, as shown in Chapter 5.

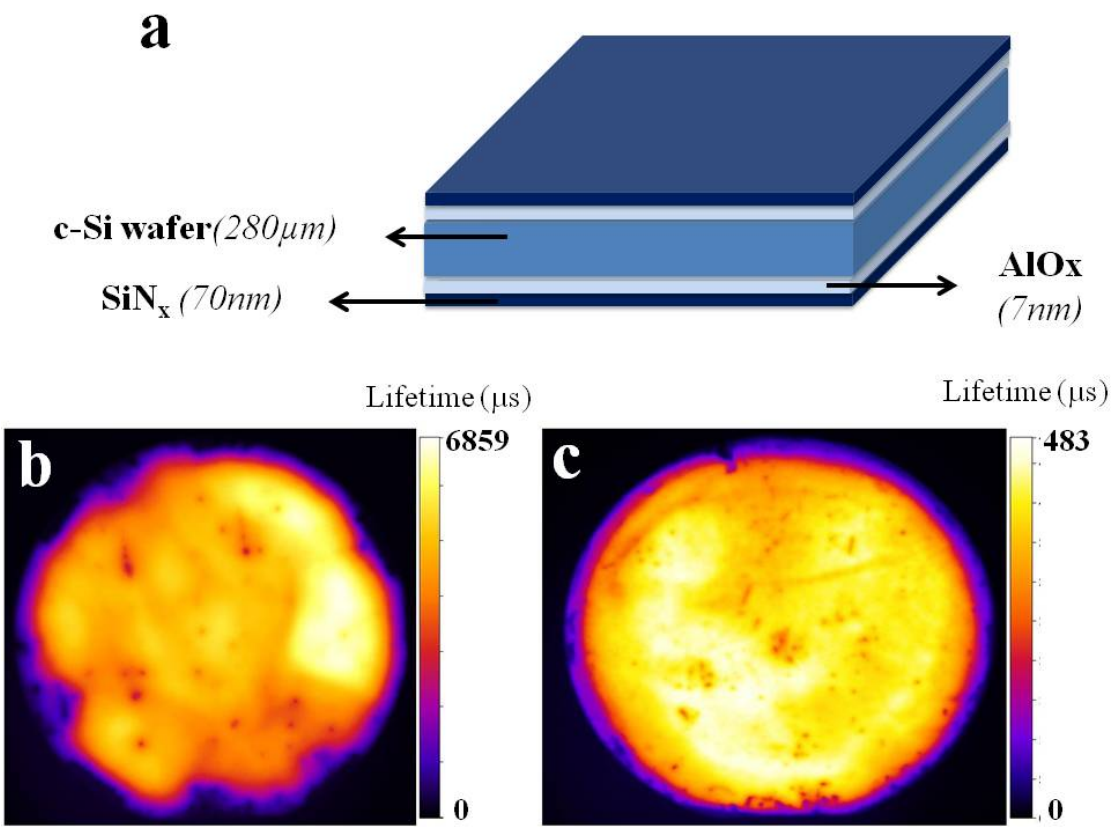

Fig. 2.10 – (a) Passivated c-Si wafer structure. (b) μ-PCD calibrated PL image of a well passivated wafer. (c) μ-PCD calibrated PL image of a poorly passivated wafer. Images are calibrated to obtain the lifetime.

2.5.2 Calibration Samples

One of the main challenges in the semiconductor industry is to be able to determine doping levels at the nano-scale [33]. To this purpose calibration samples with micro-scale steps of varying doping levels can be investigated on the cross-section using nano-scale resolution techniques. We bought crystalline silicon calibration samples from IMEC. The orientation of the wafer is (100). The n-type calibration sample is the CS01-SiAs and is doped with arsenic. The p-type calibration sample is the CS02-SiB and is doped with boron. The specifications of these calibration samples can be found in Figure 2.11.Their cross-section was investigated using Kelvin Probe Force Microscopy and Resiscope to determine if these techniques can detect the doping levels. The results are discussed in Chapter 5.

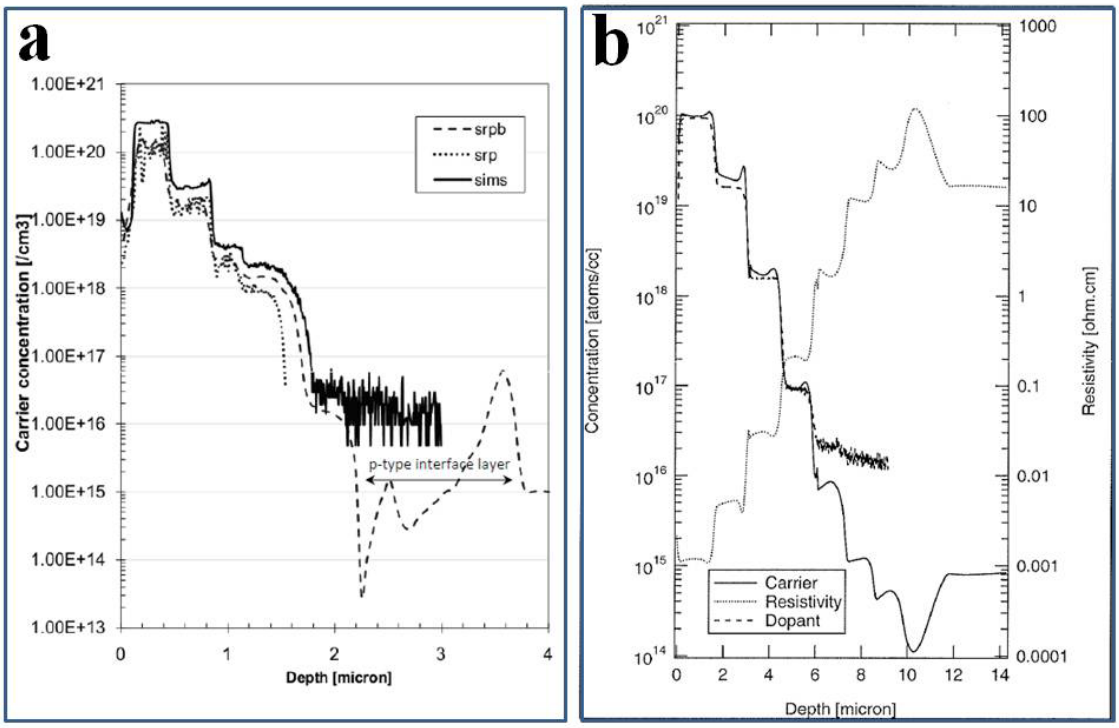

Fig. 2.11 – (a) N-type and (b) P-type c-Si calibration samples specifications. The doping levels increase when approaching the edge of the samples. The orientation of the wafer is (100). All measurements are performed at IMEC. Resisitivity is measured with SSRM, carrier concentration is measured by SRP and dopant concentration is measured with SIMS.

2.5.3 Epitaxial Silicon Solar Cells

The simplest device investigated is the epitaxial silicon solar cell. Recently, epitaxial silicon solar cells have gained attraction from the photovoltaic industry since they require less silicon material than traditional crystalline silicon solar cells, while reaching competitive efficiencies. For instance, Solexel achieved 21.2% efficiency using 35 μm wafers [34]. Epitaxial silicon solar cells using plasma-enhanced chemical vapor deposition (epi-PECVD) have been developed in our laboratory (LPICM) enabling epitaxy at very low temperatures, below 200°C [35] [36] [37].

The epitaxial silicon solar cell is made of a silicon PIN junction. Fig 2.12 shows the design of the epitaxial silicon solar cell. Heavily boron-doped (100)-Si wafers with a resistivity of 0.002-0.005 Ω.cm and a thickness of 525 μm were used as substrates for the epitaxial growth. Intrinsic epitaxial layers with a thickness of 3 μm were deposited in a RF-PECVD reactor from the dissociation of 6% silane in a hydrogen gas mixture ($SiH_4/(SiH_4+H_2)=0.06$) under a pressure of 2 Torr and an RF power density of 50 $mW.cm^{-2}$, resulting in a deposition rate of 0.15 $nm.s^{-1}$. An n^{++} hydrogenated amorphous silicon (a-Si:H) emitter layer with a thickness of 15nm was deposited on the epi-Si surface without breaking the vacuum at the constant temperature of 175°C. The area of the cell (2x2 cm^2) was defined by sputtering indium tin oxide (ITO) through a shadow mask and evaporating an aluminum contact grid above.

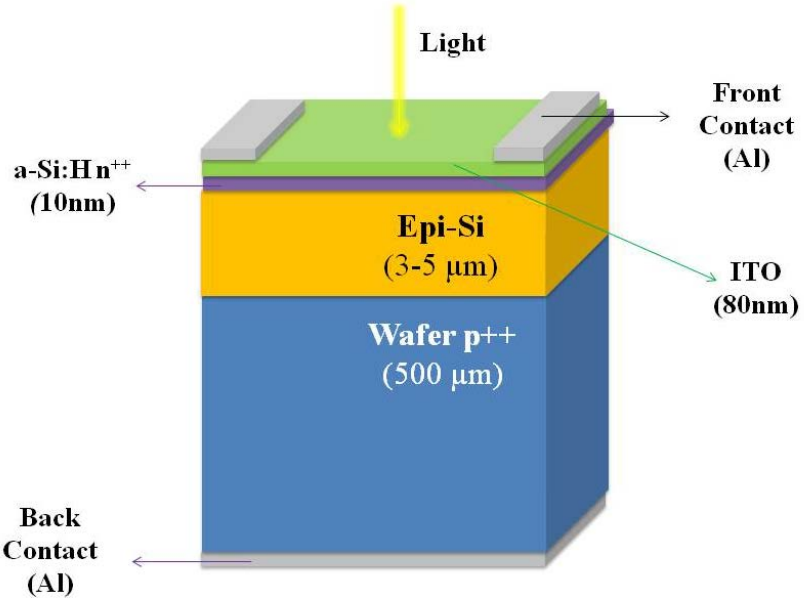

Fig. 2.12 – Epitaxial silicon solar cell structure. The epitaxial layer is grown by PECVD at low temperature (<200°C)

In order to improve the short circuit current of the solar cell, nano-photonics can be implemented on the top and back surface of the cell. The effect of nano-texturation was studied in the framework of the ANR project Nathisol and the European project PhotoNvoltaics in which LPICM and Total were involved. Figure 2.13 shows SEM pictures of the surface of periodic and random textured solar cells. The periodic texturing was done using nano-imprinted masks and reactive ion etching, and the random texturing was performed using reactive ion etching.

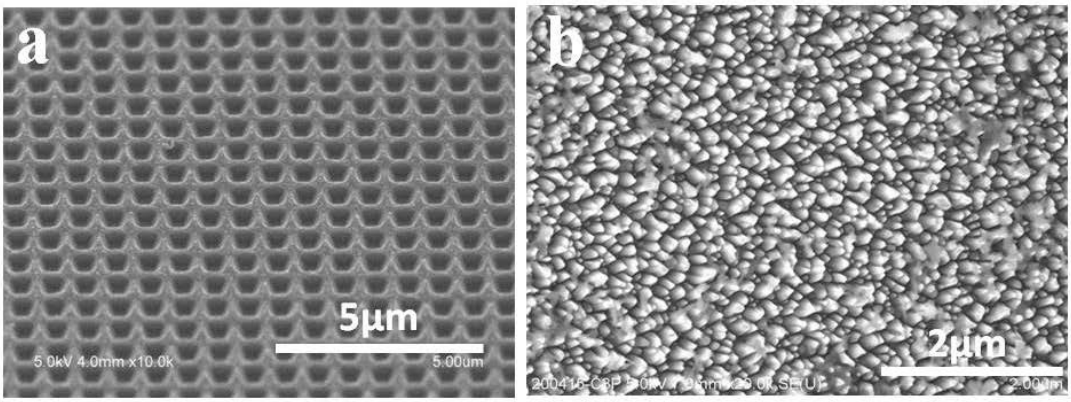

Fig. 2.13 – SEM Images of (a) Periodic and (b) random textured epitaxial silicon solar cells

Both textured and flat epitaxial silicon solar cells were investigated using Kelvin Probe Force Microscopy and Resiscope. Surface and cross-section measurements are shown in Chapter 6. The effect of illumination and electrical bias can be studied locally. These signals can also be modulated in frequency to assess locally the dynamics of the electrical behavior.

2.5.4 Interdigitated back contact solar cells

We chose to investigate a 3D design of crystalline silicon solar cells: interdigitated back contact (IBC) solar cells. Interdigitated back contact (IBC) solar cells are a promising design to reach high efficiencies. In this architecture, both contacts are positioned on the rear side of the cell with the shape of two interdigitated combs. This design avoids reflection losses on front contacts, as is the case in traditional solar cells. The latest crystalline silicon solar cells showing the record efficiencies

belong to IBC family. For instance, Sunpower has recently presented 25.2 % efficient industrially feasible solar cells [38] and Kaneka has announced a 26.33 % laboratory world record solar cell [39] using this design.

The IBC solar cells investigated were fabricated at IMEC. The architecture of the cell is depicted on Figure 1. It is a silicon heterojunction solar cell with measured energy conversion efficiency of 19.1%, a short circuit current density of 40.3 mA.cm^{-2}, an open circuit voltage of 705 mV and a fill factor of 67.3%. The series resistance was 2 Ω.cm^2. The n-type float-zone wafer has a resitivity of 2.8 Ω.cm. The front side surface of the cell was textured using wet etching leading to random pyramids, followed by the deposition of passivation and antireflective films. The backside was not textured, but directly coated by an intrinsic hydrogenated amorphous silicon layer (a-Si:H) Afterwards, n^+ doped a-Si:H and p^+ doped a-Si:H layers were deposited side by side, forming respectively the n^+ a-Si:H and the p^+ a-Si:H stripe regions. The thickness of intrinsic/ n^+ a-Si:H is around 30 nm and intrinsic/ p^+ a-Si:H around 17 nm. Finally, indium tin oxide (ITO) and copper are deposited both on the p^+ a-Si:H and n^+ a-Si:H regions in an interdigitated back contact design with a distance of 80 µm between each finger.

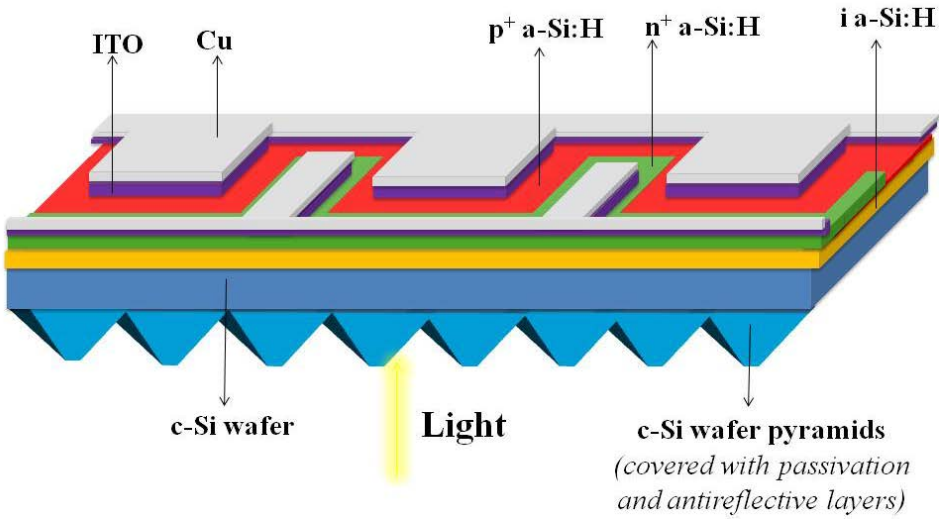

Fig. 2.14 – Interdigitated back contact heterojunction solar cells structure. The front surface is textured to enhance absorption. Both contacts are on the back side of the cell.

For IBC solar cells, only the back surface was investigated using KPFM and SEM (Chapter 6). The effect of illumination and electrical bias was studied on local measurements.

In the following two chapters (Chapter 3 and Chapter 4), we will draw a comprehensive comparison between scanning probe microscopy techniques and electron microscopy techniques for silicon solar cells investigation. In Chapter 3, we will focus on the artefacts and limitations of scanning probe microscopy techniques. In Chapter 4, we will focus on the advantages of scanning probe microscopy techniques and the new possibilities they offer compared to electron microscopy.

REFERENCES

[1] G. Binnig, C. F. Quate, and C. Gerber, "Atomic Force Microscope," *Phys. Rev. Lett.*, vol. 56, no. 9, pp. 930–933, Mar. 1986.

[2] Y. Martin, C. C. Williams, and H. K. Wickramasinghe, "Atomic force microscope–force mapping and profiling on a sub 100Å scale," *J. Appl. Phys.*, vol. 61, no. 10, pp. 4723–4729, 1987.

[3] Q. Zhong, D. Inniss, K. Kjoller, and V. B. Elings, "Fractured polymer/silica fiber surface studied by tapping mode atomic force microscopy," *Surf. Sci. Lett.*, vol. 290, no. 1, pp. L688–L692, Jun. 1993.

[4] M. Nonnenmacher, M. P. O'Boyle, and H. K. Wickramasinghe, "Kelvin probe force microscopy," *Appl. Phys. Lett.*, vol. 58, no. 25, pp. 2921–2923, Jun. 1991.

[5] Lord Kelvin, "Contact electricity of metals," *Philos. Mag. Ser. 5*, vol. 46, no. 278, pp. 82–120, Jul. 1898.

[6] W. A. Zisman, "A new method of measuring contact potential differences in metals.," *Rev. Sci. Instrum.*, vol. 3, no. 7, pp. 367–370, Jul. 1932.

[7] T. Glatzel, S. Sadewasser, and M. C. Lux-Steiner, "Amplitude or frequency modulation-detection in Kelvin probe force microscopy," *Appl. Surf. Sci.*, vol. 210, no. 1–2, pp. 84–89, Mar. 2003.

[8] W. Melitz, J. Shen, A. C. Kummel, and S. Lee, "Kelvin probe force microscopy and its application," *Surf. Sci. Rep.*, vol. 66, no. 1, pp. 1–27, Jan. 2011.

[9] S. Wu, J.-J. Yu, "Quantitative Surface Potential Measurement Using KFM: Effects of Imaging Parameters and Experimental Conditions," *Keysight Technologies Application Note*, Aug. 2014.

[10] U. Zerweck, C. Loppacher, T. Otto, S. Grafström, and L. M. Eng, "Accuracy and resolution limits of Kelvin probe force microscopy," *Phys. Rev. B*, vol. 71, no. 12, p. 125424, Mar. 2005.

[11] G. Cohen, E. Halpern, S. U. Nanayakkara, J. M. Luther, C. Held, R. Bennewitz, A. Boag, and Y. Rosenwaks, "Reconstruction of surface potential from Kelvin probe force microscopy images," *Nanotechnology*, vol. 24, no. 29, p. 295702, 2013.

[12] D. Ziegler and A. Stemmer, "Force gradient sensitive detection in lift-mode Kelvin probe force microscopy," *Nanotechnology*, vol. 22, no. 7, p. 75501, 2011.

[13] S. Morita, T. Ishizaka, Y. Sugawara, T. Okada, S. Mishima, S. Imai, and N. Mikoshiba, "Surface Conductance of Metal Surfaces in Air Studied with a Force Microscope," *Jpn. J. Appl. Phys.*, vol. 28, no. Part 2, No. 9, pp. L1634–L1636, Sep. 1989.

[14] M. Salmeron, G. Neubauer, A. Folch, M. Tomitori, D. F. Ogletree, and P. Sautet, "Viscoelastic and electrical properties of self-assembled monolayers on gold (111) films," *Langmuir*, vol. 9, no. 12, pp. 3600–3611, Dec. 1993.

[15] C. Shafai, D. J. Thomson, M. Simard-Normandin, G. Mattiussi, and P. J. Scanlon, "Delineation of semiconductor doping by scanning resistance microscopy," *Appl. Phys. Lett.*, vol. 64, no. 3, pp. 342–344, Jan. 1994.

[16] F. Houzé, R. Meyer, O. Schneegans, and L. Boyer, "Imaging the local electrical properties of metal surfaces by atomic force microscopy with conducting probes," *Appl. Phys. Lett.*, vol. 69, no. 13, pp. 1975–1977, Sep. 1996.

[17] O. Schneegans, F. Houze, R. Meyer, and L. Boyer, "Study of the local electrical properties of metal surfaces using an AFM with a conducting probe," *IEEE Trans. Compon. Packag. Manuf. Technol. Part A*, vol. 21, no. 1, pp. 76–81, Mar. 1998.

[18] M. Gadenne, O. Schneegans, F. Houzé, P. Chrétien, C. Desmarest, J. Sztern, and P. Gadenne, "First AFM observation of thin cermet films close to the percolation threshold using a conducting tip," *Phys. B Condens. Matter*, vol. 279, no. 1–3, pp. 94–97, Apr. 2000.

[19] J. P. Kleider, C. Longeaud, R. Brüggemann, and F. Houzé, "Electronic and topographic properties of amorphous and microcrystalline silicon thin films," *Thin Solid Films*, vol. 383, no. 1–2, pp. 57–60, Feb. 2001.

[20] J. Alvarez, F. Houzé, J. P. Kleider, M. Y. Liao, and Y. Koide, "Electrical characterization of Schottky diodes based on boron doped homoepitaxial diamond films by conducting probe atomic force microscopy," *Superlattices Microstruct.*, vol. 40, no. 4–6, pp. 343–349, Oct. 2006.

[21] N. Gogneau, P. Chrétien, E. Galopin, S. Guilet, L. Travers, J.-C. Harmand, and F. Houzé, "Impact of the GaN nanowire polarity on energy harvesting," *Appl. Phys. Lett.*, vol. 104, no. 21, p. 213105, May 2014.

[22] T. Massoud, V. Maurice, L. H. Klein, A. Seyeux, and P. Marcus, "Nanostructure and local properties of oxide layers grown on stainless steel in simulated pressurized water reactor environment," *Corros. Sci.*, vol. 84, pp. 198–203, Jul. 2014.

[23] P. Eyben, P. Bisiaux, A. Schulze, A. Nazir, and W. Vandervorst, “Fast Fourier transform scanning spreading resistance microscopy: a novel technique to overcome the limitations of classical conductive AFM techniques,” *Nanotechnology*, vol. 26, no. 35, p. 355702, 2015.
[24] G. Wexler, “The size effect and the non-local Boltzmann transport equation in orifice and disk geometry,” *Proc. Phys. Soc.*, vol. 89, no. 4, p. 927, 1966.
[25] Y. V. Sharvin, “On the Possible Method for Studying Fermi Surfaces,” *Sov Phys JETP*, vol. Vol: 48, pp. 655–656, Mar. 1965.
[26] J. C. Maxwell, “A Treatise on Electricity and Magnetism,” *Clarendon Press*, 1891.
[27] G. Masetti, M. Severi, and S. Solmi, “Modeling of carrier mobility against carrier concentration in arsenic-, phosphorus-, and boron-doped silicon,” *IEEE Trans. Electron Devices*, vol. 30, no. 7, pp. 764–769, Jul. 1983.
[28] J. Cazaux, “Material contrast in SEM: Fermi energy and work function effects,” *Ultramicroscopy*, vol. 110, no. 3, pp. 242–253, Feb. 2010.
[29] I. Volotsenko, M. Molotskii, Z. Barkay, J. Marczewski, P. Grabiec, B. Jaroszewicz, G. Meshulam, E. Grunbaum, and Y. Rosenwaks, “Secondary electron doping contrast: Theory based on scanning electron microscope and Kelvin probe force microscopy measurements,” *J. Appl. Phys.*, vol. 107, no. 1, p. 14510, Jan. 2010.
[30] A. K. W. Chee, R. F. Broom, C. J. Humphreys, and E. G. T. Bosch, “A quantitative model for doping contrast in the scanning electron microscope using calculated potential distributions and Monte Carlo simulations,” *J. Appl. Phys.*, vol. 109, no. 1, p. 13109, Jan. 2011.
[31] D. D. Perovic, M. R. Castell, A. Howie, C. Lavoie, T. Tiedje, and J. S. W. Cole, “Field-emission SEM imaging of compositional and doping layer semiconductor superlattices,” *Ultramicroscopy*, vol. 58, no. 1, pp. 104–113, Apr. 1995.
[32] J. T. Heath, C.-S. Jiang, and M. M. Al-Jassim, “Measurement of semiconductor surface potential using the scanning electron microscope,” *J. Appl. Phys.*, vol. 111, no. 4, p. 46103, Feb. 2012.
[33] D. Tsurumi, K. Hamada, and Y. Kawasaki, “Energy-Filtered Secondary-Electron Imaging for Nanoscale Dopant Mapping by Applying a Reverse Bias Voltage,” *Jpn. J. Appl. Phys.*, vol. 51, p. 106503, Oct. 2012.
[34] P. Kapur, M. Moslehi, A. Deshpande, V. Rana, J. Kramer, S. Seutter, H. Deshazer, S. Coutant, A. Calcaterra, S. Kommera, and others, “A manufacturable, non-plated, non-Ag metallization based 20.44% efficient, 243 cm2 area, back contacted solar cell on 40 μm thick mono-crystalline silicon,” *28th EU PVSEC Proceedings*, no. 3DO.7.6, pp. 2228-2231, 2013
[35] R. Cariou, M. Labrune, and P. Roca i Cabarrocas, “Thin crystalline silicon solar cells based on epitaxial films grown at 165 °C by RF-PECVD,” *Sol. Energy Mater. Sol. Cells*, vol. 95, no. 8, pp. 2260–2263, Aug. 2011.
[36] R. Cariou, J. Tang, N. Ramay, R. Ruggeri, and P. Roca i Cabarrocas, “Low temperature epitaxial growth of SiGe absorber for thin film heterojunction solar cells,” *Sol. Energy Mater. Sol. Cells*, vol. 134, pp. 15–21, Mar. 2015.
[37] P. Roca i Cabarrocas, R. Cariou, and M. Labrune, “Low temperature plasma deposition of silicon thin films: From amorphous to crystalline,” *J. Non-Cryst. Solids*, vol. 358, no. 17, pp. 2000–2003, Sep. 2012.
[38] D. D. Smith, G. Reich, M. Baldrias, M. Reich, N. Boitnott, and G. Bunea, “Silicon solar cells with total area efficiency above 25%,” *43rd IEEE Photovoltaic Specialists Conference (PVSC)*, 2016, pp. 3351–3355.
[39] S. Pothecary, “Kaneka achieves new efficiency record for a practical size crystalline silicon PV cell,” *PV Magazine*. Available at (http://www.pv-magazine.com/news/details/beitrag/kaneka-achieves-new-efficiency-record-for-a-practical-size-crystalline-silicon-pv-cell_100026182/). (accessed on 8 Oct. 2016)

Chapter 3 – Weaknesses of KPFM and CP-AFM techniques

Contents

3.0 Introduction

This Ph.D. project aims at understanding how scanning probe microscopy techniques can bring additional value to the electrical investigation of crystalline silicon solar cells at nano-scale. We first identified that the main competing techniques are based on electron microscopy, such as SEM and EBIC. Therefore, we decide to present the strengths and weaknesses of scanning probe microscopy techniques compared to electron microscopy techniques. From this comprehensive comparison, we define where we think scanning probe microscopy techniques can bring unique value, where they are complementary to electron microscopy and where they cannot bring value.

In Chapter 3, we focus on the weaknesses of scanning probe microscopy with respect to electron microscopy. Our focus can be divided into two kinds: the artifacts and the limitations. Artifacts are misleading alterations of the data resulting from flaws in the equipment. They are essentially errors that can affect the interpretation of the data and therefore they have to be understood and corrected if possible. Corrections can be done either through hardware improvement of the equipment or through the software data processing of results. On the other hand, limitations are possibilities that the techniques of interest do not have, while competing techniques do. Limitations do not affect the accuracy of the data but they prevent from obtaining some crucial information that other techniques may provide.

We will first address the artifacts of measurements and then the limitations of scanning probe microscopy techniques. For each weakness, we will precise if it is related to KPFM, CP-AFM or both. We will also comment if this weakness can also be present, to a lesser extent, in electron microscopy techniques. Most of them are not intrinsic weaknesses. They can be either mitigated or even suppressed. Therefore, we will discuss how these weaknesses can be circumvented, or what are the prospects to reduce these weaknesses in the future. One has to keep in mind that scanning probe microscopy is a relatively young field of research and that improvements on the techniques are still on-going.

As we will begin with artifacts, we will not detail artifacts associated with topographical Atomic Force Microscopy. Tip convolution or defects associated with the piezo actuator of the AFM (e.g. creeping, XYZ coupling, drift) are well-known and understood effects. Specific image processing can attenuate the influence of these artifacts. An exhaustive list of AFM artifacts has been reported by Giessibl *et al.* [1] and Gan *et al.*[2]. In this Chapter, we focus on the artifacts of KPFM and CP-AFM and the artifacts that are specific to the investigation of solar cells.

3.1 Parasitic Illumination from AFM laser

In Chapter 2, we have explained that an AFM laser is required to monitor the motion of the cantilever in AFM and KPFM. This laser can spill over the sample if the laser spot is larger than the cantilever or of it is not well positioned on the cantilever. This is illustrated in Figure 3.1.

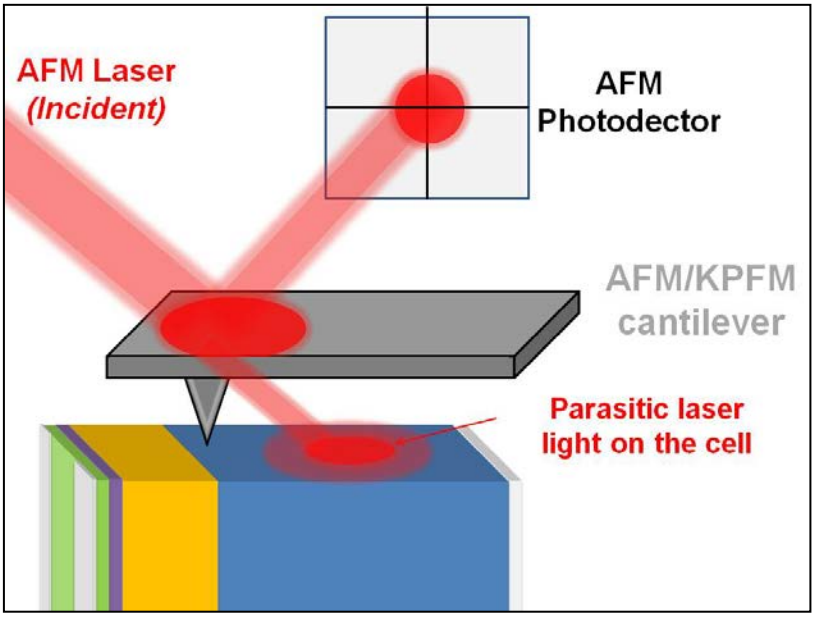

Fig. 3.1 – Scheme of the AFM laser spilling over the cantilever on the sample.

When investigating solar cells, this parasitic light does not allow performing measurements in real dark conditions. Several groups have reported this artifact [3]–[5]. A way to monitor this artifact is to measure the open circuit voltage (V_{oc}) induced by the AFM laser when the solar cell is mounted in the AFM/KPFM setup. In our case, the cantilever was smaller than the AFM laser spot and the wavelength of the laser (~680 nm) is in the range of the absorption of crystalline silicon solar cells. Therefore, the V_{oc} induced parasitic laser was never equal to 0 V. It ranged from 10 mV to 200 mV depending on the position of the laser, the quality of the solar cells investigated, and their orientation on the AFM plate. Compared to the typical V_{oc} values of solar cells under one sun illumination (~600 mV), the influence of the AFM laser is not negligible and has to be taken under consideration. It is all the more problematic, that the V_{oc} depends logarithmically on the illumination intensity. Therefore, to achieve photovoltage contrasts, much higher intensity illumination has to be used.

Figure 3.2 shows a measurement used to monitor the influence of the AFM laser during AFM scans on the cross-section of solar cells. Figure 2.a illustrates the setup. The AFM/KPFM tip is positioned on the cross-section of the solar cell. It scans across the PIN junction, going from the edge to 50 µm from the edge, back and forth. The V_{oc} is monitored continuously at all times by an oscilloscope. The V_{oc} is maximum when the tip is close to the edge and minimum when it is over the bulk. The V_{oc} evolution is recorded for three positions of the AFM laser on the cantilever (Fig 3.2.b). In position 1, the spot is centered at the tip of the cantilever. In position 2, the spot is at the tip of the cantilever and close to an edge horizontally. In position 3, the spot is on the base of the cantilever and centered horizontally. These positions are illustrated in Fig 3.2.b. For the three positions, a V_{oc} is induced by the AFM laser. It ranges from ~35 mV for position 3 (less parasitic light transmitted) to a maximum of 85 mV for position 2 (more parasitic light transmitted). Besides, for position 1 and 2, the V_{oc} depends a lot on the position of the tip during the scan. In these cases, the artifact is even more pronounced because the influence of the AFM laser is not only an offset in measured values (like in position 3) but it also induces a convolution with the profiles across the junction that are measured by KPFM and CP-AFM. If not considered, it can induce interpretation errors.

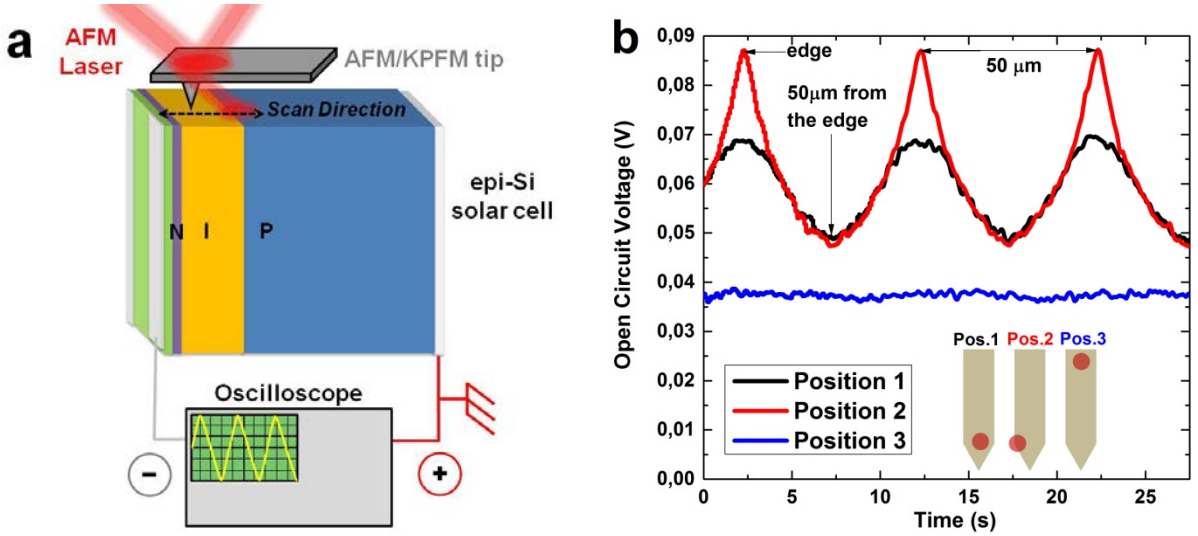

Fig. 3.2 – (a) Schematics of the setup used to record the open circuit voltage (V_{oc}) induced by the AFM laser during the scan on the cross-section of an epi-Si solar cell (b) Oscilloscope measurement of the V_{oc} for three different positions of the AFM laser on the cantilever.

In our measurements, we have carefully chosen a position of the AFM laser that induces a V_{oc} as low as possible and with the dependence on the position as small as possible. A laser positioned like in Position 3 is problematic for measurements because the amplitude of the motion of the cantilever on this point is small, leading to low signal-to-noise ratio. Therefore, a trade-off has to be found. We chose an intermediate position between position 1 and position 3. We also observe that the parasitic AFM laser induced V_{oc} is particularly sensitive to the tilt of the AFM plate. As we can change the tilt angle on our setup, this offers another parameter to reduce the influence of the AFM laser. Another mitigation strategy is to use cantilevers larger than the spot size when it is possible [6].

In the literature, some groups have reported techniques that enable to totally avoid this artifact. For instance, Takihara *et al.* have reported an AFM/KPFM technique where the motion of the cantilever is monitored by a piezoresistive sensor instead of the AFM laser [7]. Another possibility is to use AFM/KPFM equipment with an infrared AFM laser with a wavelength higher than that of the crystalline silicon bandgap [8]. Finally, CP-AFM measurements can be performed without the AFM laser on. Therefore, two-pass measurements can be performed [9]. On the first pass, the AFM laser is on and only the topography is recorded. On the second pass, the AFM laser is off, the tip follows the topography recorded and measures the current and resistance without parasitic influence of laser illumination. This solution cannot be used for KPFM because the AFM laser is required to monitor the amplitude or frequency of the cantilever to perform KPFM measurements.

3.2 Tip-induced surface degradation

We have seen previously that the scanning probe can affect measurements because of the AFM laser spilling on the solar cell. The scanning probe can also induce artifacts due to the contact between the tip and the surface. These artifacts can result either from the degradation of the surface or from the degradation of the tip. In this subsection, we detail the degradation of the surface. Some of these degradations are intrusive and can lead to non-reproducible measurements. In the following, we will highlight three main tip-induced surface degradation mechanisms: tip-induced oxidation, nano-scratching and tip-induced band bending.

3.2.1 Tip-induced oxidation

In CP-AFM and KPFM, a small conducting tip with a high voltage bias scans the surface. Therefore, there is a strong electrical confinement between the tip and the sample. When measurements are carried out under ambient conditions, water molecules are adsorbed on the surface of the sample and on the tip due to the ambient humidity. Any change in the thickness of this aqueous layer will affect KPFM or CP-AFM measurements. As a matter of fact, Sugimura *et al.* have reported a direct correlation between the KPFM contrast and the humidity level [10]. Additionally, a water meniscus is formed between the tip and the sample. When the tip is negatively biased, the high electric field ionizes the water molecules from the ambient humidity and a tip-induced electrochemical process occurs on silicon substrates: the electrons of the tip, the silicon atoms and the water react together to form silicon oxide below the tip, along with oxygen, hydrogen and hydroxide. Figure 3.3 illustrates a scheme of the reaction taking place.

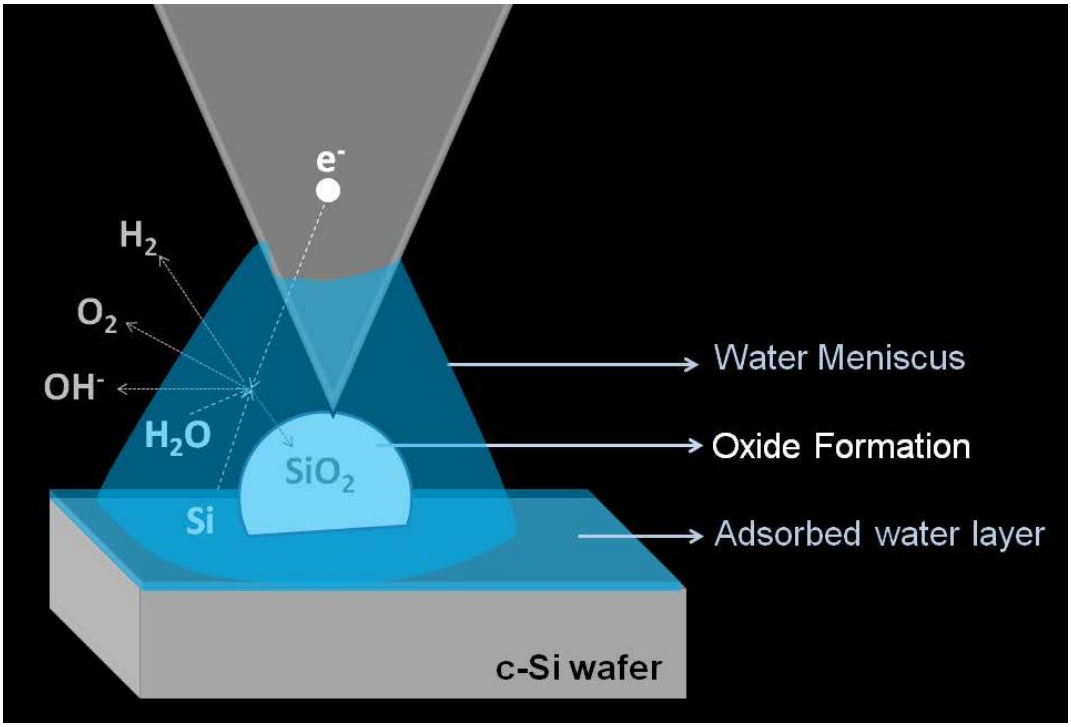

Fig. 3.3 – Scheme of water meniscus under the tip, leading to tip-induced oxidation

Tip-induced oxide layers directly degrade CP-AFM and KPFM measurements. For CP-AFM measurements, tunneling through the oxide layer takes place and affects the measurements of the current [11]–[13]. For KPFM measurements, oxide layers on the surface induce surface band bending which modifies the measured surface potential. To illustrate this phenomenon, we perform consecutive AFM and KPFM scans on the surface of a (100) crystalline silicon wafer which has just been previously HF dipped to remove the oxide layer. The measurements are performed under ambient atmospheric conditions. Every two scans, the scan area is increased so the previously scanned area becomes the center of the new image. In the end, four scan sizes are used and seven scans are performed. Figure 3.4 shows the final AFM and KPFM images associated with all these measurements. The four scanned areas are clearly distinguishable both on the AFM and KPFM images. On the AFM image, it can be seen that the more an area is scanned, the higher the surface is, proving that an oxide layer was grown (about 1nm after each scan). This oxide also strongly affects the KPFM image proving that tip-induced oxide is an artifact to be considered in Kelvin Probe Force Microscopy. Kleider *et al.* have also shown that oxide layer could also strongly affect CP-AFM signal [13].

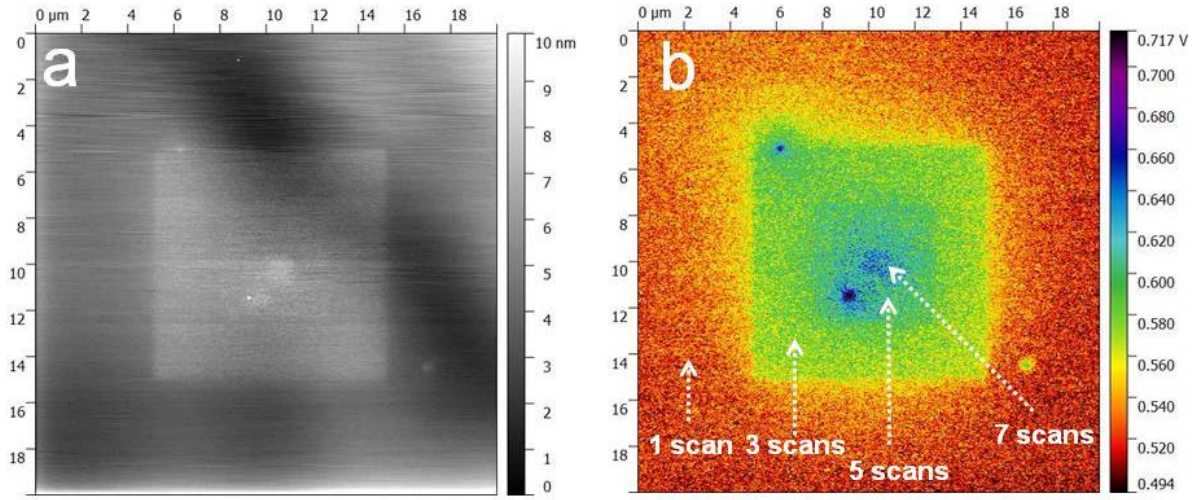

Fig. 3.4 – AFM and KPFM images on (100) crystalline silicon wafers just after an HF dip. The contrast on these images is directly linked to the number of scans performed on the areas (1, 3, 5 and 7). This proves that tip-induced oxidation affects both the topography and the surface potential at the nano-scale.

In order to suppress the effect of tip-induced oxidation, measurements have to be carried out under ultra-high vacuum (UHV) [14]. Under UHV, the sample is annealed before performing measurements to remove remaining water [15]. In our case, since we do not have access to a KPFM setup under UHV, we have to mitigate tip-induced oxidation. To do so, different strategies are possible. First, measurements under dry controlled atmosphere reduce significantly the speed of oxide growth and enable several consecutive measurements without being affected by surface oxidation. In our case, we used nitrogen atmosphere to reduce oxidation. We performed the exact same measurement as in Figure 3.4, and we hardly detected the influence of the oxide. Another way to mitigate this artifact for CP-AFM is to apply only positive voltage values on the tip to avoid the oxido-reduction reaction.

It should be noted that tip-induced oxidation can also be considered as an asset. Several groups have reported nano-lithography procedures using this technique [16]–[18]. For instance, local oxides pattern can be used to do nano-writing. It can also act as local mask for wet and dry etching. These nano-fabrication techniques have the advantage of enabling ultra-high resolution capabilities and using relatively inexpensive equipment which is easy in operation. So far, the limitation of these techniques has been the throughput. However, since scan speeds are progressively increasing and capacity for parallel operation has been introduced, these techniques could move from scientific curiosities to industrially applicable techniques.

3.2.2 Nano-Scratching

When performing CP-AFM measurements, the AFM is in contact mode and the force of the tip on the surface must be high enough to enable a large area of interaction between the tip and the sample, thus allowing more current to pass. Moreover, some groups have reported that, in the case of silicon, it was important to apply a high force to enable a phase transformation of silicon, enabling the material to be more conducting [19], [20]. Pressures higher than 10 GPa are reported in that case.

However, using these high pressures, it has been proven that the tip was scratching the surface of silicon for Resiscop measurements [5] and SSRM measurements [20]. This scratching leads to damaging of sample, making CP-AFM a destructive technique. Nano-scratched areas can be observed on the optical microscope of the AFM, as Figure 3.5.a shows. Therefore a mitigating strategy for this artifact is to find a trade-off to achieve high enough signal with minimal surface degradation. In the case of silicon, all our CP-AFM measurements result in surface scratching, but we cannot exclude that a fine optimization of CP-AFM parameters (e.g. tip force, voltage, surface cleaning) may lead to non-

destructive CP-AFM measurements on silicon materials. De Wolf *et al.* explained that the force applied on the tip needs to overcome a certain threshold for the spreading resistance to dominate. However, if lower forces are used, they do not exclude that a qualitative sensitivity to carrier profiling may remain [21]. Another mitigating strategy can be the use of CP-AFM in tapping mode (instead of contact mode), which has recently been developed [22]. Finally, improving CP-AFM to measure lower currents would reduce the nano-scratching since a lower contact area would be required. Nano-scratching artifacts only affect CP-AFM measurements and not KPFM measurements because KPFM is performed under light tapping mode.

However, this artifact can be turned in a useful nano-lithography technique. Recent studies have shown that nano-scratching is a very versatile tool to machine nano-channels [23] or other kinds of structures by properly adjusting the force applied and the number of scratch cycles. Since the force is kept constant during measurements thanks to the feedback-loop, this technique proves to be very accurate to perform nano-scale machining. In our work, we used this technique to design markers that enabled SEM and KPFM measurements at the exact same position [24]. Figure 3.5 shows optical microscope and SEM images of these marks.

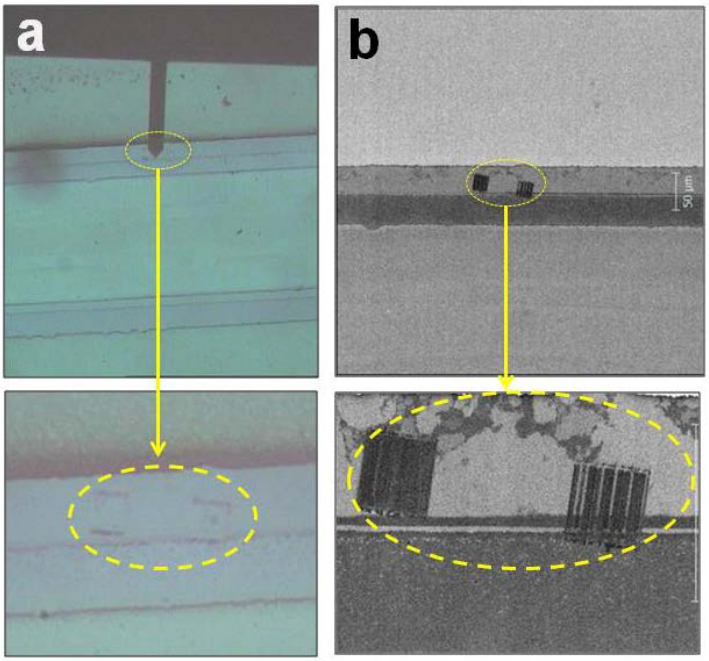

Fig. 3.5 – (a) Optical Microscope and (b) SEM image of tip-indented areas between the fingers of an IBC solar cell.

3.2.3 Tip-induced surface band bending

When a conducting tip approaches a semiconducting material, there is a possibility that the tip induces a band bending on the semiconductor surface due to a metal-insulator-semiconductor (MIS) like effect [25]. This is the case in KPFM where the AFM is in tapping mode. Therefore, the metal is that of the probe, the insulator is the air and the sample is the semiconductor. Tip-induced band bending (TIBB) is due to a Schottky effect because of the difference of work functions of the metallic tip and that of the semiconductor which also bends the energy bands. This phenomenon happens only for semiconductors and does not happen for conducting materials. It is reversible, once the tip is removed. Since the contribution of the tip-vacuum-sample in the electrostatic force is often higher than the band bending, this artifact is often considered as negligible but it is important to justify why it can be negelected, from case to case. Tip-induced band bending (TIBB) should not be confused with surface band bending (SBB), also called Fermi level pinning. This latter effect will be developed in subsection 3.8. When the applied field is high, electro-migration of charges from the tip to the sample can take place leading to surface charging [26]. These charges can lead to electrostatic screening

phenomenon where charges of one type gather around charges of opposite type to minimize the total electrostatic energy. Thus charged defects can be screened by free carriers in KPFM measurements because of tip-induced band bending.

Tip-induced band bending has been proven to electrostatically screen defects under certain conditions, therefore affecting the resolution of electronic defect imaging [27]. It is not straightforward to observe the effect of tip-induced band bending. Some groups have shown that it was possible to see it when measurements were performed on surfaces that do not suffer from Fermi level pinning effects [28], [29]. This effect can be mitigated by using low voltage amplitude of AC voltage in KPFM measurement parameters. It can be almost suppressed (reduced to a few mV) when moving to KPFM under ultra-high vacuum (UHV), as Rosenwaks *et al.* showed [27]. This effect can also be used as an advantage. Leng *et al.* have shown that, by tuning the AC bias, they could increase the band banding on certain layers and not others and therefore increase the contrast of their KPFM measurements [28][26].

3.3 Tip degradation during scans

We have seen previously that the contact between the tip and the sample can lead to degradation of the sample. In this subsection, we will see that it can also lead to a degradation of the tip and therefore of measurements. If there has been a change of signal during measurements, it is very simple to discriminate tip degradation artifacts from surface degradation artifacts: measurements on scanned and fresh areas have to be compared. If they are similar, it means that the tip was degraded. If they are different, it means that the area scanned was degraded.

In the following, we will detail two tip degradation phenomena: tip coating degradation and tip contamination. The former is a non-reversible artifact while the latter can be reversible.

3.3.1 Tip coating degradation

In subsection 3.2.2, we saw that a strong force between the tip and the sample was required in CP-AFM measurements, leading to nano-scratching of the sample. From the tip side, this strong force can lead to the degradation of the tip. In particular, we have seen that for CP-AFM and KPFM, the tip is coated with a conducting material to perform electrical measurements. When a strong force is applied on the tip, the coating wears out. This results in direct degradation of the current signal measured by CP-AFM, affecting the reproducibility of measurements. Figure 3.6 shows CP-AFM profiles before and after a set of seven CP-AFM measurements. The two measurements were performed in the exact same conditions without withdrawing the tip: the same position, the same CP-AFM parameters, and the same illumination intensity on the solar cell. It can be noticed that the signal is strongly degraded after seven image acquisitions. We propose that this change is due to tip degradation because the signal was also degraded on fresh areas that were not scanned previously.

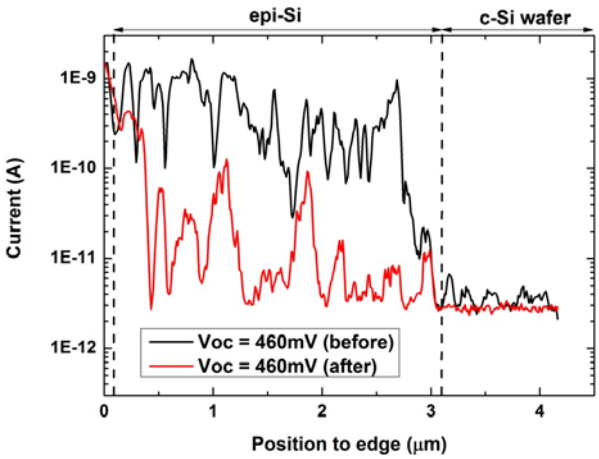

Fig. 3.6 – Current profiles measured by Resiscope on the cross-section of an epitaxial silicon solar cell under the same conditions of illumination before and after seven images taken on the same position. The degradation of the signal is associated with a tip worn out since the signal has also been degraded on fresh areas.

Tip coating degradation is a well reported phenomenon. It explains why CP-AFM tip lifetimes are much lower than KPFM tips. Since KPFM works under soft tapping mode, tip worn out is very slow and often not the limiting factor. A posteriori monitoring technique of this phenomenon is to perform an SEM image of the tip after CP-AFM measurements and to compare with SEM image before measurements. Cavalcoli *et al.* have used this technique to show the tip abrasion after CP-AFM measurements [26]. To reduce this effect and perform more CP-AFM measurements with the same probe, a mitigating strategy is to use bulk conducting probes instead of coated conducting probes. Even if the bulk probe will eventually erode, it will remain conductive for much longer time. Besides, bulk probes enable higher spatial resolution because they are sharper than coated probes which have extra layers of the coating at the edge of the tip [30]. Bulk diamond probes are much more expensive so it is usual to start developing measurements with coated tips and move on to bulk probes to improve accuracy, sensitivity and measurements throughput.

3.3.2 Tip Contamination

While the tip is scanning, adsorbed particles on the surface of the sample may stick to it, causing tip contamination. When the tip is contaminated, the contaminant will most likely dominate the interaction between the sample surface and the tip, thus affecting the electrical image. It may also affect the topographical AFM image [31]. Tip contamination affects both KPFM and CP-AFM. Contrary to tip worn out, tip contamination is very sudden since it results from a fast adsorption of particles from air and the surface. Fig 3.7 shows the sudden change of electrical signal due to tip contamination both on CP-AFM and KPFM images. For both these images, the signal change is much higher than the noise level.

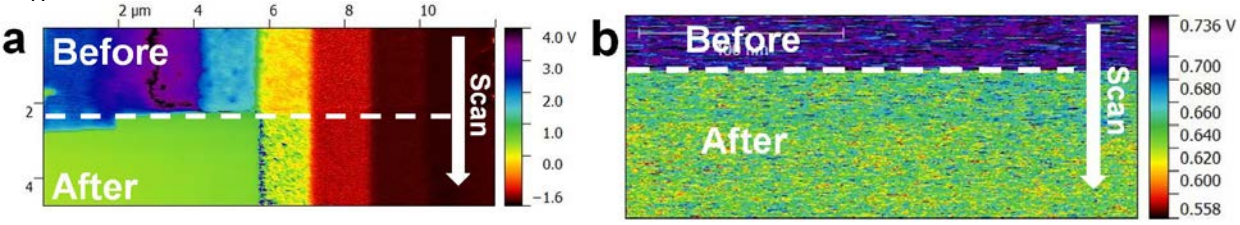

Fig. 3.7 – (a) Resiscope and (b) KPFM measurements before and after tip contamination. Scans are performed line by line, from the top to the bottom. The shift of signal is sudden when the tip is contaminated.

To avoid tip contamination, particular attention has been paid on the cleaning and storage of the samples. Use of highly purified solvent and filtered dry nitrogen is required for cleaning and drying. Sealed vials or nitrogen filed containers are recommended for samples storage. Other mitigation strategies include the use of low adhesion conducting materials for the coating of scanning probes. When the KPFM tip was contaminated, we also performed some lines in contact mode to see if we could remove the contaminant. However, to strongly reduce the risk of tip contamination, measurements have to be performed in UHV conditions after a good sample cleaning. To remove native oxide, HF dip can be used just before measurement under UHV. Some groups have taken advantage of the adhesion of particles to the tip and have developed nano-scale manipulators using AFM tips to bring molecules and atoms from a position to another [32].

3.4 Convolution to topography

CP-AFM and KPFM techniques are sensitive to the surface topography of the sample. When measuring rough surfaces, the topographical image may be imprinted in the electrical image. This artifact affects strongly the interpretation because it is hard to extract the real electrical information from the influence of topographic changes.

For CP-AFM, equation 2.12 of Chapter 2 shows that the measured resistance increases strongly when the radius of contact between the tip and the sample decreases. Therefore, the resistance measured by CP-AFM in a nano-valley will be much higher than that measured on a nano-hill. This is not because nano-hills are more conducting than nano-valleys but because the radius of contacts on the nano-hills is much lower than on nano-valleys. This strong dependence can also be observed while performing measurements on the sample cross-section. When the tip goes slightly beyond the edge, there is still a contact between the tip and the sample from the tip flank. When the tip flank touches the sample instead of the tip apex, the area of contact increases strongly, therefore the current measured increases abruptly and the resistance decreases in the same way [5]. Besides, SSRM and Resiscope are CP-AFM techniques that use logarithmic amplifiers. Therefore, the errors related to the topography are exponentially amplified. In our CP-AFM measurements, the noise associated to topography changes is the limiting noise. Other groups have shown that CP-AFM measurements can be very challenging on high aspect ratio objects such as nano-wires [33] and have proposed to use nano-indentation to detach nanowires in order to locate them and investigate them with different techniques [34].

In KPFM, the topography dependence is less pronounced than in CP-AFM, because the measurement does not rely on the area of contact. However, the electrostatic force varies if the tip “sees” a bump, or a valley or a flat surface. This leads to a topographical imprint of the KPFM surface potential image. This effect is amplified in KPFM by additional artifacts called cross-talks. These effects come from the AC voltage applied and from the photodiode, as is precisely explained by Mélin *et al.* [35] and Barbet *et al.* [36]. Cross-talks result in topography imprints on the electrical image and also artificial shifts with internal KPFM parameters. In the same article, it is explained how cross-talks can be mitigated, for instance, by precisely choosing the AC voltage frequency in KPFM.

To mitigate this artifact, different groups have also been working on de-convoluting the effect of topography from surface potential image in a posteriori image processing [37]. In KPFM, performing measurements at different distances from the surface (lift mode), has also been shown to mitigate the impact of topography on measurements [38]. Finally, a new KPFM setup called heterodyne KPFM has proven to be able to perform measurements on rough surfaces by decreasing the signal from the cantilever base, reducing the topographical coupling [39].

To monitor the effect of topography convolution, electrical and topographical images have to be compared. Using AFM image processing softwares like Gwyddion, the electrical image can be superimposed on the 3D topography image. Figure 3.8 shows CP-AFM and KPFM color images superimposed on the 3D topographical images performed on our setup. On both images, the

convolution is evident, electrical signal changes when the topography changes (bottom of the holes or edges of cross-section). Another monitoring strategy is to perform measurements with different tip radius and compare the electrical images. This way, we can have a grasp of changes due to topography and changes due to real electronic inhomogeneities.

Given this artifact, interpretations are much easier either on flat surfaces [40] or on flat areas of rough surfaces [41]. The effective tip interaction area has to be smaller than the roughness value (RMS) of the surface investigated [42]. Since the effective tip interaction is smaller than the tip radius and the tip radius is around 10nm, surfaces with RMS values below 10nm are desirable. When surfaces are too rough, a polishing step is required to achieve sufficiently flat surfaces. Polishing has to be gentle enough not to degrade electrical properties [5], [40]. In Chapter 5 and Chapter 6, we will detail the cross-section preparation techniques we have investigated to achieve ultra-flat cross-sections while trying to minimize the degradation of electrical properties.

Electron microscopy techniques also have a dependence on topography. Obviously, SEM signal has a strong dependence on material orientation and depth which is used to image surface topography at nano-scale. EBIC depedence on topopgraphy exists but it is lower because the volume of interactions has a higher influence than the surface, especially for high accelerating voltages.

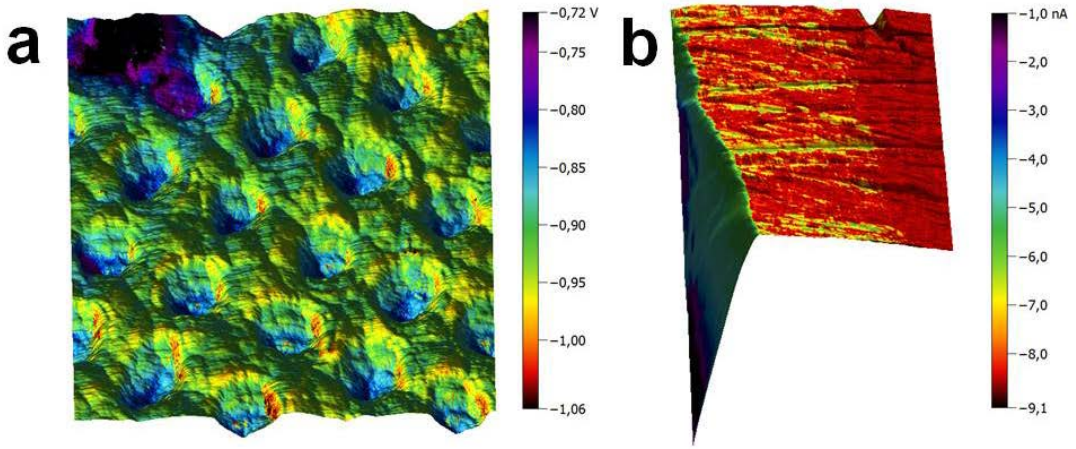

Fig. 3.8 – (a) KPFM and (b) CP-AFM images imprinted on 3D AFM topographical images of rough surfaces. The contrasts of electrical signal coincide with the topographical contrasts. This is due to topographical convolution artifact and not to electrical properties changes.

3.5 Stray Capacitances

One of the reasons why KPFM measurements are dependent on topography is stray capacitances. Stray capacitances can be at the origin of topographical artifacts as shown by Diesinger *et al.* [43].We have seen in Chapter 2 that the capacitance between the end of the tip and the surface below the tip is the one of interest. However, due to a long range of electrostatic forces, other interactions create discrepancies in the KPFM measurement. Figure 3.9 shows the stray capacitances at the origin of the discrepancies. The interactions between tip sidewall and the sample ($C_{stray\ 1}$), the interaction between cantilever and the sample ($C_{stray\ 2}$) and the interaction between the cantilever and the ground ($C_{stray\ 3}$) affect the measurement of the capacitance of interest (C_{CPD}). Several groups have reported that both surface potential and its lateral resolution are affected by stray capacitances. The resulting surface potential measured is the weighted potential of the capacitance of interest and stray capacitances. Stray capacitances explain why steep surface potential changes are challenging to measure and why the lateral resolution of KPFM is limited to about 10 nm [44]. Rosenwaks and al. have shown that below 50 nm distance, it is difficult to distinguish certain kind of defects in silicon [27]. This limits the interpretation of surface potential measurements at the interface of solar cells

[45]. The influence of the stray capacitances is more pronounced in KPFM-AM mode than in KPFM-FM mode because the electrostatic force gradient decays faster than the force [44], [46].

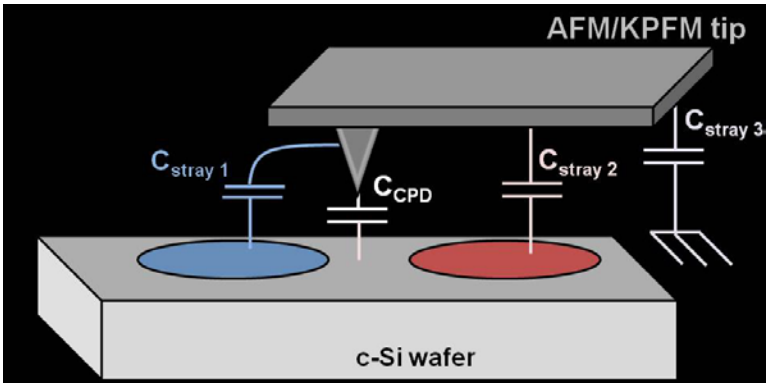

Fig. 3.9 – KPFM tip measuring an inhomogeneous sample. Stray capacitances (C_{stray}) affect the measurement of the capacitance of interest (C_{CPD}) between the tip apex and the sample surface just below the tip.

In order to monitor the effect of stray capacitances, measurements of surface potential at different distances from the surface can be performed in two-pass KPFM. In the first pass, the topography is acquired. In the second pass, the KPFM surface potential is acquired at a given distance from the surface. If surface potential values are dependent on the tip/sample distance, it can be deduced that stray capacitances have a non-negligible effect [38], [46], [47]. In a single pass mode, there is no possibility to choose the tip/sample distance during KPFM measurements because the surface potential is recorded at the same time as the topography. However, in this case, the active spacing control reduces the error on surface potential measurements. Another way to assess the extent of the averaging effect of stray capacitances is to perform KPFM measurements on islands of different sizes [48]. Over a certain size of island, the value of surface potential saturates. This limit value determines the extent of the surface potential averaging effect.

In order to mitigate stray capacitance issues, internal parameters in KPFM softwares can help rectify the tip/sample distance dependence [49], [50]. The use of longer and thinner probes with a large tip edge can also mitigate stray capacitances by increasing the ratio C_{CPD} / C_{stray} [38], [51]. Besides, as for topography convolution artifacts, de-convolution techniques can be used to recover the surface potential without stray capacitances [37], [44], [46], [52]. For instance, Zhitao *et al.* have shown that it is possible to eliminate the cantilever effect in KPFM measurements [53].

3.6 Thermal Noise

In Kelvin Probe Force Microscopy (KPFM), the major noise source is due to thermal fluctuations of the tip position [25]. The sensitivity of the technique in determining the surface potential can be estimated through the minimum detectable difference ΔV:

$$\Delta V = \frac{d}{\epsilon_0 . V_{ac} . R} \cdot \sqrt{\frac{2 . k_B . k . T . B}{\pi^3 . Q . f_0}} \qquad (3.1)$$

Where k_B is the Boltzmann constant, T is the temperature, k is the cantilever spring constant, B is the instrument bandwidth, Q is the cantilever quality factor, f_0 is the cantilever resonance frequency, d is the tip-to-sample distance, ϵ_0 is the dielectric constant of the vacuum, R is the tip radius and V_{ac} is the amplitude of the sinusoidal voltage applied to the tip (Equation 2.1).

In ambient air, Q is around 100, resulting in a minimum detectable difference between 10 and 50mV. In ultra-high vacuum, Q reaches values over 1000 because there is no effect of air damping. In this case, ΔV reaches values in the mV range [54].

Estimating the noise level is crucial to determine which signal changes are detectable. For instance, Duhayon *et al.* have shown that p-type doping of crystalline silicon between 5.10^{16} and

5.10^{20} cm^{-3} leads to surface potential differences of only 150 mV [15]. Therefore, measuring doping levels with KPFM under ambient air with ΔV of 50 mV is going to be challenging. This conclusion is also given by De Wolf *et al*. [21]. To achieve better KPFM contrasts on doping levels, some groups have been successfully using buffer intrinsic layers between different doping steps [55]. In fact, even under UHV, KPFM has been shown not to be an ideal tool for doping measurements, compared to CP-AFM and Scanning Capacitance Microscopy. In Chapter 5, we will confirm this assessment by comparing KPFM and Resiscope on n-type and p-type doping calibration samples. However, KPFM noise level is not limiting for measurements on devices where the effect of illumination and electrical bias leads to surface potential changes between 100 mV and 1 V [5], [24]. In that case, the signal to noise ratio is between 10 and 100, which is acceptable. This is why KPFM has been extensively used in this work to investigate solar cells under operating conditions, as will be presented in Chapter 6.

It should be noted that thermal noise is the limiting factor in KPFM-AM but not in KPFM-FM, where the bandwidth has an offset from the first resonance frequency and the cantilever deflection sensor is the dominant source of noise. In our KPFM-FM setup, the observed noise was too high to consider investigating solar cells in operating conditions. That is why we chose to perform our measurements in KPFM-AM. The noise level can be extracted easily from KPFM images by profile processing. To reduce the noise level on surface potential profiles, profiles can be obtained by averaging several consecutive lines. Figure 3.10 shows the noise level dependence on the number of consecutive lines used for averaging. It can be seen that the decrease is exponential. With one line, the noise level is around 50 mV. With 20 lines, it is around 10mV and with 100 lines it is around 5 mV, as in UHV conditions. This mitigating strategy works well when investigating behaviors that occur along one scan line. The denoising quality is at the expense of the lateral resolution. Other mitigating strategies enable to remove the high frequency thermal noise from the images and profiles. New KPFM techniques, like G Mode KPFM, propose to remove the noise in the acquisition process, using a low pass filter with a high time constant [56]. A strong suppressing strategy for thermal noise is to perform KPFM measurements under UHV and if possible at low temperature with a not too small tip radius. In that case, the thermal noise level reaches 1 mV and below, and becomes negligible compared to other noise sources (e.g. electronics, photodiode) [27]. However, this thermal noise can also be useful. For instance, it is used on regular basis to calibrate the spring constant of cantilevers [57].

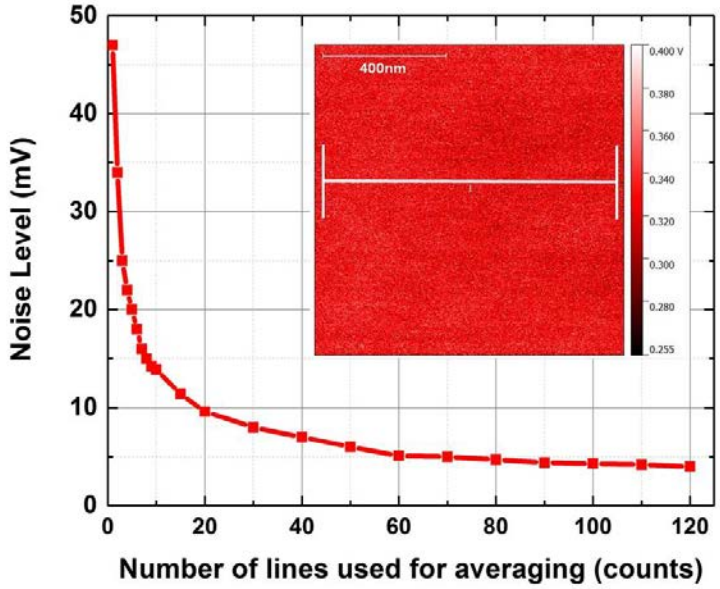

Fig. 3.10 – KPFM profile noise level versus number of lines used for averaging. The noise level decreases strongly with the number of lines used.

3.7 Limited scan speed, size and height

One of the main limitations of current scanning probe microscopy (SPM) equipments is that they are limited in scan size, scan height and scan speed. For instance, SPM images are limited to an area of around 100x100 µm whereas scanning electron microscopy enables images of over 1x1mm [58]. The scan height is often limited to about 20 µm. The two first limitations come from the piezo-electric actuator capabilities. Regarding scan speed, it usually takes about 20 minutes to perform a high resolution 20x20 µm image with 512x512 pixels, compared to 10 seconds for an SEM image of the same size. In SPM, if scan speed is too high, the tip does not have time to follow the topography and the image is quickly degraded. Figure 3.11 shows 3D topographical images at four different scan speeds, which directly correspond to the following scan rates: 0.5 line/s, 1.3 line/s, 1.8 line/s and 2.25 line/s. The degradation of the image is obvious with increasing scan speed. It also affects KPFM and CP-AFM which cannot achieve accurate measurements if the tip is not catching up with the topography.

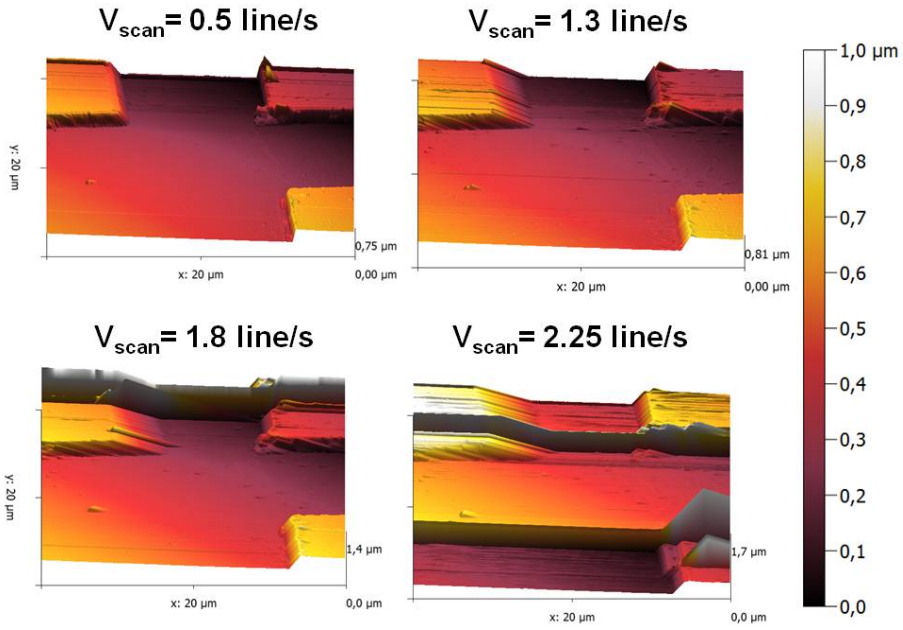

Fig. 3.11 – Four 3D AFM topographical images of the same scanned area (20x20µm) with four different scan rates: 0.5 line/s, 1.3 line/s, 1.8 line/s and 2.25 line/s.

To overcome the scan speed limitation, a lot of work has been carried out since the invention of AFM to achieve high speed [59]. One of the motivations is to have a video time resolution to be able to monitor fast dynamic processes at the nano-scale such as chemical reactions. This speed increase was often at the expense of scan size because of the required increase of rigidity. However, recent works have shown that it is possible to overcome this trade-off and to envision high speed AFM with large scan sizes in the future [60]. KPFM has also been evolving toward high speed. AM-KPFM measurements with scan speed of over 1 mm/s have been reported [61]. It is more challenging to achieve high speed with FM-KPFM and KPFM under UHV but recent progresses have shown interesting perspectives, such as heterodyne KPFM [50].

Regarding the limitations of the scan size and the scan height, a mitigation strategy is to combine electron and scanning probe microscopy (SEM). By inserting a KPFM module into an SEM setup, it is easy to locate interesting areas with the SEM, which can then be investigated with KPFM on a smaller scan area [54], [62]. This also enables to avoid areas with too high topography where the scanning height of KPFM could be a limitation. These solutions are already available commercially [63]. The combination of different microscopies in a single setup enables to take advantage of the

merits of each to reach more accurate measurements. Some research efforts have also been carried out lately to improve the scan size of scanning probe microscopy equipment [64].

3.8 Surface influence

Scanning probe microscopy is limited to acquire information only at the very surface of the sample. This limitation concerns both KPFM and CP-AFM. Rosenwaks *et al.* have shown that KPFM measurement in ambient air could not detect defects deeper than 2 nm below the surface [27]. If measurements are performed under UHV, KPFM cannot detect defects below a few tens of nanometers. Contrary to optical and electron microscopy, scanning probe microscopy has no parameter that enables to scan the signal in depth. In electron microscopy, accelerating voltage provides a depth dependence and in optical microscopy techniques (e.g. Raman spectroscopy, ellipsometry), light wavelength controls the probed depth, as Fig.3.12 shows. To access information in the depth using scanning probe microscopy, a mitigating strategy is to perform measurements on the cross-section. Measurements on the very surface can be beneficial though, to discriminate phenomena at the very surface of the sample from measurements of the bulk effects [65].

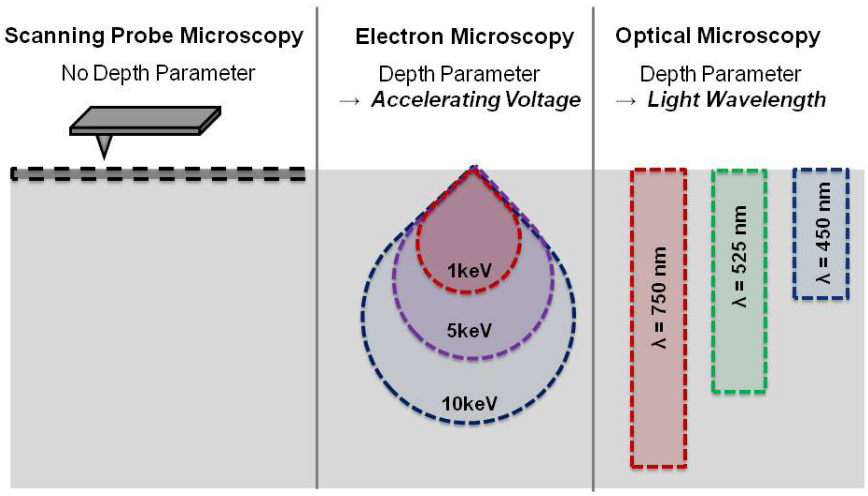

Fig. 3.12 – Scheme of the three microscopy families and their possibility to access information in the depth of a semiconductor sample. Scanning probe microscopy measurements are limited to the very surface (<10 nm). Electron and optical microscopies can access information in the depth of semiconductors through depth parameters, such as the accelerating voltage and the light wavelength, respectively.

In the case of Kelvin Probe Force Microscopy, this surface dependence is problematic because the surface potential may differ from the bulk potential, mainly due to surface states that affect the electrostatic properties leading to a surface band bending (SBB), also called Fermi level pinning. This phenomenon is enhanced for measurements on the cross-section of solar cells which have just been cleaved [6], [66], [66], [67]. It can lead to signal contrast screening [68].This band bending is not induced by the tip as in sub section 3.2.3. It is due to dangling bonds at the top of the cross-section. Because of Fermi level pinning, it has been shown that measurements were very sensitive to the way the cross-section was prepared and cleaned [67]. For instance, the impact of water layer due to air humidity is known to enhance band bending and to reduce the contrast on measurements [10]. Other works have shown that because of contamination (e.g. oxidation), the surface potential contrast was degraded over time [6], [41]. Therefore, a suppressing strategy is to find an appropriate cleaning technique to remove Fermi level pinning at the surface. The surface band bending with different cleaning strategies can be investigated with other characterization techniques such as Ultraviolet Photoelectron Spectroscopy (UPS) [67] or surface sensitive optical techniques that can be coupled with an AFM [69]. Then, measurements should ideally be performed in UHV to limit contamination in time and tip-induced oxidation, even though Fermi level pinning is also present in

UHV [70]. Lately, it has also been proposed to prepare the cross-section in-situ in the KPFM, using FIB milling [71]. This process could be used to acquire a 3D KPFM image by performing successive 2D images and digging in the material with FIB. This process assumes that FIB milling does not affect locally the electrical properties of the sample. Xu *et al.* have considered a similar concept by using nano-scratching during SSRM measurements to acquire 3D SSRM measurements. Successive SSRM images are taken on the same area and since this area is scratched while being measured, in-depth SSRM measurements can be performed [72].

A mitigating strategy for Fermi level pinning is to study the behavior of the cross-section under illumination or electrical bias. If the illumination or the electrical bias does not unpin the Fermi level, the surface potential change on the cross-sectional surface is equal to the potential change in the bulk, which relates to photovoltaic performance [66], [73], [74]. It has been reported that illumination may unpin the Fermi level [6]. This can be monitored easily by measuring the open circuit voltage (V_{oc}) of the solar cell positioned in the AFM/KPFM setup. If surface potential changes are equal to V_{oc} changes, illumination does not unpin Fermi level [66]. The same can be done with electrical bias. If changes of surface potential are equal to changes of electrical bias applied, electrical bias does not unpin Fermi level [73]. Moutinho *et al.* reported that minimum unpinning happened when the solar cell is in the reverse voltage bias [74]. In this Ph.D. project, we extensively used measurements of solar cells under illumination and electrical bias to get rid of the influence of surface band bending. In Chapter 6, we will show that consistent KPFM measurements were achieved despite surface band bending. Our measurements were compared with other characterization techniques, for this purpose.

3.9 Conclusion

In Chapter 3 we have detailed the weaknesses of KPFM and CP-AFM with respect to electron microscopy techniques. Two kinds of weaknesses were presented: artifacts and limitations. A deep analysis of both is key to understand where these techniques can bring additional value for solar cells investigations. A summary of the weaknesses is presented in Table 3.1. In bold, we have highlighted the strategies we used during this project. For each weakness, we have presented:

- **Nature of the weakness:** This part explains if the weakness is an artifact that affects the measurement of the signal, or only a limitation which is a feature of other techniques that KPFM and CP-AFM do not have.

- **Electrical extension:** This part specifies if the weakness affects CP-AFM, KPFM or both

- **Monitoring strategy:** This part highlights how the weakness can be detected and monitored in time.

- **Mitigating strategy:** This part specifies how the weakness can be mitigated. These strategies do not suppress the weakness but enable to reduce its influence. They can be either software or hardware, or both.

- **Suppressing strategies:** This part explains how these weaknesses can be suppressed. It is clear that performing measurements under ultra-high vacuum enable to suppress a lot of weaknesses, but this is at the expenses of measurement time and versatility.

- **Advantages:** This part explains how AFM users can take advantage of the weaknesses. AFM techniques can also be thought of as nano-lithography techniques and not only nano-characterization techniques.

- **In Electron Microscopy (EM)?** : This part addresses if the weakness also affect electron microscopy techniques and if so, which technique between scanning electron microscopy (SEM) and electron beam induced current (EBIC) is more affected.

In Chapter 4, we will continue our investigation of scanning probe microscopy techniques with respect to electron microscopy techniques and we will highlight the advantages of KPFM and CP-AFM, versus EBIC and SEM.

Table 3.1 – Summary table of weaknesses of KPFM and CP-AFM techniques. Bold characters were chosen for strategies we used during this Ph.D. project to mitigate the effects.

Weakness	Nature	Electrical Extension	Monitoring Strategy	Mitigating Strategy	Supressing Strategy	Advan-tages	In EM ?
Parastic Light *AFM Laser*	Artifact	CP-AFM & KPFM	*** Measurement of open circuit voltage induced by the AFM laser (voltmeter, oscilloscope)**	***Optimization of AFM laser position on the cantilever** * Use larger cantilevers	*Piezo-resistive cantilevers *IR AFM laser ($\lambda_{laser} > \lambda_{Eg(Si)}$) *Two-Passes (only for CP-AFM)	/	**No.** No light is required in EM.
Surface Degradation *Tip-induced Oxidation*	Artifact	CP-AFM & KPFM	*** Comparison of scanned area with a fresh area (e.g. larger scans over the scanned area) * Check that topography is higher on the scanned area**	*** Work under dry controlled atmosphere (e.g. nitrogen) * Avoid ranges of voltage leading to oxidation (CP-AFM)**	* Work under UHV	* Nano-lithography * Oxide patterns at nano-scale * Oxide Masks (wet and dry etching)	
Surface Degradation *Nano-Scratching*	Artifact	CP-AFM	*** Observation of scanned area after measurement with AFM optical microscope * Check that topography is lower on the scanned area**	* Optimization of measurement parameters to find a trade-off on the tip force (non-destructive CP-AFM) * Tapping CP-AFM (soft materials) * Increase detection range for low currents	/	* Nano-marking (geolocation …) * Nano-lithography	/
Surface Degradation *Charging& Tip-induced Band Bending*	Artifact	KPFM	*** Perform measurements on surface that do not have Fermi level pinning.**	*** Use lower voltage amplitude on the tip * Focus on measurements with a varying parameter (voltage bias, illumination), considering that band bending is unchanged and can be removed by subtraction**	* Work under UHV	* Increase of contrast in signal on specific samples	**Yes.** Charging is also an issue in Eletron Micrsocopy (cf. Chapter 4)
Tip Degradation *Tip Coating Degradation*	Artifact	CP-AFM	*** Progressive change of signal during scans and no contrast between fresh and scanned area (no sample modification)**	* Use bulk probes instead of coated probes	/	* Performing contact scans on the cross-section of a sample can help recover the tip coating.	**No.**

Weakness	Nature	Electrical Extension	Monitoring Strategy	Mitigating Strategy	Supressing Strategy	Advan-tages	In EM ?
Tip Degradation Conta-mination	Artifact	CP-AFM & KPFM	*** Sudden change in the electrical signal during scan * Can also affect the AFM topographical image * No contrast between fresh and scanned area**	*Storage of the sample after preparation in an adequate environment (e.g. sealed box of nitrogen) * Cleaning with highly purified solvents *** Scanning some line in contact mode to remove the contaminant** * Use low adhesion tip materials	* Appropriate cleaning and work under UHV	* Nano-Manipulation * Nano-tweezers	**No**
Convolution to topography	Artifact	CP-AFM *(Strong)* KPFM *(Intermediate)*	*** Compare topographical and electrical image (electrical image on 3D topography image)** * Choice of AC voltage frequency of voltage bias in KPFM * Different tips radii measurements	* Post-imaging data processing to de-convolute topography and capacitance effects *** Achieve "flat-enough" surfaces without degrading electrical image** * Use of lift-mode (KPFM)	* Achieve ultra-flat surfaces without degrading electrical image.	/	**Yes. SEM :** strong influence**, EBIC :** low influence
Stray Capacitance	Artifact	KPFM	* Dependence of surface potential on tip height (lift mode) * KPFM measurements on islands of different sizes	* Use of longer and narrower probing tips with a rather large radius * Post-imaging data processing to de-convolute capacitance effects	/	/	**No**
Thermal Noise	Limitation	KPFM	*** Noise level extraction from KPFM images and profiles (software)**	*** Averaging on several pixels to remove noise levels** * Using advanced denoising processes	* KPFM under UHV, with low temperature with a not too small tip radius.	* Spring constant calibration technique	**No**
Scan Speed and Size	Limitation	KPFM & CP-AFM	*** Max Scan Size : 100µm * Max Scan height <50µm * Scan Speed : ~20min for 20x20µm image**	* Combine KPFM and SEM in a single set-up to geo-locate easily	* High-speed AFM and KPFM	/	**No** * Scan Size > 1mm * Scan Speed : 10S
Surface Dependence	Limitation& Artifact	KPFM & CP-AFM	*Quantify surface band bending with other techniques such as UPS. *Alternatively removing material and measuring (3D Imaging)	*** Cross-section measurements (information in depth)** * Nano-scratching before measurement (oxide removal) * Find adequate cleaning process	* For silicon, HF dip and work under UHV	* Access ultra-shallow information	For SEM, **yes** *(escape depth)* For EBIC, **no** *(penetration depth)*

REFERENCES

[1] F. J. Giessibl, "Advances in atomic force microscopy," *Rev. Mod. Phys.*, vol. 75, no. 3, pp. 949–983, Jul. 2003.

[2] Y. Gan, "Atomic and subnanometer resolution in ambient conditions by atomic force microscopy," *Surf. Sci. Rep.*, vol. 64, no. 3, pp. 99–121, Mar. 2009.

[3] M. Moczała, N. Sosa, A. Topol, and T. Gotszalk, "Investigation of multi-junction solar cells using electrostatic force microscopy methods," *Ultramicroscopy*, vol. 141, pp. 1–8, Jun. 2014.

[4] Z. Zhang, M. Hetterich, U. Lemmer, M. Powalla, and H. Hölscher, "Cross sections of operating Cu(In,Ga)Se2 thin-film solar cells under defined white light illumination analyzed by Kelvin probe force microscopy," *Appl. Phys. Lett.*, vol. 102, no. 2, p. 23903, Jan. 2013.

[5] P. Narchi *et al.*, "Cross-Sectional Investigations on Epitaxial Silicon Solar Cells by Kelvin and Conducting Probe Atomic Force Microscopy: Effect of Illumination," *Nanoscale Res. Lett.*, vol. 11, no. 1, Dec. 2016.

[6] T. Glatzel, M. Rusu, S. Sadewasser, and M. C. Lux-Steiner, "Surface photovoltage analysis of thin CdS layers on polycrystalline chalcopyrite absorber layers by Kelvin probe force microscopy," *Nanotechnology*, vol. 19, no. 14, p. 145705, 2008.

[7] M. Takihara, T. Takahashi, and T. Ujihara, "Minority carrier lifetime in polycrystalline silicon solar cells studied by photoassisted Kelvin probe force microscopy," *Appl. Phys. Lett.*, vol. 93, no. 2, p. 21902, Jul. 2008.

[8] J. S. Yun *et al.*, "Benefit of Grain Boundaries in Organic–Inorganic Halide Planar Perovskite Solar Cells," *J. Phys. Chem. Lett.*, vol. 6, no. 5, pp. 875–880, Mar. 2015.

[9] Y. Ji *et al.*, "Characterization of the photocurrents generated by the laser of atomic force microscopes," *Rev. Sci. Instrum.*, vol. 87, no. 8, p. 83703, Aug. 2016.

[10] H. Sugimura, Y. Ishida, K. Hayashi, O. Takai, and N. Nakagiri, "Potential shielding by the surface water layer in Kelvin probe force microscopy," *Appl. Phys. Lett.*, vol. 80, no. 8, pp. 1459–1461, Feb. 2002.

[11] F. Houzé, R. Meyer, O. Schneegans, and L. Boyer, "Imaging the local electrical properties of metal surfaces by atomic force microscopy with conducting probes," *Appl. Phys. Lett.*, vol. 69, no. 13, pp. 1975–1977, Sep. 1996.

[12] O. Schneegans, F. Houze, R. Meyer, and L. Boyer, "Study of the local electrical properties of metal surfaces using an AFM with a conducting probe," *IEEE Trans. Compon. Packag. Manuf. Technol. Part A*, vol. 21, no. 1, pp. 76–81, Mar. 1998.

[13] J. P. Kleider, C. Longeaud, R. Brüggemann, and F. Houzé, "Electronic and topographic properties of amorphous and microcrystalline silicon thin films," *Thin Solid Films*, vol. 383, no. 1–2, pp. 57–60, Feb. 2001.

[14] A. Vetushka, A. Fejfar, M. Ledinský, B. Rezek, J. Stuchlík, and J. Kočka, "Comment on ``Current routes in hydrogenated microcrystalline silicon'','' *Phys. Rev. B*, vol. 81, no. 23, p. 237301, Jun. 2010.

[15] N. Duhayon *et al.*, "Assessing the performance of two-dimensional dopant profiling techniques," *J. Vac. Sci. Technol. B*, vol. 22, no. 1, pp. 385–393, Jan. 2004.

[16] A. A. Tseng, A. Notargiacomo, and T. P. Chen, "Nanofabrication by scanning probe microscope lithography: A review," *J. Vac. Sci. Technol. B*, vol. 23, no. 3, pp. 877–894, May 2005.

[17] N. Yang *et al.*, "Water-mediated electrochemical nano-writing on thin ceria films," *Nanotechnology*, vol. 25, no. 7, p. 75701, 2014.

[18] P. Avouris, R. Martel, T. Hertel, and R. Sandstrom, "AFM-tip-induced and current-induced local oxidation of silicon and metals," *Appl. Phys. A*, vol. 66, no. 1, pp. S659–S667.

[19] M. C. Gupta and A. L. Ruoff, "Static compression of silicon in the [100] and in the [111] directions," *J. Appl. Phys.*, vol. 51, no. 2, pp. 1072–1075, Feb. 1980.

[20] R. C. Germanicus *et al.*, "On the effects of a pressure induced amorphous silicon layer on consecutive spreading resistance microscopy scans of doped silicon," *J. Appl. Phys.*, vol. 117, no. 24, p. 244306, Jun. 2015.

[21] P. De Wolf, R. Stephenson, T. Trenkler, T. Clarysse, T. Hantschel, and W. Vandervorst, "Status and review of two-dimensional carrier and dopant profiling using scanning probe microscopy," *J. Vac. Sci. Technol. B*, vol. 18, no. 1, pp. 361–368, Jan. 2000.

[22] A. Vecchiola *et al.*, "Wide range local resistance imaging on fragile materials by conducting probe atomic force microscopy in intermittent contact mode," *Appl. Phys. Lett.*, vol. 108, no. 24, p. 243101, Jun. 2016.
[23] Z.-C. Lin, H.-Y. Jheng, and H.-Y. Ding, "An innovative method and experiment for fabricating bulgy shape nanochannel using AFM," *Appl. Surf. Sci.*, vol. 347, pp. 347–358, Aug. 2015.
[24] P. Narchi *et al.*, "Surface potential investigation on interdigitated back contact solar cells by scanning electron microscopy and Kelvin probe force microscopy: effect of electrical bias," *Sol. Energy Mater. Sol. Cells Submitt.*
[25] L. Kronik and Y. Shapira, "Surface photovoltage phenomena: theory, experiment, and applications," *Surf. Sci. Rep.*, vol. 37, no. 1–5, pp. 1–206, Dec. 1999.
[26] D. Cavalcoli, M. Rossi, A. Tomasi, and A. Cavallini, "Degeneracy and instability of nanocontacts between conductive tips and hydrogenated nanocrystalline Si surfaces in conductive atomic force microscopy," *Nanotechnology*, vol. 20, no. 4, p. 45702, 2009.
[27] Y. Rosenwaks, R. Shikler, T. Glatzel, and S. Sadewasser, "Kelvin probe force microscopy of semiconductor surface defects," *Phys. Rev. B*, vol. 70, no. 8, p. 85320, Aug. 2004.
[28] Y. Leng, C. C. Williams, L. C. Su, and G. B. Stringfellow, "Atomic ordering of GaInP studied by Kelvin probe force microscopy," *Appl. Phys. Lett.*, vol. 66, no. 10, pp. 1264–1266, Mar. 1995.
[29] M. Arakawa, S. Kishimoto, and T. Mizutani, "Kelvin Probe Force Microscopy for Potential Distribution Measurement of Cleaved Surface of GaAs Devices," *Jpn. J. Appl. Phys.*, vol. 36, no. Part 1, No. 3B, pp. 1826–1829, Mar. 1997.
[30] D. Álvarez, J. Hartwich, M. Fouchier, P. Eyben, and W. Vandervorst, "Sub-5-nm-spatial resolution in scanning spreading resistance microscopy using full-diamond tips," *Appl. Phys. Lett.*, vol. 82, no. 11, pp. 1724–1726, Mar. 2003.
[31] H.-Y. Nie and N. S. McIntyre, "A Simple and Effective Method of Evaluating Atomic Force Microscopy Tip Performance," *Langmuir*, vol. 17, no. 2, pp. 432–436, Jan. 2001.
[32] S. Mekid, S. Bashmal, and H. M. Ouakad, "Nanoscale Manipulators: Review of Conceptual Designs Through Recent Patents," *Recent Pat. Nanotechnol.*, vol. 10, no. 1, pp. 44–58, Apr. 2016.
[33] A. Fejfar *et al.*, "Microscopic measurements of variations in local (photo)electronic properties in nanostructured solar cells," *Sol. Energy Mater. Sol. Cells*, vol. 119, pp. 228–234, Dec. 2013.
[34] A. Fejfar *et al.*, "Correlative microscopy of radial junction nanowire solar cells using nanoindent position markers," *Sol. Energy Mater. Sol. Cells*, vol. 135, pp. 106–112, Apr. 2015.
[35] T. Mélin, S. Barbet, H. Diesinger, D. Théron, and D. Deresmes, "Note: Quantitative (artifact-free) surface potential measurements using Kelvin force microscopy," *Rev. Sci. Instrum.*, vol. 82, no. 3, p. 36101, Mar. 2011.
[36] S. Barbet, M. Popoff, H. Diesinger, D. Deresmes, D. Théron, and T. Mélin, "Cross-talk artefacts in Kelvin probe force microscopy imaging: A comprehensive study," *J. Appl. Phys.*, vol. 115, no. 14, p. 144313, Apr. 2014.
[37] T. Machleidt, E. Sparrer, D. Kapusi, and K.-H. Franke, "Deconvolution of Kelvin probe force microscopy measurements—methodology and application," *Meas. Sci. Technol.*, vol. 20, no. 8, p. 84017, 2009.
[38] H. O. Jacobs, H. F. Knapp, S. Müller, and A. Stemmer, "Surface potential mapping: A qualitative material contrast in SPM," *Ultramicroscopy*, vol. 69, no. 1, pp. 39–49, Aug. 1997.
[39] Z. M. Ma, L. Kou, Y. Naitoh, Y. J. Li, and Y. Sugawara, "The stray capacitance effect in Kelvin probe force microscopy using FM, AM and heterodyne AM modes," *Nanotechnology*, vol. 24, no. 22, p. 225701, 2013.
[40] H. Li, C. S. Jiang, W. K. Metzger, C. K. Shih, and M. Al-Jassim, "Microscopic Real-Space Resistance Mapping Across CdTe Solar Cell Junctions by Scanning Spreading Resistance Microscopy," *IEEE J. Photovolt.*, vol. 5, no. 1, pp. 395–400, Jan. 2015.
[41] B. E. McCandless and S. Rykov, "Cross-section potential analysis of CdTe/CdS solar cells by kelvin probe force microscopy," in *33rd IEEE Photovoltaic Specialists Conference, 2008. PVSC '08*, 2008, pp. 1–4.
[42] P. Eyben *et al.*, "Development and optimization of scanning spreading resistance microscopy for measuring the two-dimensional carrier profile in solar cell structures," *Phys. Status Solidi A*, vol. 208, no. 3, pp. 596–599, Mar. 2011.
[43] H. Diesinger, D. Deresmes, and T. Mélin, "Capacitive Crosstalk in AM-Mode KPFM," Chapter 3 in *Kelvin Probe Force Microscopy*, S. Sadewasser and T. Glatzel, Eds. Springer Berlin Heidelberg, 2012, pp. 25–44.

[44] U. Zerweck, C. Loppacher, T. Otto, S. Grafström, and L. M. Eng, "Accuracy and resolution limits of Kelvin probe force microscopy," *Phys. Rev. B*, vol. 71, no. 12, p. 125424, Mar. 2005.
[45] T. Glatzel, H. Steigert, S. Sadewasser, R. Klenk, and M. C. Lux-Steiner, "Potential distribution of Cu(In,Ga)(S,Se)2-solar cell cross-sections measured by Kelvin probe force microscopy," *Thin Solid Films*, vol. 480–481, pp. 177–182, Jun. 2005.
[46] Ł. Borowik, K. Kusiaku, D. Théron, and T. Mélin, "Calculating Kelvin force microscopy signals from static force fields," *Appl. Phys. Lett.*, vol. 96, no. 10, p. 103119, Mar. 2010.
[47] O. Vatel and M. Tanimoto, "Kelvin probe force microscopy for potential distribution measurement of semiconductor devices," *J. Appl. Phys.*, vol. 77, no. 6, pp. 2358–2362, Mar. 1995.
[48] F. Krok, K. Sajewicz, J. Konior, M. Goryl, P. Piatkowski, and M. Szymonski, "Lateral resolution and potential sensitivity in Kelvin probe force microscopy: Towards understanding of the sub-nanometer resolution," *Phys. Rev. B*, vol. 77, no. 23, p. 235427, Jun. 2008.
[49] A. Kibel, "KFM Modes in Picoview 1.10.4," Application Note, 2011.
[50] J. L. Garrett and J. N. Munday, "Fast, high-resolution surface potential measurements in air with heterodyne Kelvin probe force microscopy," *Nanotechnology*, vol. 27, no. 24, p. 245705, 2016.
[51] T. Hochwitz, A. K. Henning, C. Levey, C. Daghlian, and J. Slinkman, "Capacitive effects on quantitative dopant profiling with scanned electrostatic force microscopes," *J. Vac. Sci. Technol. B*, vol. 14, no. 1, pp. 457–462, Jan. 1996.
[52] G. Cohen *et al.*, "Reconstruction of surface potential from Kelvin probe force microscopy images," *Nanotechnology*, vol. 24, no. 29, p. 295702, 2013.
[53] Z. Yang and M. G. Spencer, "Improve the Accuracy of Scanning Kelvin Probe Microscopy by Eliminating the Cantilever Effect," *MRS Online Proc. Libr. Arch.*, vol. 838, Jan. 2004.
[54] A. Kikukawa, S. Hosaka, and R. Imura, "Vacuum compatible high-sensitive Kelvin probe force microscopy," *Rev. Sci. Instrum.*, vol. 67, no. 4, pp. 1463–1467, Apr. 1996.
[55] I. Volotsenko *et al.*, "Secondary electron doping contrast: Theory based on scanning electron microscope and Kelvin probe force microscopy measurements," *J. Appl. Phys.*, vol. 107, no. 1, p. 14510, Jan. 2010.
[56] L. Collins *et al.*, "Multifrequency spectrum analysis using fully digital G Mode-Kelvin probe force microscopy," *Nanotechnology*, vol. 27, no. 10, p. 105706, 2016.
[57] R. Proksch, T. E. Schäffer, J. P. Cleveland, R. C. Callahan, and M. B. Viani, "Finite optical spot size and position corrections in thermal spring constant calibration," *Nanotechnology*, vol. 15, no. 9, p. 1344, 2004.
[58] J. T. Heath, C. S. Jiang, and M. M. Al-Jassim, "Diffused junctions in multicrystalline silicon solar cells studied by complementary scanning probe microscopy and scanning electron microscopy techniques," in *2010 35th IEEE Photovoltaic Specialists Conference (PVSC)*, 2010, pp. 000227–000232.
[59] T. Ando, "High-speed atomic force microscopy coming of age," *Nanotechnology*, vol. 23, no. 6, p. 62001, 2012.
[60] I. Soltani Bozchalooi, A. Careaga Houck, J. M. AlGhamdi, and K. Youcef-Toumi, "Design and control of multi-actuated atomic force microscope for large-range and high-speed imaging," *Ultramicroscopy*, vol. 160, pp. 213–224, Jan. 2016.
[61] A. K. Sinensky and A. M. Belcher, "Label-free and high-resolution protein/DNA nanoarray analysis using Kelvin probe force microscopy," *Nat. Nanotechnol.*, vol. 2, no. 10, pp. 653–659, Oct. 2007.
[62] N. Anspach, F. Hitzel, F. Zhou, and S. Eyhusen, "Hybrid SEM/AFM System from Carl Zeiss Revolutionizes Analysis of Functional Micro- and Nanostructured Specimen," *Microsc. Microanal.*, vol. 20, no. S3, pp. 992–993, Aug. 2014.
[63] A. Lewis, A. Komissar, A. Ignatov, O. Fedoroyov, E. Maayan, and D. Yablon, "AFM Integrated with SEM/FIB for Complete 3D Metrology Measurements," *Microsc. Microanal.*, vol. 20, no. S3, pp. 1112–1113, Aug. 2014.
[64] U. Gysin *et al.*, "Large area scanning probe microscope in ultra-high vacuum demonstrated for electrostatic force measurements on high-voltage devices," *Beilstein J. Nanotechnol.*, vol. 6, pp. 2485–2497, Dec. 2015.
[65] B. Bhushan and A. V. Goldade, "Measurements and analysis of surface potential change during wear of single-crystal silicon (100) at ultralow loads using Kelvin probe microscopy," *Appl. Surf. Sci.*, vol. 157, no. 4, pp. 373–381, Apr. 2000.

[66] C.-S. Jiang, D. J. Friedman, J. F. Geisz, H. R. Moutinho, M. J. Romero, and M. M. Al-Jassim, "Distribution of built-in electrical potential in GaInP2/GaAs tandem-junction solar cells," *Appl. Phys. Lett.*, vol. 83, p. 1572, Aug. 2003.

[67] T. Glatzel, D. Fuertes Marron, T. Schedel-Niedrig, S. Sadewasser, and M. C. Lux-Steiner, "CuGaSe2 solar cell cross section studied by Kelvin probe force microscopy in ultrahigh vacuum," *Appl. Phys. Lett.*, vol. 81, no. 11, pp. 2017–2019, 2002.

[68] A. Kikukawa, S. Hosaka, and R. Imura, "Silicon pn junction imaging and characterizations using sensitivity enhanced Kelvin probe force microscopy," *Appl. Phys. Lett.*, vol. 66, no. 25, pp. 3510–3512, Jun. 1995.

[69] S. Moreno Flores and J. L. Toca-Herrera, "The new future of scanning probe microscopy: Combining atomic force microscopy with other surface-sensitive techniques, optical microscopy and fluorescence techniques," *Nanoscale*, vol. 1, no. 1, p. 40, 2009.

[70] S. Sadewasser *et al.*, "Characterization of the CuGaSe2/ZnSe Interface Using Kelvin Probe Force Microscopy," *MRS Online Proc. Libr. Arch.*, vol. 668, Jan. 2001.

[71] R. Saive *et al.*, "Imaging the Electric Potential within Organic Solar Cells," *Adv. Funct. Mater.*, vol. 23, no. 47, pp. 5854–5860, Dec. 2013.

[72] M. W. Xu, T. Hantschel, and W. Vandervorst, "Three-dimensional carrier profiling of InP-based devices using scanning spreading resistance microscopy," *Appl. Phys. Lett.*, vol. 81, no. 1, pp. 177–179, Jul. 2002.

[73] C.-S. Jiang, A. Ptak, B. Yan, H. R. Moutinho, J. V. Li, and M. M. Al-Jassim, "Microelectrical characterizations of junctions in solar cell devices by scanning Kelvin probe force microscopy," *Ultramicroscopy*, vol. 109, no. 8, pp. 952–957, Jul. 2009.

[74] H. R. Moutinho, R. G. Dhere, C.-S. Jiang, Y. Yan, D. S. Albin, and M. M. Al-Jassim, "Investigation of potential and electric field profiles in cross sections of CdTe/CdS solar cells using scanning Kelvin probe microscopy," *J. Appl. Phys.*, vol. 108, no. 7, p. 74503, Oct. 2010.

Chapter 4 – Strengths of KPFM and CP-AFM techniques

Contents

4.0 Introduction

After presenting the weaknesses of scanning probe microscopy (SPM) techniques with respect to electron microscopy (EM) in Chapter 3, we will highlight in Chapter 4 the strengths of these techniques. We will show that these strengths enable nano-scale measurements that are impossible with electron microscopy. The core advantage of scanning probe microscopy over electron and optical microscopy (OM) is that it does not require injection of carriers to perform measurements. SPM "touches" the matter at nano-scale when EM and OM "see" the matter at nano-scale. This non-intrusiveness results in several advantages that we will detail and explain in this chapter.

As for Chapter 3, we will focus on KPFM and CP-AFM techniques among scanning probe microscopy techniques, because these are the two techniques we used during this PhD project. For each strength, we will present monitoring strategies and improvement paths. We will also directly compare with capabilities of electron microscopy techniques and explain what possibilities these strengths enable. All the information is summed up in a table at the conclusion of this chapter. This will enable us to take a step back and determine situations where CP-AFM and KPFM can bring additional value to the measurement of solar cells.

4.1 Spatial Resolution

One of the main benefits of scanning probe microscopy techniques is the spatial resolution. Both standard KPFM and CP-AFM setups even under ambient air can reach resolutions better than 10 nm [1], [2]. Under ultra-high vacuum, KPFM has proven to be able to achieve sub-nanometer resolution using FM mode [3], [4]. At this atomic scale, the interaction between the KPFM tip and the atoms is still not well understood because some additional interactions have to be interpreted, such as covalent interactions between the front tip atom and the surface atoms [3], [4]. Comparison between simulation and experiments is required, to be able to interpret these atomic scale images [5], [6]. In particular, the effect of the tip size and shape has to be taken into account [5]. If a precise understanding of these images was achieved, KPFM under UHV could be used as an "atom identification technique" [4].

Electron microscopy has a spatial resolution that is very dependent on the techniques (section 2.4). Transmission Electron Microscopy (TEM) reaches atomic scale resolution but it is intrinsically a highly destructive technique since it requires the sample to have a thickness of a few tens of nanometers. Scanning electron microscopy (SEM) can reach resolution between 1 and 20 nm depending on the instrument. The spatial resolution of Electron Beam Induced Current (EBIC) is strictly related to the interaction volume of electrons, depending on material properties such as density, and it can range from few nanometers to tens of microns. For high diffusion length materials, such as high quality crystalline silicon wafers, the EBIC signal is strongly convoluted with the diffusion length and a resolution over 10 µm can be reached. That is why, EBIC is sometimes challenging for the investigation of high quality crystalline silicon solar cells. One strong advantage of KPFM and CP-AFM compared to EBIC is that the resolution is not material dependent. This is all the more important when investigating hetero-junctions or multi-junction solar cells, where different materials are present on the same area under investigation.

For scanning probe microscopy techniques such as KPFM and CP-AFM, the lateral resolution strongly depends on the tip radius and shape. For instance, CP-AFM measurements with the best resolution (<5 nm) are achieved with bulk diamond probes instead of diamond coated silicon probes [2], [7]. Because they are not coated, the obtained radius of the tip can be smaller and thus enable better lateral resolution. It has been shown that for CP-AFM measurements at an interface, the resistance signal convolution is only present within two tip radius distance from the interface [2], [8]. Additionally, these tips are less sensitive to degradation as discussed in Section 3.3. The only limitations for smaller tip radius in CP-AFM are the wear-off speed and the resistance signal which is

much higher for smaller tip radii [2]. If the equipment could detect higher resistances than $10^{12}\Omega$ and advanced materials, such as carbon nanotubes [9] enabled low radius with high mechanical resistance, there is no reason why the spatial resolution of CP-AFM cannot be improved.

Different kinds of cantilevers and coatings are used for KPFM measurements. The most popular cantilevers are heavily doped silicon cantilevers, Pt/Ir-coated silicon cantilevers and Au or Cr coated silicon cantilevers [1]. Heavily doped silicon cantilevers are routinely used to produce high-resolution images under UHV but native oxide has to be removed before measurements by heating, ion bombardment or etching. This step is one of the reasons why measurements in UHV are time consuming. Pt/Ir-coated silicon cantilevers do not require substantial tip preparation but yield to lower spatial resolutions for KPFM. We have been using this kind of cantilevers because they are well adapted for measurements under ambient air. Finally, Au or Cr coated silicon can be used for the high resolution imaging. The advantage is that materials like Cr are less reactive in air than bare silicon. However, a fine optimization on the Cr thickness has to be done to obtain the best spatial resolution. As for CP-AFM, the tip radius is crucial to achieve high resolution images [1].

To measure the resolution of the techniques, calibration samples can be used. In our case, we designed our own calibration by digging nano-holes with focused ion beam (FIB) technique on the surface of crystalline silicon wafers. These nano-holes had three different radii (50 nm, 100 nm, 250 nm) and six different depths (1 nm, 3 nm, 5 nm, 10 nm, 20 nm, 50 nm) as Figure 4.1 shows. Topographical and KPFM images associated to this sample are also given. We can notice that the lateral resolution of KPFM depends on the holes depth. For depths of 50 nm and 20 nm, the resolution is better than 50 nm because 50nm large holes can be seen on the KPFM image. For depths of 10nm and 5 nm, the resolution is between 50 nm and 100 nm and for depths of 3 nm and 1 nm, the resolution is over 100 nm. This highlights that the lateral resolution also depends on the singal-to-noise ratio of the equipment and the sample.

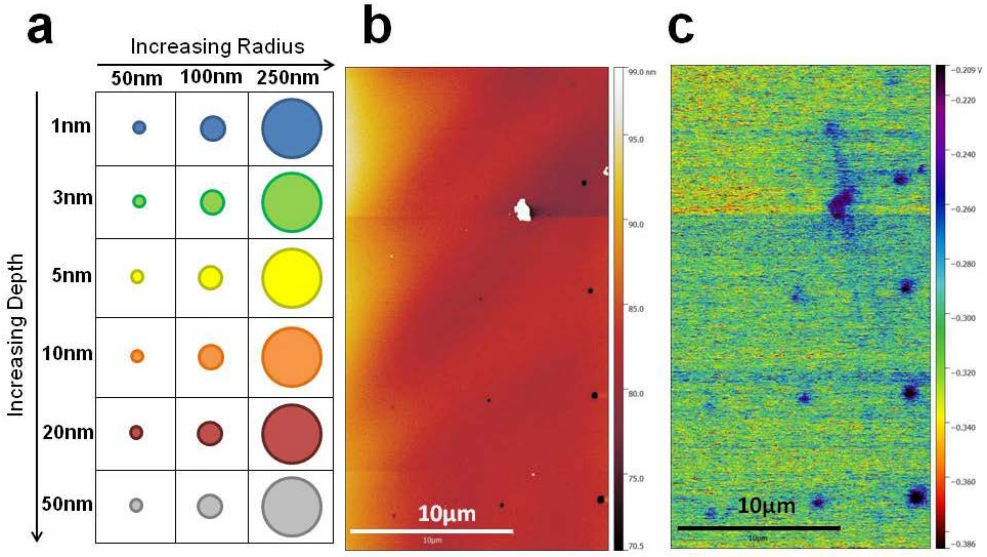

Fig. 4.1 – a) Scheme, b) Topography image and c) KPFM image of nano-holes with different radius and depths on the surface of silicon designed with Focused Ion Beam (FIB)

To improve the spatial resolution of CP-AFM and KPFM, two obvious strategies are: i) working with smaller tip radius and ii) working under ultra-high vacuum. Another strategy is to tilt the sample to increase the spatial resolution, as shown by Zhang *et al.* [10].

Contrary to Secondary Ion Mass Spectrometry (SIMS) and capacitance technique, both scanning probe and electron microscopy techniques have 2D scanning capabilities with nano-scale resolution. 2D scanning capability associated with nano-scale resolution is of prime interest for two kinds of investigations in solar cells: investigation of nano-objects at the surface of solar cells and

investigation of the cross-section of solar cells. On the one hand, surface investigation represents an incremental improvement with respect to conventional characterization techniques with micro-scale resolution. By using nano-scale resolution techniques, we are now able to map smaller defects, such as grain boundaries [11] or the surface of single grains [12]. On the other hand, cross-section investigations are disruptive improvements. These measurements were impossible with standard micro-scale characterization techniques because the thickness of solar cell layers range between a few microns (e.g. epitaxial layers) and a few atoms (e.g. AlO_x layers deposited by atomic layer deposition). Using nano-scale resolution techniques, we can investigate the properties of the PN junction on the cross-section of solar cell which is the heart of the device [13], [14]. Besides, the properties of the PN junction can be investigated under operating conditions such as illumination [15] or electrical bias [16]. In Chapter 6, we present surface and cross-section measurements using KPFM and CP-AFM where we extensively investigate the properties of PN junctions under operating conditions.

4.2 Sensitivity to illumination

The core advantage of scanning probe microscopy over electron and optical microscopy is that it does not rely on the injection of carriers to perform a measurement. This fundamental difference results in several precise advantages that will be described in this Chapter.

One of the most valuable advantages for the investigation of solar cells is that scanning probe microscopy techniques can measure the effect of illumination at the nano-scale, while electron microscopy cannot because the solar cell is already locally saturated with high electron carrier concentration. In order to quantify this phenomenon, we propose to compare the injection level of electrons in a SEM with the injection level corresponding to one sun illumination. To do so, we will calculate the generation rates in a given volume of a crystalline silicon wafer with high diffusion length (L_D), in these two conditions. The generation rate corresponds to the number of electron/hole pairs created in the silicon wafer in one second. To simplify, we chose not to take into account the diffusion of carriers and we focus only on the generation of carriers.

First, we consider an electron beam focused on the crystalline silicon wafer. We assume that the electron energy E is 10keV and the initial beam current is 10µA, which correspond to the conditions used in EBIC. In these conditions, the current beam reaching the surface I_b is measured to be 0.89nA [17]. Schroder *et al.* calculate the generation rate G_{el} [18] by the expression:

$$G_{el} = \frac{I_b N_{ehp}}{q} \tag{4.1}$$

where q is the electron charge and N_{ehp} is the average number of electrons/hole pairs created by an incident electron with an energy E. According to Schroder *et al.*, N_{ehp} is equal to 2.5×10^3 [18]. So, in the interaction volume, G_{el} is equal to $1.4 \times 10^{13} s^{-1}$. The interaction volume is a sphere with a diameter equal to the penetration depth D_e, with D_e (Si) = $10^{-11} E^{1.75}$ [18]. In our case, we calculate D_e = 1 µm.

Second, we calculate the optical generation rate. To do so, we imagine a beam of light with a diameter equal to the penetration depth D_e. The volume of generation is the semi-infinite cylinder in the wafer with a diameter of D_e. We consider a light source with a photon flux at the surface N_0 equal to one sun illumination: $N_0 = 1.4 \times 10^{21} m^{-2}.s^{-1}$. We assume that every photon absorbed produces an electron hole/pair in the volume. Therefore, the optical generation rate in this cylinder is given by the expression:

$$G_{opt} = \pi \left(\frac{D_e}{2}\right)^2 N_0 \tag{4.2}$$

We calculate this expression numerically and we find G_{opt} is equal to $1.1 \times 10^9 s^{-1}$. Finally, we compare the generation rates G_{el} and G_{opt} and we find that G_{el} is 10,000 times bigger than G_{opt}. This shows that the effect of one sun external illumination is totally negligible compared with the incident electron beam used in SEM and EBIC measurements. This is reinforced by the fact that the photovoltage increases logarithmically with illumination intensity. Therefore these techniques cannot

be used to monitor the effect of illumination at the nano-scale. However, electron microscopy techniques can detect easily the effect of an electrical bias. This is why, in Chapter 6, we chose to compare SEM and KPFM for solar cells under electrical bias.

Measuring without direct injection of carriers makes scanning probe microscopy techniques unique tools to monitor the effect of illumination at the nano-scale. Extensive work has been done to investigate the effect of different parameters of illumination using KPFM and CP-AFM. For instance, the effect of light intensity has been studied on crystalline wafers [19], epitaxial silicon solar cells [15], polycrystalline silicon solar cells [20], multi-junction [21] and Cu(In,Ga)Se_2 solar cells [10]. Other works have focused on the influence of light wavelength on KPFM measurements on III-V solar cells [22] and epitaxial silicon solar cells [23]. Some groups have also studied the influence of the beam position on measurements [24] or using the frequency modulated illumination determined lifetime at the nano-scale [20], [25], [26]. These measurements will be extensively discussed in Chapter 5 and Chapter 6 of this manuscript.

A monitoring strategy in these measurements is the comparison between nano-scale photovoltage measurements with KPFM and macro-scale open-circuit voltage measurements with a voltmeter, when the cell is mounted in the KPFM setup. If these values are equal, we know the effects of artifacts are limited and measurements can be considered as quantitative. Photovoltage measurements using KPFM can be used for instance, to determine minority carriers diffusion lengths [27] or to investigate photovoltage at nano-scale on nano-defects [11].

4.3 Low charging effect and activation

In both scanning probe microscopy and electron microscopy, the surface investigated can be charged, leading to charging issues that alter the measurements and their reproducibility. However, this issue is more problematic in electron microscopy where the intensity of injected carriers is high [28], [29], as shown in sub-chapter 4.2. For instance, in electron beam induced current (EBIC), it is challenging to perform measurements on high lifetime crystalline silicon wafers because of charging issues. Figure 4.2 shows three consecutive EBIC measurements on the cross-section of a lowly doped crystalline silicon wafer. Measurements are performed in the exact same conditions. On Figure 4.2.a, only a small part of the image was previously scanned, then we zoomed out to acquire the image. The EBIC signal is higher on the exposed area than on the rest of the cross-section. When exposing the entire cross-section (Figure 2.b and Figure 2.c), the signal increases on the whole cross-section. It is no longer possible to see the first small area exposed, which we explain as the saturation of the signal. Our EBIC measurements on the cross-section of HIT solar cells proved to be very challenging because of these charging issues.

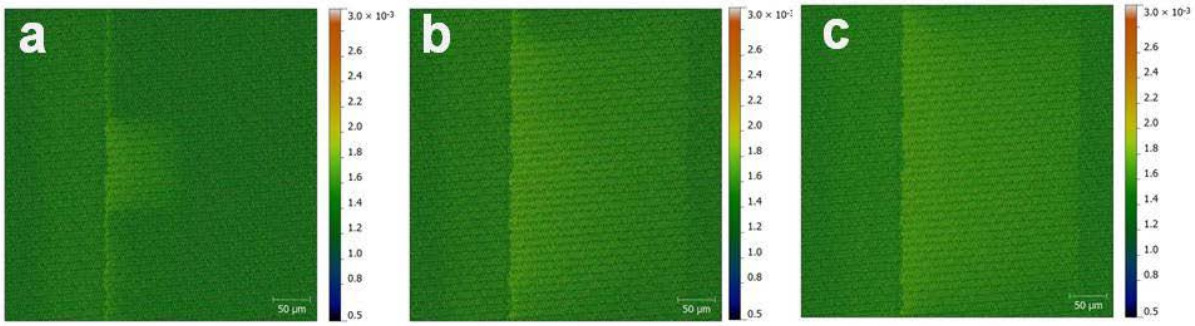

Fig. 4.2 –Three consecutive EBIC images on the cross-section of a lowly doped crystalline silicon wafer. a) In the first image, only a small area was previously exposed leading to higher EBIC signal. b) – c) Consecutive images were the whole area was exposed leading to EBIC saturation

Charging effects are reversible. Less than one hour after exposure, we could recover the initial quality of the image. However, in some cases, the signal did not recover causing the technique to be destructive. We explain this phenomenon by carbon contamination, which is a well-known problem in SEM environment [30]–[32]. Residual hydrocarbons in the SEM chamber are cracked by the primary electron beam and a layer of amorphous carbon is formed, at a rate increasing with the magnification. Therefore, only a limited amount of time can be spent measuring an area with SEM without degrading it. This was reported in our article comparing SEM and KPFM on an interdigitated back contact solar cell [33]. Figure 4.3 shows the SEM image of an area that has been scanned during 30 minutes. The SEM image was still degraded two hours later.

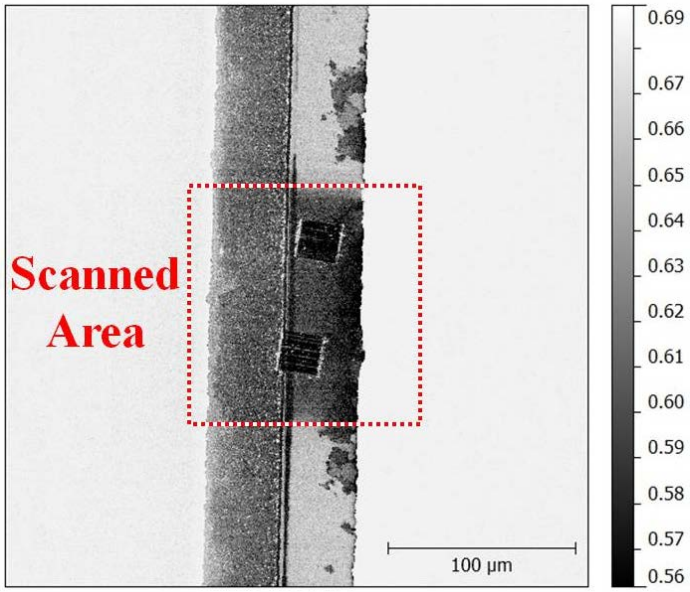

Fig. 4.3 – Carbon contamination effect in SEM. The SEM image shows an area which has been scanned for 30 minutes. The scanned area is darker due to carbon contamination.

In scanning probe microscopy, tip-induced charging effects occur marginally. When the field applied between the tip and the sample is high, electro-migration of charges from the tip to the sample can occur leading to surface charging [34]. These charges can lead to electrostatic screening phenomenon where charges of one type gather around charges of the opposite type to minimize the total electrostatic energy. This phenomenon is especially present in dielectric materials [35]. Figure 4.4 shows the effect of a charge deposited on the cross-section of a lowly doped crystalline silicon wafer during two consecutive measurements. Measurements performed twenty minutes later showed that this charge faded away and the image was recovered. In this case, charging is less problematic, because it happens only on a part of the image, and it can be easily identified. Besides, in our experiments, these charging issues were pretty rare, so they did not limit our measurements.

KPFM has low charging issues and does not indent the material during measurements like CP-AFM. Therefore it is a low-intrusion technique. If tip-induced oxidation is limited by working under a controlled atmosphere, KFPM images are highly reproducible. This is a great advantage of KPFM and it makes it a good tool to monitor degradation phenomena as a function of time or to study the influence of an external parameter (e.g. light or electrical bias) by making successive images of the same area under different external conditions.

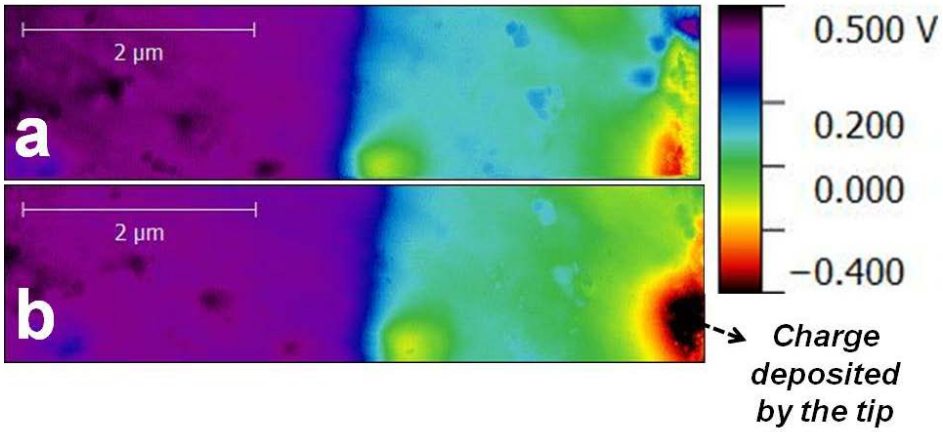

Fig. 4.4 – Charging effect taking place during two consecutive KPFM measurements on the same area. a) Surface potential image before charging. b) Surface potential image after charging.

4.4 Direct Electrical Measurements

The electrical properties measured at the nano-scale by CP-AFM and KPFM are quantities that are used to characterize solar cells at macro-scale and define if a solar cell is good or not. CP-AFM measures the current locally and KPFM measures the voltage (or potential) locally. This is of prime interest to compare local measurements with global electrical measurements. For instance, in our setup, we could compare the photovoltage measured locally by the KPFM and the V_{oc} measured by a voltmeter when the cell was inside the KPFM setup [15]. This comparison gives us information about the quality of the measurements and the influence of the AFM laser. In the same way, the J(V) curve measured by CP-AFM can be compared with J(V) curves performed at macro-scale on the solar cell [36], [37].

Unlike KPFM and CP-AFM, electronic microscopy techniques do not measure quantities that are directly comparable to macro-scale properties of solar cells. For instance, EBIC measures a current which is induced by a local electron beam and therefore different from that induced by a global one sun illumination. Electronic properties of the solar cell (e.g. space charge region length [38], diffusion lengths [39]) can be deduced from this signal but it requires data processing and fine understanding of the measurement to achieve quantitative information.

Another example is SEM which measures the secondary electrons current emitted by sample surface atoms excited by a primary electron beam. Even though this technique is routinely used to study the topography at the nano-scale, it has been shown that SEM signal is also sensitive to surface potential and enables to detect doping contrast [40], [41]. It has also been used to study the influence of the electrical bias on the PN junction of solar cells and to compare with KPFM [32]. However, it is challenging to achieve quantitative measurements of doping levels or surface potential changes by measuring the secondary electrons current, considering also that the origin of SEM contrast is not yet fully understood [30], [40]. Therefore, SEM is deemed as a qualitative technique to investigate electric properties at nano-scale [8]. It requires a robust model for quantification that is not available yet, even though several groups are actively working on this topic [42], [43].

For KPFM and CP-AFM, no intermediate signal is used to detect the current and voltage at the nano-scale. By reducing the number of intermediate signals, the number of data processing steps is limited and therefore it is easier to achieve quantitative measurements. For instance, it has been shown by several authors that CP-AFM (including SSRM and Resiscope) is the most appropriate technique to achieve quantitative nano-scale mapping of carrier concentrations [2], [8], [44].

Since scanning probe microscopy techniques can measure quantities of interest with a nano-scale resolution, they can be used to geo-locate defective areas that directly affect these quantities. For instance, solar cells are often limited by series resistance. The total series resistance is visible on the IV curve of the solar cell. However, the origin of the series resistance is not always easy to identify. For instance, series resistances can come from a problem of contacting, or from insufficient doping in the semiconductor. Since series resistance induces a potential drop for high currents, KPFM can detect locally the effect of series resistance in forward voltage bias, where the current is high. We have studied series resistance and diode effects on epitaxial silicon solar cells [23] and interdigitated back contact solar cells [45]. These results will be presented in Chapter 6. Measurements of series resistance can be used as inputs in simulation tools to improve the numerical modeling of solar cells. This investigation of series resistance is not possible with SEM and EBIC that are sensitive to diodes and space charge regions effects.

4.5 Versatility

The techniques belonging to the scanning probe microscopy (SPM) family are known to be very versatile. First, SPM techniques offer the possibility to work under a broad range of pressures, temperatures and humidity levels [46], [47]: ambient air, controlled atmosphere, ultra-high vacuum and even in liquids. KPFM can also be used in a liquid environment through electrochemical force microscopy [48]; this environment is challenging for CP-AFM. However, CP-AFM and KPFM can perform measurements under ambient air, controlled atmosphere and ultra-high vacuum. Figure 4.5 shows Kelvin Probe Force microscopy setups under ambient air/controlled atmosphere that we used at LPICM and a KPFM setup under ultra-high vacuum.

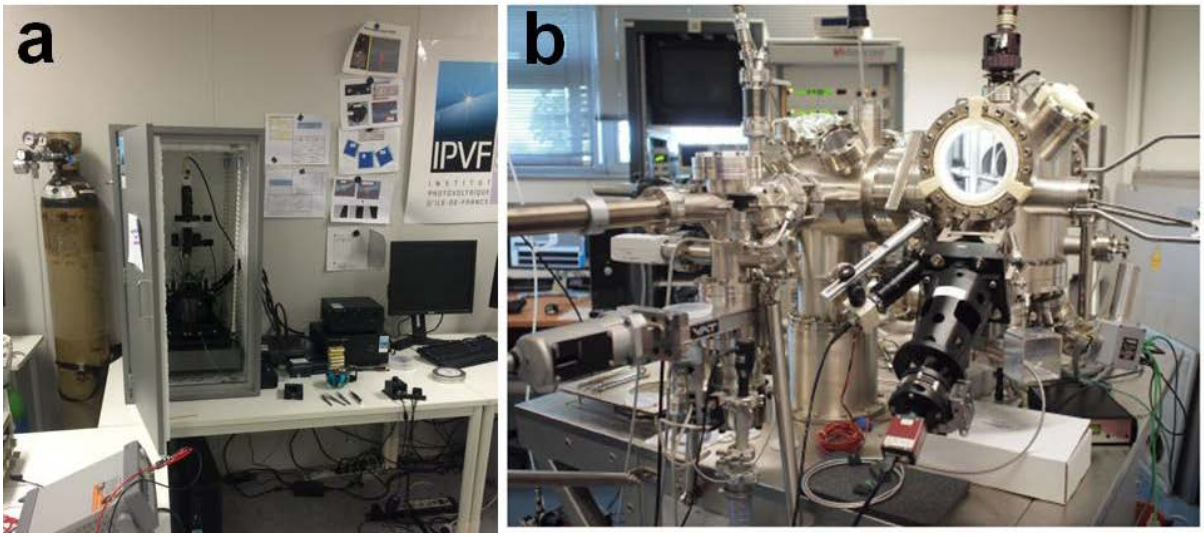

Fig. 4.5 –a) KPFM setup at ambient air or controlled nitrogen atmosphere *(LPICM, Palaiseau, France)* b) KPFM setup under ultra-high vacuum *(IEMN, Villeneuve d'Ascq, France)*

We have shown in Chapter 3 that many artifacts can be mitigated or suppressed under ultra-high vacuum. However, measurements under ambient air and under controlled atmosphere offer the advantage of performing fast acquisitions and allowing a high throughput. To give an order of magnitude, measurements in ambient air can take less than one hour whereas a single measurement under ultra-high vacuum is challenging to perform in less than one day. Therefore, combining work under ambient environment and ultrahigh vacuum can be very valuable. Measurements under ambient environment can help build proof of concept measurements and design experiments quite quickly. It is very easy to bring external excitation sources (e.g. illumination, electrical bias) in SPM setups under ambient environment. Once the measurement is well understood, measurements can be conveyed

under ultra-high vacuum to achieve quantitative high resolution measurements which are more time consuming.

Since scanning probe microscopy techniques use versatile and compact equipments, they can easily be integrated into other characterization setups. In particular, they have been combined with a large range of optical microscopy techniques [49] such as ellipsometry [50] or Raman spectroscopy [51]. Scanning probe microscopy techniques have also shown a good capability to integrate in electron microscopy setups [52] and to combine with time-of-flight mass spectrometer [53] and X-Ray spectroscopy [54]. These combinations are very powerful because they enable to detect artifacts of both techniques, and to perform different kinds of measurements on the exact same areas. Besides, the combination of scanning probe microscopies offers an even wider range of possibilities. For instance, during our CP-AFM and KPFM measurements, mechanical information (e.g. friction, phase, deflection) were recorded along with topographical and electrical images. These complementary signals can help find correlations and strengthen interpretations.

Scanning probe microscopy can also be used in-situ to monitor fabrication steps. This is especially the case for KPFM which is a very low intrusiveness technique. For instance, nano-structuring of organic solar cells has been investigated in-situ with KPFM by Watanabe *et al.* [55]. The very low intrusiveness of KPFM also enables the in-situ investigation of degradation phenomena, such as light-induced and potential-induced degradations. We will propose these kinds of studies as perspective studies on solar cells.

Besides SPM techniques are often referred to as material agnostic techniques. A broad range of materials can be investigated using these techniques. Soft and fragile materials, such as organics, can be investigated because SPM can be low intrusive. Interfaces with different materials as in the case of heterojunctions and multi-junction solar cells can be finely studied because the electrical signals measured have low dependence on materials. This is not the case of electron microscopy techniques where the signal is highly related to materials properties such as diffusion length. Besides, some samples cannot be investigated under ultra-high vacuum (UHV) such as hydrated samples, requiring complicated and expensive sample preparation. But, since scanning probe microscopy can work under ambient air, it can investigate these kinds of samples.

Finally, compared to electron microscopy, CP-AFM and KPFM are relatively low acquisition and maintenance cost. For instance, maintenance contract for standard SEM are around 10,000 euros a year, whereas no maintenance contract is required for SPM and the cost of tips rarely exceeded 3,000 euros in our case.

Scanning probe microscopies versatility could be further improved by enhancing standardization in the scanning probe community [46]. Examples of standardization improvements include better data management (e.g. unique data file for all instruments) and more versatile data processing softwares with exhaustive and precise tutorials. Another example of standardization is the definition of calibration samples for all the different techniques. For KPFM, for instance, it is not clear which calibration to use when one starts with the technique, even though some calibration samples can be proposed [56], [57]. Some effort could be put on defining precise guidelines for operational procedures that would go beyond every equipment provider. In particular, more transparence on the measurement parameters could be provided by manufacturers. Today, it is still difficult to switch from one brand of KPFM to another and to perform precise measurements straightaway. Finally, improvement in versatility of KPFM measurements under UHV could make this technique more accessible and less time consuming, and would enable to perform accurate surface potential measurements within a few hours.

4.6 Acquisition time and dynamic measurements

One strength of scanning probe microscopy that is rarely mentioned is that it has a high temporal resolution (<1 ms), enabling to monitor the evolution of the electrical signal in time. To our knowledge, a small number of articles have been reported on time resolved CP-AFM [58]. However, a lot of work has been carried out to investigate temporal properties with electrostatic AFM extensions and in particular KPFM. For KPFM, a temporal resolution of about 20 µs has been reported [59]. On our setup, measurements with time steps of 240 µs could be performed. In section 5.2, we will show that measurements on passivated wafers with lifetime over 1 ms are possible, which is of high interest for high efficiency solar cells. Figure 4.6.a shows a KPFM image of the surface of a passivated p-type crystalline silicon wafer with a lifetime of 2.2 ms. On this image, we chose to monitor decay times on 3 positions, as shown in Figure 4.6.b. Decay times can be produced by illumination (light on / light off) [60] or electrical bias, either +/- V_b [61] or bias on / bias off [62]. We chose the two first in our measurements. This technique enables us to investigate low lifetime regions at nano-scale. It will be further described in Chapter 6.

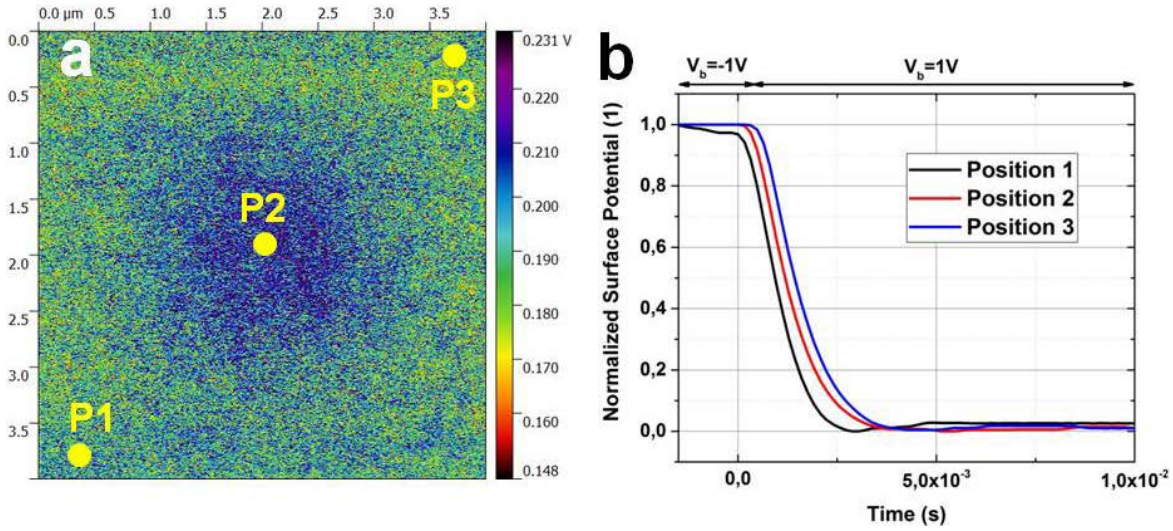

Fig. 4.6 – a) KPFM image of the surface of a passivated crystalline silicon wafer. b) KPFM spectroscopy decay times observed on the 3 points indicated on the KPFM image.

However, it is frequent for solar cells to have lifetimes below the millisecond. In that case, traditional KPFM is limited in temporal resolution and two possibilities can be considered.

The first possibility is the use of new electrostatic techniques, such as time-resolved electrostatic force microscopy (tr-EFM), which can access to rise and decay times down to 10 ns [63], [64]. This has been enabled by removing feedback signals from KPFM and the use of signal averaging and cantilever motion analysis. tr-EFM has been extensively used so far to investigate lifetime of organic solar cells [64]–[66]. New KPFM setups with ultrahigh frequency photodetectors (10 MHz) are promising to achieve high temporal resolution [67]. Other new KPFM setups without feedback loop have been proposed. They achieve accurate surface potential measurements and offer the perspective of performing time resolved KPFM (tr-KPFM) measurements [60]. The temporal resolution of tr-KPFM is expected to improve with the arrival of new modes, such as the recently-introduced G-mode KPFM [67]. This mode simplifies signal detection, solves frequency-shift artifacts and captures the whole cantilever dynamics in the frequency domain. It will probably enable temporal resolution studies below the microsecond.

The second possibility is to use the time-averaging ability of KPFM. When a sample is sensitive to an excitation source (e.g. illumination or electrical bias), the surface potential changes

with the intensity of the excitation. When this excitation is modulated at high frequency, the KPFM will time-average the signal. Therefore, by varying the frequency of the excitation, information on lifetime in the nano and microsecond range can be achieved. For instance, KPFM measurements under modulated frequency illumination have proven to be a powerful tool to investigate low lifetime solar cells at nano-scale [20], [25], [26]. We found that KPFM measurements under modulated frequency electrical bias could also be used to investigate the carrier lifetime at the nano-scale [68]. More details on these measurements will be given in Chapter 6.

For all these nano-scale measurements, the monitoring strategy is to compare lifetime measurements at nano-scale using KPFM with lifetime measurements at macro-scale with other techniques such as time resolved microwave conductivity (TRMC) [68], time resolved photoluminescence (tr-PL), transient photovoltage (TPV) [26] or other surface potential techniques like x-ray photoelectron spectroscopy (XPS) [25]. These comparisons are useful to assess the reliability of KPFM measurements.

In electron microscopy, fast acquisition setups have also been proposed to capture ultrafast dynamics of charge carriers on material surfaces [69] but to our knowledge, no work has been done on solar cells so far using this technique. We have shown previously in Section 4.2 that SEM signal can hardly be sensitive to illumination because of the high number of injected electrons. Therefore, photo-signal decays cannot be investigated with SEM and other electron microscopy techniques. In our work, we have performed SEM measurements under modulated frequency electrical bias. The idea was to compare with the results we obtained with KPFM under modulated frequency voltage bias [68]. However, when switching the electrical bias applied on the PIN junction of the solar cell, the SEM image is shifting in vertical direction, as Figure 4.7 shows. The reason for this phenomenon is that the surface potential deviates incident and emitted electrons from the surface. Therefore, when the electrical bias is modulated at high frequencies (Fig.4.7.c), the SEM image is blurry and it is very challenging to interpret the data. That is why scanning probe microscopy in general and KPFM in particular, is a powerful tool to investigate carrier lifetimes of materials and devices at the nano-scale.

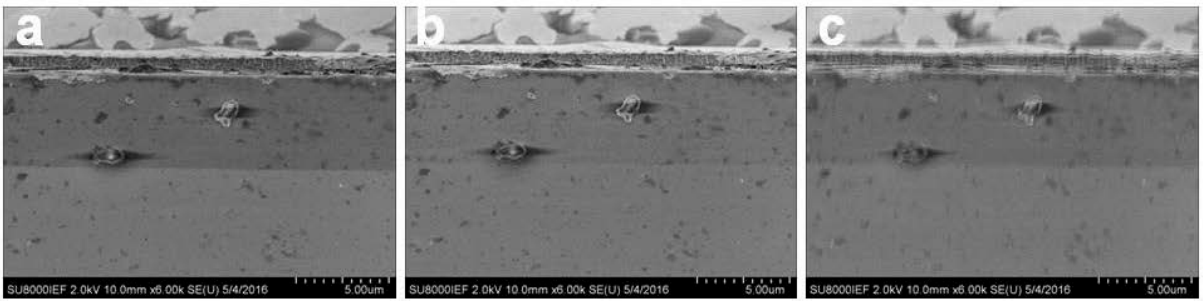

Fig. 4.7 – SEM image of a PIN Junction under three voltage bias conditions : a) V_b =0.5V, b) V_b =-0.5V, c) Modulated frequency voltage bias between -0.5V and 0.5V with a frequency of 500kHz. A spatial shift in the vertical can be observed between V_b =0.5V and V_b =-0.5V. This shift is reversible. It traduces in a blurry image when the voltage is frequency modulated.

4.7 Conclusion

In this Chapter we have detailed the strengths of KPFM and CP-AFM with respect to electron microscopy techniques. A summary of the strengths is presented in the table 4.1. For each strength, we have presented:

- **Features:** This part explains the characteristic of the strength for CP-AFM, KPFM or both.
- **Possibilities:** This part explains the measurements that the strength enables
- **Monitoring strategy:** This part explains how to monitor the effect of the strength.
- **Improvement Path:** This part explains how to improve the strength even further.
- **Comparison to EM:** This part analyses the features of electron microscopy (EM) on this particular topic.

Table 4.1 – Summary table of strengths of KPFM and CP-AFM techniques.

Strength	Features	Possibilities	Monitoring strategy	Improvement Paths	Compared to EM
Spatial Resolution	* CP-AFM <1nm-10nm + KPFM (air) ~10nm * KPFM (UHV) < 1nm *(atomic resolution)* * 2D capabilities for the three techniques	* Cross-section measurements * Identification of nano-defects	* Use of calibration with given size of nano-objects	* Bulk Probes with lower radius * Work under UHV * Post-processing *(e.g. de-convolution of tip shape, stray capacitance)* * Use of "bevel technique" to improve resolution of cross-section measurements	* Resolution in EM is dependent on materials * SEM : 0.5nm – 20nm * EBIC : 1nm - 10µm *(depending on the diffusion length of the material)* * TEM < 1nm *(atomic resolution)*
Sensitivity to Light	* No injection of carriers in CP-AFM and KPFM * AFM laser is the only stray illumination source (<1sun)	* Photovoltage, Photocurent at nano-scale * Monitor the effect of different parameters of light: intensity, wavelength, frequency of pulse, beam position.	* Comparison between nano-scale photovoltage *(KPFM)* and macro-scale V_{oc} *(voltmeter)* when the cell is inside the AFM setup.	* Work under totally dark environment * Reduce or suppress the parasitic effect of AFM laser (cf. section 3.1)	* Electron injection of electrons is much higher than one sun. So, the effect of one sun illumination hard to be seen.
Small charging effects	* Tip-induced charging in KPFM *(punctual, rare, recoverable)*	* Measurements can be performed on the same area for a long time without charging	* Sudden change of electrical image at a certain point of the image. * Zoom out after performing a succession of measurements on an area	* Use low voltages for measurements on high diffusion length materials.	* Electron microscopy: recurrent charging, on the whole image, quick process. * Recoverable if only charging, but not recoverable if carbon contamination is induced.
Direct Electrical Measure-ments	* Direct measurement of quantities of interest (current, voltage/potential) at nano-scale.	* Localization of series resistance *(KPFM)* * Give additional inputs to simulation of solar cells (resistance, diodes, …)	* Direct comparison with macro-scale information (V_{oc}, J_{sc}, external bias)	* Reduce the influence of artifacts between the quantity of interest and the quantity measured *(e.g band bending, topographical artifacts)*	* SEM and EBIC do not have direct measurements of electrical quantities of interest. They only have a correlation. * These techniques can detect electric fields of diodes but not series resistances.

Strength	Features	Possibilities	Monitoring strategy	Improvement Paths	Compared to EM
Versatility	*Work under ambient environment, controlled atmosphere and UHV. * Work under liquid environment *(KPFM)* * Easy to couple with optical andelectron microscopy techniques * Low acquisition/operating costs	* Comparison with other microscopy techniques * Possibility to use in-situ for some processes * Combined work: .quick design of measurements under ambient air .precise measurements under UHV	* Easy to design experiments with external excitations (light through optical fibers, electrical bias through wirings, …)	* Standardization of data management and treatment, dimensional calibration, reference materials and guidelines for operational procedures * Proper use in ambient air and under UHV should be standardized * Data Processing & Management	* Relatively high acquisition/operating costs * Mainly limited to work under UHV * Coupling with other techniques is possible but more complicated
Acquisiton Time and Dynamic Measure-ments	* KPFM Temporal Resolution : 100µs – 1ms * Time Averaging Capability of KPFM with periods down to 10^{-8} s * Few articles on time resolved CP-AFM measurements to our knowledge.	* Straight measurement of decay times at nano-scale (>1ms) * Measurement of lifetimes through modulated frequency illumination or electrical bias (10ns<t <0.1ms)	* Observe minimum measurable decay time by performing measurements on low lifetimes. * Compare with other characterization techniques (e.g. TRMC, tr-PL, µ-PCD)	* Toward nano-second resolution using time resolved electrostatic force microscopy (tr-EFM)	* High temporal resolution can be reached with time resolved SEM but no work has been done on solar cells using this technique. * No sensitivity to illumination = no possibility to investigate photo-signal decays. * No time averaging possibility. Blurry SEM images when modulated frequency electrical bias is applied.

REFERENCES

[1] W. Melitz, J. Shen, A. C. Kummel, and S. Lee, "Kelvin probe force microscopy and its application," *Surf. Sci. Rep.*, vol. 66, no. 1, pp. 1–27, Jan. 2011.

[2] D. Álvarez, J. Hartwich, M. Fouchier, P. Eyben, and W. Vandervorst, "Sub-5-nm-spatial resolution in scanning spreading resistance microscopy using full-diamond tips," *Appl. Phys. Lett.*, vol. 82, no. 11, pp. 1724–1726, Mar. 2003.

[3] F. Krok, K. Sajewicz, J. Konior, M. Goryl, P. Piatkowski, and M. Szymonski, "Lateral resolution and potential sensitivity in Kelvin probe force microscopy: Towards understanding of the sub-nanometer resolution," *Phys. Rev. B*, vol. 77, no. 23, p. 235427, Jun. 2008.

[4] K. Okamoto, K. Yoshimoto, Y. Sugawara, and S. Morita, "KPFM imaging of Si(1 1 1)53×53-Sb surface for atom distinction using NC-AFM," *Appl. Surf. Sci.*, vol. 210, no. 1–2, pp. 128–133, Mar. 2003.

[5] F. Bocquet, L. Nony, C. Loppacher, and T. Glatzel, "Analytical approach to the local contact potential difference on (001) ionic surfaces: Implications for Kelvin probe force microscopy," *Phys. Rev. B*, vol. 78, no. 3, p. 35410, Jul. 2008.

[6] L. Kronik and Y. Shapira, "Surface photovoltage phenomena: theory, experiment, and applications," *Surf. Sci. Rep.*, vol. 37, no. 1–5, pp. 1–206, Dec. 1999.

[7] T. Hantschel, P. Niedermann, T. Trenkler, and W. Vandervorst, "Highly conductive diamond probes for scanning spreading resistance microscopy," *Appl. Phys. Lett.*, vol. 76, no. 12, pp. 1603–1605, Mar. 2000.

[8] P. De Wolf, R. Stephenson, T. Trenkler, T. Clarysse, T. Hantschel, and W. Vandervorst, "Status and review of two-dimensional carrier and dopant profiling using scanning probe microscopy," *J. Vac. Sci. Technol. B*, vol. 18, no. 1, pp. 361–368, Jan. 2000.

[9] T. S. Druzhinina, S. Hoeppener, and U. S. Schubert, "Microwave-Assisted Fabrication of Carbon Nanotube AFM Tips," *Nano Lett.*, vol. 10, no. 10, pp. 4009–4012, Oct. 2010.

[10] Z. Zhang, M. Hetterich, U. Lemmer, M. Powalla, and H. Hölscher, "Cross sections of operating Cu(In,Ga)Se2 thin-film solar cells under defined white light illumination analyzed by Kelvin probe force microscopy," *Appl. Phys. Lett.*, vol. 102, no. 2, p. 23903, Jan. 2013.

[11] T. Glatzel, M. Rusu, S. Sadewasser, and M. C. Lux-Steiner, "Surface photovoltage analysis of thin CdS layers on polycrystalline chalcopyrite absorber layers by Kelvin probe force microscopy," *Nanotechnology*, vol. 19, no. 14, p. 145705, 2008.

[12] S. Sadewasser, T. Glatzel, M. Rusu, A. Jäger-Waldau, and M. C. Lux-Steiner, "High-resolution work function imaging of single grains of semiconductor surfaces," *Appl. Phys. Lett.*, vol. 80, no. 16, pp. 2979–2981, Apr. 2002.

[13] J.-P. Kleider, J. Alvarez, A. V. Ankudinov, A. S. Gudovskikh, E. V. Gushchina, M. Labrune, O. A. Maslova, W. Favre, M.-E. Gueunier-Farret, P. R. i Cabarrocas, and E. I. Terukov, "Characterization of silicon heterojunctions for solar cells," *Nanoscale Res. Lett.*, vol. 6, no. 1, p. 152, Feb. 2011.

[14] A. Breymesser, V. Schlosser, D. Peiró, C. Voz, J. Bertomeu, J. Andreu, and J. Summhammer, "Kelvin probe measurements of microcrystalline silicon on a nanometer scale using SFM," *Sol. Energy Mater. Sol. Cells*, vol. 66, no. 1–4, pp. 171–177, Feb. 2001.

[15] P. Narchi, J. Alvarez, P. Chrétien, G. Picardi, R. Cariou, M. Foldyna, P. Prod'homme, J.-P. Kleider, and P. R. i Cabarrocas, "Cross-Sectional Investigations on Epitaxial Silicon Solar Cells by Kelvin and Conducting Probe Atomic Force Microscopy: Effect of Illumination," *Nanoscale Res. Lett.*, vol. 11, no. 1, Dec. 2016.

[16] C. S. Jiang, H. R. Moutinho, R. Reedy, M. M. Al-Jassim, and A. Blosse, "Two-dimensional junction identification in multicrystalline silicon solar cells by scanning Kelvin probe force microscopy," *J. Appl. Phys.*, vol. 104, no. 10, p. 104501, 2008.

[17] P. Lavenus, A. Messanvi, L. Rigutti, A. D. L. Bugallo, H. Zhang, F. Bayle, F. H. Julien, J. Eymery, C. Durand, and M Tchernycheva, "Experimental and theoretical analysis of transport properties of core–shell wire light emitting diodes probed by electron beam induced current microscopy," *Nanotechnology*, vol. 25, no. 25, p. 255201, 2014.

[18] D. K. Schroder, *Semiconductor Material and Device Characterization*. John Wiley & Sons, 2006.

[19] C. Loppacher, U. Zerweck, S. Teich, E. Beyreuther, T. Otto, Stefan Grafström, and L. M. Eng, "FM demodulated Kelvin probe force microscopy for surface photovoltage tracking," *Nanotechnology*, vol. 16, no. 3, p. S1, 2005.
[20] M. Takihara, T. Takahashi, and T. Ujihara, "Minority carrier lifetime in polycrystalline silicon solar cells studied by photoassisted Kelvin probe force microscopy," *Appl. Phys. Lett.*, vol. 93, no. 2, p. 21902, Jul. 2008.
[21] M. Moczała, N. Sosa, A. Topol, and T. Gotszalk, "Investigation of multi-junction solar cells using electrostatic force microscopy methods," *Ultramicroscopy*, vol. 141, pp. 1–8, Jun. 2014.
[22] S. Saraf, R. Shikler, J. Yang, and Y. Rosenwaks, "Microscopic surface photovoltage spectroscopy," *Appl. Phys. Lett.*, vol. 80, no. 14, pp. 2586–2588, Apr. 2002.
[23] P. Narchi, G. Picardi, R. Cariou, M. Foldyna, P. Prod'homme, and P. Roca i Cabarrocas, "Kelvin Probe Force Microscopy Study of Electric Field Homogeneity in Epitaxial Silicon Solar Cells Cross-Section," *31st EU PVSEC Proceedings*, no. 3BO.6.1, pp. 1026–1029, 2015
[24] A. Ankudinov, "Solar cell diagnostics using Kelvin force microscopy and local photoexcitation," *Microsc. Anal*, 2012.
[25] Ł. Borowik, H. Lepage, N. Chevalier, D. Mariolle, and O. Renault, "Measuring the lifetime of silicon nanocrystal solar cell photo-carriers by using Kelvin probe force microscopy and x-ray photoelectron spectroscopy," *Nanotechnology*, vol. 25, no. 26, p. 265703, 2014.
[26] G. Shao, M. S. Glaz, F. Ma, H. Ju, and D. S. Ginger, "Intensity-Modulated Scanning Kelvin Probe Microscopy for Probing Recombination in Organic Photovoltaics," *ACS Nano*, vol. 8, no. 10, pp. 10799–10807, Oct. 2014.
[27] T. Meoded, R. Shikler, N. Fried, and Y. Rosenwaks, "Direct measurement of minority carriers diffusion length using Kelvin probe force microscopy," *Appl. Phys. Lett.*, vol. 75, no. 16, pp. 2435–2437, Oct. 1999.
[28] T. Kato, T. Matsukawa, H. Koyama, K. Fujikawa, and R. Shimizu, "Scanning electron microscopy of charging effect on silicon," *J. Appl. Phys.*, vol. 46, no. 5, pp. 2288–2292, May 1975.
[29] M. P. Davidson and N. T. Sullivan, "Investigation of the effects of charging in SEM-based CD metrology," 1997, vol. 3050, pp. 226–242.
[30] D. Tsurumi, K. Hamada, and Y. Kawasaki, "Energy-Filtered Secondary-Electron Imaging for Nanoscale Dopant Mapping by Applying a Reverse Bias Voltage," *Jpn. J. Appl. Phys.*, vol. 51, p. 106503, Oct. 2012.
[31] J. T. Heath, C.-S. Jiang, and M. M. Al-Jassim, "Measurement of semiconductor surface potential using the scanning electron microscope," *J. Appl. Phys.*, vol. 111, no. 4, p. 46103, Feb. 2012.
[32] J. T. Heath, C. S. Jiang, and M. M. Al-Jassim, "Diffused junctions in multicrystalline silicon solar cells studied by complementary scanning probe microscopy and scanning electron microscopy techniques," *35th IEEE Photovoltaic Specialists Conference (PVSC)*, pp. 000227–000232, 2010.
[33] P. Narchi, V. Neplokh, V. Piazza, T. Bearda, F. Bayle, M. Foldyna, C. Toccafondi, P. Prod'homme, M. Tchernycheva, and P. Roca i Cabarrocas, "Surface potential investigation on interdigitated back contact solar cells by scanning electron microscopy and Kelvin probe force microscopy: effect of electrical bias," Submitted to *Sol. Energy Mater. Sol. Cells*
[34] D. Cavalcoli, M. Rossi, A. Tomasi, and A. Cavallini, "Degeneracy and instability of nanocontacts between conductive tips and hydrogenated nanocrystalline Si surfaces in conductive atomic force microscopy," *Nanotechnology*, vol. 20, no. 4, p. 45702, 2009.
[35] S. V. Kalinin and D. A. Bonnell, "Surface potential at surface-interface junctions in SrTiO3 bicrystals," *Phys. Rev. B*, vol. 62, no. 15, pp. 10419–10430, Oct. 2000.
[36] D. C. Coffey, O. G. Reid, D. B. Rodovsky, G. P. Bartholomew, and D. S. Ginger, "Mapping Local Photocurrents in Polymer/Fullerene Solar Cells with Photoconductive Atomic Force Microscopy," *Nano Lett.*, vol. 7, no. 3, pp. 738–744, Mar. 2007.
[37] Y. Kutes, B. A. Aguirre, J. L. Bosse, J. L. Cruz-Campa, D. Zubia, and B. D. Huey, "Mapping photovoltaic performance with nanoscale resolution," *Prog. Photovolt. Res. Appl.*, vol. 24, no. 3, pp. 315–325, Mar. 2016.
[38] D. Lausch, M. Werner, V. Naumann, J. Schneider, and C. Hagendorf, "Investigation of modified p-n junctions in crystalline silicon on glass solar cells," *J. Appl. Phys.*, vol. 109, no. 8, p. 84513, Apr. 2011.

[39] J.-M. Bonard and J.-D. Ganière, "Quantitative analysis of electron-beam-induced current profiles across p–n junctions in GaAs/Al0.4Ga0.6As heterostructures," *J. Appl. Phys.*, vol. 79, no. 9, pp. 6987–6994, May 1996.

[40] I. Volotsenko, M. Molotskii, Z. Barkay, J. Marczewski, P. Grabiec, B. Jaroszewicz, G. Meshulam, E. Grunbaum, and Y. Rosenwaks, "Secondary electron doping contrast: Theory based on scanning electron microscope and Kelvin probe force microscopy measurements," *J. Appl. Phys.*, vol. 107, no. 1, p. 14510, Jan. 2010.

[41] T. H. P. Chang and W. C. Nixon, "Electron beam induced potential contrast on unbiased planar transistors," *Solid-State Electron.*, vol. 10, no. 7, pp. 701–704, Jul. 1967.

[42] A. K. W. Chee, R. F. Broom, C. J. Humphreys, and E. G. T. Bosch, "A quantitative model for doping contrast in the scanning electron microscope using calculated potential distributions and Monte Carlo simulations," *J. Appl. Phys.*, vol. 109, no. 1, p. 13109, Jan. 2011.

[43] D. D. Perovic, M. R. Castell, A. Howie, C. Lavoie, T. Tiedje, and J. S. W. Cole, "Field-emission SEM imaging of compositional and doping layer semiconductor superlattices," *Ultramicroscopy*, vol. 58, no. 1, pp. 104–113, Apr. 1995.

[44] N. Duhayon, P. Eyben, M. Fouchier, T. Clarysse, W. Vandervorst, D. Álvarez, S. Schoemann, M. Ciappa, M. Stangoni, W. Fichtner, P. Formanek, M. Kittler, V. Raineri, F. Giannazzo, D. Goghero, Y. Rosenwaks, R. Shikler, S. Saraf, S. Sadewasser, N. Barreau, T. Glatzel, M. Verheijen, S. a. M. Mentink, M. von Sprekelsen, T. Maltezopoulos, R. Wiesendanger, and L. Hellemans, "Assessing the performance of two-dimensional dopant profiling techniques," *J. Vac. Sci. Technol. B*, vol. 22, no. 1, pp. 385–393, Jan. 2004.

[45] P. Narchi, T. Bearda, M. Foldyna, G. Picardi, P. Prod'homme, and P. Roca i Cabarrocas, "Interdigitated back contact silicon solar cells: diode and resistance investigation at nanoscale using Kelvin Probe Force Microscopy," *43rd IEEE Photovoltaic Specialists Conference (PVSC)*, pp. 3082–3085, 2016

[46] D. Fujita, K. Onishi, and M. Xu, "Standardization of nanomaterials characterization by scanning probe microscopy for societal acceptance," *J. Phys. Conf. Ser.*, vol. 159, no. 1, p. 12002, 2009.

[47] V. Palermo, M. Palma, and P. Samorì, "Electronic Characterization of Organic Thin Films by Kelvin Probe Force Microscopy," *Adv. Mater.*, vol. 18, no. 2, pp. 145–164, Jan. 2006.

[48] L. Collins, S. Jesse, J. I. Kilpatrick, A. Tselev, M. B. Okatan, S. V. Kalinin, and B. J. Rodriguez, "Kelvin probe force microscopy in liquid using electrochemical force microscopy," *Beilstein J. Nanotechnol.*, vol. 6, pp. 201–214, Jan. 2015.

[49] S. Moreno Flores and J. L. Toca-Herrera, "The new future of scanning probe microscopy: Combining atomic force microscopy with other surface-sensitive techniques, optical microscopy and fluorescence techniques," *Nanoscale*, vol. 1, no. 1, p. 40, 2009.

[50] P. Karageorgiev, H. Orendi, B. Stiller, and L. Brehmer, "Scanning near-field ellipsometric microscope-imaging ellipsometry with a lateral resolution in nanometer range," *Appl. Phys. Lett.*, vol. 79, no. 11, pp. 1730–1732, Sep. 2001.

[51] R. M. Stöckle, Y. D. Suh, V. Deckert, and R. Zenobi, "Nanoscale chemical analysis by tip-enhanced Raman spectroscopy," *Chem. Phys. Lett.*, vol. 318, no. 1–3, pp. 131–136, Feb. 2000.

[52] N. Anspach, F. Hitzel, F. Zhou, and S. Eyhusen, "Hybrid SEM/AFM System from Carl Zeiss Revolutionizes Analysis of Functional Micro- and Nanostructured Specimen," *Microsc. Microanal.*, vol. 20, no. S3, pp. 992–993, Aug. 2014.

[53] A. Wetzel, A. Socoliuc, E. Meyer, R. Bennewitz, E. Gnecco, and C. Gerber, "A versatile instrument for insitu combination of scanning probe microscopy and time-of-flight mass spectrometry," *Rev. Sci. Instrum.*, vol. 76, no. 10, p. 103701, Oct. 2005.

[54] C. Fauquet, M. Dehlinger, F. Jandard, S. Ferrero, D. Pailharey, S. Larcheri, R. Graziola, J. Purans, A. Bjeoumikhov, A. Erko, I. Zizak, B. Dahmani, and D. Tonneau, "Combining scanning probe microscopy and x-ray spectroscopy," *Nanoscale Res. Lett.*, vol. 6, no. 1, p. 308, 2011.

[55] S. Watanabe, Y. Fukuchi, M. Fukasawa, T. Sassa, A. Kimoto, Y. Tajima, M. Uchiyama, T. Yamashita, M. Matsumoto, and T. Aoyama, "In Situ KPFM Imaging of Local Photovoltaic Characteristics of Structured Organic Photovoltaic Devices," *ACS Appl. Mater. Interfaces*, vol. 6, no. 3, pp. 1481–1487, Feb. 2014.

[56] T. Machleidt, E. Sparrer, D. Kapusi, and K.-H. Franke, "Deconvolution of Kelvin probe force microscopy measurements—methodology and application," *Meas. Sci. Technol.*, vol. 20, no. 8, p. 84017, 2009.

[57] G. Cohen, E. Halpern, S. U. Nanayakkara, J. M. Luther, C. Held, R. Bennewitz, A. Boag, and Y. Rosenwaks, "Reconstruction of surface potential from Kelvin probe force microscopy images," *Nanotechnology*, vol. 24, no. 29, p. 295702, 2013.

[58] D. Axford, J. J. Davis, N. Wang, D. Wang, T. Zhang, J. Zhao, and B. Peters, "Molecularly Resolved Protein Electromechanical Properties," *J. Phys. Chem. B*, vol. 111, no. 30, pp. 9062–9068, Aug. 2007.

[59] E. Strelcov, S. M. Yang, S. Jesse, N. Balke, R. K. Vasudevan, and S. V. Kalinin, "Solid-state electrochemistry on the nanometer and atomic scales: the scanning probe microscopy approach," *Nanoscale*, vol. 8, no. 29, pp. 13838–13858, Jul. 2016.

[60] M. Beu, K. Klinkmüller, and D. Schlettwein, "Use of Kelvin probe force microscopy to achieve a locally and time-resolved analysis of the photovoltage generated in dye-sensitized ZnO electrodes," *Phys. Status Solidi A*, vol. 211, no. 9, pp. 1960–1965, Sep. 2014.

[61] D. W. Cardwell, A. R. Arehart, C. Poblenz, Y. Pei, J. S. Speck, U. K. Mishra, S. A. Ringel, and J. P. Pelz, "Nm-scale measurements of fast surface potential transients in an AlGaN/GaN high electron mobility transistor," *Appl. Phys. Lett.*, vol. 100, no. 19, p. 193507, May 2012.

[62] E. Strelcov, S. Jesse, Y.-L. Huang, Y.-C. Teng, I. I. Kravchenko, Y.-H. Chu, and S. V. Kalinin, "Space- and Time-Resolved Mapping of Ionic Dynamic and Electroresistive Phenomena in Lateral Devices," *ACS Nano*, vol. 7, no. 8, pp. 6806–6815, Aug. 2013.

[63] R. Giridharagopal, G. E. Rayermann, G. Shao, D. T. Moore, O. G. Reid, A. F. Tillack, D. J. Masiello, and D. S. Ginger, "Submicrosecond Time Resolution Atomic Force Microscopy for Probing Nanoscale Dynamics," *Nano Lett.*, vol. 12, no. 2, pp. 893–898, Feb. 2012.

[64] D. U. Karatay, J. S. Harrison, M. S. Glaz, R. Giridharagopal, and D. S. Ginger, "Fast time-resolved electrostatic force microscopy: Achieving sub-cycle time resolution," *Rev. Sci. Instrum.*, vol. 87, no. 5, p. 53702, May 2016.

[65] J. R. O'Dea, L. M. Brown, N. Hoepker, J. A. Marohn, and S. Sadewasser, "Scanning probe microscopy of solar cells: From inorganic thin films to organic photovoltaics," *MRS Bull.*, vol. 37, no. 7, pp. 642–650, Jul. 2012.

[66] D. C. Coffey and D. S. Ginger, "Time-resolved electrostatic force microscopy of polymer solar cells," *Nat. Mater.*, vol. 5, no. 9, pp. 735–740, Sep. 2006.

[67] L. Collins, A. Belianinov, S. Somnath, B. J. Rodriguez, N. Balke, S. V. Kalinin, and Stephen Jesse, "Multifrequency spectrum analysis using fully digital G Mode-Kelvin probe force microscopy," *Nanotechnology*, vol. 27, no. 10, p. 105706, 2016.

[68] P. Narchi, R. Cariou, M. Foldyna, P. Prod'homme, and P. R. i Cabarrocas, "Nanoscale Investigation of Carrier Lifetime on the Cross Section of Epitaxial Silicon Solar Cells Using Kelvin Probe Force Microscopy.", accepted by IEEE Journal of Photovoltaics.

[69] J. Sun, A. Adhikari, B. S. Shaheen, H. Yang, and O. F. Mohammed, "Mapping Carrier Dynamics on Material Surfaces in Space and Time using Scanning Ultrafast Electron Microscopy," *J. Phys. Chem. Lett.*, vol. 7, no. 6, pp. 985–994, Mar. 2016.

Chapter 5 – Material Investigations

Contents

5.0 Introduction

Considering the strengths/weaknesses analysis presented in Chapters 3 and 4, we highlight measurements where CP-AFM and KPFM bring additional value to the investigation of crystalline silicon solar cells (with respect to electron microscopy techniques). Chapter 5 and 6 present the results we obtained on measurements we deemed of interest.

Chapter 5 addresses material investigations with KPFM and CP-AFM techniques. We have focused our investigations on two topics related to crystalline silicon wafers: doping at nano-scale using CP-AFM and lifetime at nano-scale using KPFM. We have seen that both techniques were affected by strong topographical dependence (Section 3.4). Therefore, we have limited our analysis to ultra-flat surfaces. In the case of doping, we investigated sample cross-sections which were mechanically polished. In the case of lifetime, we have investigated surface polished wafers and micro-cleaved cross-sections of crystalline silicon wafers.

Compared to KPFM, CP-AFM has the advantage of not being limited by thermal noise (section 3.6). Besides, CP-AFM techniques have a high sensitivity to carrier concentration (section 4.4). Therefore, when investigating doping levels at nano-scale, CP-AFM techniques like Resiscope and Scanning Spreading Resistance Microscopy have a high signal-to-noise ratio compared to other scanning probe microscopy techniques [1], [2]. In section 5.1, we will compare KPFM and Resiscope on doped calibration samples and we will confirm that CP-AFM is a very powerful tool to investigate doping levels in crystalline silicon solar cells at the nano-scale.

KPFM has the possibility to record the signal evolution as a function of time with the resolution below the millisecond (Section 4.6) and is much less intrusive and more reproducible than CP-AFM which degrades the sample (Section 3.2) and the tip (section 3.3). Therefore, KPFM is a good tool to investigate signal decays related to the lifetime. Because our setup was limited to lifetime measurements of over 1 millisecond, we chose to investigate passivated crystalline silicon wafers with lifetimes in the milliseconds range. The results are presented in section 5.2. We will show that a good correlation can be observed with microwave photoconductivity decay (μ-PCD) both on the surface and on the cross-section of passivated wafers.

5.1 Doping measurements at the nano-scale

5.1.1 Context

In the semiconductor and photovoltaic industries, the importance of developing nanometer-scale measurements of carrier concentration has been highlighted by different roadmaps [3], [4]. The resolution of the measurements has to catch up with the size of microelectronic and photovoltaic components. For solar cells, these measurements are of prime interest because a fine control of the doping leads to a control of the electric field inside the cells which is at the heart of the photovoltaic process.

De Wolf *et al.* have identified four categories of techniques which can perform 2D mapping of doping with nanometer-resolution: 2D techniques which are based on widely used one dimensional (1D) technique (e.g. 2D SIMS), electron microscopy based techniques (e.g. field effect SEM), inverse modeling techniques and scanning probe microscopy techniques [2].

These techniques are compared according to specific standards that have been defined: accuracy of carrier concentration, spatial resolution, dynamic range, sensitivity, quantification ability and applicability to real devices. Several groups have worked on comparing the techniques according to this merit order [1], [2]. These studies have shown that scanning probe microscopy techniques were very good candidates to achieve doping measurements with nano-scale resolution.

The scanning probe microscopy techniques considered are usually Scanning Spreading Resistance Microscopy (SSRM), Scanning Capacitance Microscopy (SCM), Kelvin Probe Force Microscopy (KPFM), Scanning Tunneling Microscopy (STM) and Scanning Surface Harmonic Microscopy (SSHM). Among them, SSRM and SCM have clearly been identified as the two most valuable techniques to measure doping levels in silicon at the nano-scale [1], [2], [5].

Both SSRM and SCM can measure the carrier concentration with a resolution below 10nm within the dynamic range of interest [10^{15}-10^{20} cm^{-3}]. However, SSRM presents several advantages over SCM [1]. First, the sample preparation step does not require oxidation of the sample. Oxide is actually degrading the SSRM signal, as opposed to SCM signal. Second, the sensitivity of SSRM is linear in all the dynamic range but for SCM it is exponential. Therefore, the sensitivity of SCM is best between 10^{15} and 10^{17} atoms.cm^{-3}, and worst for higher concentrations. Third, SCM signal is very dependent on the choice of tip bias applied, in order to obtain a monotonic behavior. This is why Eyben *et al.* consider that SSRM is "the only method combining high spatial resolution, sensitivity, and the possibility to perform quantification" [6]. SSRM have been used by several groups to investigate implantation mechanisms [6], [7], contacting issues [8], [9] and to assist the development of processes for new solar cell architectures [8], [10].

Compared to SSRM and SCM, KPFM proves to be less suited for quantification of doping at nano-scale. The main limitation of KPFM is its low sensitivity [1], [5]. In ambient air, PN junctions can be easily detected, but for a same type of doping (n-type or p-type), it is very challenging to detect doping contrasts [1]. Therefore, buffer layers have to be used to measure the surface potential difference between two doping levels of the same type [11], [12]. Besides, the spatial resolution is limited to about 10nm in ambient air. Under ultra-high vacuum, more contrast can be observed and better resolutions can be reached [1] but the sensitivity is still lower than SSRM and the preparation process becomes very complex, affecting the practical application of the technique [1].

In this part, we test the capabilities of Resiscope for measurements of doping level at the nano-scale. We have shown previously that SSRM and Resiscope are very similar techniques, i.e. conducting probe AFM techniques with a logarithmic amplifier to investigate a large range of resistance. Extensive works have been published proving that SSRM was a reference tool to investigate doping at the nano-scale [1], [2], [13]. However, no publication yet addressed the possibility of doing the same kind of measurements with Resiscope. Kleider *et al.* have proven that it is possible to investigate electronic properties of solar cells, such as inversion layers, using Resiscope [14] but no quantitative work had been carried out on doping levels previously.

Therefore, we present here proof of concept work on measurement of doping levels on calibration samples using Resiscope. Calibration samples are used to compare the performance of different techniques. They are also used as references to quantify measurements on arbitrary structures, using specific algorithms [15].

5.1.2 Our approach

We investigated the n-type and p-type calibration samples (section 2.6.2) using Resiscope (section 2.3). These samples were investigated on the cross-section. We have shown in Chapter 3 that CP-AFM measurements are strongly correlated with the topography. Therefore, we performed a mechanical polishing step before measurements. For this purpose, we use grinding disks with diamond grains with decreasing sizes. Figure 5.1 shows the roughness obtained after polishing with the six different grain size disks. The 3D topographical images obtained after polishing with three grain size disks (30 µm, 7 µm, 0.5 µm) are also shown. After the last polishing disk, ultra-flat surfaces were achieved (rms<10 nm)

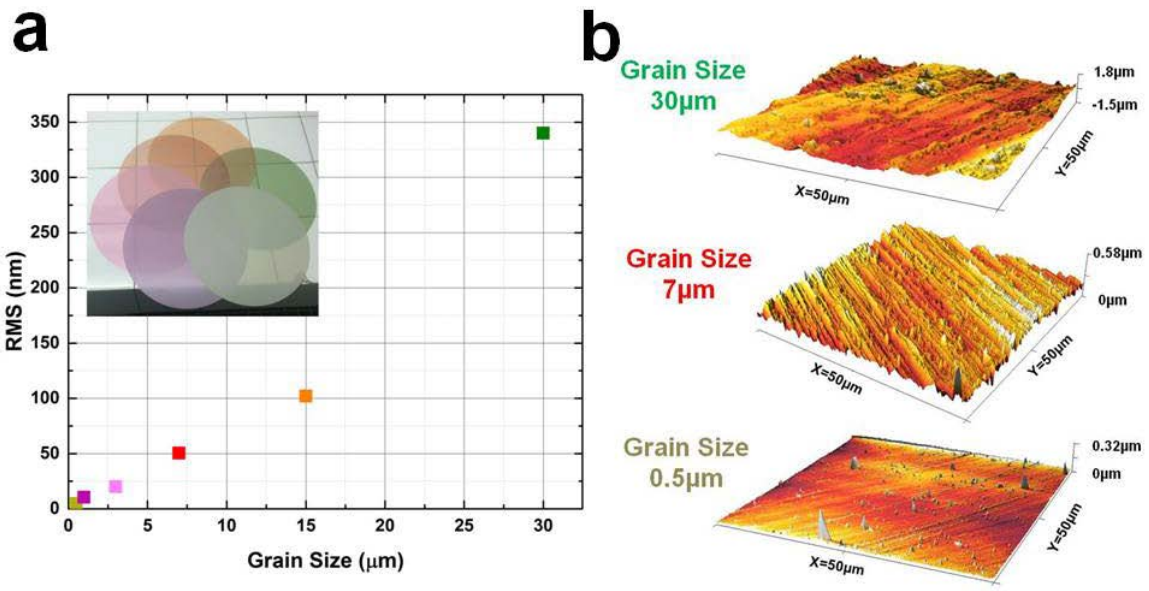

Fig. 5.1 – Mechanical polishing with grain diamond disks. a) RMS roughness rms as a function of the grain size of the disks. b) 3D AFM images of the silicon sample after polishing with three grain sizes disks: 30 µm, 7 µm and 0.5 µm.

After the polishing step, we performed a metallization step. Figure 5.2 shows the three configurations we investigated. On the first configuration (Fig. 5.2.a), the sample was placed on the cross-section holder but not metalized. It was isolated from the back. No contrast could be observed in this configuration. On the second configuration we used metallization with silver paste to decrease the influence associated with the sample resistance, which screens the spreading resistance of interest. In this configuration, the contrast was visible but not clear. On the third configuration, the silver paste was deposited on the cross-section of the sample. This configuration enables to approach as close as required from the silver stripe. Therefore, the sample resistance associated with the electrical path between the tip and the silver paste, is minimized. Using this configuration, we observed the best contrast in our Resiscope measurements.

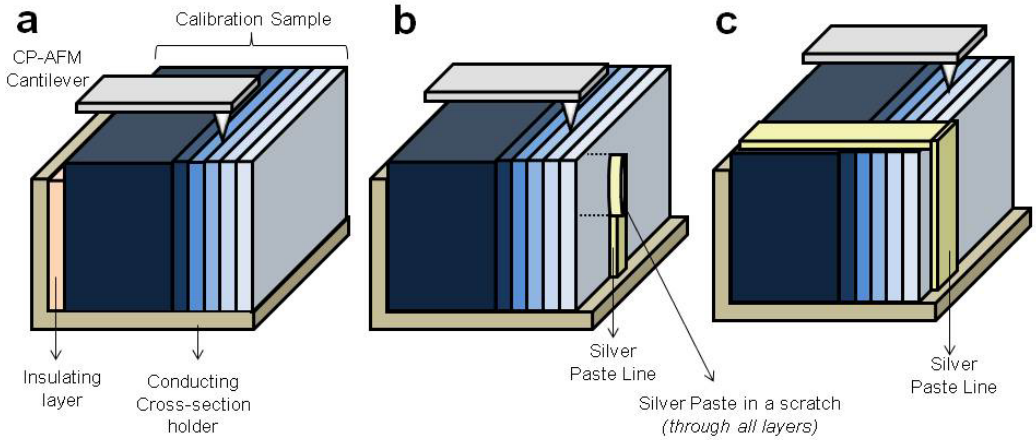

Fig. 5.2 – Three contacting configurations considered for Resiscope measurements on calibration samples: a) the sample is positioned on the conducting cross-section holder and isolated from the back, b) the sample is scratched and conducting silver paint contacts all the layers to the bottom of the cross-section holder, c) the silver paint is deposited on the cross-section and on the surface of the sample and contacts all the layers with the cross-section holder. We obtained the best Resiscope images with this configuration.

To perform Resiscope measurements, we used diamond coated silicon probes with a spring constant ranging from 1 to 10N/m and from 30 to 150N/m. The best signal-to-noise ratio images were obtained with spring constants between 1 and 10N/m. We used a tip force in the µN range, as for SSRM measurements. This range of force enables to penetrate the native oxide and to establish a stable electrical contact leading to a dominance of spreading resistance. Measurements were performed in controlled nitrogen atmosphere. We applied voltages between 0.25 V and 0.75 V. Figure 5.3 shows the setup used for Resiscope measurements on calibration samples and the optical camera image taken from the top of the AFM setup. We also chose to perform KPFM measurement profiles on this sample to confirm that KPFM is not an ideal tool to investigate doping levels. SEM images were also recorded on these samples but no contrast was observed. As for KPFM, the sensitivity of SEM can be limiting to observe and quantify doping levels [1], [11].

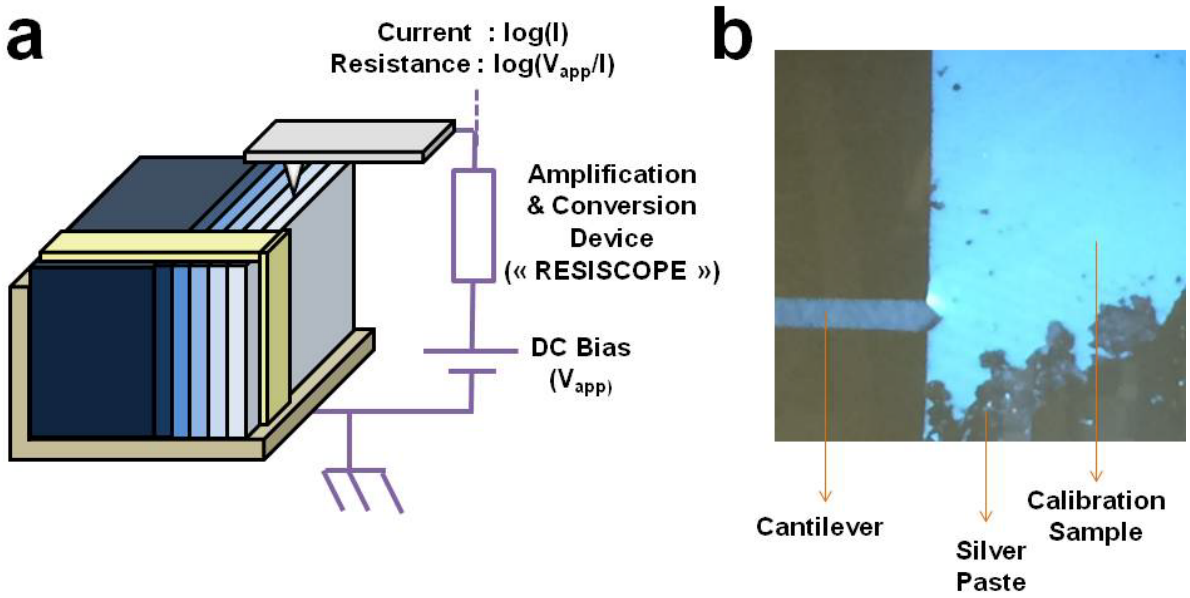

Fig. 5.3 – a) Resiscope setup to measure current and resistance on the cross-section of the calibration sample. b) Optical microscope image of the top view above the calibration sample. The width of the cantilever is about 30 µm.

5.1.3 Results

We first present measurements performed on the cross-section of p-type calibration devices. Figure 5.4 presents 12x12 µm topographical and resistance images obtained on this sample. The resistance image shows clearly the different doped layers, proving that Resiscope can be used to detect doping level changes. It should be noted that these layers were challenging to image in other positions along the cross-section. We attribute this phenomenon to a degradation of the cross-section in some areas or to possible local contaminations. For instance, it was observed that the contrast was clearer after one or two passes because the tip sweeps impurities out of the surface under investigation.

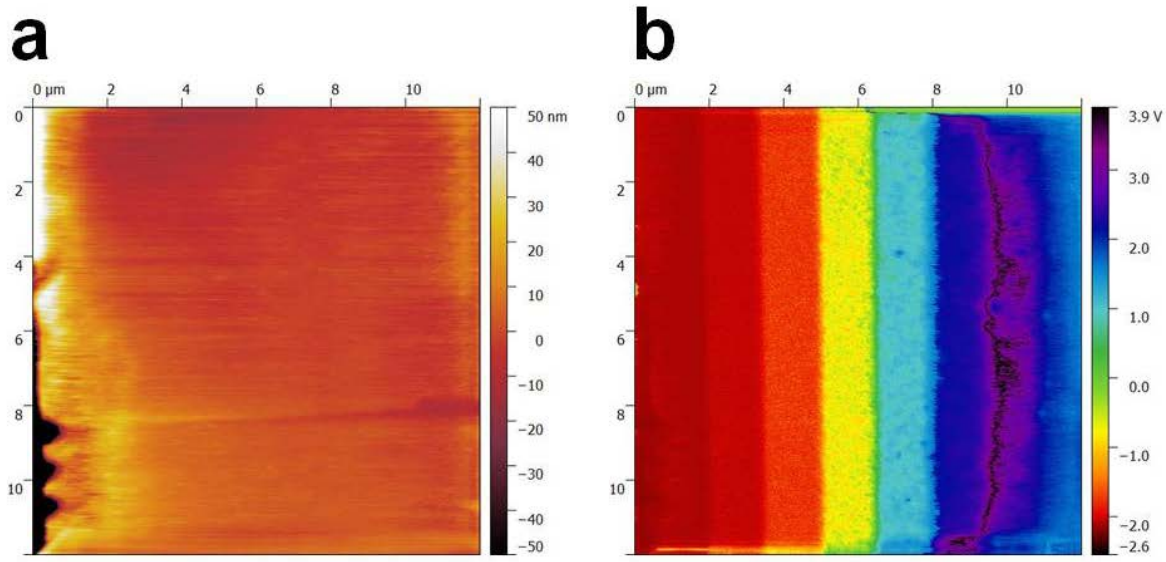

Fig. 5.4 – a) Topography and b) Resistance image of a p-type calibration sample by Resiscope.

Figure 5.5 shows the resistance profile obtained with Resiscope, compared to the specification SSRM resistance profile given by IMEC. The three curves on IMEC specification sheets are: resistivity measured with Scanning Spreading Resistance Microscopy (SSRM), carrier concentration measured with Spreading Resistance Profiling (SRP) and dopant concentration measured with Secondary Ion Mass Spectrometry (SIMS) [16]. The Resiscope profile was obtained by averaging 30pixels across the doping steps. It can be observed that for low doping levels, the resistance profiles are similar. However, for high doping levels, the height of the steps is lower for Resiscope than for specifications. This phenomenon was also reported with SSRM [6]. When the sample is heavily doped (>10^{18} atoms.cm^{-3}), the spreading resistance decreases and it reaches the level of parasitic resistances such as the resistance of the probe. If the probe resistance dominates, the resistance measured is no longer linked with the resistivity and contrasts of carrier concentrations can no longer be detected.

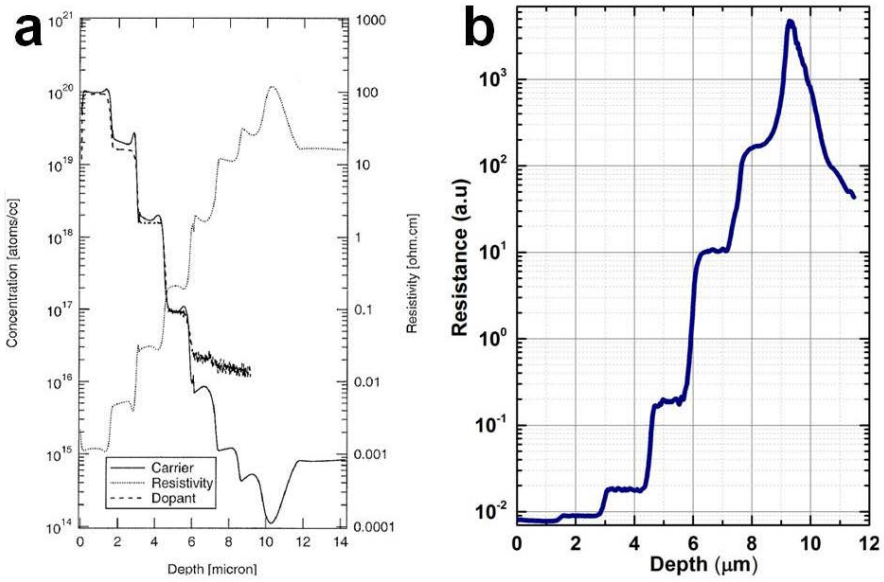

Fig. 5.5 – a) p-type calibration sample specifications of IMEC. All measurements are performed at IMEC. Resisitivity is measured with SSRM, carrier concentration is measured by SRP and dopant concentration is measured with SIMS and b) Resistance profile obtained by Resiscope on p-type calibration sample

Figure 5.6 shows the topography and the resistance images of the n-type calibration sample using the Resiscope. As for the p-type calibration sample, the different layers can be clearly distinguished. On the edge of the sample, the influence of topography can be seen on the resistance image. Figure 5.7 shows the resistance profiles across the sample, with respect to the specification SSRM resistance profile provided by IMEC [16]. As for the p-type calibration sample, the profile fits well the specification profile at low doping levels. However for high doping levels, the contrast between resistance steps is lower, due to the parasitic effect of the probe resistance, as explained previously for p-type calibration samples and shown by Eyben *et al.* [6].

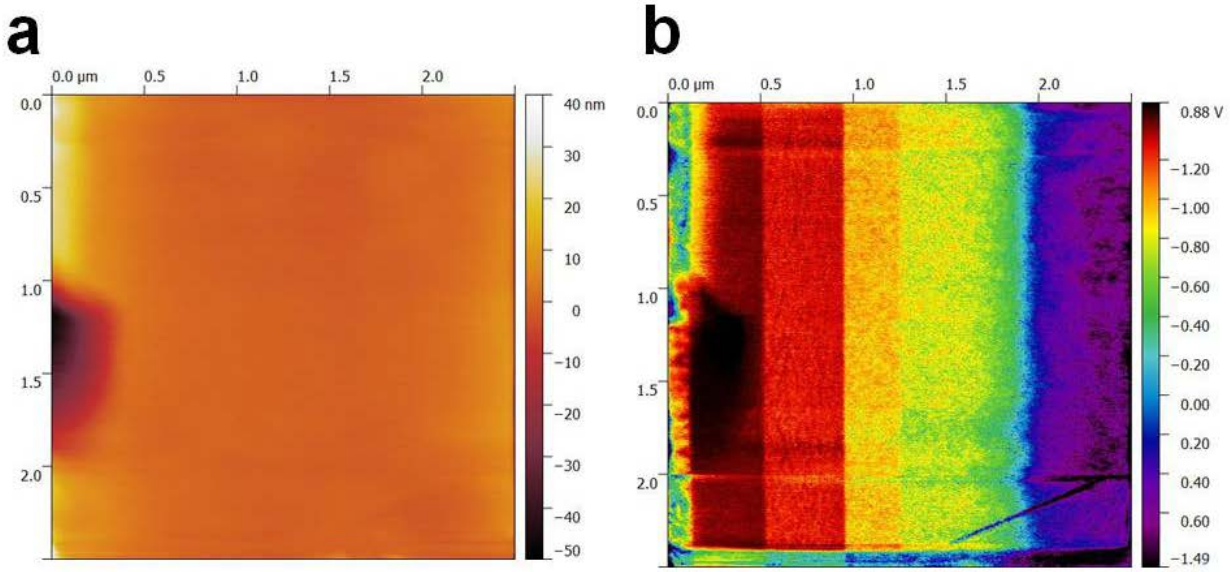

Fig. 5.6 – a) Topography and b) Resistance image of n-type calibration sample by Resiscope.

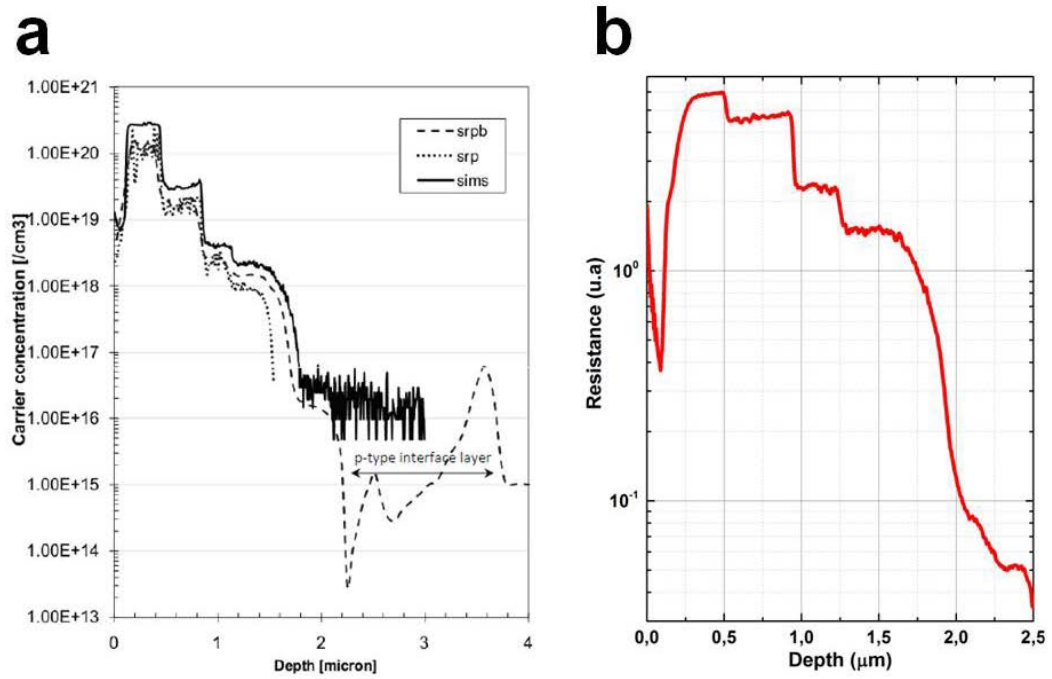

Fig. 5.7 – a) n-type calibration sample specifications of IMEC. All measurements are performed at IMEC. Resisitivity is measured with SSRM, carrier concentration is measured by SRP and dopant concentration is measured with SIMS. b) Resistance profile obtained by Resiscope on the n-type calibration sample

After both measurements on n-type and p-type calibration samples, we observed that the area investigated was nano-indented, proving that measurements can be destructive.

These proof of concept measurements have shown that it was possible to investigate doping levels at the nano-scale unsing Resiscope. Various approaches can be considered to improve measurements. To improve the resolution and the reliability of measurements, bulk diamond probes can be used, as mentioned by Hantschel *et al.* [17]. To improve the sensitivity of measurements for high doping layers, the measurements of spreading resistance should be isolated from the measurement of parasitic resistances. For instance, Eyben *et al.* proposed an innovative technique called Fast Fourier Transform Scanning Spreading Resistance Microscopy (FFT-SSRM) [6]. The principle of this technique is to apply a sinusoidal modulation of the force on the tip which will generate a modulation of the contact size and in turn of the spreading resistance. Since the other parasitic resistances do not depend on the contact size, this technique enables to decouple the spreading resistance from the parasitic resistances. Other perspectives include to work under ultra-high vacuum to reduce tip-induced oxidation effects [7], [18], or at least under highly controlled atmosphere. Eyben *et al.* have shown that an environment with less than 0.1ppm of H_2O and O_2 was desirable [6], [19]. To improve our measurements, the effect of the AFM laser could also be considered. Jiang *et al.* have shown that there was an influence of this laser on SSRM measurements on PN junctions [20]. Finally, some groups have reported innovative ways to achieve 3D SSRM measurements, either by performing successive SSRM scans on the same area and using the fact that the area is indented [21] or by cleaving nano-objects at different positions of their growth process and considering that all the objects are homogeneous from an electronic point of view [18], [22]. This perspective could also be considered with Resiscope setup.

Using our KPFM setup under controlled atmosphere, we performed measurements on the n-type and p-type calibration samples. Figure 5.8 shows the surface potential profiles associated with these samples. It is not possible to indentify the doping steps on these profiles. However, slope changes can be identified and may be correlated with the doping changes. These measurements confirm that KPFM under controlled atmosphere is not the right tool to investigate doping at the nano-scale. However we have shown that Resiscope has the potential to become a tool for quantitative doping levels investigation, as for scanning spreading resistance microscopy (SSRM).

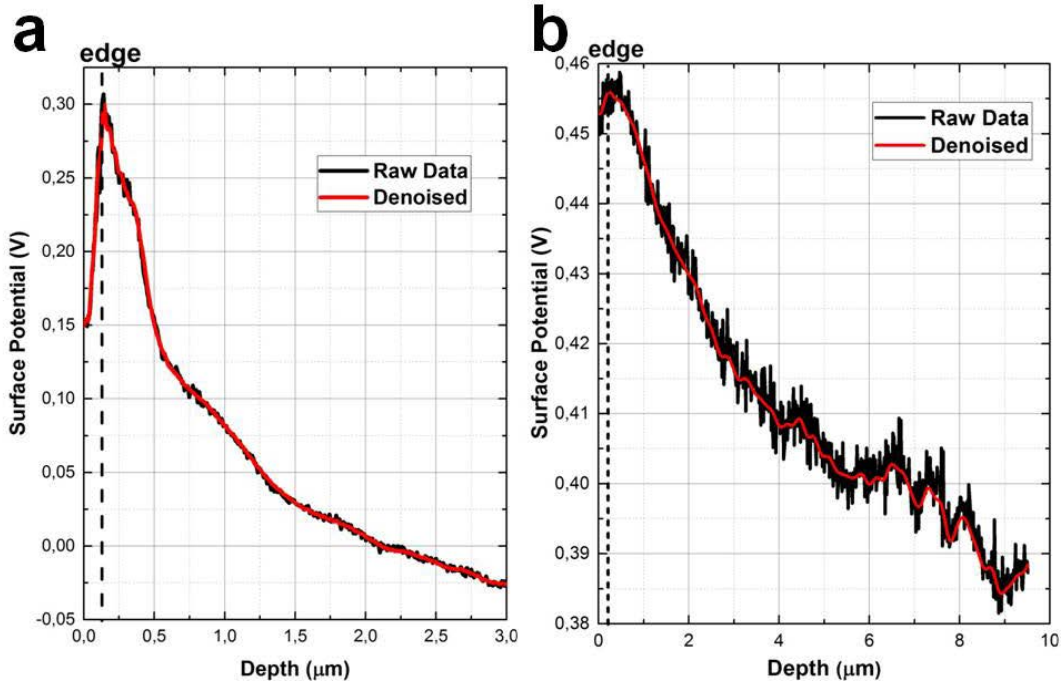

Fig. 5.8 – a) Surface potential profile obtained by KPFM on the n-type calibration sample and b) Surface potential obtained by KPFM on p-type calibration sample. The two figures have different scales, explaining the impression of different noise levels.

5.2 Lifetime measurement at the nano-scale

5.2.1 Context

Minority carrier lifetime is a key property to characterize solar cells. It makes the link between the efficiency of the device and the quality of materials and interface defects. Several lifetime measurement techniques have been developed such as microwave photoconductance decay (μPCD) [23], time-resolved microwave conductivity (TRMC) [24] or photoluminescence (PL) [25]. However, their spatial resolution is limited by the diffraction limit (>100 nm). Therefore, it is challenging to investigate the effect of nano-scale defects at the surface or on the cross-section of materials used for solar cells processing.

Scanning probe microscopy techniques are good candidates to map lifetimes at nano-scale because of their high resolution (section 4.1). Besides, we have shown that scanning probe microscopy can have a high time resolution and that the acquisition time was a benefit of these techniques (section 4.6). In particular, two AFM electrostatic modes have proved to be able to measure fast decay times: time resolved Kelvin Probe Force Microscopy (tr-KPFM) and time resolved Electrostatic Force Microscopy (tr-EFM). Both techniques monitor the signal decay time when switching from one state to another.

In tr-KPFM, the surface potential decay time has been measured when switching the applied electrical bias between two values (+/- V_b) [26] or between an applied bias and open circuit (bias on / bias off) [27] or when switching illumination (light on/light off) [28]. Using tr-KPFM, decay times between tens of milliseconds [27], [28] and seconds [26] have been investigated. Decay times below the millisecond could even be measured in the future using new KPFM modes such as G-Mode KPFM [29], [30].

In tr-EFM, the electrostatic force decay time is measured when switching the illumination between on and off modes. This technique has been introduced by D.C. Coffey and D.S. Ginger [31] and has been extensively used to investigate organic photovoltaics [31]–[35]. Recently, Kataray *et al.* have shown that tr-EFM could achieve time resolution down to 10 ns [36]. Reid *et al.* have shown KFPM and tr-EFM could be combined to investigate organic solar cells at the nano-scale. In particular, they showed tr-EFM decays had a good correlation with internal quantum efficiencies (IQE) curves, even for photon energies below the bandgap [32], [34]. It is reported that a main advantage of tr-EFM compared to KPFM is that it is less sensitive to the tip contamination [35] because tr-EFM measures a rate of change rather than an absolute value so it is less sensitive to contamination and is therefore a more robust technique [35].

5.2.2 Our approach

We used tr-KPFM to investigate passivated crystalline silicon wafers (section 2.6.1) because their lifetimes can reach values over 1ms, which is the time resolution of our KPFM. Previous tr-KPFM studies were limited to lifetime measurements over 10 ms [30]. In this study, we show that it is possible to measure lifetimes between 1 and 10 ms. Besides the choice of the sample, we have innovated by investigating its cross-section. The choice to investigate the cross-section and not the surface, comes from the willingness to answer a question that we have regularly been asked: “Can we extract valuable information on the cross-section of solar cells, given that it is not passivated and therefore sensitive to surface band bending due to dangling bonds?”. To answer this question, we chose to perform decay times on the cross-section of passivated wafers. The lifetime of a non-passivated wafer is in the microsecond range. Therefore, if the decay times measured with KPFM are in the microsecond range, this means that the non-passivated cross-section is only partly limiting the measurements. Otherwise, if the decay time is in the millisecond range, this means that the cross-section is not limiting and the measurement is sensitive to the lifetime of the wafer.

To prepare the cross-section for measurement, we could not use the mechanical polishing technique (section 5.1.2) because this technique is too intrusive and the wafers passivation can easily degrade while polishing. Instead, we have used micro-cleavage technique. This technique is similar to a manual wafer cleavage, but with a better control of the pressure applied on the wafers and a more stable position of the wafer. This technique enables to achieve ultra-flat cross-section with a good success rate compared with manual cleavage. Figure 5.9.a shows the micro-cleavage setup used. The success of a micro-cleavage can be seen directly with naked eye. If the cleavage succeeds, the cross-section is mirror-like (Figure 5.9.b). Otherwise, the cross-section is grayish (Figure 5.9.c). We tried to perform measurements just after micro-cleavage, because we observed that if the wafers were kept too long in ambient air, moistering effects lead to degradation of lifetimes overtime, especially in regions close to the edge [37].

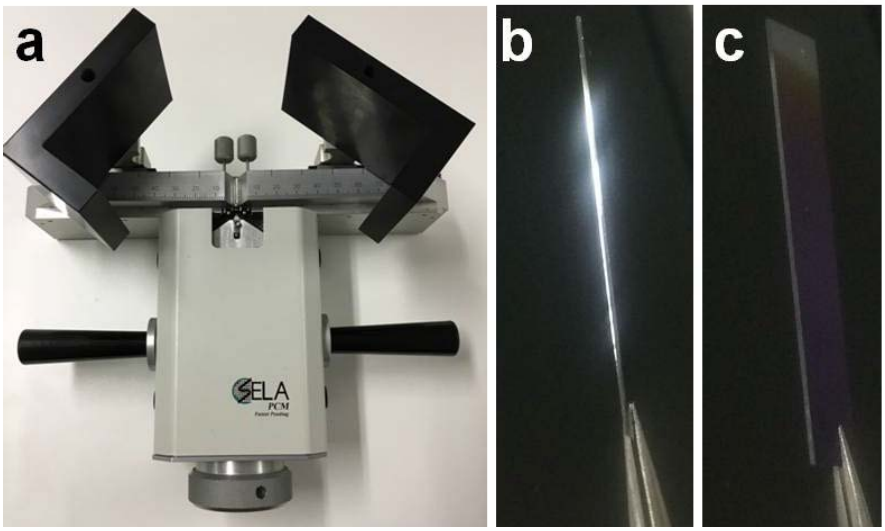

Fig. 5.9 – a) Micro-cleavage setup used to achieve ultra-flat cross-section. b) Ultra-flat cross-section obtained with micro-cleavage showing mirror-like reflection. c) Rough cross-section obtained with regular manual cleavage.

We investigated the decay times of surface potential under two different configurations. For both configurations, the tip is positioned on a fix position of the cross-section and we observe the surface potential evolution when switching from one state to another. In the first configuration, illumination was successively switched on and off and the surface potential decay time was measured. Figure 5.10 shows the setup used for this configuration.

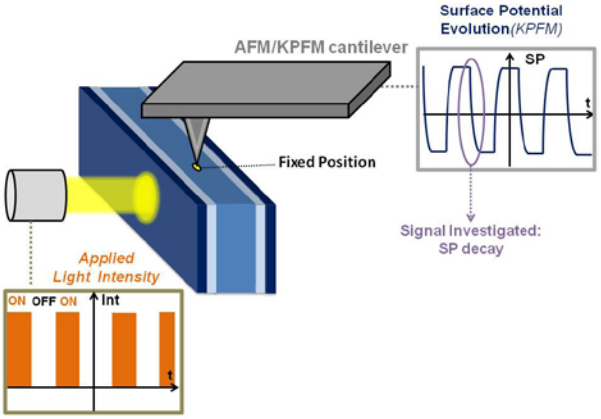

Fig. 5.10 – Setup to measure decay time under illumination of passivated crystalline silicon wafer using KPFM. Note that the cross-section is not passivated.

In the second configuration, the crystalline silicon wafer was contacted from both sides and the electrical bias was switched from one value to another. We observed the decay time during and after switching. Figure 5.11 shows the setup used for this configuration.

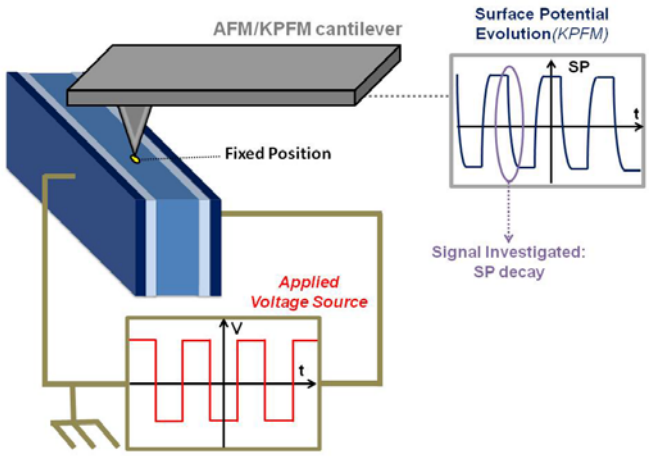

Fig. 5.11 – Setup to measure decay time under electrical bias of passivated crystalline silicon wafer using KPFM. Note that the cross-section is not passivated.

The advantage of this configuration is that the amplitude of the applied electrical bias can be chosen. In the configuration with illumination (Fig. 5.10), the photovoltage increases logarithmically with the illumination intensity. Therefore, it is challenging to obtain a very high photovoltage value. Figure 5.12 shows the surface potential decays observed for different voltage bias amplitude. Each voltage bias amplitude corresponds to a switching between a value and its opposite. For instance, for an amplitude of Δ=2 V, the electrical bias is switched from V_b=-1 V and V_b=1 V. The decay times are in the millisecond range proving that the non-passivated cross-section is probably not limiting too much our measurements (the time constant of the setup is around 1 ms). Figure 5.12.a shows decay curves without normalization. At t=0, the voltage bias is switched from positive to negative voltage. It can be observed that the surface potential difference follows the amplitude of the voltage bias applied. Since the decay time cannot be compared easily for different amplitude of the applied voltage, we perform normalization of the curves (Figure 5.12.b). We observe that the normalized decay curves are similar for the different amplitudes of applied voltage bias. Slight differences are observed for low amplitude curves. We explain this difference by the fact that the signal-to-noise ratio of these curves is too low and affects the decay curve. Therefore, we chose to use an amplitude of 2 V for our decay time measurements under electrical bias. In this condition, the decay curve has a clear exponential form.

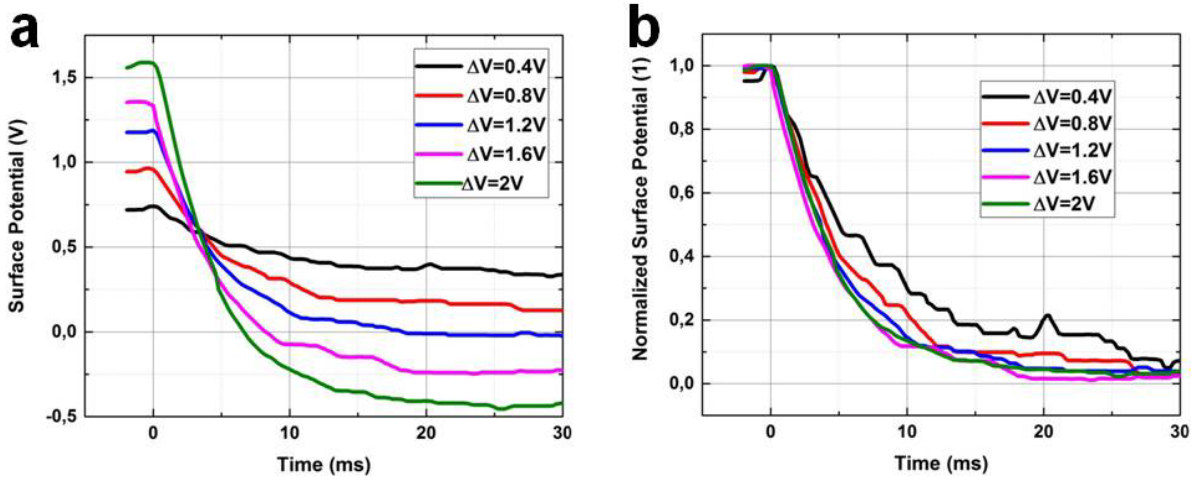

Fig. 5.12 – Decay time obtained with KPFM for different amplitudes of electrical biases: a) before normalization and b) after normalization. The decay times are single shots.

5.2.3 Results

We first want to compare the decay times obtained with the configuration under illumination and the configuration under electrical bias. Since our setup enables to use the two configurations without removing the tip, we performed decay times on the same position using illumination and electrical bias. Figure 5.13 shows the two decay curves obtained, before normalization (Fig.5.13.a) and after normalization (Fig.5.13.b). From Figure 5.13.a, it can be observed that the difference of surface potential under illumination (light on/light off) is 0.4 V, whereas the difference under electrical bias (+1V/-1 V) is about 1.6 V. Therefore, the signal-to-noise ratio is four times higher for electrical bias than for illumination. Figure 5.13.b shows that after the normalization, the decay curves are similar, but the decay curve with illumination has a lower signal-to-noise ratio, which makes decay time extraction more challenging. This is why, we preferred working under electrical bias for these measurements. However, the results obtained under illumination will also be presented. We have also measured decay times under electrical bias in the dark and under illumination. The decay times obtained were exactly the same. Therefore, we can conclude that the stray AFM laser illumination has a negligible influence on our measurements.

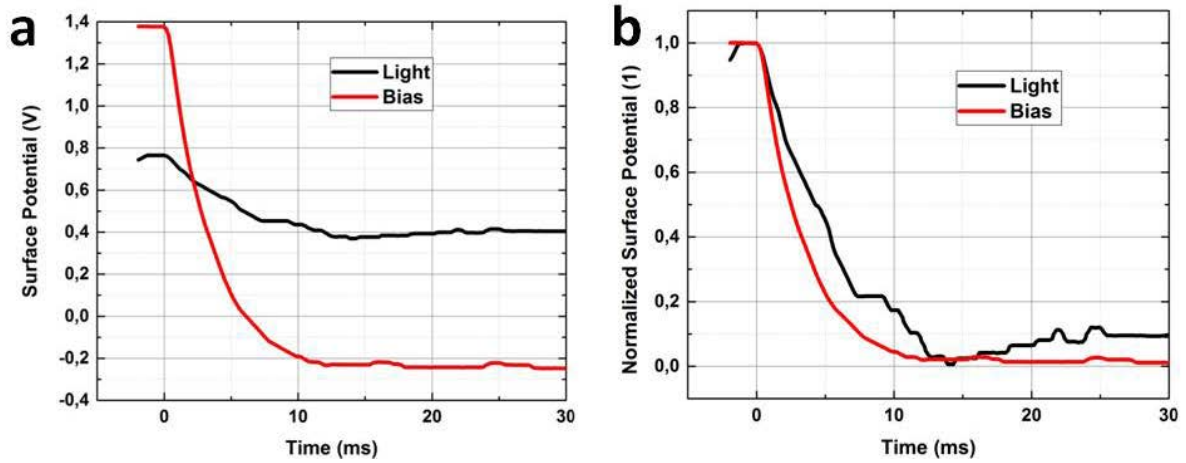

Fig. 5.13 – Decay curve obtained with KPFM with electrical bias (+/-1V) and illumination (light on/ light off): a) before normalization and b) after normalization. Since the amplitude of surface potential with illuminationt is lower, the normalized decay profile has more noise than under electrical bias.

We performed decay time measurements on the cross-section of n-type wafers with different qualities of passivation: a non-passivated wafer ($\tau << 1$ ms), a bad passivation wafer ($\tau \sim 1.8$ ms), an intermediate passivation wafer ($\tau \sim 5$ ms), and a good passivation wafer ($\tau \sim 10$ ms). Figure 5.14 shows the normalized surface potential decays for these four wafers, measured under electrical bias. Two main observations can be done from this figure. First, the decay curves show a good correlation with the passivation quality. The better the passivation quality, the longer the measured decay times. The second observation is that for the non-passivated wafer, signal can still be observed after a time of about 1ms. This is not expected because the lifetime of a non-passivated wafer is in the microsecond range. Two hypotheses are given to explain this phenomenon. First, the measured decay time may be limited by the transient time of the modulated frequency voltage source. Second, the decay time may be limited by the KPFM acquisition time, since the KPFM frequency used is 10 kHz, leading to a period of 0.1 ms.

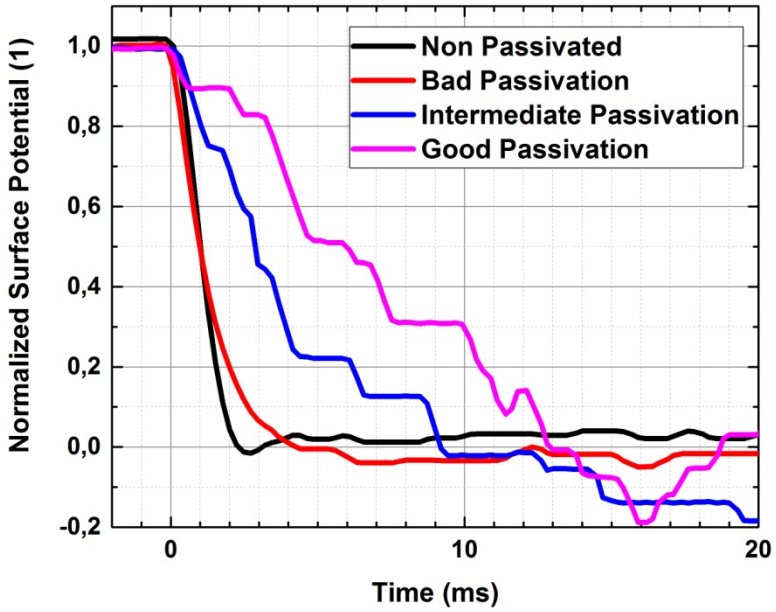

Fig. 5.14 – Decay time under electrical bias obtained for four different qualities of passivation: non-passivated (<<1 ms), bad passivation (1.8 ms), intermediate passivation (2.4 ms), good passivation (9.6 ms)

To determine if the transient time of the voltage source is limiting our measurements, we measured the transient time using an oscilloscope. After normalization, we compared it to the decay time of a non-passivated wafer and of a good passivation wafer. Figure 5.15 shows the four normalized decay curves. We observe that the transient time of the voltage source is much faster than the decay time of non-passivated wafer decay time. Therefore, we conclude that there is a minimum measurable decay time due to the KPFM measurement procedure. Since we are investigating wafers with a lifetime over the millisecond, this minimum measurable lifetime is not limiting for our measurements (except for poorly passivated wafers).

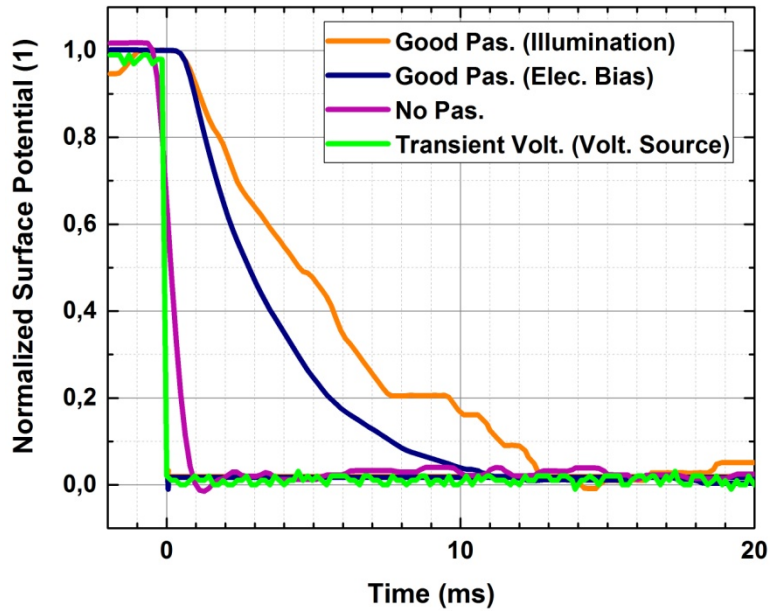

Fig. 5.15 – Comparison between voltage source transient times and voltage and decay times measured by KPFM on a non-passivated wafer, and good passivation wafer under illumination and electrical bias.

In order to assess the uncertainty of our measurements, we perform a statistical study of decay times. For each of the four n-type wafers previously mentioned, we performed ten measurements just after micro-cleavage: five measurements in electrical bias configuration and five measurements under illumination. From each of the decay curve obtained, we extracted a decay time by using an exponential fitting on the curve. In Figure 5.16, we present the maximum, minimum and average decay times obtained for each quality of wafer. Figure 5.16.a shows measurements under electrical bias configuration and Figure 5.16.b shows measurements under illumination configuration. Under illumination, we observe no photovoltage contrast on non-passivated wafers, so only three wafers are presented in Figure 5.16.b.

From Figure 5.16, we observe that a good correlation can be obtained for both measurements under electrical bias and illumination. This proves that our measurements can help study the passivation quality at the nano-scale. However, the uncertainty of our measurements is quite high, judging from the error bars. This is especially true for intermediate and good passivation wafers for which the error bar is well above 1 ms. This uncertainty can be explained by the influence of measurement parameters (e.g. tip/sample distance) which can make measurements vary. Another explanation is the dependence on the position on the wafer cross-section. Because of the micro-cleavage, the local lifetime inhomogeneities could be increased. For non-passivated and badly passivated wafers, the error bar is smaller because it is limited by the minimum measurable decay time around 1 ms, that we have previously highlighted.

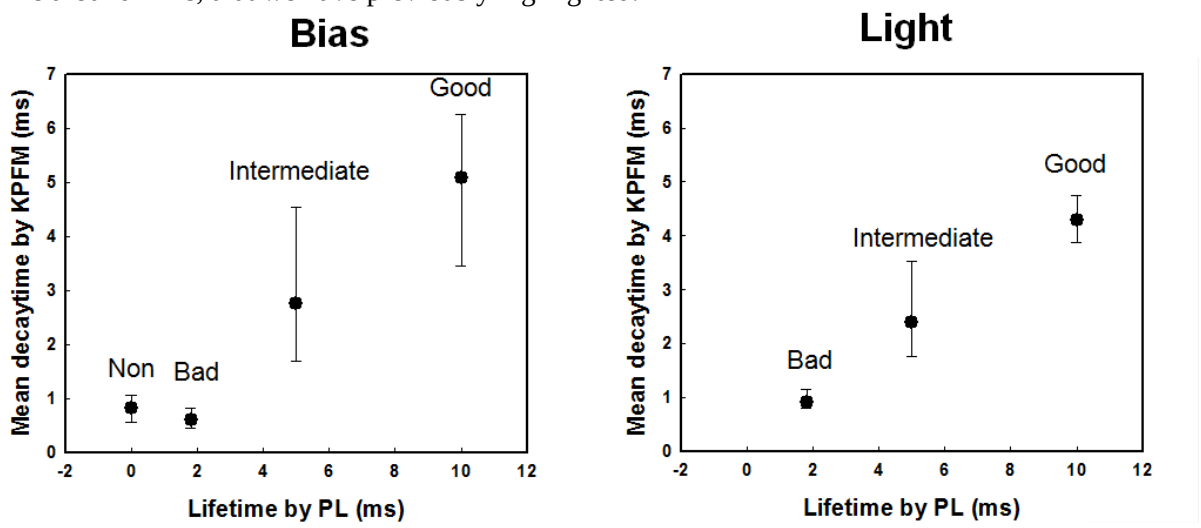

Fig. 5.16 – n-type wafers: Graph showing mean decay times a) under electrical bias and b) under illumination, for three qualities of passivation. The central value is the average of five measurements and the error bar is composed of the maximum and minimum decay time measured. The non-passivated wafer is shown for measurements under electrical bias, but not under illumination because no effect of illumination was observed on this wafer.

In table 5.1, we compare the lifetimes measured by microwave photoconductive decay (µ-PCD) with the average value of mean decay times obtained with illumination and electrical bias. We observe that the lifetimes obtained with illumination and electrical bias are close. However, they are lower than the lifetime measured by µ-PCD. We explain this difference by the fact that the lifetime is observed on the cross-section of the passivated wafer and by border effects. Figure 5.17 shows that on the edge of passivated c-Si wafers, the lifetime is lower than the maximum lifetime measured on the wafer due to edge effects. This phenomenon is visible for all passivated crystalline silicon wafers.

Table 5.1 – Decay times by KPFM (electrical bias and illumination) and Lifetime measured by µ-PCD for the four qualities of passivation on n-type wafers.

n-type	Non	Bad	Intermediate	Good
Decay time Bias (ms)	0.8	0.6	2.8	5.1
Decay time Light (ms)	x	0.9	2.4	4.3
Lifetime by µ-PCD (ms)	x	1.8	5	9.6

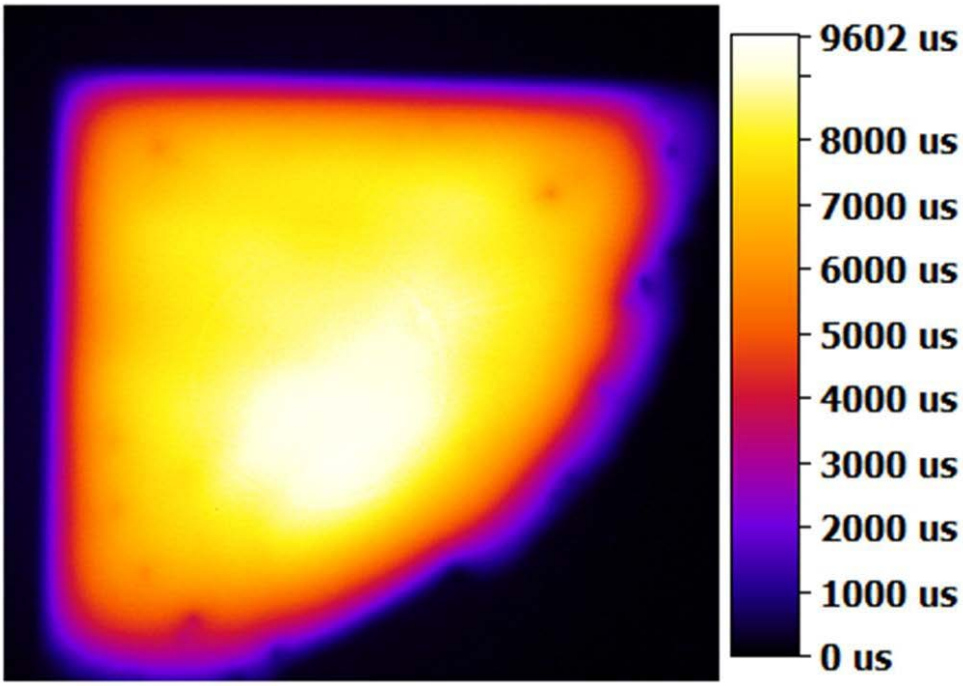

Fig. 5.17 – µ-PCD/PL image of passivated n-type crystalline silicon quarter of wafer. The lifetime on the edge of the wafer is lower. The sample investigated with KPFM is cleaved from this quarter of wafer.

We performed the same set of measurements for passivated p-type crystalline silicon wafers (Fig 5.18). These passivated p-type wafers have lower lifetimes, due to the absence of inversion layers and a poorer quality of the crystalline silicon wafers. In this measurement, the good passivation p-type wafer has a lifetime of 4 ms, the intermediate passivation p-type wafer has a lifetime of 1.4 ms and the bad passivation wafer has a lifetime of 1ms. As for passivated n-type crystalline silicon wafers, the tendency is clear. Contrary to n-type wafers, the uncertainty of measurements seems to be higher under the illumination than for electrical bias. For the moment, we have no clear explanation to this phenomenon.

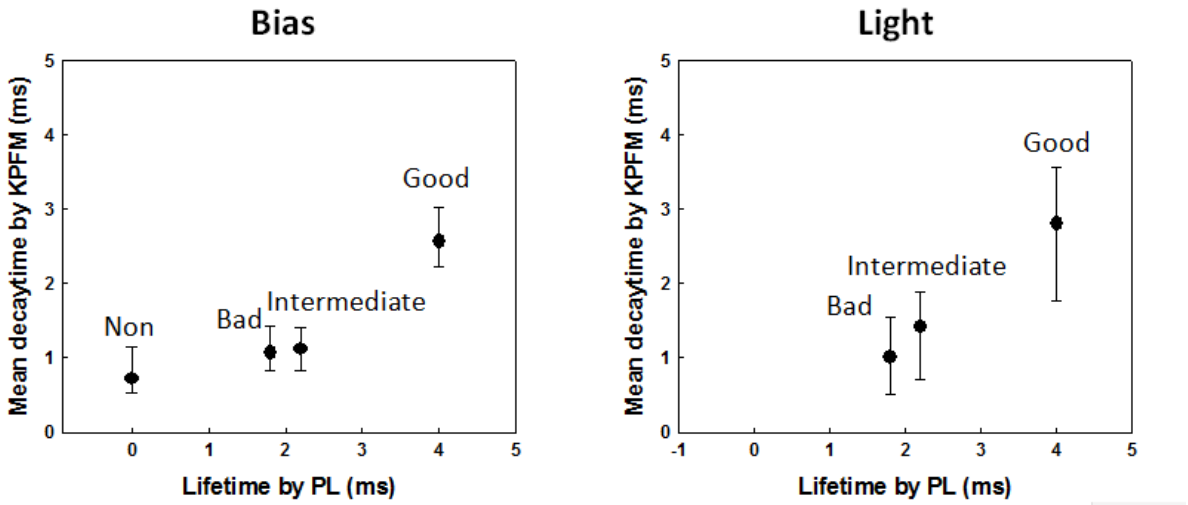

Fig. 5.18 – p-type wafers: Graph showing mean decay times a) under electrical bias and b) under illumination for three qualities of passivation. The central value is the average of five measurements and the error bar is composed of the maximum and minimum decay time measured. The non-passivated wafer is shown for measurements under electrical bias, but not under illumination because no effect of illumination was observed on this wafer.

As for measurements on n-type wafers, average lifetime measurements obtained with illumination and electrical bias are almost similar. But these values are underestimated compared to the maximum lifetime measured by µ-PCD on the wafer, because of edge effects as in the case of n-type wafers.

Table 5.2 – Decay times by KPFM (electrical bias and illumination) and Lifetime measured by µ-PCD for the four qualities of passivation on p-type wafers.

p-type	Non	Bad	Intermediate	Good
Decay time Bias (ms)	**0.7**	**1.1**	**1.1**	**2.6**
Decay time Light (ms)	**x**	**1**	**1.4**	**2.8**
Lifetime by µ-PCD (ms)	**x**	**1.8**	**2.2**	**4**

In conclusion, we have shown that KPFM can be considered as a potential tool to investigate lifetimes in the 1ms-10ms range. Two configurations are presented: configuration under illumination and under electrical bias. Both these configurations give very close decay time values. We preferred using the electrical bias because it has a higher signal-to-noise ratio and it enables to investigate all the wafers (even the non-passivated one). The decay times measured by KPFM have a good correlation with the lifetimes measured by µ-PCD. This proves that consistent measurements can be obtained, despite the fact that the cross-section is not passivated. However, the lifetime values measured by KPFM are lower than the lifetime values measured by µ-PCD because of an edge effect. Besides, measurements on intermediate and good passivation wafers show high uncertainty.

Therefore, further work should be carried on reducing the uncertainties due to KPFM measurement parameters. The origin of these uncertainties should be investigated and may lead to further understanding of lifetimes in the crystalline silicon wafers. Another perspective is to carry similar measurements on the surface of passivated crystalline silicon wafers. In this measurement, uncertainties due to cleavage and non-passivated cross-section measurements could be reduced.

Besides, these measurements would not require cleaving, as opposed to cross-section measurements. We tried to measure illumination decays on the surface of passivated wafers but the photovoltage obtained was too low to extract a decay time. We attributed this low photovoltage to stray AFM laser illumination (Section 3.1). However, we have recently observed that surface measurements on passivated wafers are very sensitive to the electrical bias, enabling to extract decay times. The measurements must be performed close enough from the frontside electrode. This opens an interesting perspective to investigate the lifetime of crystalline silicon wafers from the surface of the wafer.

5.3 Conclusion

In Chapter 5, we have highlighted two material measurements of interest for crystalline silicon solar cells using scanning probe microscopy techniques.

We have shown that CP-AFM is a powerful tool to investigate doping levels at the nano-scale. In our work, we have used an upgraded version of CP-AFM called Resiscope. This version is very close to Scanning Spreading Resistance Microscopy. To our knowledge, we have shown for the first time that Resiscope was able to detect doping levels at the nano-scale with a good sensitivity and was able to match well profiles of SSRM for low doping levels [10^{15}-10^{18}] atoms.cm^{-3}. For higher doping levels [10^{18}-10^{20}] atoms.cm^{-3}, the sensitivity is degraded due to lower spreading resistance-to-parasitic resistance ratio. Perspectives are proposed to go toward a higher dynamic range of doping levels measurable and to properly quantify measurements. We also confirmed that KPFM under ambient air is not the appropriate tool to investigate doping at nano-scale because of its low sensitivity due to thermal noise (section 3.6) and to its sensitivity to surface states and Fermi level pinning (section 3.8).

We have also shown, for the first time to our knowledge, that KPFM could be used to investigate high lifetime passivated crystalline silicon wafers. This work was motivated by the fact that KPFM can acquire decay times in the millisecond range (section 4.6) and has a low intrusiveness compared to CP-AFM (section 3.2 and 3.3). We have compared decay times under illumination (light on/light off) and electrical bias (+/-1V) for different qualities of passivation of both n-type and p-type crystalline silicon wafers. We have shown that decay time measurements with KPFM have a good correlation with lifetimes measured by µ-PCD on these wafers and that for low lifetime wafers, a minimum measurable lifetime of about 1ms was detected. We have carried out statistical work to assess the error bars on our measurements. We found out that for high lifetimes, the error bar was important, even though the tendency was preserved. We proposed as perspective to go toward more reliable lifetime measurements on crystalline silicon wafers using KPFM.

The two studies are examples of how scanning probe microscopies can perform material measurements at the nano-scale that would be challenging for other techniques such as electron microscopy, bringing additional possibilities to advanced characterization of solar materials. In Chapter 6, we will show that scanning probe microscopy techniques can also enable new kind of measurements on crystalline silicon solar cells.

REFERENCES

[1] N. Duhayon, P. Eyben, M. Fouchier, T. Clarysse, W. Vandervorst, D. Álvarez, S. Schoemann, M. Ciappa, M. Stangoni, W. Fichtner, P. Formanek, M. Kittler, V. Raineri, F. Giannazzo, D. Goghero, Y. Rosenwaks, R. Shikler, S. Saraf, S. Sadewasser, N. Barreau, T. Glatzel, M. Verheijen, S. a. M. Mentink, M. von Sprekelsen, T. Maltezopoulos, R. Wiesendanger, and L. Hellemans, "Assessing the performance of two-dimensional dopant profiling techniques," *J. Vac. Sci. Technol. B*, vol. 22, no. 1, pp. 385–393, Jan. 2004.

[2] P. De Wolf, R. Stephenson, T. Trenkler, T. Clarysse, T. Hantschel, and W. Vandervorst, "Status and review of two-dimensional carrier and dopant profiling using scanning probe microscopy," *J. Vac. Sci. Technol. B*, vol. 18, no. 1, pp. 361–368, Jan. 2000.

[3] P. Gargini, J. Glaze, and O. Williams, "The SIA's 1997 National Technology Roadmap for Semiconductors," *Solid State Technol.*, vol. 41, no. 1, pp. 73–76, Jan. 1998.

[4] The international Technology Roadmap for Semiconductors (ITRS), Metrology, 2013, (https://www.dropbox.com/sh/6xq737bg6pww9gq/AACQWcdHLffUeVloszVY6Bkla?dl=0.) (accessed on 8 Oct. 2016)

[5] P. De Wolf, E. Brazel, and A. Erickson, "Electrical characterization of semiconductor materials and devices using scanning probe microscopy," *Mater. Sci. Semicond. Process.*, vol. 4, no. 1–3, pp. 71–76, Feb. 2001.

[6] P. Eyben, P. Bisiaux, A. Schulze, A. Nazir, and W. Vandervorst, "Fast Fourier transform scanning spreading resistance microscopy: a novel technique to overcome the limitations of classical conductive AFM techniques," *Nanotechnology*, vol. 26, no. 35, p. 355702, 2015.

[7] L. Zhang, Y. Mitani, A. Kinoshita, S. Takeno, K. Suguro, I. Mizushima, S. Mori, K. Yamamoto, J. Koga, K. Hara, Y. Hayase, and S. Ogata, "Direct observation of boron dopant fluctuation by site-specific scanning spreading resistance microscopy," IEEE *Reliability Physics Symposium* pp. 2D.4.1-2D.4.5, 2012

[8] P. Eyben, F. Seidel, T. Hantschel, A. Schulze, A. Lorenz, A. U. De Castro, D. Van Gestel, J. John, J. Horzel, and W. Vandervorst, "Development and optimization of scanning spreading resistance microscopy for measuring the two-dimensional carrier profile in solar cell structures," *Phys. Status Solidi A*, vol. 208, no. 3, pp. 596–599, Mar. 2011.

[9] A. Uruena, J. John, G. Beaucarne, P. Choulat, P. Eyben, G. Agostinelli, E. Van Kerschaver, J. Poortmans, and R. Mertens, "Local Al-alloyed contacts for next generation Si solar cells," *24th EU PVSEC Proceedings*, no. 2CV.2.22, pp. 1483–1486, 2009

[10] L. Carnel, I. Gordon, D. V. Gestel, D. Vanhaeren, P. Eyben, G. Beaucarne, and J. Poortmans, "Impact of Preferential P-Diffusion Along the Grain Boundaries on Fine-Grained Polysilicon Solar Cells," *IEEE Electron Device Lett.*, vol. 28, no. 10, pp. 899–901, Oct. 2007.

[11] I. Volotsenko, M. Molotskii, Z. Barkay, J. Marczewski, P. Grabiec, B. Jaroszewicz, G. Meshulam, E. Grunbaum, and Y. Rosenwaks, "Secondary electron doping contrast: Theory based on scanning electron microscope and Kelvin probe force microscopy measurements," *J. Appl. Phys.*, vol. 107, no. 1, p. 14510, Jan. 2010.

[12] C. Baumgart, M. Helm, and H. Schmidt, "Quantitative dopant profiling in semiconductors: A Kelvin probe force microscopy model," *Phys. Rev. B*, vol. 80, no. 8, p. 85305, Aug. 2009.

[13] C.-S. Jiang, I. L. Repins, C. Beall, H. R. Moutinho, K. Ramanathan, and M. M. Al-Jassim, "Investigation of micro-electrical properties of Cu2ZnSnSe4 thin films using scanning probe microscopy," *Sol. Energy Mater. Sol. Cells*, vol. 132, pp. 342–347, Jan. 2015.

[14] J.-P. Kleider, J. Alvarez, A. V. Ankudinov, A. S. Gudovskikh, E. V. Gushchina, M. Labrune, O. A. Maslova, W. Favre, M.-E. Gueunier-Farret, P. R. i Cabarrocas, and E. I. Terukov, "Characterization of silicon heterojunctions for solar cells," *Nanoscale Res. Lett.*, vol. 6, no. 1, p. 152, Feb. 2011.

[15] P. D. Wolf, T. Clarysse, and W. Vandervorst, "Quantification of nanospreading resistance profiling data," *J. Vac. Sci. Technol. B*, vol. 16, no. 1, pp. 320–326, Jan. 1998.

[16] IMEC, "Calibration standards and test samples", *Available at:* (http://www2.imec.be/be_en/services-and-solutions/cams/products/calibration-standards-and-test-s.html) (accessed on 8 Oct. 2016)

[17] T. Hantschel, P. Niedermann, and W. Vandervorst, "Highly conductive diamond probes for scanning spreading resistance microscopy," *Appl. Phys. Lett.*, vol. 76, no. 12, pp. 1603–1605, Mar. 2000.

[18] A. Schulze, T. Hantschel, P. Eyben, A. S. Verhulst, R. Rooyackers, A. Vandooren, and W. Vandervorst, "Quantitative three-dimensional carrier mapping in nanowire-based transistors using scanning spreading resistance microscopy," *Ultramicroscopy*, vol. 125, pp. 18–23, Feb. 2013.

[19] P. Eyben, J. Mody, A. Nazir, A. Schulze, T. Clarysse, T. Hantschel, and W. Vandervorst, "Subnanometer Characterization of Nanoelectronic Devices," in *Fundamentals of Picoscience*, Chapter 6, CRC Press, pp. 677–704, 2013

[20] H. Li, C. S. Jiang, W. K. Metzger, C. K. Shih, and M. Al-Jassim, "Microscopic Real-Space Resistance Mapping Across CdTe Solar Cell Junctions by Scanning Spreading Resistance Microscopy," *IEEE J. Photovolt.*, vol. 5, no. 1, pp. 395–400, Jan. 2015.

[21] M. W. Xu, T. Hantschel, W. Vandervorst, "Three-dimensional carrier profiling of InP-based devices using scanning spreading resistance microscopy," *Appl. Phys. Lett.*, vol. 81, no. 1, pp. 177–179,2002.

[22] J. Mody, G. Zschätzsch, S. Kölling, A. De Keersgieter, G. Eneman, A. K. Kambham, C. Drijbooms, A. Schulze, T. Chiarella, N. Horiguchi, and others, "3D-carrier profiling in FinFETs using scanning spreading resistance microscopy," in *Electron Devices Meeting (IEDM)*, 2011, pp. 5–7.

[23] M. Wilson, A. Savtchouk, J. Lagowski, K. Kis-Szabo, F. Korsos, A. Toth, R. Kopecek, and V. Mihailetchi, "QSS-µPCD measurement of lifetime in silicon wafers: advantages and new applications," *Energy Procedia*, vol. 8, pp. 128–134, 2011.

[24] I. Cosme, R. Cariou, W. Chen, M. Foldyna, R. Boukhicha, P. Roca i Cabarrocas, K. D. Lee, C. Trompoukis, and V. Depauw, "Lifetime assessment in crystalline silicon: From nanopatterned wafer to ultra-thin crystalline films for solar cells," *Sol. Energy Mater. Sol. Cells*, vol. 135, pp. 93–98, 2015

[25] J. A. Giesecke, M. C. Schubert, B. Michl, F. Schindler, and W. Warta, "Minority carrier lifetime imaging of silicon wafers calibrated by quasi-steady-state photoluminescence," *Sol. Energy Mater. Sol. Cells*, vol. 95, no. 3, pp. 1011–1018, Mar. 2011.

[26] D. W. Cardwell, A. R. Arehart, C. Poblenz, Y. Pei, J. S. Speck, U. K. Mishra, S. A. Ringel, and J. P. Pelz, "Nm-scale measurements of fast surface potential transients in an AlGaN/GaN high electron mobility transistor," *Appl. Phys. Lett.*, vol. 100, no. 19, p. 193507, May 2012.

[27] E. Strelcov, S. Jesse, Y.-L. Huang, Y.-C. Teng, I. I. Kravchenko, Y.-H. Chu, and S. V. Kalinin, "Space- and Time-Resolved Mapping of Ionic Dynamic and Electroresistive Phenomena in Lateral Devices," *ACS Nano*, vol. 7, no. 8, pp. 6806–6815, Aug. 2013.

[28] M. Beu, K. Klinkmüller, and D. Schlettwein, "Use of Kelvin probe force microscopy to achieve a locally and time-resolved analysis of the photovoltage generated in dye-sensitized ZnO electrodes," *Phys. Status Solidi A*, vol. 211, no. 9, pp. 1960–1965, Sep. 2014.

[29] L. Collins, A. Belianinov, S. Somnath, B. J. Rodriguez, N. Balke, S. V. Kalinin, and Stephen Jesse, "Multifrequency spectrum analysis using fully digital G Mode-Kelvin probe force microscopy," *Nanotechnology*, vol. 27, no. 10, p. 105706, 2016.

[30] E. Strelcov, S. M. Yang, S. Jesse, N. Balke, R. K. Vasudevan, and S. V. Kalinin, "Solid-state electrochemistry on the nanometer and atomic scales: the scanning probe microscopy approach," *Nanoscale*, vol. 8, no. 29, pp. 13838–13858, Jul. 2016.

[31] D. C. Coffey and D. S. Ginger, "Time-resolved electrostatic force microscopy of polymer solar cells," *Nat. Mater.*, vol. 5, no. 9, pp. 735–740, Sep. 2006.

[32] P. A. Cox, M. S. Glaz, J. S. Harrison, S. R. Peurifoy, D. C. Coffey, and D. S. Ginger, "Imaging Charge Transfer State Excitations in Polymer/Fullerene Solar Cells with Time-Resolved Electrostatic Force Microscopy," *J. Phys. Chem. Lett.*, vol. 6, no. 15, pp. 2852–2858, Aug. 2015.

[33] G. Shao, G. E. Rayermann, E. M. Smith, and D. S. Ginger, "Morphology-Dependent Trap Formation in Bulk Heterojunction Photodiodes," *J. Phys. Chem. B*, vol. 117, no. 16, pp. 4654–4660, Apr. 2013.

[34] O. G. Reid, G. E. Rayermann, D. C. Coffey, and D. S. Ginger, "Imaging Local Trap Formation in Conjugated Polymer Solar Cells: A Comparison of Time-Resolved Electrostatic Force Microscopy and Scanning Kelvin Probe Imaging," *J. Phys. Chem. C*, vol. 114, no. 48, pp. 20672–20677, 2010.

[35] R. Giridharagopal, G. E. Rayermann, G. Shao, D. T. Moore, O. G. Reid, A. F. Tillack, D. J. Masiello, and D. S. Ginger, "Submicrosecond Time Resolution Atomic Force Microscopy for Probing Nanoscale Dynamics," *Nano Lett.*, vol. 12, no. 2, pp. 893–898, Feb. 2012.

[36] D. U. Karatay, J. S. Harrison, M. S. Glaz, R. Giridharagopal, and D. S. Ginger, "Fast time-resolved electrostatic force microscopy: Achieving sub-cycle time resolution," *Rev. Sci. Instrum.*, vol. 87, no. 5, p. 53702, May 2016.

[37] W. Liang, K. J. Weber, D. Suh and J. Bullock, "Humidity degradation and repair of ALD Al2O3 passivated silicon," *39th IEEE Photovoltaic Specialists Conference (PVSC)*, pp. 038–044, 2013

Chapter 6 – Devices Investigations

Contents

6.0 Introduction

In Chapter 5 we have achieved materials measurements of interest for crystalline silicon solar cells. In Chapter 6 we focus on devices measurements.

KPFM and CP-AFM present several advantages to investigate solar cell devices at the nano-scale. First, they have a spatial resolution (<10 nm) which enables to investigate PN junctions (section 4.1) since such a resolution is in the range of space charge regions widths (1 nm-1 µm). Second, they allow to perform direct electrical measurements (section 4.4). Therefore the quantities measured at the nano-scale (e.g. voltage with KPFM and current with Resiscope) can be directly compared with external macro-scale device quantities (e.g. open circuit voltage, applied voltage bias, photocurrent). Besides, CP-AFM and KPFM are sensitive to illumination because they don't use incident carriers (e.g. electrons or photons) to perform measurements as in electron and optical microscopy (section 4.2). Despite the parasitic effect of AFM laser (section 3.1), they are unique tools to investigate the effect of illumination at the nano-scale on the solar cell device. Finally, these techniques are very versatile (section 4.5). Since, they can be operated under ambient air, it is very easy to bring external excitation sources (e.g. illumination and electrical bias) to study the solar cell device under operating conditions.

Compared to KPFM, CP-AFM is a quite destructive technique because the force applied on the tip can degrade both the tip and the surface investigated (section 3.2&3.3). Therefore, it is challenging to study the influence of external excitations on devices with CP-AFM because in these studies, successive measurements have to be performed on the same area, under different operating conditions. Measurements on different areas lead to uncertainties due to possible inhomogeneity in the device. CP-AFM studies of the effect of illumination at nano-scale on solar cells will be shown in section 6.2. A quick degradation of the electrical signal with time will be highlighted for CP-AFM.

KPFM presents the advantage of being a very low intrusive technique compared to other nano-scale resolution techniques (section 3.2&3.3&4.3). However, we have shown that KPFM studies are often limited by the low sensitivity of KPFM due to thermal noise (section 3.6). To circumvent this limitation, only signal changes well above the noise level (~30 mV) can be studied. Typically, surface potential changes above 100mV can provide a signal-to-noise ratio high enough to perform valuable interpretations of KPFM measurements. In a solar cell, two main excitation sources can provide voltage changes above 100mV: electrical voltage bias and illumination. Therefore, in this Chapter, we will study the effect of electrical bias (section 6.1) and illumination (section 6.2) at the nano-scale using KPFM. It should be noted that other external excitations (e.g. temperature [1] or mechanical pressure [2]) can be thought of to change the electrical properties of the solar cell at the nano-scale. But, illumination and electrical bias provide easier ways to achieve high voltage changes in a versatile way. Besides, illumination and electrical bias are the two main excitation sources when studying a photovoltaic device. KPFM measurements can also be performed without external excitation [3], [4] but the interpretation is challenging because surface effects can induce band bending affecting the signal (section 3.8). Using an external excitation source enables to subtract the signals with different excitation values and therefore limit the surface band bending effects [5]–[7]. It also has the advantage of increasing the signal-to-noise ratio. Changes over 100 mV can be studied and controlled by finely tuning excitation parameters (e.g. illumination intensity, wavelength or electrical bias and frequency). These parameters will be extensively studied in this chapter and we will show how to extract valuable information for crystalline silicon solar cells using these measurements.

6.1 Devices investigation under electrical bias

6.1.1 Measurements under constant electrical bias

6.1.1.1 Context

In a solar cell, the potential is sensitive to the applied electrical bias. The potential difference between the contacts of the cell is equal to the value of the applied electrical bias. The dependence of surface potential of the PN junction on applied voltage bias has been explained qualitatively in Section 2.5. The value of the applied voltage is limited by the inability of the solar cell to withstand high absolute voltage values. For instance, we observed that the epitaxial silicon solar cells (Section 2.6) can degrade irreversibly for voltages below -0.5 V and over 0.5 V. Therefore, measurements can be performed with a maximum voltage amplitude of 1 V. This is much higher than the noise level of our measurements (~30 mV), so a high signal-to-noise ratio can be achieved. For IBC solar cells (Section 2.6), this voltage amplitude exceeds 2 V.

Several groups have studied the influence of the electrical bias on solar cells at the nano-scale using Kelvin Probe Force Microscopy (KPFM). Different technologies of solar cells have been investigated such as multi-junction solar cells [8], III-V PN junctions [6], quantum dot solar cells [9], amorphous silicon solar cells [6], [10] and multi-crystalline silicon solar cells [11]. These measurements enable to obtain the distribution of the built-in potential across the PN junctions of photovoltaic devices. This is a key factor to understand the physics of the device and to investigate the homogeneity of its electrical properties at the nano-scale. Contrary to techniques used so far to study built-in potential (e.g. current-voltage, capacitance voltage or electroabsorption), KPFM provides a direct spatial measurement of the built-in potential profile.

Scanning Electron Microscopy has also proven to be sensitive to surface potential and therefore to the influence of electrical bias [12]–[15]. In particular, it has been shown that SEM enabled to detect doping contrasts [16], [17]. For instance, doping contrast imaging in low acceleration voltage is a well-known technique used for wafer inspection [18]. In section 2.5, we have qualitatively explained the origin of the contrast. Even though the origin of this sensitivity is not totally understood, recent theoretical works have provided explanations to this sensitivity and achieved quantitative surface potential measurements with low voltage SEM that could be compared with KPFM [17]. Other studies have shown the influence of electrical bias on SEM images of PN junctions of different materials [12], [13], [15]. Using this technique, it has been shown that the PN junction could be precisely characterized and a good estimation of the size of the space charge region can be obtained [12], [13].

Both Kelvin Probe Force Microscopy and Scanning Electron Microscopy enable to assess the effect of electrical bias on the surface potential of the layers of a solar cell. Therefore, recent studies comparing SEM and KPFM on the cross-section of solar cells under different values of electrical bias have been carried out and have shown a good correlation, enabling to discuss the assets of each technique [13].

6.1.1.2 Our approach

In this section we performed a comparison between SEM and KPFM under electrical bias on the exact same position of two crystalline silicon solar cell designs: the back surface of interdigitated back contact solar cells (IBC) and the cross-section of epitaxial silicon solar cells (epi-Si). Our approach [19] has three originalities compared to previous studies [13]. The first is that measurements are performed on the exact same position of the solar cell thanks to nano-scratching markers (section 3.2.2). The second is that proof on concept measurements are performed on interdigitated back

contact (IBC) solar cells. Contrary to previous work, KPFM measurements on IBC solar cells allow to characterize the PN junction without cleaving the solar cell. Therefore, uncertainties due to electrical properties of a non-passivated cross-section are removed and interpretations are more accurate. The third originality is that we compared our SEM and KPFM measurements with Resiscope measurements under external electrical bias, which is the first measurement of this kind to our knowledge.

Figure 6.1 shows the two setups used to perform KPFM measurements on interdigitated back contact solar cells and epitaxial silicon solar cells. The exact same setups are used for SEM measurements, replacing the AFM/KPFM cantilever by an incident beam of electrons. For measurements on epitaxial silicon solar cells, the cross-section is either µ-cleaved (Section 5.2.2) or cleaved and polished with diamond disks (Section 5.1.2). Isopropanol cleaning was performed before each measurement. KPFM measurements were performed under controlled nitrogen atmosphere and SEM measurements were performed under ultra-high vacuum (UHV). KPFM and SEM measurements are performed on and between the contacts of the solar cells for different values of electrical bias applied. Both interdigitated back contact solar cell and epitaxial silicon solar cell are nano-indented to be able to perform KPFM and SEM measurements on adjacent positions. SEM analysis show that the surface potential contrasts are not affected close to the nano-indented areas. The contrast on these areas is similar to that observed far from the nano-indented areas. Only the nano-indented areas are electrically affected.

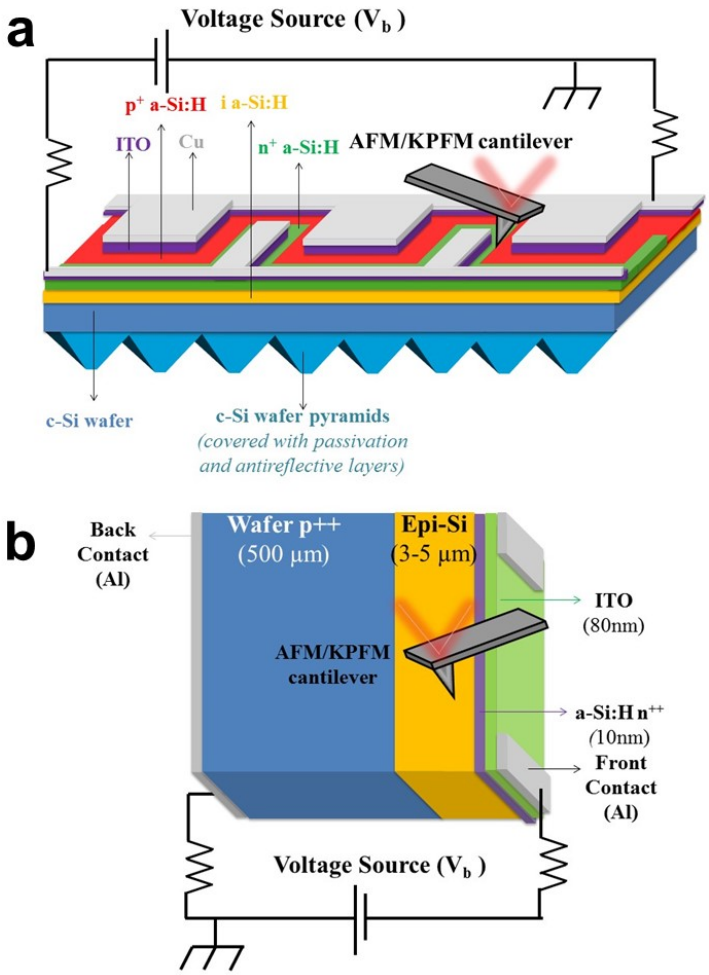

Fig. 6.1 – a) Setups used to investigate a) the back surface of an interidigitated back contact solar cell and b) the cross-section of an epitaxial silicon solar cell under electrical bias using KPFM

6.1.1.3 Results

- ***Interdigitated back contact solar cell***

At the time of the Ph.D. manuscript writing, the measurements performed on interdigitated back contact solar cells have been submitted to Solar Energy Materials and Solar Cells [19]. Early preliminary results were published in a conference paper [20].

Figure 6.2 shows SEM images of the Cu/ITO/n^+ a-Si:H contact, the Cu/ITO/p^+ a-Si:H contact and the area between metallic contacts with the n^+ a-Si:H and the p^+ a-Si:H layers (Figure 6.1.a). Each image corresponds to an electrical bias applied to the cell. We used a low accelerating voltage (V_{acc} = 0.5 kV) to be sensitive only to the very surface of the IBC solar cell.

According to Monte Carlo simulations, the penetration depth of electrons is estimated at around 10 nm and the escape depth is estimated around 3 nm. The secondary electrons are emitted from the escape depth; hence collected secondary electrons have only been reemitted from the amorphous layers. Since KPFM in air is only sensitive to defects as deep as 2 nm (sub-section 3.8), the comparison between SEM and KPFM measurements is possible.

The two indented squares are visible at the interface between the two amorphous layers. One indented area is more visible than the other because the AFM tip used to perform nano-indentation degraded quickly while indenting them. One can also notice a dust spot below the bottom indented square and the topographical bump between the two amorphous layers. The secondary electron image is sensitive to surface potential as well as topographical and compositional changes. However, by making measurements on the same position and varying the electrical bias, we can extract the influence of the surface potential. Among the parameters affecting the SEM, surface potential is the only one that is sensitive to the electrical bias [16][17].

As expected theoretically (section 2.5), the SEM signal is higher on the Cu/ITO/p^+ a-Si:H electrode than on the Cu/ITO/n^+ a-Si:H electrode. The SEM signal remains constant on the Cu/ITO/p^+ a-Si:H electrode with applied electrical bias because it is grounded. On the Cu/ITO/n^+ a-Si:H electrode, the SEM signal increases with increasing electrical bias and the contrast between the two contacts decreases, until it is reversed in forward electrical bias. This inversion of contrast is also visible when analyzing the profiles (Fig. 6.4.a). It was also reported by Heath *et al.* [13]. It can be noticed, that the contrast decrease is also visible on the amorphous layers. This means that an electric field is also present at the interface between the two highly doped amorphous silicon layers. Besides, the contrast increase in reverse electrical bias is also valid for topographical irregularities. Note that the scratched area overlaps between p and n-type a-Si:H. In this region, both materials have the same behavior with applied bias indicating that the doping effect has been masked by the defects introduced by nano-scratching. For instance, the contrast on the indented areas is much stronger at V_b =-1 V than at V_b=0.75 V. This suggests that SEM images under strong reverse electrical bias could also be used to reveal defects in the devices affecting the amorphous silicon layers. One example of defects is material remaining on the a-Si:H layers, such as ITO grains which locally bend the surface potential. For forward biases above 0.5 V, the changes in SE images are much less visible than for reverse electrical bias. We explain this phenomenon by a series resistance due to the contact between the electrodes and the contacts of the IBC solar cell. Indeed, in forward bias, the diode output current is high and the potential drop due to parasitic contact series resistance increases. The area where this potential drop occurs is not visible on Figure 6.2. Thus, the images in forward electrical bias are very similar. Other groups have reported measurements without saturation at high forward voltage [12], [13]. Therefore we suggest that if contacting on our setup was improved, series contact resistance due to probes would disappear and the local series resistance in the device could be detected.

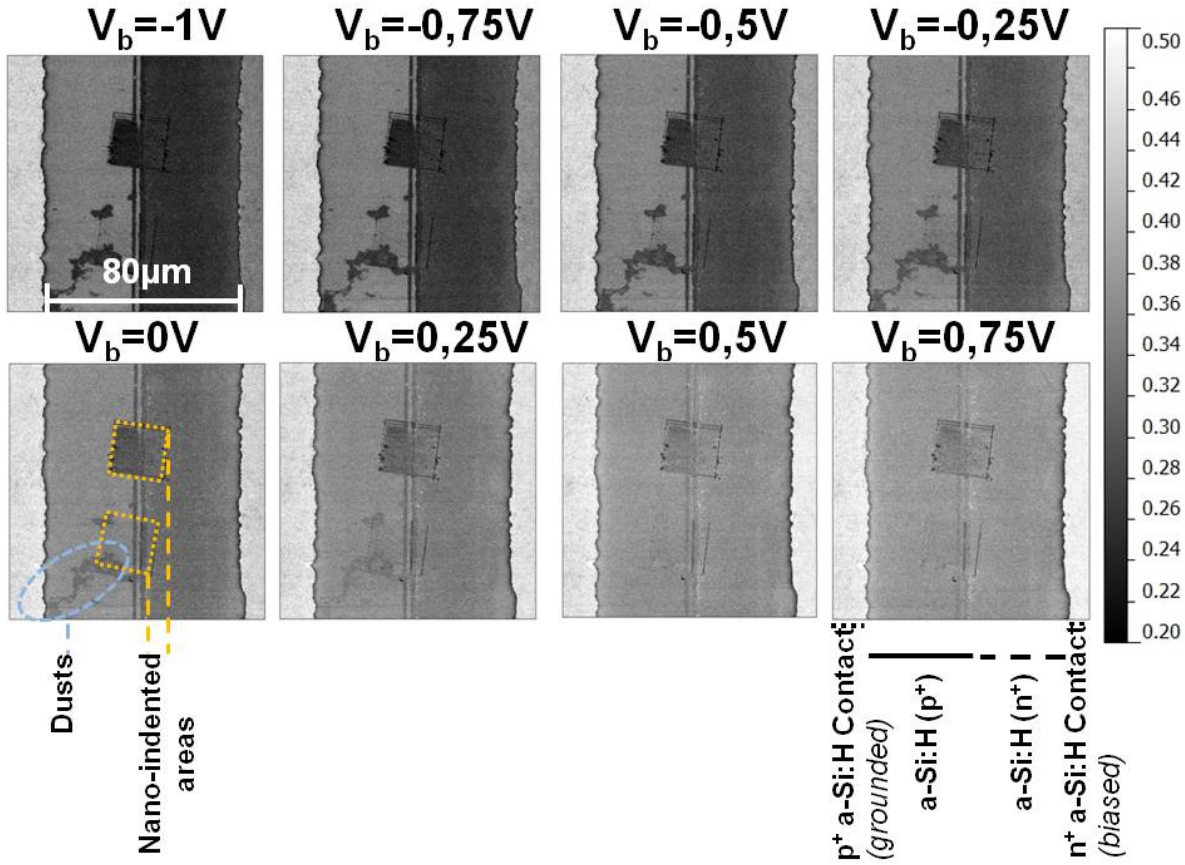

Fig. 6.2 – SEM images of the back surface of an IBC solar cell under different electrical bias, including the contacts.

Figure 6.3 shows KPFM images between the contacts of the IBC solar cell under different electrical biases. It was very challenging to acquire an image with both contacts and inter-contacts region because of the scan size which is limited to 90x90 μm^2 (section 3.7). Besides, the abruptness of the metallic contact risks degrading the KPFM tip during scanning. Therefore, we performed KPFM measurements between contacts first and on each contact later, and then we compared with the SEM ones. Measurements were carried out on a region adjacent to the SEM images (<5µm distance) in order to avoid the influence of local defects between areas of measurements or possible carbon contamination (section 4.3). The influence of AFM laser was minimized to an open circuit voltage of 20 mV, which is negligible compared to the electrical voltage steps applied (V_b =0.25 V).

KPFM measurements yield results in agreement with what is expected theoretically:

- Since the Cu/ITO/p^+ a-Si:H contact is grounded, the surface potential is not expected to change on this contact while varying the electrical bias. KPFM measurements performed on the Cu/ITO/p^+ a-Si:H contact confirmed the low sensitivity of the surface potential to applied electrical bias.
- When a forward bias is applied, the quasi Fermi levels split and the quasi Fermi level of electrons increases over the quasi Fermi level of holes by a value equal to the applied bias multiplied by the absolute charge of an electron. On the negative Cu/ITO/n^+ a-Si:H contact, the surface potential is the difference between the vacuum level and the quasi Fermi level of electrons because they are majority carriers. Therefore the surface potential on the Cu/ITO/n^+ a-Si:H contact decreases with forward bias by a value equal to the bias applied bias times the charge of the electron. Experimentally, KPFM measurements on the Cu/ITO/n^+ a-Si:H confirmed the expected sensitivity of surface potential to applied electrical bias.

- In Figure 6.1.a, one can identify three junctions in the interdigitated back contact solar cell: the a-Si:H (p^+)/a-Si:H (i)/c-Si (n) PIN diode, the a-Si:H (p^+)/a-Si:H (n^+) diode and the c-Si (n)/ a-Si:H (i)/ a-Si:H (n^+) PIN diode. These three junctions are oriented the same way, so the surface potential is expected to evolve in the same way as the Cu/ITO/n^+ a-Si:H contact with varying bias. The surface potential applied on the Cu/ITO/n^+ a-Si:H contact is supposed to be divided between these three junctions and is expected to decrease with increasing voltage bias, on the three junctions (as for the Cu/ITO/n^+ a-Si:H contact). In the following, we chose to plot the negative value of the surface potential measured by KPFM in order to have the same evolution as that of the SEM signal with electrical bias and to make comparisons easier.

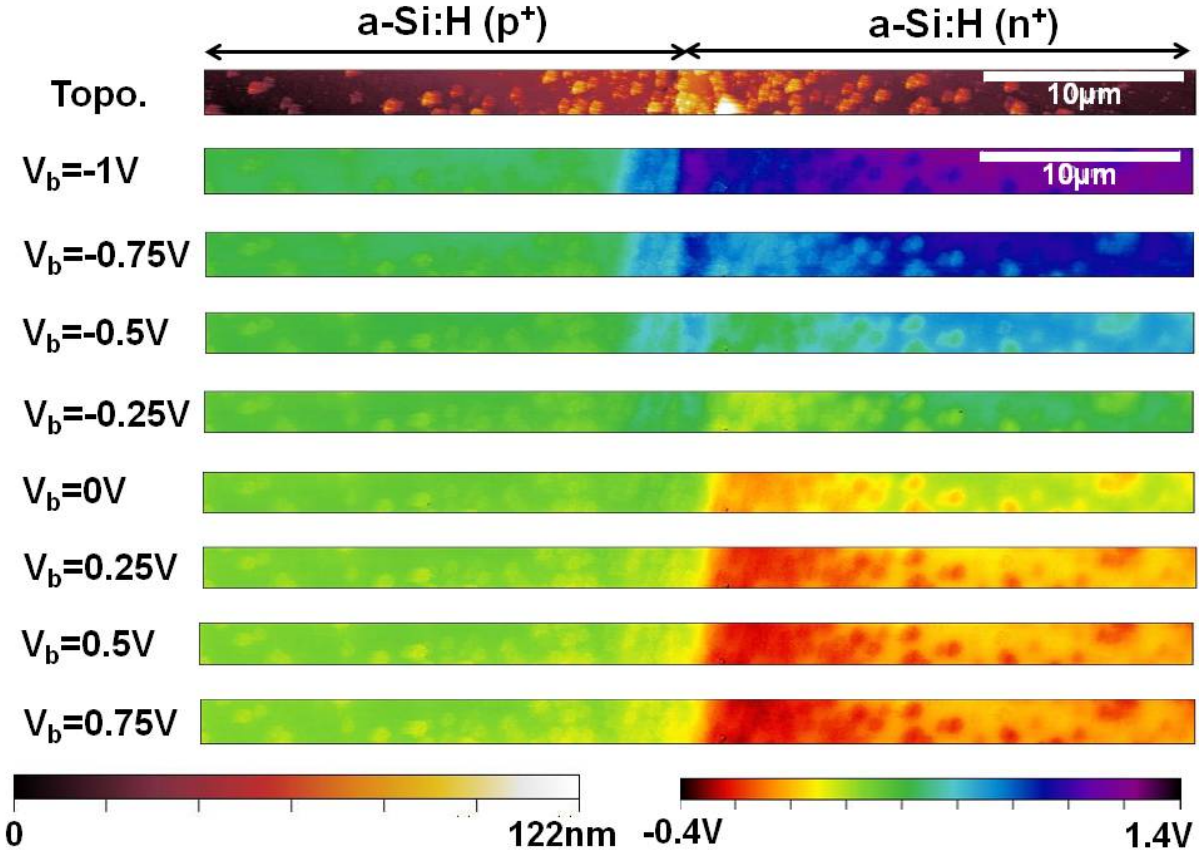

Fig. 6.3 – Topographical AFM image and KPFM surface potential images under different applied electrical biases between the contacts of an interdigitated back contact solar cell. The contacts are not included in this image.

Figure 6.4 shows the SEM and KPFM profiles under different values of electrical bias applied between the contacts of the IBC cell. The line profiles were obtained by averaging over 30 scan lines. We compare the SEM signal to the opposite of the surface potential signal so that both signals increase with increasing electrical bias, making comparisons easier.

As expected theoretically, both the SEM signal and the opposite of surface potential increase with electrical bias. On both profiles, the effect of the topographical bump of about 10 nm between the two amorphous layers can be seen and it is more prominent at reverse bias. The topographical artifact of this bump is more important for SEM than KPFM indicating that SEM signal is probably more sensitive to topography than KPFM. Besides, it can be noticed that the signal-to-noise ratio is better for KPFM than for SEM in our measurements (the white noise is visible on SEM profiles contrary to KPFM profiles). The behavior of p^+ and n^+ hydrogenated amorphous silicon layers is the same for both measurements. The noise on KPFM surface potential profiles (Fig 6.4.b) is associated to topographical artifacts due to nano-grains remaining from the process (Fig 6.4.c).The main

difference is that the alignment of signals on the n^+ and p^+ amorphous silicon layers does not occur at the same value of the electrical bias for SE and KPFM measurements. For SEM, it occurs around 0.25 V and for KPFM it happens around -0.25 V. The difference of alignment voltages is expected to give the value of the built-in voltage of the cell [12]. Therefore, the negative voltage V_b=-0.25 V given by KPFM does not seem to be accurate. We propose as a possible explanation the fact that there is an inversion layer below the p^+ a-Si:H layer which is particularly sensitive in reverse electrical bias [21]. Therefore, the interaction between the KPFM tip and the surface of the sample could change as a function of the electrical bias

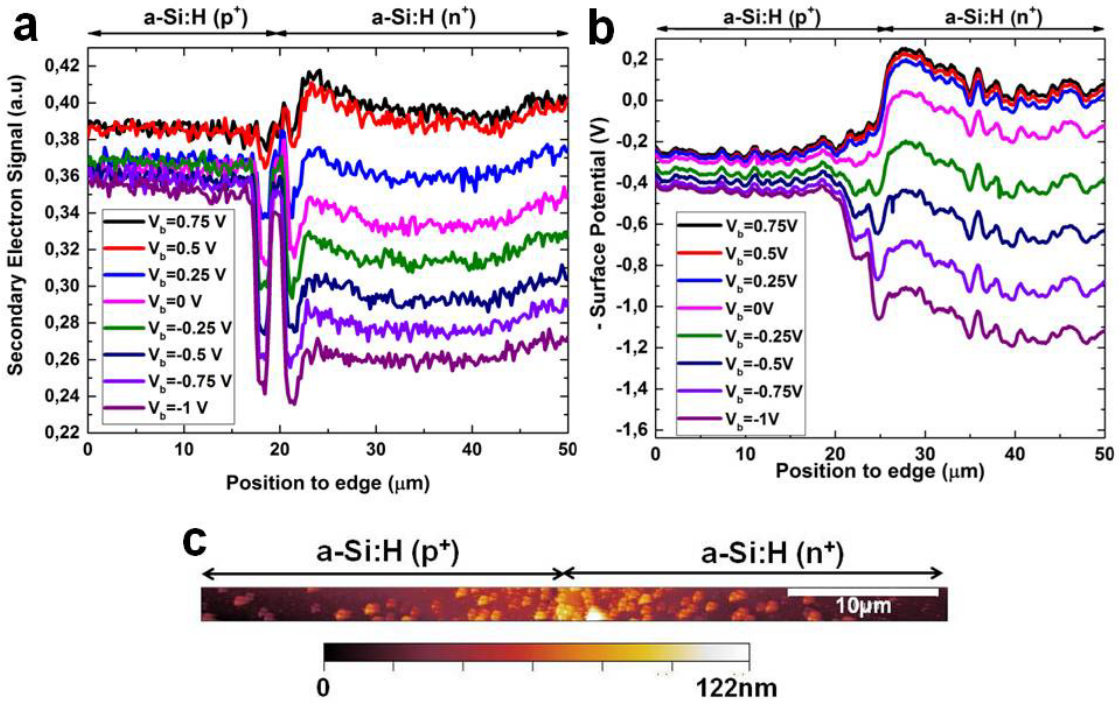

Fig. 6.4 – (a) SEM and (b) KPFM profiles between the contacts under different values of electrical bias. The KPFM signal displayed is the measured surface potential with changed sign, in order to have the same evolution as the SEM signal and make the comparison easier. (c) Topography image associated to the KPFM measurement. The observed nano-grains remain from the process.

In order to compare the sensitivity of SEM and KPFM measurements to electrical bias, we have studied its effect on the average signal from the four regions of the cell: the Cu/ITO/p^+ a-Si:H electrode, the Cu/ITO/n^+ a-Si:H electrode, the n^+ a-Si:H layer and the p^+ a-Si:H layer. We performed KPFM measurement on the contacts under bias, additionally to KPFM measurements between contacts. For SEM, we averaged the signal on the different areas of the cells for each value of the applied bias. Figure 6.5 shows the SEM and the KPFM curves obtained. Both measurements show linearity with applied electrical bias in the reverse bias mode, in good agreement with literature results [12], [13], [15]. The areas which are the closest to the biased electrode have the highest slopes. For KPFM, the slope on the Cu/ITO/n^+ a-Si:H electrode is equal to 1, which means that our measurements are quantitatively correct: if we apply an electrical bias of -1 V for instance, the surface potential drop equals to -1 V. For both measurements, saturation happens quickly in forward bias because of a high series resistance due to non-ideal contacting on both systems. This explanation is confirmed by J(V) curves on each setup, compared to that performed on a regular probe station under a solar simulator. The saturation occurs for lower voltages in KPFM than in SEM, which is consistent with the higher series resistance on the J(V) curve of KPFM setup compared to the SEM setup.

On the Cu/ITO/p^+ a-Si:H electrode, a difference between measurements can be noticed. Contrary to KPFM signal, SEM signal seems to be dependent on the applied electrical bias (Figure 6.5.a). We explain this phenomenon by the fact that a series resistance could be present between the voltage source and the Cu/ITO/p^+ a-Si:H electrode in SEM setup and not in KPFM setup. The reason is that the electrode contacting the Cu/ITO/p^+ a-Si:H electrode in the KPFM setup, is directly grounded because it is connected to the AFM plate which is grounded. By minimizing the distance between the contact and the ground, the series resistance between the Cu/ITO/p^+ a-Si:H electrode and the voltage source on the KPFM setup is expected to be much smaller than on the SEM setup.

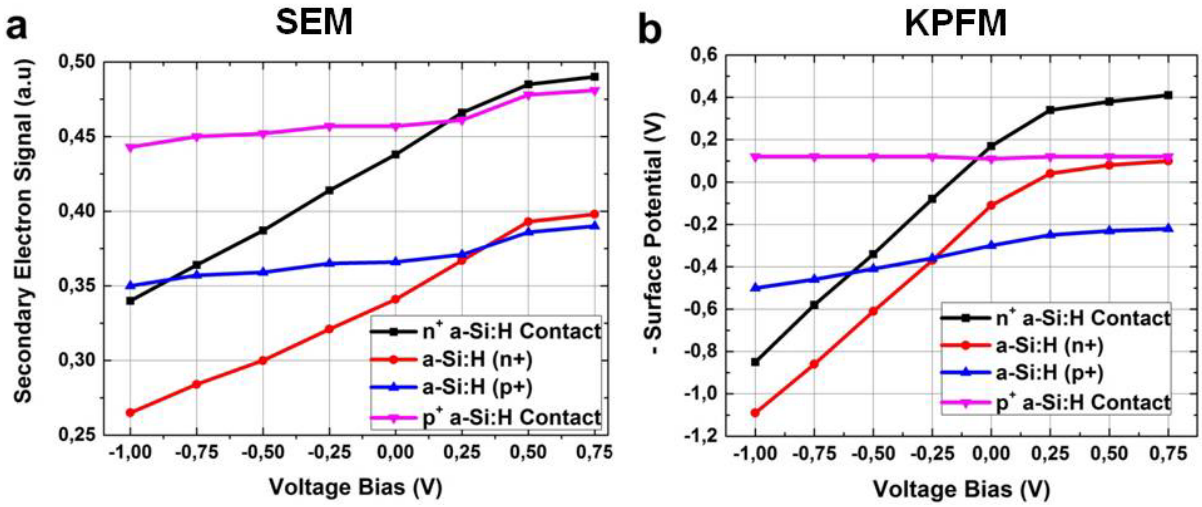

Fig. 6.5 – Average values of a) SEM and b) KPFM signals as functions of the applied voltage for the four different regions of the IBC solar cell. The displayed KPFM signal is the measured surface potential with changed sign, in order to have the same evolution as the SEM signal and make the comparison easier.

These measurements show a good agreement between SEM and KPFM techniques on IBC solar cells. Limitations due to series resistance in experimental setups and KPFM tip-induced band bending artifacts (section 3.2.3) due to the inversion layer in reverse bias are also presented. Despite these limitations, SEM and KPFM prove to be complementary techniques to investigate solar cells under electrical bias. The following study shows similar measurements performed on the cross-section of epitaxial silicon solar cells.

- ***Epitaxial silicon solar cell***

The measurements performed on epitaxial silicon solar cells under constant electrical bias have been published in a conference paper [22] and provide preliminary results for a peer-reviewed journal paper [23]. Figure 6.6 shows measurements performed on the top surface of a nanostructured epitaxial silicon solar cell under electrical bias. The reason of the nanostructuration is to increase the light path in the solar cell in order to maximize the absorption for a given thickness. The setup used is shown in Figure 6.6.a. The solar cell is grounded from the back side. Figure 6.6.b shows the topography image and the surface potential image for three different applied voltage biases: V_b =-0.3 V, V_b =0 V and V_b =0.3 V. The spatially average surface potential (SP) measured for these voltages are respectively SP=-0.33 V, SP=-0.64 V and SP=-0.94 V. Therefore, surface potential differences are equal to the applied biases differences. Quantitative voltage drops can be measured using this technique, which can be used for contact investigation at the nano-scale. When the ground is applied on the front surface, the surface potential is no longer sensitive to the applied electrical bias, as expected.

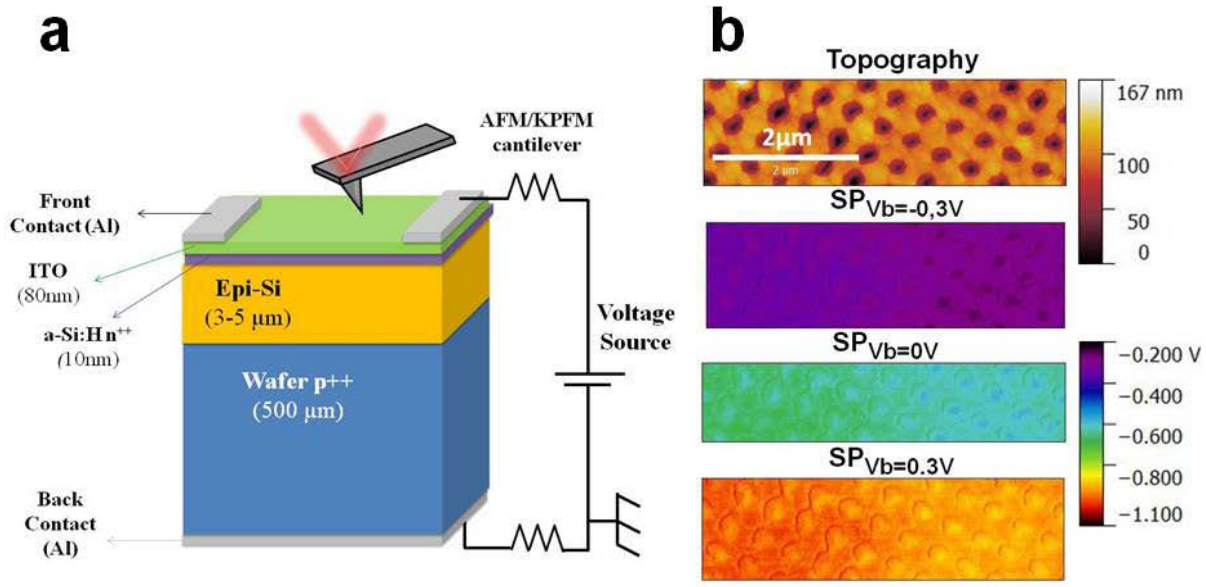

Fig. 6.6 – a) Setup used to investigate the top surface of nanostructured epitaxial silicon solar cell under electrical bias with KPFM. b) Topographical AFM image and KPFM surface potential images under three voltage biases: V_b=-0.3V, V_b=0V and V_b=0.3V.

Figure 6.7 shows SEM images of the cross-section of an epitaxial silicon solar cell under two applied electrical biases V_b=-0.4 V and V_b=-0.3 V. The p-type wafer appears brighter than the non-intentionally n-doped epitaxial silicon layer, because p-type region has a lower affinity since the Fermi levels equilibrate at the junction, as has been explained by Dapor *et al.* [24]. When applying a reverse electrical bias, the electric field in the space charge region is increased, therefore the SEM contrast increases on the PN junction. It has been shown by several groups that the SEM contrast evolves linearly with the applied electrical bias [12], [13], [15] and that the SEM image enables to determine the position of the PN junction and provides a good estimation of the space charge region. This phenomenon is confirmed with our measurements on the epitaxial silicon solar cells. The contrast drop is sharp at the epi-Si/c-Si wafer interface, suggesting either that the epitaxial silicon layer is probably n-doped leading to a PN^-N junction, instead of a PIN junction as expected; or that the defective interface has strong electrical influence. The epi-Si/a-Si:H (n^{++}) interface is not visible on this image. Two explanations can be given. The first explanation is that the amorphous layer is so thin that it was removed on the edge, when cleaving. The second explanation is that since the epi-Si layer is non-intentionally n doped, the electric field at the epi-Si (n)/a-Si:H (n^{++}) and therefore, the surface potential drop is too small and below the thermal noise level. Therefore, it cannot be detected by SEM.

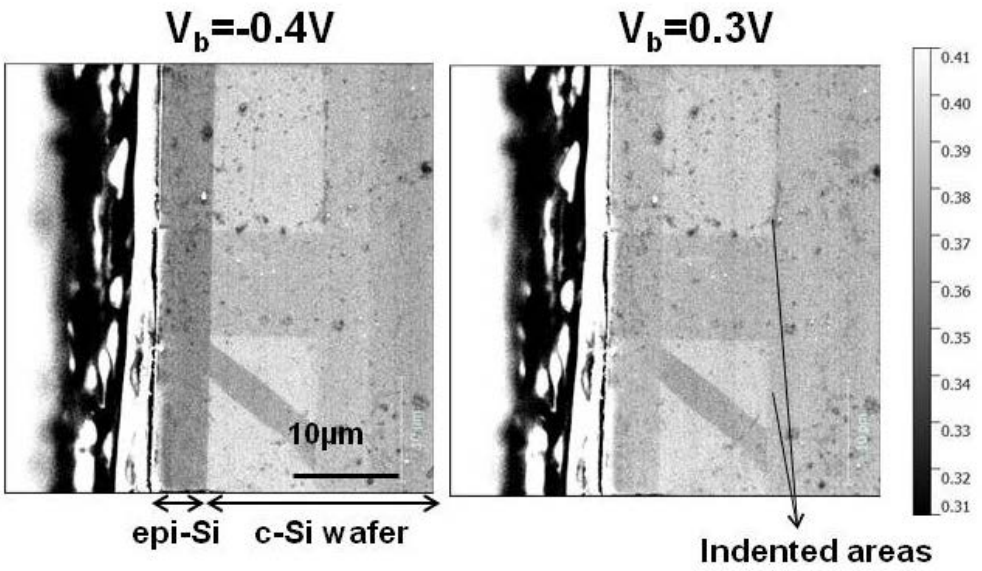

Fig. 6.7 – SEM images under different electrical bias of the cross-section of an epitaxial silicon solar cell.

Figure 6.8 which shows the KPFM image obtained on the cross-section of the epitaxial silicon solar cell under different electrical biases. The measurements are in agreement with what is expected theoretically:

When an electrical bias is applied to the solar cell, the quasi-Fermi levels of holes and electrons split. This affects the surface potential profile. The evolution of the surface potential along the PIN junction is expected to change as follows:

- On the p^{++} doped crystalline silicon wafer, the surface potential remains unchanged under electrical bias because the wafer is highly doped and grounded. The quasi-Fermi levels of electrons and holes remain constant.
- On the n^{++} a-Si:H layer, the surface potential is defined by the difference between the vacuum level and the quasi Fermi level of electrons because electrons are majority carriers in this layer. The vacuum level remains constant when changing the electrical bias. When increasing the voltage bias, the quasi-Fermi level of electrons in the n^{++} a-Si:H layer increases over the quasi-Fermi level of holes in the p^{++} c-Si wafer by a value equel to the bias applied. Therefore, the surface potential in the n^{++} a-Si:H layer is expected to decrease by this value when increasing voltage bias.
- On the intrinsic epitaxial layer, when applying a positive electrical bias, the surface potential decreases by a value going progressively from 0V (close to the p^{++} doped crystalline silicon wafer) to the applied bias value (close to the n^{++} a-Si:H layer).

We also performed measurements where the n^{++} a-Si:H was grounded and the bias was applied on the p^{++} doped crystalline silicon wafer. In this case, the surface potential on the n^{++} a-Si:H layer was not sensitive to applied electrical bias. The surface potential of the p^{++} doped crystalline silicon wafer was sensitive to electrical bias and changing by values equal to the applied bias.

As for SEM images, it can be seen that surface potential profiles decrease strongly at the c-Si/epi-Si interface confirming that the electric field is confined at the interface due to non intentional n-type doping or to a defective interface. The second surface potential drop at epi-Si/n^{++} a-Si:H is not visible on the images, as for SEM images. The contrast we observe on the edge is here due to a change of topography, as can be seen on the topographical image.

As for interdigitated back contact solar cells, the alignment of signals does not happen at the same voltage bias value. For SEM it happens at voltage bias superior to 0.3V and for KPFM it happens around 0V. In this case, we consider two hypothesis to explain this difference. The first

hypothesis is that KPFM tip-induced band bending was not the same on the p^{++} c-Si wafer and on the epi-Si layer. The second hypothesis is that the SEM was performed on a µ-cleaved solar cell and the KPFM was performed on a mechanically polished solar cell. Therefore, the electrical properties were more degraded in the case of the KPFM measurements that in the case of SEM measurements.

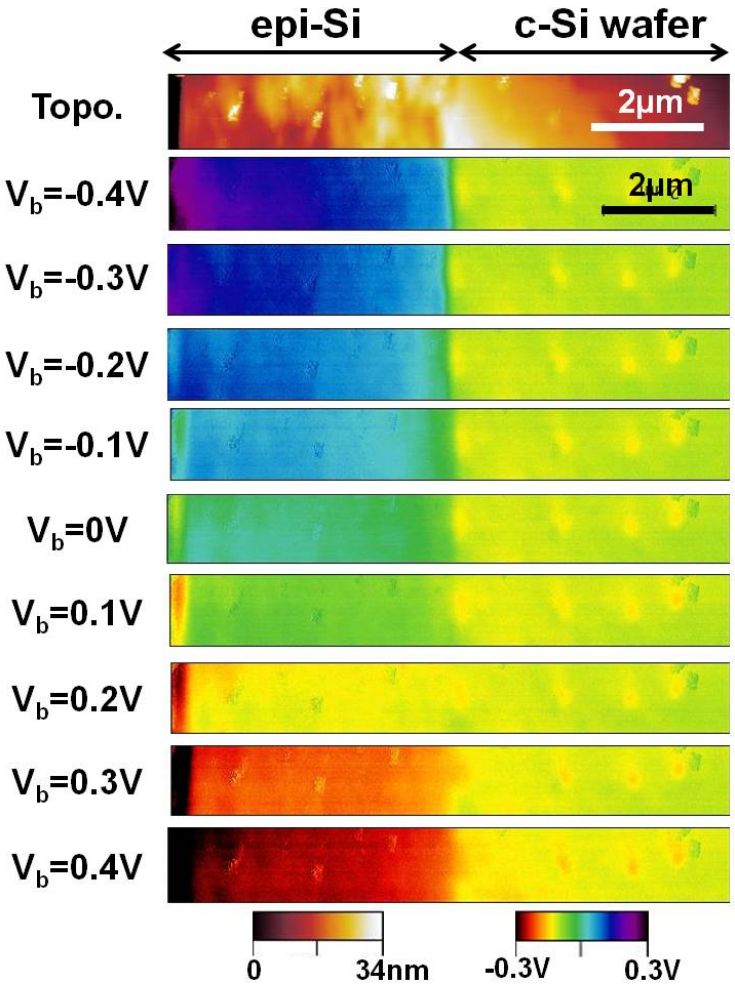

Fig. 6.8 –Topographical AFM image and KPFM surface potential images under different electrical biases between the contacts of an epitaxial silicon solar cell.

Figure 6.9.a shows the surface potential profiles on the cross-section of epitaxial silicon solar cells under different electrical biases. To reduce the noise in the surface potential profiles, we obtained a profile by averaging on 60 consecutive horizontal scan lines, as discussed in section 3.6.

The profiles show that the tendency with increasing voltage bias is the same as the one explained above. On the edge of the cross-section, the steps between surface potentials are constant as the applied voltage bias is changed also by a constant value. Figure 6.9.b shows the surface potential averaged on different areas of the cross-section with respect to applied electrical bias. On the edge of the epitaxial silicon layer (pink curve), the dependence is almost linear. There is a slight difference of slope between forward and reverse voltage biases associated to a shunt resistance effect in the reverse voltage bias because the slope is smaller in this range of voltages. Besides, it can be observed that the slopes are smaller than 1. This means that the surface potential differences are not equal to the applied biases, contrary to the case of the interdigitated back contact solar cell in reverse bias, investigated previously (Figure 6.5). This phenomenon was also reported by Jiang *et al.* [6], [11]. They attributed it to two possible phenomena. First, voltage losses on the conduction path from AFM tip to the ground

of KPFM electronics. In our case, it could be due to series resistances effects in the ITO layer for instance. Moczala *et al.* also used this explanation for too small surface potential drops [8]. Second, stray capacitances due to the cantilever or other regions of the tip rather than the tip apex can lead to reduction of surface potential drops (section 3.5). We also add that surface band bending effects (i.e Surface Fermi level pinning) could also affect the value of measured surface potential changes (section 3.8).

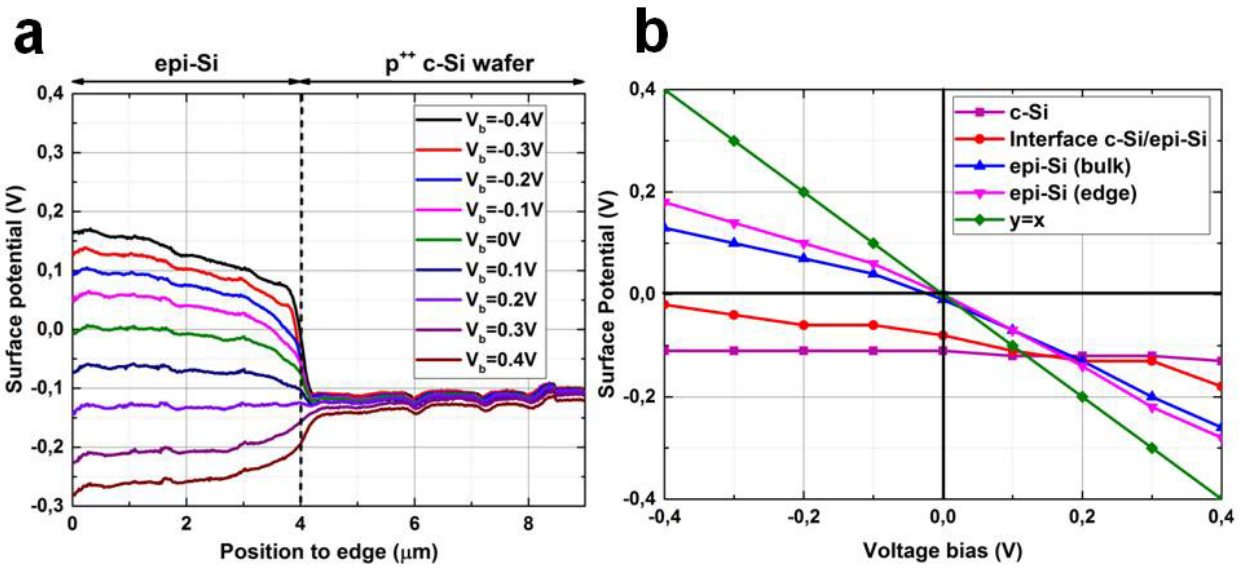

Fig. 6.9 – a) Surface potential profiles across the PIN junction of the epitaxial silicon solar cell under different electrical biases. b) Average values of KPFM signals as a function of the applied voltage for the four different regions of the epitaxial silicon solar cell.

At the interface between the p^{++} c-Si wafer and the epi-Si layer, the surface potential shape associated to diode effect can be clearly distinguished. We will explain in the following sub-section how we extract electric field changes from these surface potential profiles. The decrease of the surface potential on the wafer for positive surface potential values superior to 0.3V can be explained by a series resistance in the wafer that appears for high current values. The ability to monitor resistance effects is an advantage of KPFM compared to SEM and EBIC which are only sensitive to diode effect (section 4.4). KPFM proves to be a powerful tool to investigate diode and resistance effects at the nano-scale. Thereby, it could help detect local power losses in solar cell devices. Besides, obtaining nano-scale resistance and diode can help improve solar cells modelling by giving additional inputs in the models.

Finally, we performed Resiscope measurements on the cross-section of the epitaxial silicon solar cell under electrical bias. Figure 6.10.a shows the setup used to perform this measurement. Figure 6.10.b shows the profiles of resistance obtained. As expected, the resistance remains constant in the c-Si wafer because it is grounded. In the epitaxial silicon layer, the resistance decreases when the electrical bias increases because the current highly increases in forward voltage bias.

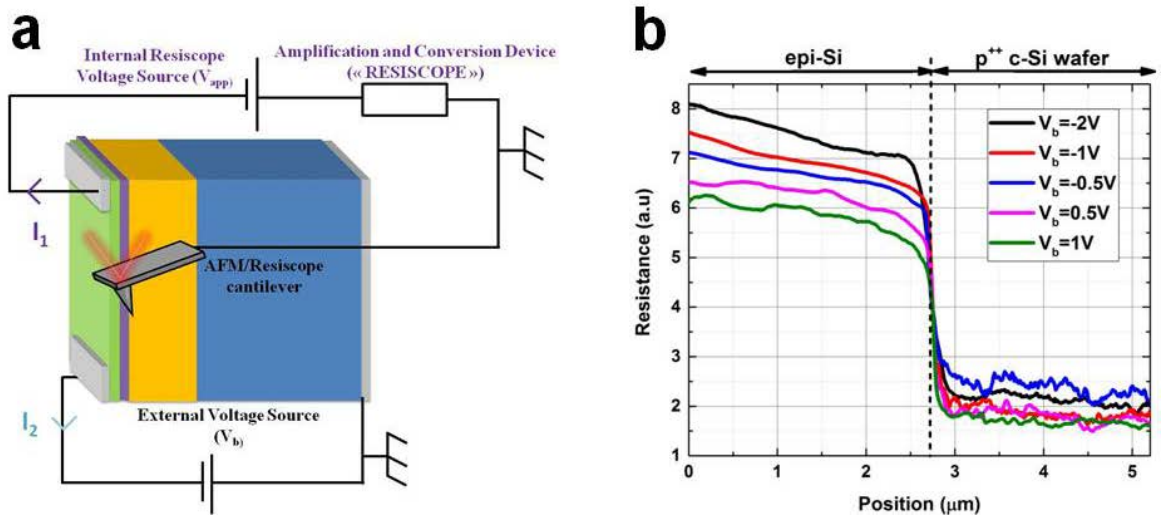

Fig. 6.10 – a) Resiscope setup to investigate the cross-section of the epitaxial silicon solar under different electrical biases. b) Resistance profiles across the PIN junction of the epitaxial silicon solar cell under different electrical biases.

However, Resiscope is a complex technique to investigate solar cell devices under electrical bias because two parallel electrical circuits, each with a voltage source, have to be considered, as can be seen in Figure 6.10. This makes accurate interpretations challenging. Besides, the fact that Resiscope is very intrusive makes measurements on the same area complex (section 3.2 & 3.3).

On the other hand, KPFM proves to be a powerful tool to investigate solar cell devices under electrical bias. It is a low intrusiveness technique. The surface potential can be directly compared with the applied bias value, to check the measurements accuracy and the effect of potential artifacts. It enables to see both diode and resistance effects to investigate power losses and to be used as inputs in simulation models. However, KPFM can be limited by its acquisition time and its limited scan size (section 3.7). Besides, artifacts such as stray capacitances (section 3.5) and tip-induced band bending (section 3.2.3) can alter interpretations.

Therefore, we propose that KPFM can be complemented with SEM under applied electrical bias. SEM provides fast acquisition on a large scale and does not suffer KPFM artifacts but faces challenges due to a surface modification under the electron beam exposure, mostly attributed to carbon contamination (section 4.3). Therefore, these complementary techniques could be combined in a single setup that would benefit from the advantages of both. This seems possible, given the fact that some manufacturers already provide combinations of SEM and AFM. A measurement protocol can be proposed as follows. SEM could perform quick, low magnification surface potential images under an electrical bias. Once a defective area is located with SEM, KPFM could take over and analyze more precisely and quantitatively the importance of this defect, without risking to degrade the area. KPFM measurements can be carried out both under electrical bias and illumination. Many benefits would come from the association of these techniques: accurate repositioning for KPFM would be easier inside an SEM setup, the evolution of the tip could be monitored by SEM and the intrusiveness of SEM could be mitigated thanks to the capabilities of KPFM. Additionally, an effective and reliable probing system could also be added to prevent from series resistances due to the setup. The combinaison of the two techniques could be a powerful tool to investigate power losses at the nano-scale in different areas of devices, such as PN junctions or contacts.

6.1.2 Electric field investigation

6.1.2.1 Context

Using surface potential measurements under electrical bias on the cross-section of solar cells, Jiang *et al.* have proposed a technique to extract the change of electric field induced by the bias [6], [10], [11], [25]. To minimize the surface effect, Jiang *et al.* propose to work on the difference of surface potentials [11]. The idea is to subtract parasitic surface effect (section 3.8) when subtracting surface potential profiles. Therefore, the influence of parasitic surface effect becomes negligible in the difference signal, if we consider the Fermi level pinning value is the same for every applied bias. Jiang *et al.* perform the difference between V_{bias} and V=0V. They observed that doing so; the profiles were smoother and symmetric to the positive and negative bias. Then, since the electric field is the first derivative of the built-in potential, Jiang *et al.* performed a first derivative of the surface potential difference profiles to access the electric field changes. However, since profiles were still very noisy, a denoising step is necessary to enable to access electric field. Therefore the surface potential difference profile was first fitted with a 20 order polynomial [11]. Then, the first derivative was performed on the fitted curve.

Using this technique, Jiang *et al.* have investigated electric field changes in hydrogenated amorphous silicon solar cells [6], [11], multi-crystalline silicon solar cells [10], [25] and III-V solar cells [6]. This technique does not allow to directly measure the value of the "intrinsic depletion" width but only the change of electric field under an electrical bias. However, they have shown that, despite certain artifacts, these measurements enabled to determine the location of the PN junction for a given bias value [6], [11], to assess the space charge region width [6] and to obtain qualitative doping information at nano-scale, such as non-intentional doping in intrinsic layers of amorphous silicon solar cells [11]. Despite some discrepancies of KPFM measurement with respect to capacitance voltage (C-V) measurements, attributed to stray capacitances (section 3.5), the KPFM measurements evolution with applied bias was consistent with C-V measurements, confirming that KPFM under electrical bias is a good tool to locate the PN junction [6]. This is a strong advantage compared to electron beam induced current (EBIC) technique which can detect wide depletion regions but faces challenges to determine the exact position of p/n interface [14], [26].

6.1.2.2 Our approach

In this study, we investigated the cross-section of epitaxial silicon under electrical bias using KPFM as shown in section 6.1.1. The results of electric field assessment in epitaxial silicon solar cells have been published in a conference paper [22]. Epitaxial silicon solar cells are made of a PIN junction with the epitaxial layer being intrinsic and non-intentionally doped (section 2.6.3). However, impurities are incorporated at the interfaces and in the epitaxial layer during the low-temperature plasma enhanced chemical vapor deposition (PECVD), inducing non-intentional doping as discussed previously and confirmed by Cariou *et. al.* [27], [28]. Figure 6.11 shows a secondary ion mass spectrometry (SIMS) profile of the epitaxial silicon sample on a c-Si substrate. It can be observed that even though the epitaxial layer is non- intentionally doped, there is an incorporation of oxygen inside the epitaxial silicon layer which can make it lightly n type. Besides, SIMS profiles also show that the interface between epitaxial silicon layer and crystalline silicon wafer is particularly defective with a sharp increase of carbon, hydrogen and oxygen atoms. The presence of this defective interface, followed by an improvement of the epitaxy quality when the epi layer gets thicker, has been confirmed by micro-Raman spectroscopy and in-situ ellipsometry [27], [28].

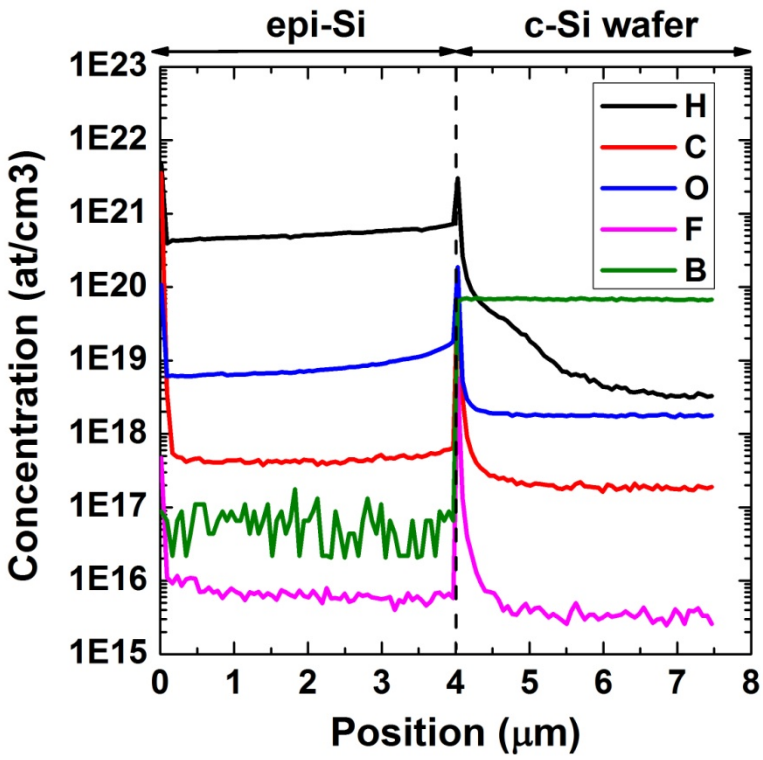

Fig. 6.11 – SIMS profile of 4μm epi-Si layer on a c-Si wafer

Because of the defective interface and the non-intentional n-doping of the epitaxial layer, the epitaxial silicon solar cell is no longer a PIN junction, but rather a PN^-N junction, as previously discussed. The consequence is that instead of having a constant electric field along the epitaxial layer, the electric field is highly concentrated at the interface between the wafer and the epitaxial layer. Therefore, the higher the electric field concentration, the higher the unintentional n doping inside the epitaxial layer. This kind of investigation was also carried out in amorphous silicon solar cells by Jiang *et al.* [11]. There is no reason why the unintentional doping should be homogeneous in the epitaxial silicon solar cell. Therefore, we propose that this technique could be used to investigate the electric field homogeneity along the PIN junction.

However, our approach slightly differs from that of Jiang *et al.* in the measurement procedure [22]. Instead of subtracting surface potentials at V_{bias} and 0V, we chose to subtract surface potentials at V_{bias} and 0.45V. The reason is that 0.45V is the maximum voltage value the epitaxial silicon solar cell can reach without risking to be degraded irreversibly. By choosing this minimum value, we can reach a maximum voltage amplitude when using V_{bias}=-0.45 V. With the highest amplitude possible, the signal-to-noise ratio is maximal and it is easier to compare electric field changes along the PIN junction.

Figure 6.12 shows the different data processing steps used to extract the electric field. After subtracting surface potential profiles at V_{bias}=-0.45 V and V_{bias}=0.45 V, the profile is denoised by removing high frequency noises. The third image shows the surface potential denoised and the noise removed from the profile. It can be seen that the noise removed is constant almost on all the profile. Finally, the first derivative profile of the denoised surface potential is extracted, leading the electric field change of interest.

If the epitaxial layer was perfectly intrinsic, both electric field at V_{bias}=-0.45 V and V_{bias}=0.45 V should extend all along the epitaxial layer. Therefore the difference of electric field should also extend along the epitaxial layer. However, if the epitaxial layer is n-doped, the electric fields will concentrate at the interface between the epitaxial silicon layer and the crystalline silicon wafer. Therefore the difference of electric fields will also be concentrated at the interface. The higher

the doping level of the epitaxial silicon layer, the smaller the space charge region and the smaller the electric field extension for V_{bias}=-0.45 V and V_{bias}=0.45 V, and therefore the smaller the extension of the difference of electric fields between V_{bias}=-0.45 V and V_{bias}=0.45 V. That is why we propose this technique to investigate the homogeneity of unintentional doping in intrinsic layers.

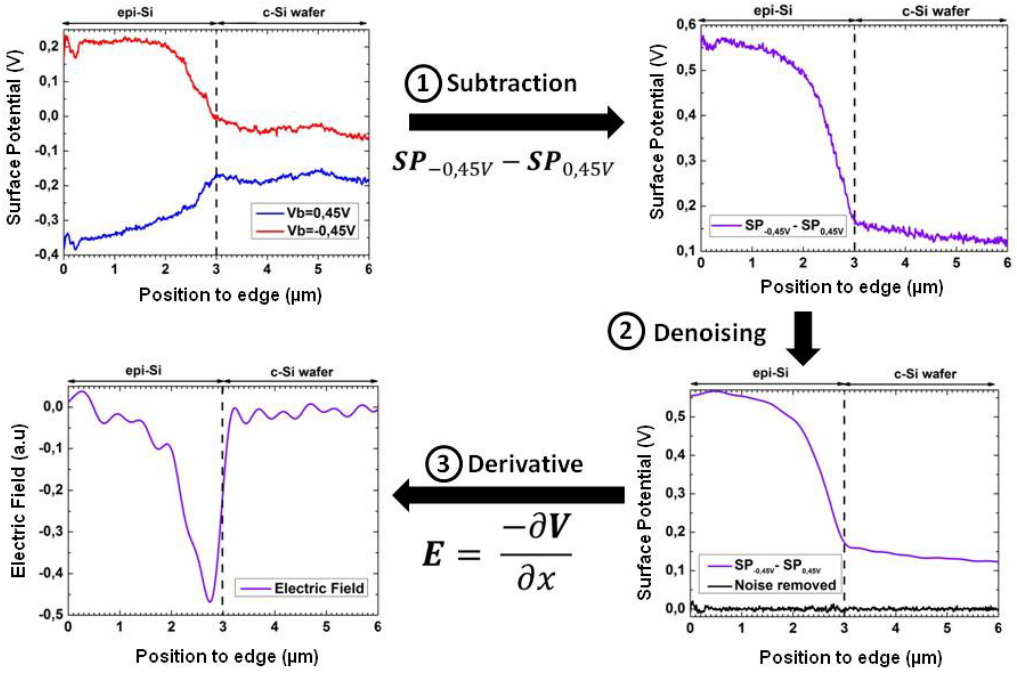

Fig. 6.12 – Data processing steps used to extract the profiles of electric field changes from surface potential profiles

6.1.2.3 Results

Figure 6.13 shows the electric field changes profile obtained by subtracting surface potentials (SP): SP(V_{bias})-SP(0 V), as used by Jiang *et al.* (Fig.6.13.a), and by subtracting SP(V_{bias})-SP(0.45 V), as we propose in our approach (Fig.6.13.b). Profiles are obtained for different applied electrical biases.

It can be observed that the profile associated to SP(0.5 V)-SP(0.45 V) has the highest amplitude and lowest signal-to-noise ratio, enabling more accurate comparisons between peaks at different locations. In the case of profiles associated to SP(V_{bias})-SP(0 V), the signal-to-noise ratio is too low for all the voltages applied. In the case of Jiang *et al.*, bias between -1 V and +1 V could be applied on hydrogenated amorphous silicon solar cells. Therefore, high signal-to-noise ratio could be obtained, even with SP(V_{bias})-SP(0 V) [11].

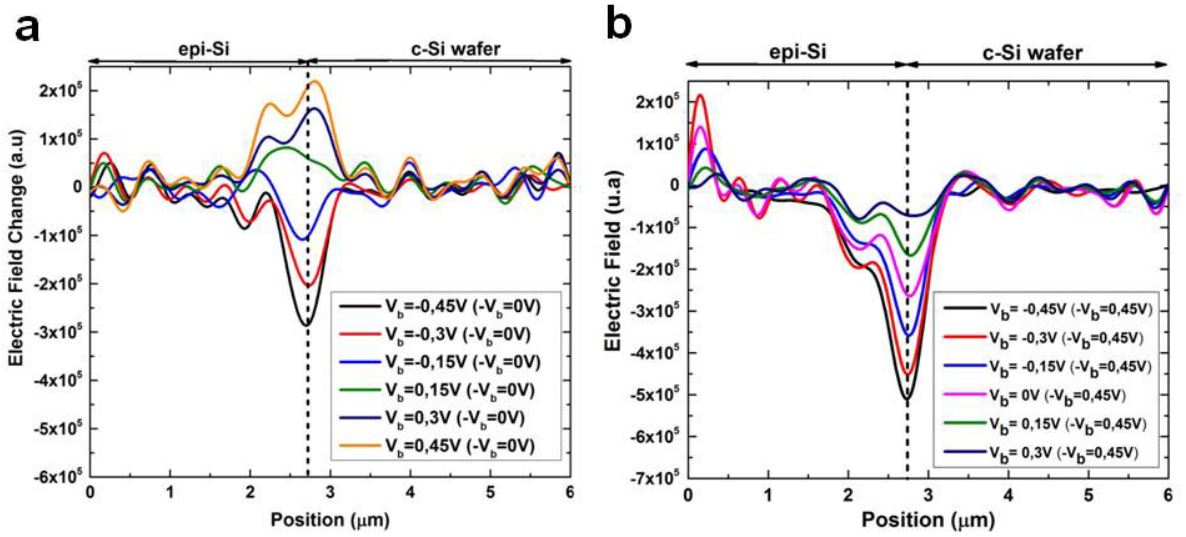

Fig. 6.13 – Electric field change profiles obtained by using the surface potential difference: a) SP(V_{bias})-SP(0V) and b) SP(V_{bias})-SP(0.45V)

Figure 6.14 shows the electric field obtained using this method on three different zones at the p^{++} c-Si/epi-Si interface. It can be seen that for three different profiles the electric field peak is centred at the interface between the c-Si wafer and the epitaxial layer. Besides it does not extend deeply inside the epitaxial layer, which provides a strong indication that the epitaxial film is probably lightly n-doped. Moreover, the shape of the profiles is different. In scan area 2 and 3, the peak is asymmetric, low amplitude and broad whereas in scan area 1, the peak in more symmetric, higher and narrower. These measurements show the impact of the non-intentional doping of the epitaxial silicon layer and/or of defective interface layer. Besides these measurements suggest that both non-intentional doping and defective interface may be inhomogeneous along the PIN interface of the epitaxial silicon solar cell.

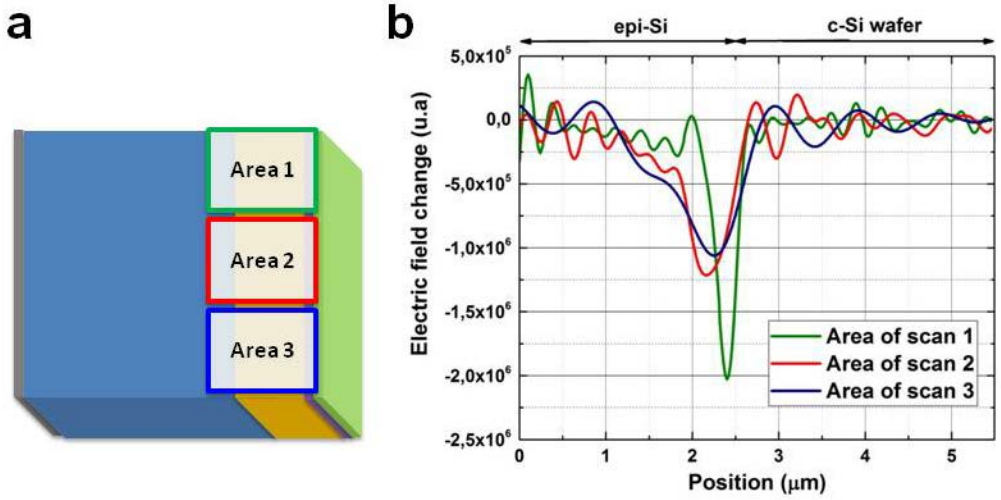

Fig. 6.14 – a) Three positions investigated along the PIN junction of the epitaxial silicon solar cell. b) Electric field changes obtained after data processing the electric field along the PIN junction.

As a perspective work, this study should be continued by comparing the measurements with other nano-scale doping measurement techniques. On our devices, EBIC measurements proved to be challenging but quantitative CP-AFM measurements (Section 5.2) could be performed on different areas of the cross-section. Since CP-AFM is highly intrusive and would require short circuiting the solar cell device with silver paste, KPFM measurements should be performed first. Spatially resolved

SIMS could also help investigate the homogeneity of the material in the epitaxial silicon solar cell. Another perspective work is to perform the same measurements with KPFM under UHV. This would help reduce the stray capacitances and surface band bending which may affect the accuracy of measurements.

6.1.3 Measurements under modulated frequency electrical bias

6.1.3.1 Context

We have shown in Section 5.3 that it was possible to measure lifetimes over 1ms with KPFM by monitoring the surface potential decay when switching the electrical bias. This technique enables to assess lifetime with a nano-scale resolution, which is challenging with standard lifetime measurement techniques.

In this section, we will discuss a technique to measure lifetimes well below 1ms using KPFM and a modulated frequency excitation source. The core of this technique is that even though KPFM does not have a nanosecond time resolution, we can measure lifetimes in the nano-second range by using a modulated frequency excitation source with a nanosecond time period. In this technique, we take advantage of the time averaging possibilities of KPFM (section 4.6). That way, we obtain a higher time resolution than the KPFM feedback time constant can provide.

Previous works have shown that the use of modulated frequency illumination enables to assess the minority carrier lifetime τ of solar cells at nano-scale using Kelvin Probe Force Microscopy [29]–[31]. Since KPFM is a slow measuring technique, it acts as a low-pass filter and measures a time averaged surface photovoltage (V_{av}). V_{av} is dependent on the frequency of modulation of light and this dependence is directly linked to τ. Hence, using τ as a fitting parameter in the curve of V_{av} versus frequency, the minority carrier lifetime can be determined.

Lifetime measurements on different technologies of solar cells have been performed. Takihara *et al.* have performed lifetime measurements on different grain areas of polycrystalline silicon solar cells [29]. They also performed similar measurements on grain boundaries of $Cu(In,Ga)Se_2$ solar cells [32]. Borowik *et al.* have performed lifetime measurements on silicon nanocrystal solar cells and have shown a very good agreement with x-ray photoelectron spectroscopy [30]. Shao *et al.* have performed lifetime measurements on local ITO defects in organic solar cells and show a good agreement with transient photovoltage measurements (TPV) [31]. Schumacher *et al.* have proposed an improvement of the technique reducing the uncertainty of surface photo-voltage measurement and reducing the tip-sample capacitive changes, making the technique more accurate and reproducible [33]. In a following publication, they have proved that KPFM measurements could be sensitive to decay times as low as 1ps [34] opening a wide window of dynamic measurements at the nano-scale.

6.1.3.2 Our approach

In our approach, we chose to use modulated frequency electrical bias, instead of modulated frequency illumination. These results have been published in a peer-reviewed journal [23]. The advantage of this technique is that modulated frequency voltage bias enables a higher range of signal, avoids light induced degradation and is less expensive than a modulated illumination solution. The principle of this measurement is very similar to that under illumination. In forward bias, there is an excess of minority carriers at the junction [35] as it is the case under illumination [30]. In reverse bias, there is a lack of minority carriers at the junction, as it is the case in the dark.

The time to go from forward to reverse bias (reverse recovery time) is higher than the time to go from reverse to forward voltage bias (forward recovery time). The reason is that the recombination of the excess minority carriers is much slower than the injection of minority carriers [36]. Since minority carrier lifetime is directly linked to the recombination velocity, the reverse and forward

recovery time is closely linked to τ [35]–[38]. Using the averaging possibility of KPFM, we propose that KPFM under modulated frequency voltage bias can also be used to assess minority carrier lifetime at the nano-scale.

Figure 6.15.a shows the setup used to perform measurements under modulated frequency electrical bias on the cross-section of epitaxial silicon solar cells. The epitaxial silicon solar cell is µ-cleaved and measurements are performed under controlled nitrogen atmosphere. The setup is the same as the one used for measurements under constant bias (Figure 6.1.a) but the constant voltage source is replaced with a modulated frequency voltage source. Figure 6.15.b shows the shape of the modulated electrical bias applied to the epitaxial silicon solar cell. It is a square wave centered on 0 V with an amplitude of 0.6 V and a duty cycle of 50 %. The frequency is varied between 50 kHz and 50 MHz, corresponding to time periods between 20 µs and 20 ns respectively.

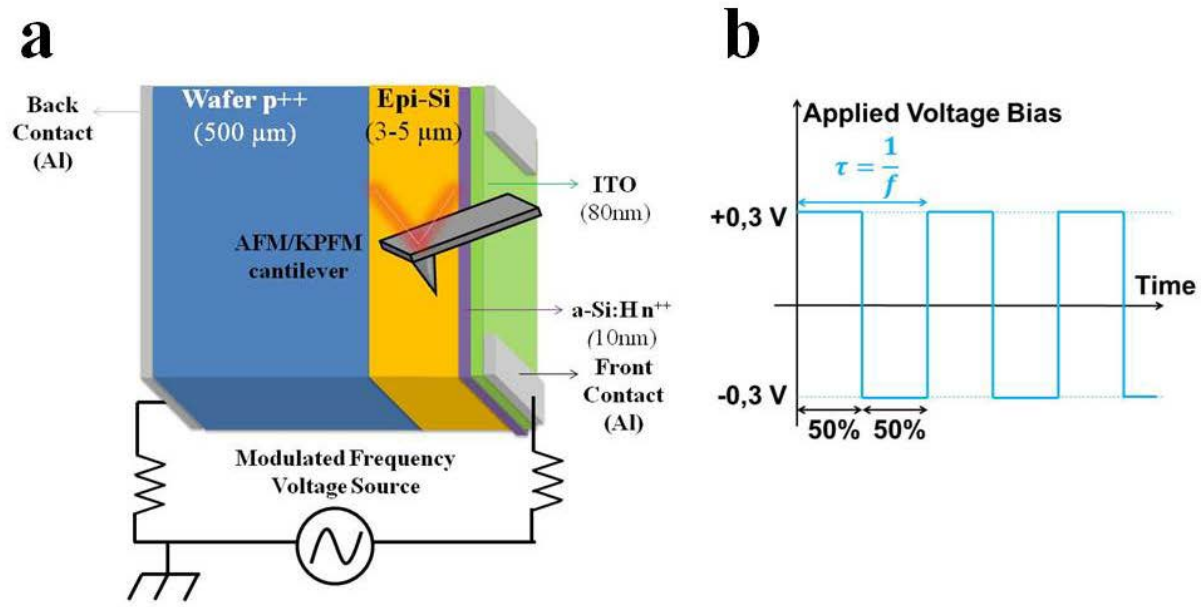

Fig. 6.15 – a) Setup used to measure epitaxial silicon solar cell under modulated frequency voltage. b) Modulated electrical bias signal applied to the epi-Si solar cell.

We first performed macro-scale lifetime measurements to compare with the lifetimes obtained with KPFM. Figure 6.16 shows lifetime measurements that are performed by time resolved microwave conductivity (TRMC) on 5 µm epi-Si layer after HF-dipping. A long decay time (>10 µs) and a short decay time (0.1-1 µs) are obtained. The short decay time is considered to be the effective lifetime and the long decay time is attributed to trapping-detrapping effects that are common in crystalline silicon [39].

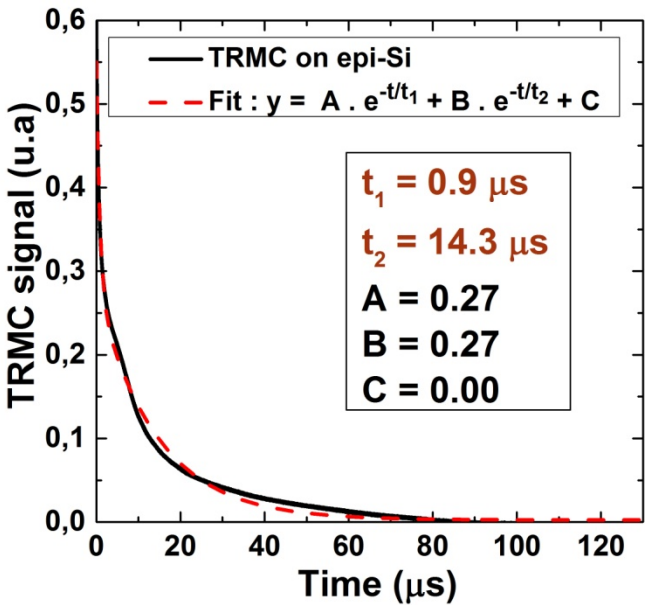

Fig. 6.16 – TRMC measurement on 5µm both sides HF passivated epi-Si sample. A fitting with two exponential curves is required. The first time constant is around 1µs. The second time constant is around 10µs.

6.1.3.3 Results

Figure 6.17 displays the topography image along with the surface potential images obtained at different frequencies and at 0V DC.

For frequencies of 5 MHz and 50 MHz, the surface potential image remains the same and the profile is very close to the profile at 0 V. These frequencies are too high and no significant recombination of carriers occurs. Between 5MHz and 1MHz, the surface potential starts to decrease at the c-Si/epi-Si interface and remains unchanged in other areas. This is probably because the interface is a defective layer as shown in SIMS profile (Fig.6.11). Therefore, the lifetime in this region is lower and recombination starts at a higher rate affecting the surface potential. The corresponding lifetimes to this frequency range are 0.2-1 µs which corresponds to the short decay time measured by TRMC (0.1-1µs). Between 500 kHz and 50 kHz, the surface potential at the interface stabilizes at a minimum but it starts increasing in the bulk of the epitaxial layer. These frequencies correspond to a lifetime range of 2-20 µs which is in the range of the high decay time measured by TRMC (>10 µs). For these low frequencies, recombination starts to happen inside the epitaxial layer and affects the surface potential.

We tried to perform similar measurements using SEM instead of KPFM. However, the SEM image shifts vertically with applied voltage bias due to a deviation of emitted electrons with surface potential, as Figure 4.7 shows. Therefore, when a modulated frequency electrical bias is applied, the SEM image gets blurry.

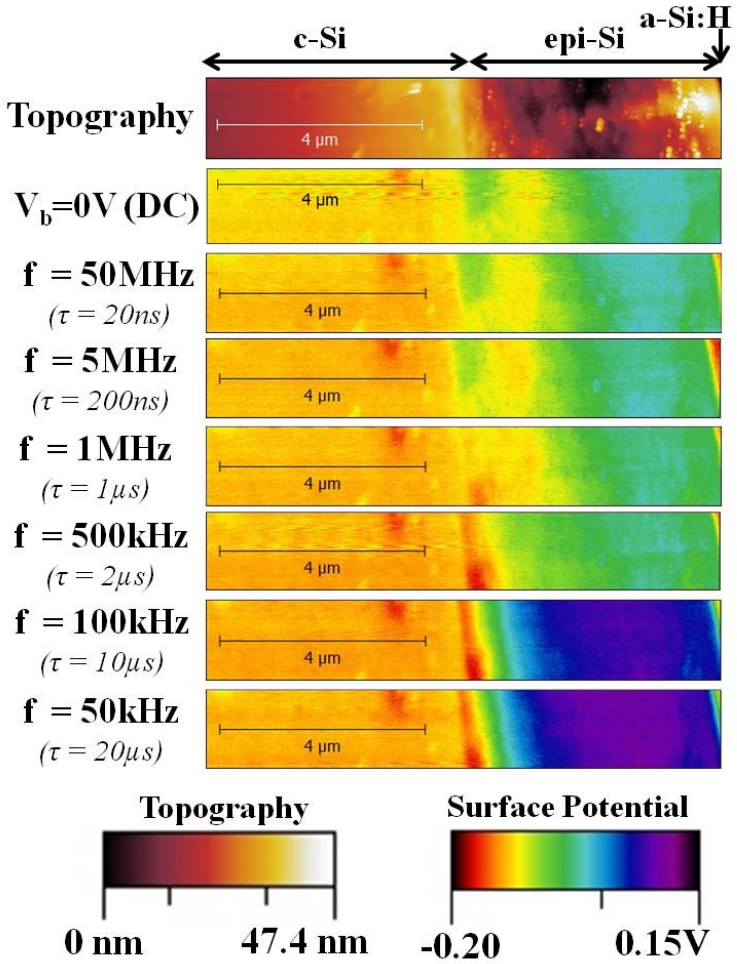

Fig. 6.17 – Surface potential images associated to 0V DC and different frequencies of modulated electrical bias.

Figure 6.18 shows the difference between the profile at a given frequency and the profile at 0 V DC. Figure 6.19 shows the surface potential averaged over three areas (c-Si wafer, interface and epi-Si layer), as a function of the frequency f and the modulation period T=1/f.

The change of the surface potential in the epitaxial silicon layer is about 150 mV (Fig 6.18) and that at the interface is about 50 mV. The latter is just above the noise level of KPFM (~20 mV). The fact that profiles were averaged makes the noise level lower and enables to detect clearly the surface potential change at the interface. Because Fig 6.19 is in logarithmic abscissa scale, it can be noticed that the surface potential at the interface evolves exponentially, as measurements under modulated frequency illumination also showed [29]–[31].

Hence, the above results of KPFM under modulated frequency electrical bias allow us to formulate the hypothesis that the carrier lifetime of epitaxial silicon solar cells is limited by the defective c-Si/epi-Si interface. We believe that this technique can potentially help to localize defective low lifetime layers and interfaces in solar cells with a nano-scale resolution.

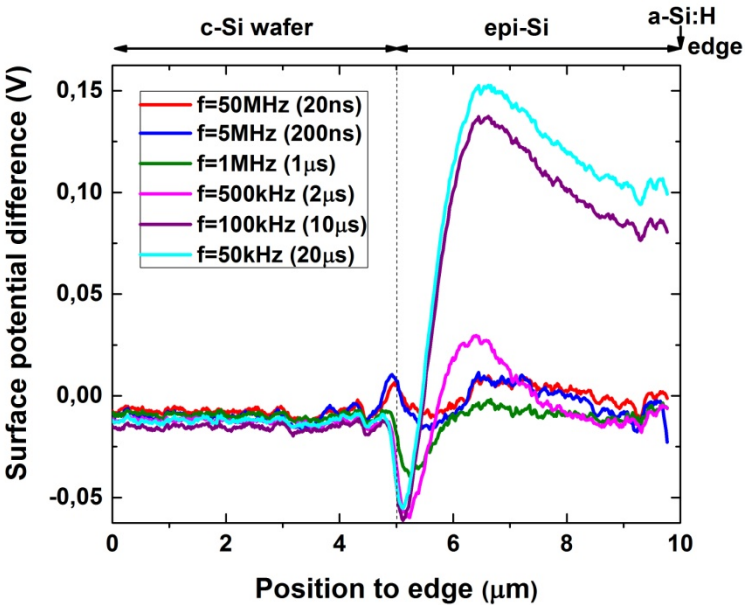

Fig. 6.18 – Surface potential (SP) difference profiles: SP(frequency)-SP(0V)

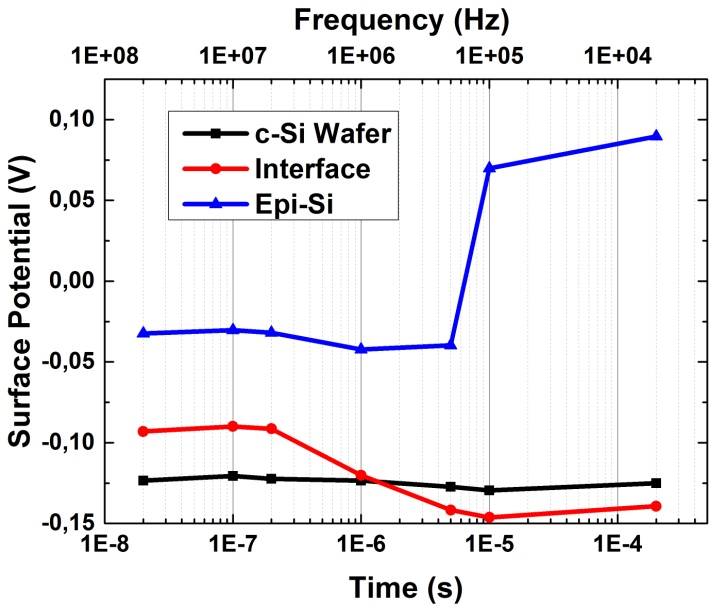

Fig. 6.19 – Surface potential averaged on three areas (c-Si wafer, interface and epi-Si) as a function of frequency and the modulation period.

6.1.4 Conclusion

In section 6.1, we investigated solar cell devices under electrical bias using Kelvin Probe Force Microscopy (KPFM) and Scanning Electron Microscopy (SEM). We have shown that these two techniques are complementary for this purpose and we propose that they should be combined in a single setup. In the conclusion of this Ph.D. manuscript, we will detail an ideal KPFM/SEM setup to investigate solar cells at nano-scale.

Our measurements under electrical bias have shown that SEM and KPFM can be used to localize PN junctions (section 6.1), to estimate space charge regions and electric field changes (section 6.2). These measurements also help to assess local doping levels and to analyze their uniformity at the nano-scale level. KPFM and SEM are complementary to investigate these diode effects. However, contrary to SEM, KPFM proves to be able to investigate series resistance effects at

the nano-scale (section 6.1). This makes KPFM a powerful tool to investigate power losses in solar cells. Besides, acquiring both diode and resistance effects at the nano-scale can provide valuable inputs for advanced modeling of solar cells. Finally, we have shown that thanks to the time-averaging capabilities of KPFM, measurement of decay times with a resolution down to ~10 ns is possible (section 6.3). This enabled to identify a reason for low lifetime of epitaxial silicon solar cell, which is the defective interface c-Si wafer/epi-Si layer. Lifetime measured by KPFM showed a good agreement with macro-scale lifetime measured by Time Resolved Microwave Conductivity (TRMC). This technique could help detect limiting layers and interfaces in different technologies of solar cells, including multi-junction solar cells. It could also help investigate the homogeneity of the quality of interfaces.

6.2 Devices investigation under illumination

6.2.1 Measurements under different illumination intensities

- ***6.2.1.1 Context***

In this section, we will investigate solar cells under illumination using scanning probe microscopy (SPM) techniques. Since we have shown that electron microscopy (EM) techniques are not sensitive to illumination (section 4.2), SPM measurements will not be compared to EM techniques in this part.

However, we will compare photovoltage measurements using KPFM and photocurrent measurements using CP-AFM. Both kinds of measurements have been carried out on the surface and the cross-section of solar cells solar cells previoulsy.

Photovoltage surface measurements using KPFM have been carried out on CIGS solar cells [40] and multicrystalline silicon solar cells to investigate grain boundaries [29]. These measurements have also been carried out on the surface of different technologies of solar cells to compare their sensitivity to illumination [41]. Photovoltage measurements on the surface of silicon PN junctions have also been used to investigate PN junctions properties at the nano-scale [42]. Finally photovoltage measurements under modulated frequency illumination have also been performed to investigate carrier lifetimes at nano-scale on the surface of silicon nanocrystal solar cells [30], organic solar cells [31] and polycrystalline silicon solar cells [29], [43].

Photovoltage measurements on the cross-section of solar cells have also been proven to be of interest to investigate PN junction properties of different technologies of solar cell devices. Different studies have been performed on CIGS solar cells [44], III-V solar cells [45], [46], multi-junctions [5], [8], [47], [48] and silicon PN junction [49]. These measurements help revealing photogeneration effects and local surface potential shifts with the illumination intensity. Detailed theoretical work on photovoltage has been published by Kronik *et al.* [50] and explains how to extract valuable information from these measurements.

Photocurrent measurements using CP-AFM technique have also been performed on solar cells under illumination. Surface photocurrent measurements have been performed on CdTe solar cells [51], polysilicon solar cells [52], silicon nanowire solar cells [53], diamond photodetectors [54] and organic solar cells [55]. Recently, photocurrent measurements on the cross-section of solar cells have also been performed to investigate the current at different positions from the junction [56].

All these studies have at least addressed the influence of illumination intensity on either the photocurrent or the photovoltage. Some studies have also studied other parameters of illumination such as light wavelength [45], [48], [52], the modulation frequency of illumination [29]–[31], [43], the position of light beam [48] or light polarization [57]. Most recent studies have shown that it is

possible to extract the local open circuit voltage (V_{oc}), short-circuit current (J_{SC}), fill factor (FF) and maximum power (P_{max}) from these measurements [51].

- ***6.2.1.2 Our approach***

In this subsection, we studied the influence of illumination intensity on photocurrent and photovoltage measurements. Measurements on epitaxial silicon solar cells are presented first and measurements on interdigitated back contact (IBC) solar cells are presented after. Figure 6.20 shows the setups used to investigate the two solar cells. Our setups enable to measure the V_{oc} of the solar cells when placed on the AFM stage. Therefore nano-scale KPFM photovoltage measurements can be compared directly to macro-scale voltmeter photovoltage measurements. We use the macro-scale V_{oc} to assess the effect of illumination intensity. These setups also enabled to apply an electrical bias, which enables to assess the effect of illumination for a given applied electrical bias. They also enabled to perform in-situ IV curves to assess a possible light induced degradation.

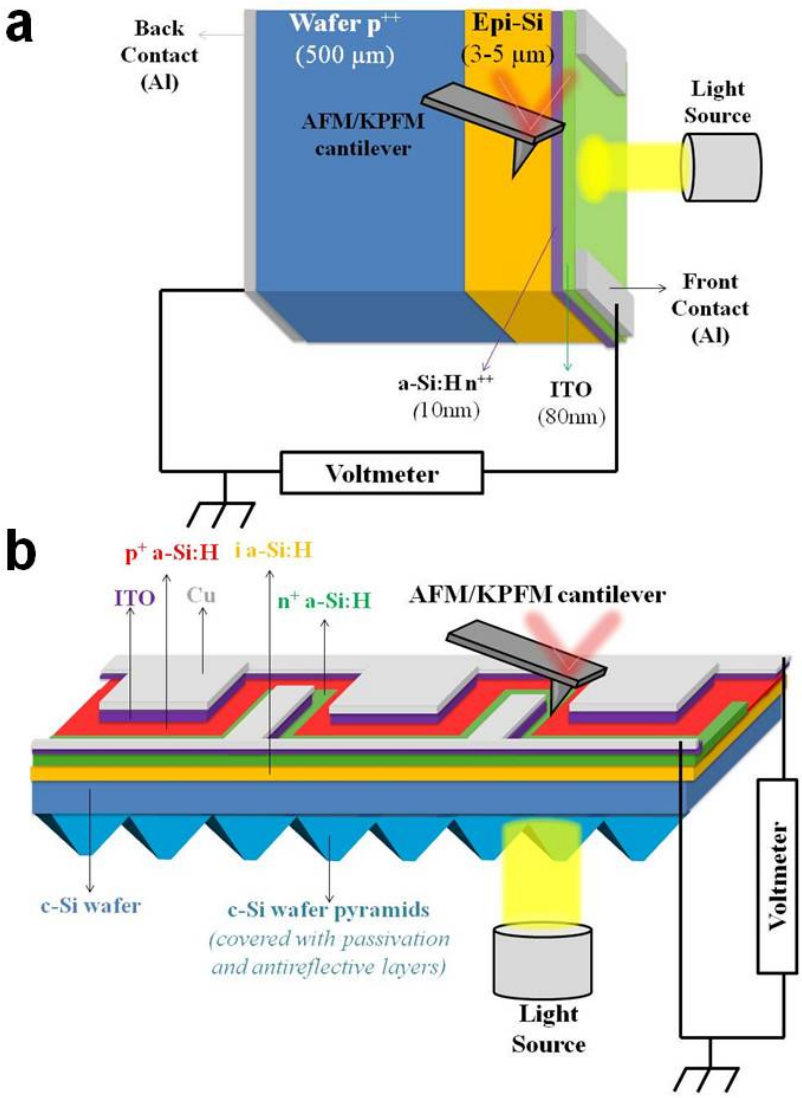

Fig. 6.20 – a) KPFM setups used to investigate a) the cross-section of epitaxial silicon solar cells and b) the back surface of interidigitated back contact solar cells under illumination.

We have seen previously that photovoltage and photocurrent measurements have extensively been performed, on different technologies of solar cells. However, our approach is innovative in three ways:

- First, we analyze two designs of silicon solar cells that have not been investigated previously to our knowledge. In particular, the IBC solar cell is a complex design since several diode effects are at stake. This makes our study original and innovative.
- Second, our study on epitaxial silicon solar cell compares photocurrent and photovoltage measurements under the same illumination intensities performed at less than 100µm from each other thanks to nano-indentation. To our knowledge, we are the first group to present both photocurrent and photovoltage on the same solar cell. This enables a comprehensive comparison of KPFM and CP-AFM and to indentify artifacts of both techniques. This comparison has not been done for IBC solar cells because the indentation of amorphous silicon layers would have degraded the solar cell.
- Finally, the CP-AFM setup has been adapted to be only sensitive to the photocurrent. Contrary to previous works on photoconductive AFM measurements [54], [56], we adapted our Resiscope setup to be able to perform measurements with no voltage bias applied externally between the tip and the sample, as Figure 6.21 shows. Therefore, the only current source in the electrical circuit is the solar cell itself when illuminated. This configuration makes the interpretation of results much easier.

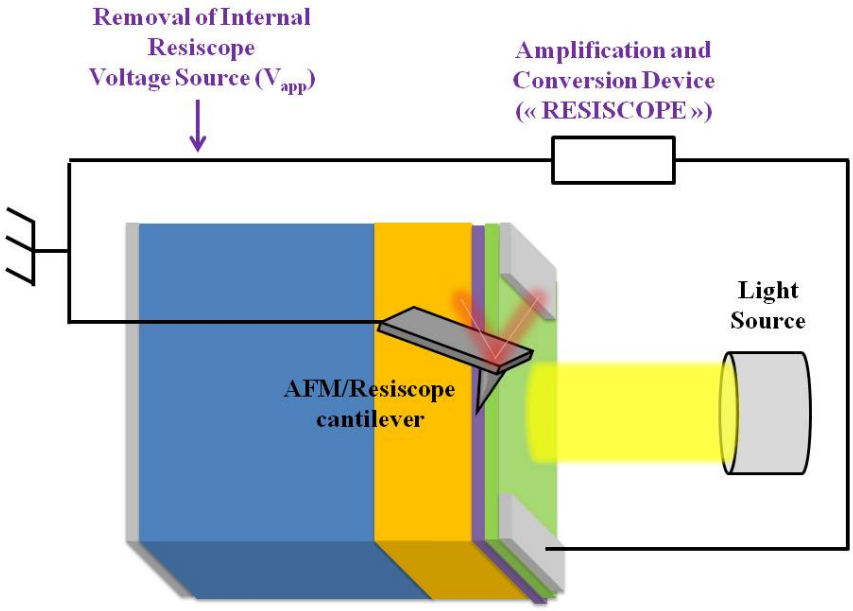

Fig. 6.21 – Resiscope setup used to investigate the cross-section of epitaxial silicon solar cell under illumination. Compared to the conventional Resiscope setup, the DC voltage source has been removed to be sensitive only to the photocurrent.

6.2.1.3 Results

- *Epitaxial silicon solar cells*

We first consider measurements performed on the cross-section of an epitaxial silicon solar cell. These measurements have been published in a peer-reviewed journal [58] and in a conference paper [22].

We have not performed photovoltage measurements on the top surface of epitaxial silicon solar cells because our AFM scanner is too cumbersome. The space between the scanner and the sample is very narrow to enable the approach of the tip. This made it difficult on our equipement to illuminate from the top. Therefore, we focused on cross-section measurements of the epitaxial silicon solar cells. The cross-section preparation process was similar to that used for measurements under

electrical bias (section 6.1.1). The solar cell was first investigated with Resiscope under illumination and then with KPFM under the same illumination intensities.

Figure 6.22 shows KPFM and CP-AFM images with and without LED illumination and the topography images associated to each of them. Full illumination corresponds to a light intensity close to one sun (0,1 $W.cm^{-2}$) since the open circuit voltage is 460mV under full LED illumination, comparable to 530mV measured in a solar cell simulator under one sun. Scanning dimensions are 2.5 x 5µm. The edge of the sample with the n^{++} a-Si:H layer is on the right side of the picture. It can be noted that the roughness in the topography images is different: KPFM uses tapping mode, which is very soft and hence more sensitive to the surface. That is why the topography image shows surface roughness (Fig.6.22.a). CP-AFM uses contact mode which is intrusive on the surface and may smooth out the surface roughness (see Fig.6.22.b). This is also reported by Li *et al.* [53] who showed the intrusiveness of CP-AFM measurement. Using a strong force on the tip is necessary to achieve a good contact. On the other hand, it degrades the material and the tip. The advantage is that CP-AFM is less sensitive to the contamination of the sample surface than KPFM. The effect of the illumination is visible on the epitaxial silicon layer in both photocurrent and photovoltage images [Fig.6.22 (c,d,e,f)]. The wafer does not show any difference with and without illumination because it is highly doped and grounded. Both a-Si:H and ITO layers are not visible on these images due to their very small thickness compared to the scan size and also possibly because they might have been degraded or removed during the polishing step of the cross-section (rounding effect).

The sensitivity of the KPFM surface potential to illumination can be explained as follows:

- On the p^{++} doped crystalline silicon wafer, the surface potential remains unchanged under illumination because the wafer is highly doped and grounded. The quasi-Fermi level of holes under illumination is the same than the Fermi level under dark conditions. The photovoltage is equal to 0V on the wafer.
- On the n^{++} a-Si:H layer, surface potential illumination is defined by the difference between the vacuum level and the quasi Fermi level of electrons because electrons are majority carriers in this layer. The vacuum level remains constant with increasing light intensity. Under illumination, the quasi-Fermi level of electrons in the n^{++} a-Si:H layer splits from the quasi-Fermi level of holes in the p^{++} c-Si wafer by the V_{oc} value if we assume surface effects are negligible. This is explained in details in the theory of photovoltage on pn junction [50]. Therefore the surface potential on the n^{++} a-Si:H layer is supposed to decrease by a value close to the open circuit voltage (V_{oc}) with increasing illumination.
- On the intrinsic epitaxial layer, the photovoltage profile decreases progressively from 0V on the p^{++} doped crystalline silicon wafer to the V_{oc} on the n^{++} doped a-Si:H layer.

The sensitivity of the CP-AFM current to illumination can be explained as follows. As we increase the light intensity, the photocurrent increases in the epitaxial silicon and a-Si:H layer but no photocurrent is visible in the crystalline wafer since it is highly doped. The photocurrent increase in the epitaxial layer can be understood as a decrease of the contact resistance. Werber et al. explained that the measured contact resistance R_c is the sum of a geometrical resistance R_g and a barrier resistance R_b [59]. For a low contact radius between the sample and the tip, R_c is very close to R_b and decreases exponentially with the electron concentration. With increasing illumination, the electron concentration in the epitaxial layer increases. Hence, R_c which is predominant in the circuit, decreases exponentially. Therefore, the photocurrent increases exponentially with illumination intensity in the epitaxial silicon layer.

In Figure 6.22.d, some areas in photocurrent images acquired from measurements without LED illumination, show photocurrent values above the lowest measurable level (10^{-12} A).This is due to the fact that AFM laser diode spills over the cantilever and creates a non-desired photocurrent (section 3.1). This phenomenon is amplified on rough areas where the cantilever undergoes both a deflection and a torsion causing an increase of AFM laser induced current. We measured the influence of the AFM laser on both setups by measuring the open circuit voltage when all the sources of

illumination were turned off, except for the AFM laser. The photovoltage reaches 14mV for CP-AFM setup and 51 mV for KPFM setup. On the photocurrent images (Fig.6.22.d-f), the imprint of the topographical image is quite evident: on the trenches (caused by the polishing) and on the edge of the sample, the current is much higher. This is due an increase of the effective contact area between the probe and the sample, as discussed in section 3.4. Therefore more current can pass through the circuit. To achieve a more homogeneous image, either the polishing process has to be improved or micro-cleavage technique can be used. KPFM measurements also show an imprint of topography on the surface potential images, especially on the edge of the sample. However, the influence of topography on the measured values is smaller for KPFM than CP-AFM because stray capacitances in KPFM lead to averaging the signal on a wider area which screens local topographical influences (section 3.5).

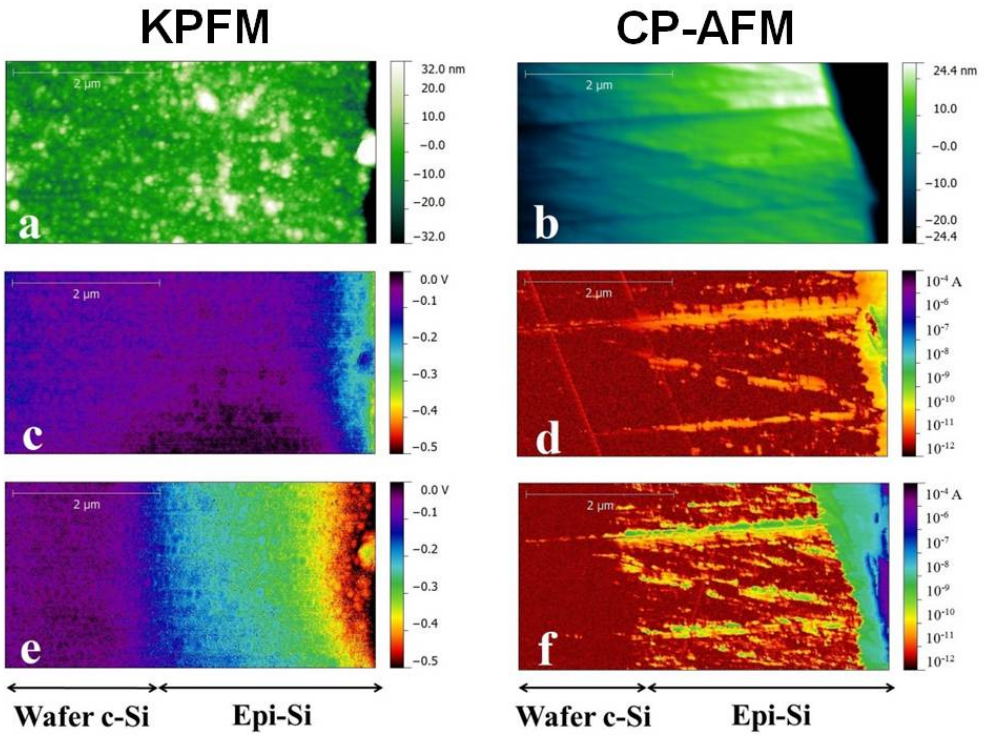

Fig. 6.22 – Topography image associated respectively to surface potential (KPFM) and current (CP-AFM) measurements a) and b) respectively. Surface potential and current images without LED c) and d) respectively and at full LED illumination e) and f) respectively. The scan area is 2.5x5 µm for all the images

Figure 6.23 shows KPFM and CP-AFM profiles along the PIN heterojunction without LED illumination and under two illumination intensities. As the open circuit voltage (V_{oc}) increases logarithmically with the illumination intensity and it is easy to monitor, we present the profiles obtained under two levels of illumination resulting in V_{oc} of 340 mV and 460 mV. To reduce the noise in photovoltage measurement, we obtained a profile by averaging 128 consecutive horizontal scan lines (which corresponds to 1,2 µm total vertical displacement). For photocurrent measurements, we took advantage of the signal increase inside the scratches and averaged on 13 horizontal scan lines which correspond to 120 nm. Successive AFM images have a tendency to drift. Therefore profiles were drawn on easily identifiable areas of the photocurrent and photovoltage images. Then, they were reported as shown in Figure 6.23.

The profiles show coherent behavior: when the illumination intensity increases, the current increases in the intrinsic epi-Si layer (Fig.6.23.b) and the surface potential decreases by a difference correlated to the measured V_{oc} (Fig.6.23.a). Photovoltage profiles show a small noise related to thermal fluctuations of the cantilever, however this noise has been reduced by averaging (section 3.6).

Contrary to what is expected theoretically, the junction at the interface between the crystalline silicon wafer and the epitaxial layer is not visible on the surface potential profile in the dark (Fig.6.23.a). Surface states leading to band bending complicate the analysis of KPFM measurement on PN junctions under open circuit conditions in the dark, as shown in section 3.8 and reported by Kikukawa et al. [60]. This interpretation is confirmed in Fig.6.22.a which shows nanograins at the top of the cross-sections. These nanograins can mask the potential contrast at the PN junction. The band bending is also the most likely reason for the surface potentials measured at the edge being only correlated and not equal to the V_{oc} of the solar cell. The difference in the surface potential on the wafer side between dark condition and under illumination is not expected and may result from a degradation phenomenon such as local oxidation or tip abrasion. Photocurrent profiles (Fig.6.23.b) allow to precisely locate the c-Si/epi-layer. However they show noise related to the topography, as discussed previously (section 4.1). When the probe is close to the edge of the cell, the current suddenly increases because the side of the tip touches the edge and hence the effective surface of contact is larger.

In Figure 6.23, both KPFM and CP-AFM measurements along the cell cross section show that the profiles with and without illumination deviate strongly at the epi-Si/wafer p^{++} interface. Further in the epitaxial layer, the deviation between the two profiles is much smaller, as the profiles remain at a constant distance close to the edge. This is not expected for a standard PIN junction where the distance between profiles with and without illumination should increase progressively all along the intrinsic layer. Therefore, from the cross-analysis of KPFM and CP-AFM measurements we confirm the influence of the unintentional n-doping of the epitaxial silicon layer and the highly defective interface between crystalline silicon wafer and epitaxial silicon layer (Figure 6.11). It should be noted that the defective layer could have important fluctuations along the cross-section leading to important inhomogeneity. Hence, CP-AFM and KPFM are powerful tools to investigate the incidence of undesired process phenomena on different areas of the cross-section.

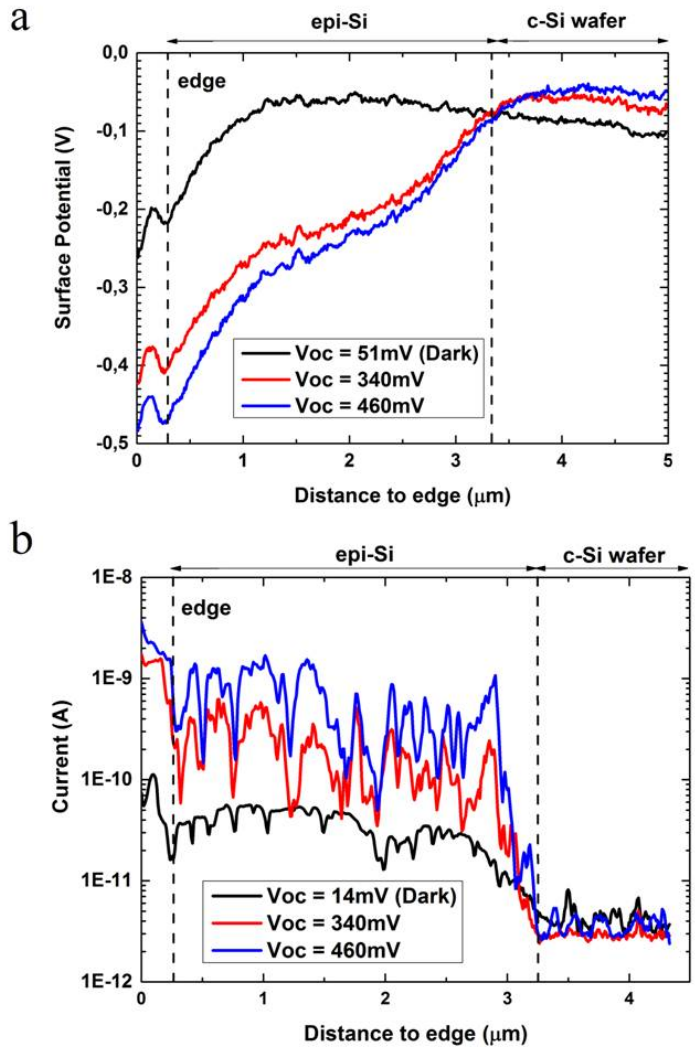

Fig. 6.23 – a) Surface potential and b) current profiles measured at the sample cross-section without LED illumination (dark) and under two intensities of illumination leading to V_{oc} = 340 mV and V_{oc} = 460 mV

We have also investigated the degradation of the photocurrent and photovoltage. For that purpose, the profiles under the same illumination were performed before and after six scans under illumination for both discussed methods. Fig. 6.24.a shows that the photovoltage has changed on the c-Si wafer side. This may result from a modification of the sample: tip-induced oxidation might happen despite the controlled nitrogen atmosphere (section 3.2.1). Also, we cannot exclude other effects related to the measurement itself, as degradation of the tip (its coating or in the tip radius), as discussed in section 3.3. Moreover, these changes can also be attributed to surface effects induced by illumination like local light induced degradation or long lived deep trap states, as was discussed by Zhang et al [44].

Fig. 6.24.b shows a strong degradation of photocurrent after six scans. This is particularly visible in the epitaxial silicon layer because the current signal in the wafer p^{++} region is below the detection level of the instrument (~10^{-12} A) so we can consider that it is equal to zero. The causes of degradation may again come from both the measurement process and/or a degradation of the sample (section 3.2 and 3.3). First, as above, there might be an abrasion of the tip coating and also a drift of the AFM laser on the photodetector during measurements. In fact, this can affect sensibly the force applied by the tip on the surface because a cantilever with strong spring constant (48 N/m) was used. Secondly, the degradation of the sample surface can result both from the indentation phenomena and from tip-induced oxidation during the scans. It should be noted that close to the edge of the sample, the values of current seem to be repeatable. This is due to two reasons: first, the area of contact corresponds to

the flank of the tip which is larger and probably less degraded during the scans. Second, this region locally undergoes much less pressure than the flat region. Therefore, it is less degraded and the tip-induced oxidation is probably lower.

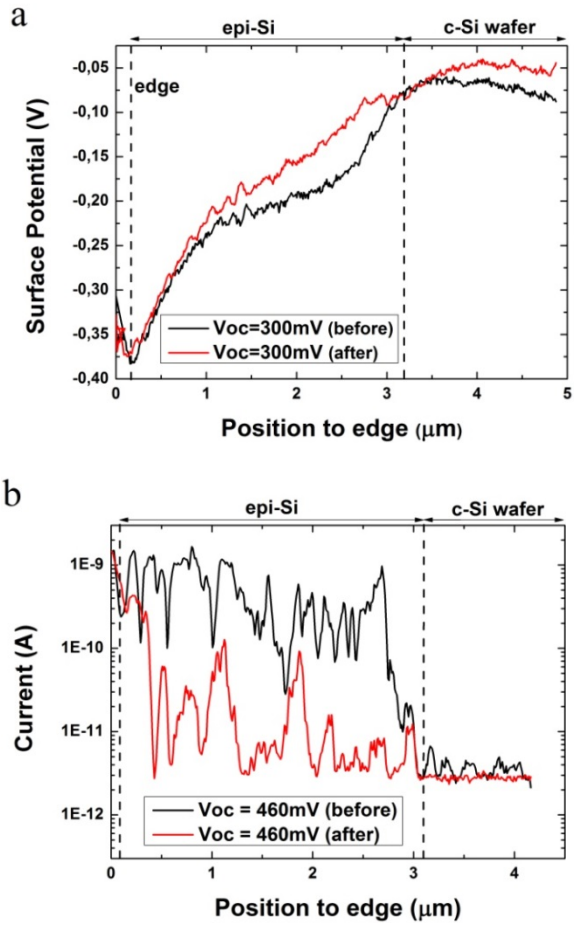

Fig. 6.24 – (a) Surface potential profiles under an illumination corresponding to a V_{oc} of 300mV before and after six scans. (b) Current measurements corresponding to a V_{oc} of 460mV before and after six scans.

- *Interdigitated back contact solar cells*

We investigated interdigitated back contact solar cells under different illumination intensities. These measurements have been published in a conference paper [20]. The setup used is shown in Figure 6.20.b. The IBC solar cell is placed top down. Illumination is brought from the bottom and KPFM measurements are performed between the Cu/ITO/n^+ a-Si:H contact and the Cu/ITO/p^+ a-Si:H contact for different light intensities. Open circuit voltage increases logarithmically with light intensity. We chose to present measurements for increasing values of open circuit voltage, which correspond to increasing values of light intensity.

Figure 6.25 shows the topographical AFM image and KPFM surface potential images for different light intensities leading to different open circuit voltages. Since the Cu/ITO/p^+ a-Si:H contact is grounded, the p^+ a-Si:H is almost insensitive to illumination. The n^+ a-Si:H layer is sensitive to illumination intensity because of the PN junction at the interface between p^+ a-Si:H and n^+ a-Si:H layers. We observe inhomogeneities of surface potential on the n^+ a-Si:H layer, which might be due to ITO remains on the amorphous layer. The surface potential decreases with increasing illumination intensity because electrons are majority carriers on the n^+ a-Si:H layer. Therefore, the surface potential on this layer is the difference between the vacuum level and the Fermi level of electrons.

Under illumination, the quasi-Fermi level of electrons splits from the quasi Fermi level of holes by the V_{oc} value. Therefore the surface potential on the n^+ a-Si:H layer decreases by a value close to V_{oc}. Therefore, theory and measurements are in good agreement.

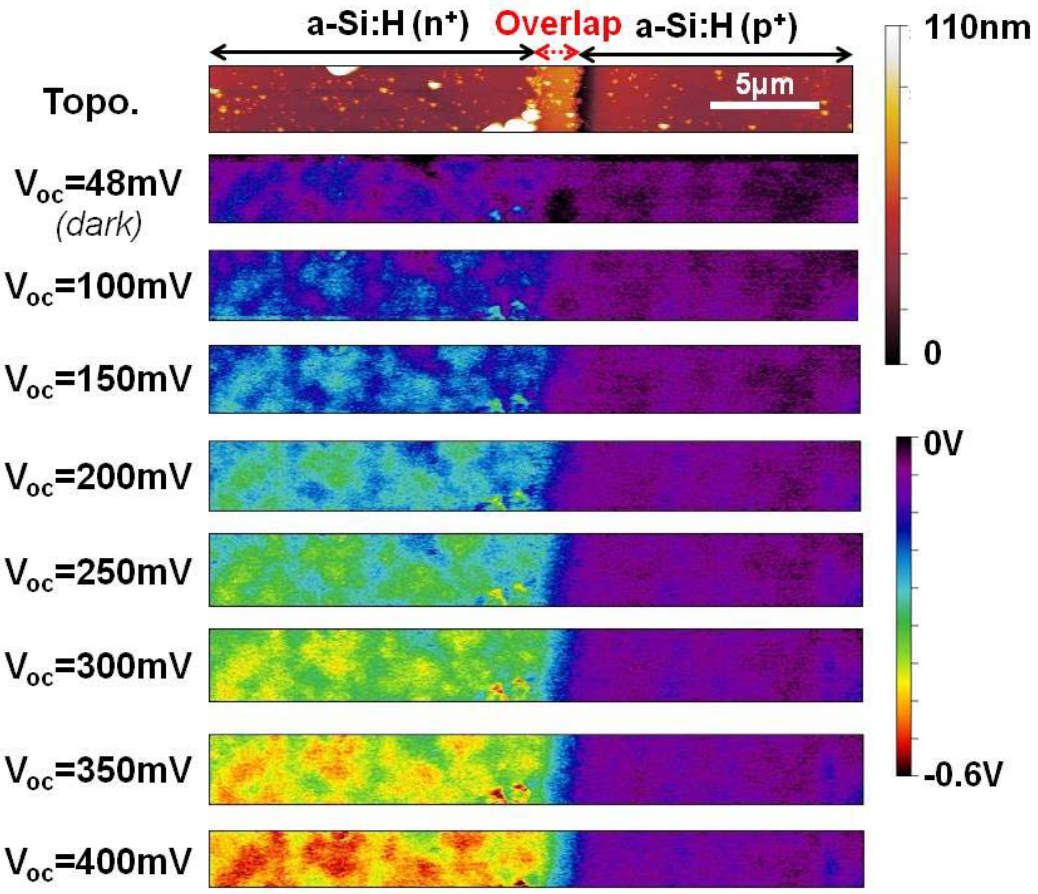

Fig. 6.25 – Topographical AFM image and KPFM surface potential images between the contacts of an interdigitated back contact solar cell under different illumination intensities leading to different open circuit voltage values. The contacts are not included in this image.

To determine if our measurements are quantitative we perform profiles on the KPFM images for the different illumination intensities, as shown in Figure 6.26.a. It can be observed that the surface potential changes measured at the nano-scale by KPFM are equal to the open circuit voltage values measured with the voltmeter. In order to compare the sensitivity of SEM and KPFM measurements to illumination, we have studied its effect on the average signal from the four regions of the cell: the Cu/ITO/p^+ a-Si:H electrode, the Cu/ITO/n^+ a-Si:H electrode, the n^+ a-Si:H layer and the p^+ a-Si:H layer. We performed KPFM measurement on the contacts under illumination in open circuit conditions, additionally to KPFM measurements between contacts. Figure 6.26.b shows the curves we obtained. We observe that measurements have a linear correlation with the open circuit voltage on the n^+ a-Si:H layer and on the Cu/ITO/n^+ a-Si:H contact, with a slope equal to 1. This proves that the technique can measure quantitative photovoltage changes. Besides, unlike measurements under electrical bias (Figure 6.5), measurements under illumination do not show any saturation effect. The reason is that in open circuit conditions, no current is produced by the device. Therefore, possible series resistances do not have any effect on surface potential profiles.

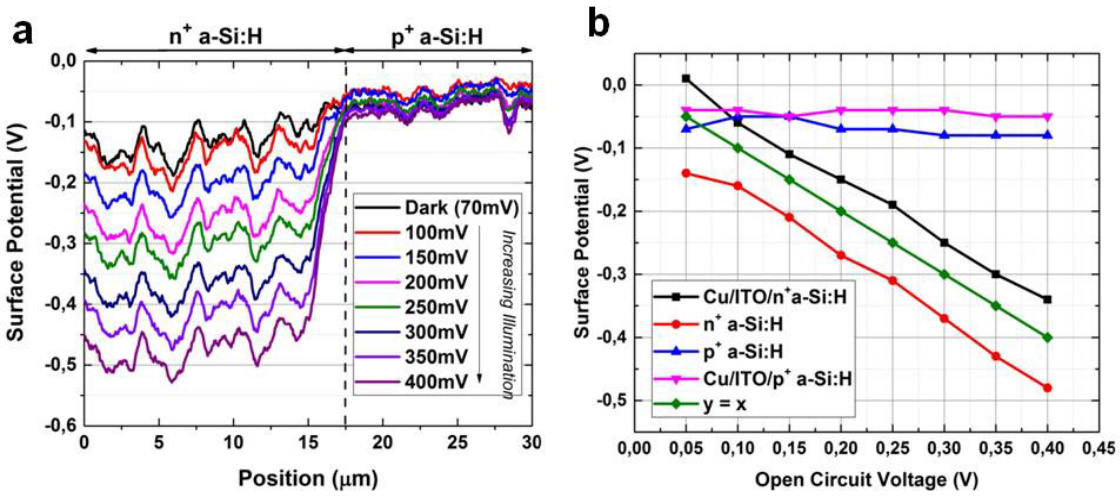

Fig. 6.26 – a) Surface potential profiles associated with scans between p^+ a-Si:H and n^+ a-Si:H contacts during which the illumination was increased leading to open circuit voltages of 0.4 V, 0.35 V, 0.3 V, 0.25 V, 0.2 V, 0.15 Vand 0.1 V. The IBC solar cell is in open circuit conditions. In the dark, the AFM laser induces a V_{oc} of 0.05 V. b) Average value of KPFM signal as a function of the open circuit voltage under different illumination intensities measured with a voltmeter.

Finally, we performed photovoltage measurements under different applied voltage values and we compared it to a measurement in open circuit voltage conditions (Fig 6.27). The profiles are obtained by subtracting profiles with and without illumination, for different electrical biases. We observed that measurements under reverse electrical bias are more sensitive to illumination than measurements under forward voltage, because measurements under forward bias are closer to flat band conditions. We propose that investigation under particular light conditions (wavelength, modulation frequency, intensity) could be carried out under reverse voltage bias to enhance the signal-to-noise ratio.

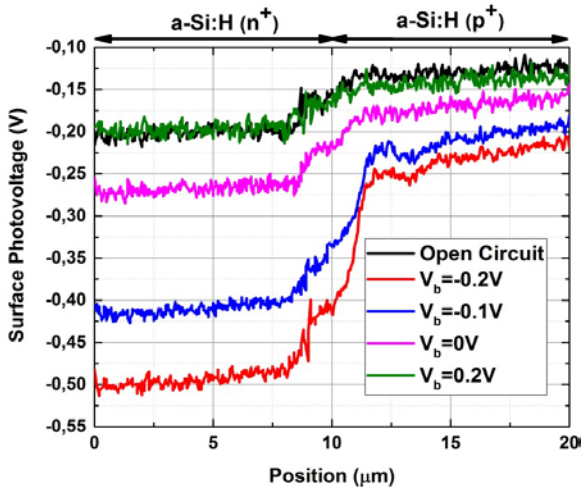

Fig. 6.27 – Photovoltage profiles for the same light intensity applied, under different applied electrical biases as well as under open circuit conditions.

As mentioned previously, the illumination intensity is the most studied illumination parameter using scanning probe microscopy techniques. However, other illumination parameters can be studied such as light wavelength, modulation frequency and polarization. In the next subsection, we will study the effect of light wavelength on photovoltage measurements performed using KPFM on epitaxial silicon solar cells and IBC solar cells.

6.2.2 Measurements under different illumination wavelengths

6.2.2.1 Context

In this subsection, we study the effect of illumination wavelength on silicon solar cells using KPFM. To our knowledge, only a small number of articles have discussed these kind of measurements previously. Saraf *et al.* have performed spectrally resolved photovoltage measurements at different positions of the PN junction in GaP solar cells [45]. They have shown differences of photovoltage behavior close and far from the space charge region, for certain wavelength ranges. These measurements were in good agreement with macroscale photovoltage measurements. Ankudinov *et al.* have compared the effect of red and blue illumination at different positions of multijunctions solar cells: top, middle and bottom cells [48]. They show how the different cells are sensitive to the wavelengths, using surface photovoltage profiles. This work suggests that KPFM could help detect problems of current matching at nano-scale. Tennyson *et al.* have studied the influence of wavelength illumination on the surface of CIGS solar cells and have investigated grain cores and grain boundaries, using this technique [61]. They have shown that the surface potential increases for longer wavelengths because they are less sensitive to the grain's interface since long wavelengths photons are absorbed far from the surface. Heo et al. have used CP-AFM to investigate the effect of light wavelength at the nano-scale on the surface of poly-silicon solar cells. They have shown a good agreement between external quantum efficiencies (EQE) and open circuit voltages measured by CP-AFM, only in a certain range of wavelengths [52].

6.2.2.2 Our approach

In our approach, we compare the internal quantum efficiency (IQE) of the solar cells to the KPFM photovoltage of epitaxial silicon solar cells and interdigitated back contact (IBC) solar cells. In particular, we are interested in trying to detect differences on surface potential profiles for low IQE and high IQE wavelengths. The idea is that for a low IQE wavelength, the recombination rate is high: only a small portion of the photons absorbed lead to an electron/hole pair collected in the electrical circuit. The reason is that the electron/hole pairs recombine before reaching the contacts of the solar cell. Therefore, a difference between low IQE and high IQE wavelengths would mean that KPFM could be used to localize the areas of recombination for low IQE regions.

For this study, we used the exact same setup as the one used to perform measurements under different intensities of illumination (Figure 6.20) and the exact same process of preparation of epitaxial and IBC solar cells. We used different illumination wavelengths: infrared (λ=850 nm), red (λ=625 nm), green (λ=530 nm), blue (λ=455 nm), and ultraviolet (λ=405 nm). Figure 6.28 shows three pictures of the epitaxial silicon solar cell placed on the AFM plate with three illumination wavelengths (red, green and blue). For each solar cell, IQE measurements are performed in the wavelength range [350 nm-1100 nm]. We present measurements on epitaxial silicon solar cells.

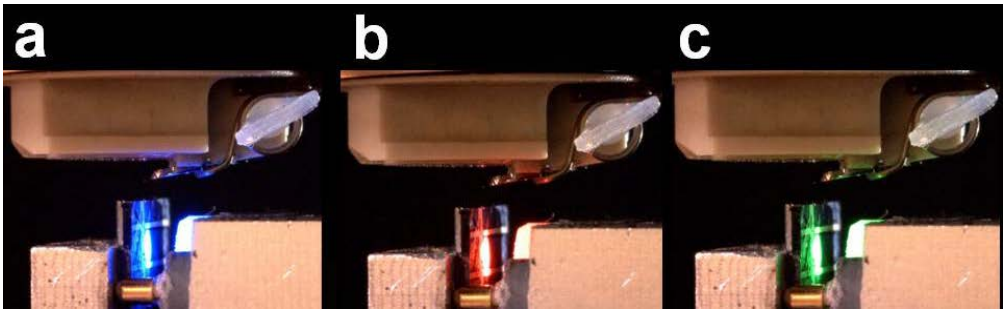

Fig. 6.28 – Image of the setup used to investigate epitaxial silicon solar cells under different wavelength illumination: a) blue (λ=455 nm), b) red (λ=625 nm), c) green (λ=530 nm)

6.2.2.3 Results

Our work on the influence of illumination wavelength on epitaxial silicon solar cells has been partly published in a conference paper [22]. We have continued this work since then by using wavelengths where the IQE of the epitaxial silicon solar cell is poor.

Figure 6.29.a show the IQE curve obtained on epitaxial silicon solar cells. The two curves are associated to transferred solar cell (when the epitaxial silicon layer is detached from the crystalline silicon wafer) and non transferred solar cell. Since the epitaxial silicon layer of the transferred solar cell is thicker, the IQE is better for high wavelengths because transmission losses are avoided. For both cells, the IQE is relatively high [60%-80%] for the blue (λ=455 nm), green (λ=530 nm) and red (λ=625 nm) wavelengths. The IQE is relatively low [40%-50%] for the violet (λ=405 nm) and infrared (λ=850 nm) wavelengths.

Figure 6.29.b shows KPFM surface photovoltage profiles on the PIN junction of an epitaxial silicon solar cell. These profiles result from the subtraction between a measurement under illumination at a given wavelength and a measurement in the dark. In this measurement the illumination from AFM laser was negligible (<10 mV). We increased illumination for all wavelengths to reach a open circuit voltage of 225 mV measured with the voltmeter. Measurements were performed on the same position on the cross-section of the epitaxial silicon solar cell. We can observe on Figure 6.29.b that surface potential profiles are strictly the same, whether the wavelength used leads to high or low IQE. This means that KPFM cannot detect the area of recombination for low IQE wavelengths. An explanation is that recombinations either do not lead to surface potential changes or lead to surface potential changes that are below the noise level. Another explanation could be that since the cross-section is not passivated, the recombination rate on the cross-section is the same for photocarriers generated for low or high IQE wavelengths.

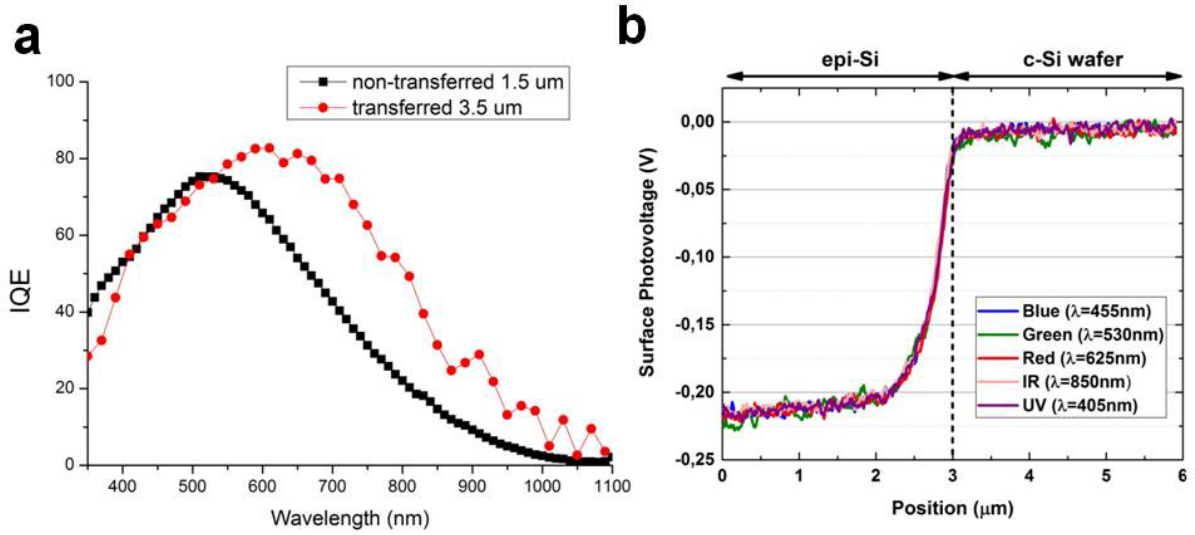

Fig. 6.29 – a) Internal Quantum Efficiency (IQE) curve of the epi-Si solar cell *(courtesy of Wanghua Chen)* b) Surface potential profiles on epi-Si solar cell under different wavelength illumination λ: 405 nm, 455 nm, 530 nm, 625 nm, 850 nm

6.2.3 Conclusion

In section 6.2, we have investigated crystalline silicon solar cells under illumination using Kelvin Probe Force Microscopy and Resiscope. We first investigated the influence of the illumination intensity (section 6.2.1). Photovoltage and photocurrent were measured on the cross-section of epitaxial silicon solar cells and photovoltage was also measured on and between the contacts of IBC

solar cells. The photovoltage changes observed on IBC solar cells were equal to the open circuit voltage changes measured with a voltmeter, which means that quantitative investigations can be carried out using KPFM. On the epitaxial solar cells, the surface potential changes were proportional to the open circuit voltage changes but not equal, probably because of additional surface potential losses between the area of measurement and the ground.

Then, we investigated the influence of the illumination wavelength (section 6.2.2). Photovoltage measurements under different wavelengths were performed on epitaxial silicon solar cells for a fixed open circuit voltage. The idea was to see if surface potential profiles were different for low and high IQE wavelengths. This would have enabled to identify the areas of recombinations for low IQE solar cells. However, no difference was observed for both solar cell devices. This shows that either recombinations do not lead to any surface potential change or that the changes are too small compared to KPFM performed in ambient air. Perspectives are proposed to improve this measurement and spectrally resolved KPFM measurements are also proposed on multi-junction solar cells. On these technologies, these measurements could enable to detect valuable information (for instance current mismatches at the nano-scale).

These two illumination parameters (intensity and wavelength) seemed the most valuable to us on crystalline silicon solar cells but other illumination parameters can be thought of (e.g. light polarization, light beam position, light modulation frequency). Since our illumination is brought to the solar cell through an optical fiber, these measurements are very easy to design provided we find the appropriate fiber coupled light sources.

Measurements under illumination are complementary to measurements under electrical bias. Since they only need a bottom contact for grounding, measurements under illumination can be performed at different steps of the device process flow. However, measurements under illumination on the front side of the device can be challenging because the AFM scanner is often cumbersome and the cantilever may lead to shadowing effects. Therefore, for certain KPFM setups, measurements under electrical bias can be more adapted for frontside investigations. Even for measurements under illumination, it is useful to have the solar cells contacted. It enables to measure the open circuit voltage at all times and to assess the parasitic effect of the AFM laser. Besides, it enables to investigate the effect of illumination under different applied electrical biases. The combination of illumination and electrical bias opens the door for customization of scanning probe microscopy investigations depending on the device investigated.

6.3 Conclusion

In Chapter 6, we have highlighted scanning probe microscopy measurements on crystalline silicon solar cells under operating conditions, namely electrical bias (section 6.1) and illumination (section 6.2).

On the one hand, CP-AFM does not appear to us to be well suited for devices investigation at nano-scale. The first reason is that it is highly intrusive. In order to acquire a signal, the silicon layers have to be scratched (section 3.2) and the conducting coating of the tip is often degraded (section 3.3). This makes measurements on the same area challenging. In the case of measurements on fragile layers (e.g. amorphous silicon layers of IBC solar cells), the intrusiveness is prohibitive because it directly affects the local electronic properties of the solar cell. The second reason is that measurements under applied electrical biases are challenging to interpret. CP-AFM is a contact technique. Therefore, when an external electrical bias is applied, a parallel electrical circuit with two voltage sources has to be considered (Figure 6.10.a). This makes interpretations of CP-AFM measurements under electrical bias challenging.

On the other hand, KPFM appears to us to be a powerful tool for the investigation of solar cells under operating conditions.

- The first reason is that KPFM is a very low intrusive technique. The same area can be scanned several times before starting to see a degradation of the signal due to either sample or tip deterioration.
- The second reason is that surface potential changes measured by KPFM can be directly compared to macro-scale voltages (e.g. open circuit voltage and applied electrical bias) to assess if measurements are quantitative or to identify areas of voltage losses. This makes KPFM a powerful tool to investigate diodes and resistances at the nano-scale. The effect of the series resistance can be enhanced in forward electrical bias, reduced under reverse bias or even suppressed in open circuit conditions under illumination. The effect of the diode is visible, under the different operating conditions. Therefore KPFM can be used to investigate power losses (by identifying parasitic resistances) and it can also provide valuable additional inputs for advanced modeling of solar cells.
- The third reason is that, even though KPFM under ambient air is limited by a relatively high thermal noise (section 3.6), illumination and electrical bias induce surface potential changes in the solar cell which are one to two orders of magnitude higher than the noise level. This opens a wide range of operating conditions to be investigated by KPFM. For instance, we have studied the influence of illumination intensity (section 6.3.1), illumination wavelength (section 6.3.2), applied electrical bias value (section 6.2.1) and the frequency of modulated electrical bias (section 6.2.3). However, other parameters can be investigated. For instance the light beam position, the frequency of modulated illumination, light polarization, the duty cycle of modulated electrical bias could also be considered. In the conclusion of this manuscript, we will present the perspective measurements that seem of interest to us. The influence of temperature will also be considered. If the noise level is too high for certain kind of measurements under ambient air, measurements can be carried out under ultra-high vacuum (UHV) because the noise level is one order of magnitude lower (section 3.6). We suggest that a combination between ambient air KPFM and KPFM under UHV can be valuable. KPFM under ambient air is versatile and helps quickly perform measurements customized for the solar cell of interest. Once the proof of concept is achieved, KPFM measurements under UHV can take over to provide more accurate and higher signal-to-noise ratio measurements, because they are more costly and time consuming to perform.
- The fourth reason is that KPFM has a time-averaging capability that enables to be sensitive to decay times below its time resolution (section 6.2.3). Other groups have shown that KPFM measurements under modulation frequency illumination enabled lifetime assessment on the surface of solar cells with a nano-scale lateral resolution. We have shown that KPFM measurements under modulated frequency electrical bias enable lifetime assessment on the cross-section of solar cells with a nano-scale lateral resolution.

However, KPFM is limited by some artifacts (section 3.1 & 3.2.3 & 3.5) and by its acquisition time and sampling area (section 3.7). Therefore, SEM could be a complementary technique to investigate solar cells under electrical biases based on the comprehensive comparison between KPFM and SEM presented in section 6.2. Compared to KPFM, SEM is limited by carbon contamination making measurement intrusive for long time exposures (section 4.3). Besides, SEM is not sensitive to illumination (section 4.2), it has a lower signal-to-noise ratio compared to KPFM and does not have the time averaging capabilities of KPFM (section 4.6). A combination between KPFM and SEM would enable to combine the benefits of both techniques: first, large SEM images could be performed to identify the defective areas. This step would be performed quickly to avoid carbon contamination. Then, KPFM would investigate the defective areas of the solar cell by performing measurements on the same area under operating conditions. The operating conditions (e.g. illumination parameters, electrical bias parameters, temperature) can be customized to the solar cell investigated and to the opto-electronic properties of interest (e.g. space charge region width, doping levels of layers (section 6.2.1), electric field profiles (section 6.2.2), carrier lifetime at nano-scale (section 6.2.3), open circuit voltage at nano-scale (section 6.3.1), current mismatch in multi-junction solar cells (section 6.3.2)).

REFERENCES

[1] E. Radziemska, "The effect of temperature on the power drop in crystalline silicon solar cells," *Renew. Energy*, vol. 28, no. 1, pp. 1–12, Jan. 2003.

[2] D. Lange, P. Roca i Cabarrocas, N. Trantafyllidis, and D. Daineka, "Mechanical loading effects on the resistivity of thin film semiconductors," *29th EU PVSEC Proceedings, no.* 3DV.4.8, pp. 1890–1893, 2014

[3] J. B. Li, V. Chawla, and B. M. Clemens, "Investigating the Role of Grain Boundaries in CZTS and CZTSSe Thin Film Solar Cells with Scanning Probe Microscopy," *Adv. Mater.*, vol. 24, no. 6, pp. 720–723, Feb. 2012.

[4] C.-S. Jiang, I. L. Repins, C. Beall, H. R. Moutinho, K. Ramanathan, and M. M. Al-Jassim, "Investigation of micro-electrical properties of Cu2ZnSnSe4 thin films using scanning probe microscopy," *Sol. Energy Mater. Sol. Cells*, vol. 132, pp. 342–347, Jan. 2015.

[5] C.-S. Jiang, D. J. Friedman, J. F. Geisz, H. R. Moutinho, M. J. Romero, and M. M. Al-Jassim, "Distribution of built-in electrical potential in GaInP2/GaAs tandem-junction solar cells," *Appl. Phys. Lett.*, vol. 83, p. 1572, Aug. 2003.

[6] C.-S. Jiang, A. Ptak, B. Yan, H. R. Moutinho, J. V. Li, and M. M. Al-Jassim, "Microelectrical characterizations of junctions in solar cell devices by scanning Kelvin probe force microscopy," *Ultramicroscopy*, vol. 109, no. 8, pp. 952–957, Jul. 2009.

[7] H. R. Moutinho, R. G. Dhere, C.-S. Jiang, Y. Yan, D. S. Albin, and M. M. Al-Jassim, "Investigation of potential and electric field profiles in cross sections of CdTe/CdS solar cells using scanning Kelvin probe microscopy," *J. Appl. Phys.*, vol. 108, no. 7, p. 74503, Oct. 2010.

[8] M. Moczała, N. Sosa, A. Topol, and T. Gotszalk, "Investigation of multi-junction solar cells using electrostatic force microscopy methods," *Ultramicroscopy*, vol. 141, pp. 1–8, Jun. 2014.

[9] R. Ihly, S. U. Nanayakkara, J. Gao, J. Zhang, M. Law, and J. M. Luther, "Imaging interfacial layers and internal fields in nanocrystalline junctions," *40th IEEE Photovoltaic Specialist Conference (PVSC)*, pp. 3498–3501, 2014

[10] C. S. Jiang, H. R. Moutinho, R. Reedy, M. M. Al-Jassim, and A. Blosse, "Two-dimensional junction identification in multicrystalline silicon solar cells by scanning Kelvin probe force microscopy," *J. Appl. Phys.*, vol. 104, no. 10, p. 104501, 2008.

[11] C.-S. Jiang, H. R. Moutinho, M. J. Romero, M. M. Al-Jassim, Y. Q. Xu, and Q. Wang, "Distribution of the electrical potential in hydrogenated amorphous silicon solar cells," *Thin Solid Films*, vol. 472, no. 1–2, pp. 203–207, Jan. 2005.

[12] J. T. Heath, C.-S. Jiang, and M. M. Al-Jassim, "Measurement of semiconductor surface potential using the scanning electron microscope," *J. Appl. Phys.*, vol. 111, no. 4, p. 46103, Feb. 2012.

[13] J. T. Heath, C. S. Jiang, and M. M. Al-Jassim, "Diffused junctions in multicrystalline silicon solar cells studied by complementary scanning probe microscopy and scanning electron microscopy techniques," *35th IEEE Photovoltaic Specialists Conference (PVSC)*, 2010, pp. 000227–000232.

[14] P. Tchoulfian, F. Donatini, F. Levy, A. Dussaigne, P. Ferret, and J. Pernot, "Direct Imaging of p–n Junction in Core–Shell GaN Wires," *Nano Lett.*, vol. 14, no. 6, pp. 3491–3498, Jun. 2014.

[15] D. Tsurumi, K. Hamada, and Y. Kawasaki, "Energy-Filtered Secondary-Electron Imaging for Nanoscale Dopant Mapping by Applying a Reverse Bias Voltage," *Jpn. J. Appl. Phys.*, vol. 51, p. 106503, Oct. 2012.

[16] T. H. P. Chang and W. C. Nixon, "Electron beam induced potential contrast on unbiased planar transistors," *Solid-State Electron.*, vol. 10, no. 7, pp. 701–704, Jul. 1967.

[17] I. Volotsenko, M. Molotskii, Z. Barkay, J. Marczewski, P. Grabiec, B. Jaroszewicz, G. Meshulam, E. Grunbaum, and Y. Rosenwaks, "Secondary electron doping contrast: Theory based on scanning electron microscope and Kelvin probe force microscopy measurements," *J. Appl. Phys.*, vol. 107, no. 1, p. 14510, Jan. 2010.

[18] D. Venables, "Secondary electron imaging as a two-dimensional dopant profiling technique: Review and update," *J. Vac. Sci. Technol. B.*, vol. 16, no. 1, p. 362, Jan. 1998.

[19] P. Narchi, V. Neplokh, V. Piazza, T. Bearda, F. Bayle, M. Foldyna, C. Toccafondi, P. Prod'homme, M. Tchernycheva, and P. Roca i Cabarrocas, "Surface potential investigation on interdigitated back contact solar cells by scanning electron microscopy and Kelvin probe force microscopy: effect of electrical bias," Submitted to *Sol. Energy Mater. Sol. Cells*

[20] P. Narchi, T. Bearda, M. Foldyna, G. Picardi, P. Prod'homme, and P. Roca i Cabarrocas, "Interdigitated back contact silicon solar cells: diode and resistance investigation at nanoscale using

Kelvin Probe Force Microscopy," *43rd IEEE Photovoltaic Specialists Conference (PVSC)*, pp. 3082–3085, 2016

[21] M. Filipič, Z. C. Holman, F. Smole, S. D. Wolf, C. Ballif, and M. Topič, "Analysis of lateral transport through the inversion layer in amorphous silicon/crystalline silicon heterojunction solar cells," *J. Appl. Phys.*, vol. 114, no. 7, p. 74504, Aug. 2013.

[22] P. Narchi, G. Picardi, R. Cariou, M. Foldyna, P. Prod'homme, and P. Roca i Cabarrocas, "Kelvin Probe Force Microscopy Study of Electric Field Homogeneity in Epitaxial Silicon Solar Cells Cross-Section," *31st EU PVSEC Proceedings*, vol. 3BO.6.1, pp. 1026–1029, 2015.

[23] P. Narchi, R. Cariou, M. Foldyna, P. Prod'homme, and P. R. i Cabarrocas, "Nanoscale Investigation of Carrier Lifetime on the Cross Section of Epitaxial Silicon Solar Cells Using Kelvin Probe Force Microscopy." Accepted by *IEEE Journal of Photovoltaics.*

[24] M. Dapor, B. J. Inkson, C. Rodenburg, and J. M. Rodenburg, "A comprehensive Monte Carlo calculation of dopant contrast in secondary-electron imaging," *EPL Europhys. Lett.*, vol. 82, no. 3, p. 30006, 2008.

[25] C. S. Jiang, J. T. Heath, H. R. Moutinho, J. V. Li, and M. M. Al-Jassim, "Two-dimensional measurement of n+-p asymmetrical junctions in multicrystalline silicon solar cells using AFM-based electrical techniques with nanometer resolution," *37th IEEE Photovoltaic Specialists Conference (PVSC)*, pp. 001972–001977, 2011

[26] J. D. Major, L. Bowen, R. Treharne, and K. Durose, "Assessment of photovoltaic junction position using combined focused ion beam and electron beam-induced current analysis of close space sublimation deposited CdTe solar cells," *Prog. Photovolt. Res. Appl.*, vol. 22, no. 10, pp. 1096–1104, Oct. 2014.

[27] R. Cariou, W. Chen, I. Cosme-Bolanos, J.-L. Maurice, M. Foldyna, V. Depauw, G. Patriarche, A. Gaucher, A. Cattoni, I. Massiot, S. Collin, E. Cadel, P. Pareige, and P. Roca i Cabarrocas, "Ultrathin PECVD epitaxial Si solar cells on glass via low-temperature transfer process," *Prog. Photovolt. Res. Appl.*, vol. 24, no. 8, pp. 1075–1084, Aug. 2016.

[28] R. Cariou, "Epitaxial growth of Si(Ge) materials on Si and GaAs by low temperature PECVD: towards tandem devices," Ph.D. thesis, Ecole Polytechnique, 2014.

[29] M. Takihara, T. Takahashi, and T. Ujihara, "Minority carrier lifetime in polycrystalline silicon solar cells studied by photoassisted Kelvin probe force microscopy," *Appl. Phys. Lett.*, vol. 93, no. 2, p. 21902, Jul. 2008.

[30] Ł. Borowik, H. Lepage, N. Chevalier, D. Mariolle, and O. Renault, "Measuring the lifetime of silicon nanocrystal solar cell photo-carriers by using Kelvin probe force microscopy and x-ray photoelectron spectroscopy," *Nanotechnology*, vol. 25, no. 26, p. 265703, 2014.

[31] G. Shao, M. S. Glaz, F. Ma, H. Ju, and D. S. Ginger, "Intensity-Modulated Scanning Kelvin Probe Microscopy for Probing Recombination in Organic Photovoltaics," *ACS Nano*, vol. 8, no. 10, pp. 10799–10807, Oct. 2014.

[32] Y. Nakajima, M. Takihara, T. Minemoto, and T. Takahashi, "Photovoltage decay measurements on Cu(In,Ga)Se2 solar cells by photo-assisted Kelvin probe force microscopy," *38th IEEE Photovoltaic Specialists Conference (PVSC)*, pp. 001736–001738, 2012.

[33] Z. Schumacher, Y. Miyahara, A. Spielhofer, and P. Grutter, "Measurement of Surface Photovoltage by Atomic Force Microscopy under Pulsed Illumination," *Phys. Rev. Appl.*, vol. 5, no. 4, p. 44018, Apr. 2016.

[34] Z. Schumacher, A. Spielhofer, Y. Miyahara, and P. Grutter, "The lower limit for time resolution in frequency modulation atomic force microscopy," *ArXiv160902362 Cond-Mat*, Sep. 2016.

[35] R. H. Kingston, "Switching Time in Junction Diodes and Junction Transistors," *Proceedings of the IRE*, vol. 42, no. 5, pp. 829–834, May 1954.

[36] C. L. Ma and P. O. Lauritzen, "A simple power diode model with forward and reverse recovery," *22nd Annual IEEE Power Electronics Specialists Conference PESC*, pp. 411–415, 1991

[37] Yamazaki, Kobayashi, and Shinohara, "Forward transient behavior of PiN and super junction diodes," *16th International Symposium on Power Semiconductor Devices and ICs (ISPSD)* pp. 197–200, 2014

[38] D. C. Lewis, "On the determination of the minority carrier lifetime from the reverse recovery transient of pnR diodes," *Solid-State Electron.*, vol. 18, no. 1, pp. 87–91, Jan. 1975.

[39] D. Macdonald and A. Cuevas, "Trapping of minority carriers in multicrystalline silicon," *Appl. Phys. Lett.*, vol. 74, no. 12, pp. 1710–1712, Mar. 1999.

[40] T. Glatzel, M. Rusu, S. Sadewasser, and M. C. Lux-Steiner, "Surface photovoltage analysis of thin CdS layers on polycrystalline chalcopyrite absorber layers by Kelvin probe force microscopy," *Nanotechnology*, vol. 19, no. 14, p. 145705, 2008.
[41] E. M. Tennyson, J. L. Garrett, J. A. Frantz, J. D. Myers, R. Y. Bekele, J. S. Sanghera, J. N. Munday, and M. S. Leite, "Nanoimaging of Open-Circuit Voltage in Photovoltaic Devices," *Adv. Energy Mater.*, vol. 5, no. 23, p. n/a-n/a, Dec. 2015.
[42] C. Loppacher, U. Zerweck, S. Teich, E. Beyreuther, T. Otto, Stefan Grafström, and L. M. Eng, "FM demodulated Kelvin probe force microscopy for surface photovoltage tracking," *Nanotechnology*, vol. 16, no. 3, p. S1, 2005.
[43] T. Takahashi, "Photoassisted Kelvin Probe Force Microscopy on Multicrystalline Si Solar Cell Materials," *Jpn. J. Appl. Phys.*, vol. 50, no. 8, p. 08LA05, Aug. 2011.
[44] Z. Zhang, M. Hetterich, U. Lemmer, M. Powalla, and H. Hölscher, "Cross sections of operating Cu(In,Ga)Se2 thin-film solar cells under defined white light illumination analyzed by Kelvin probe force microscopy," *Appl. Phys. Lett.*, vol. 102, no. 2, p. 23903, Jan. 2013.
[45] S. Saraf, R. Shikler, J. Yang, and Y. Rosenwaks, "Microscopic surface photovoltage spectroscopy," *Appl. Phys. Lett.*, vol. 80, no. 14, pp. 2586–2588, Apr. 2002.
[46] T. Meoded, R. Shikler, N. Fried, and Y. Rosenwaks, "Direct measurement of minority carriers diffusion length using Kelvin probe force microscopy," *Appl. Phys. Lett.*, vol. 75, no. 16, pp. 2435–2437, Oct. 1999.
[47] C.-S. Jiang, H. R. Moutinho, D. J. Friedman, J. F. Geisz, and M. M. Al-Jassim, "Measurement of built-in electrical potential in III–V solar cells by scanning Kelvin probe microscopy," *J. Appl. Phys.*, vol. 93, no. 12, pp. 10035–10040, Jun. 2003.
[48] A. Ankudinov, "Solar cell diagnostics using Kelvin force microscopy and local photoexcitation," *Microsc. Anal*, 2012.
[49] R. Nowak, D. Moraru, T. Mizuno, R. Jablonski, and M. Tabe, "Potential profile and photovoltaic effect in nanoscale lateral pn junction observed by Kelvin probe force microscopy," *Thin Solid Films*, vol. 557, pp. 249–253, Apr. 2014.
[50] L. Kronik and Y. Shapira, "Surface photovoltage phenomena: theory, experiment, and applications," *Surf. Sci. Rep.*, vol. 37, no. 1–5, pp. 1–206, Dec. 1999.
[51] Y. Kutes, B. A. Aguirre, J. L. Bosse, J. L. Cruz-Campa, D. Zubia, and B. D. Huey, "Mapping photovoltaic performance with nanoscale resolution," *Prog. Photovolt. Res. Appl.*, vol. 24, no. 3, pp. 315–325, Mar. 2016.
[52] J. Heo and S. Won, "Scanning probe study on the photovoltaic characteristics of a Si solar cell by using Kelvin force microscopy and photoconductive atomic force microscopy," *Thin Solid Films*, vol. 546, pp. 353–357, Nov. 2013.
[53] A. Fejfar, M. Hývl, M. Ledinský, A. Vetushka, J. Stuchlík, J. Kočka, S. Misra, B. O'Donnell, M. Foldyna, L. Yu, and P. Roca i Cabarrocas, "Microscopic measurements of variations in local (photo)electronic properties in nanostructured solar cells," *Sol. Energy Mater. Sol. Cells*, vol. 119, pp. 228–234, Dec. 2013.
[54] J. Alvarez, J. P. Kleider, F. Houzé, M. Y. Liao, and Y. Koide, "Local photoconductivity on diamond metal-semiconductor-metal photodetectors measured by conducting probe atomic force microscopy," *Diam. Relat. Mater.*, vol. 16, no. 4–7, pp. 1074–1077, Apr. 2007.
[55] D. C. Coffey, O. G. Reid, D. B. Rodovsky, G. P. Bartholomew, and D. S. Ginger, "Mapping Local Photocurrents in Polymer/Fullerene Solar Cells with Photoconductive Atomic Force Microscopy," *Nano Lett.*, vol. 7, no. 3, pp. 738–744, Mar. 2007.
[56] H. Li, C. S. Jiang, W. K. Metzger, C. K. Shih, and M. Al-Jassim, "Microscopic Real-Space Resistance Mapping Across CdTe Solar Cell Junctions by Scanning Spreading Resistance Microscopy," *IEEE J. Photovolt.*, vol. 5, no. 1, pp. 395–400, Jan. 2015.
[57] M. Gwon, A. Sohn, Y. Cho, S.-H. Phark, J. Ko, Y. Sang Kim, and D.-W. Kim, "Plasmon-Enhanced Surface Photovoltage of ZnO/Ag Nanogratings," *Sci. Rep.*, vol. 5, Nov. 2015.
[58] P. Narchi, J. Alvarez, P. Chrétien, G. Picardi, R. Cariou, M. Foldyna, P. Prod'homme, J.-P. Kleider, and P. R. i Cabarrocas, "Cross-Sectional Investigations on Epitaxial Silicon Solar Cells by Kelvin and Conducting Probe Atomic Force Microscopy: Effect of Illumination," *Nanoscale Res. Lett.*, vol. 11, no. 1, Feb. 2016.
[59] L. Weber, M. Lehr, and E. Gmelin, "Electrical properties of silicon point contacts," *Phys. Rev. B*, vol. 43, no. 5, pp. 4317–4322, Feb. 1991.

[60] A. Kikukawa, S. Hosaka, and R. Imura, “Silicon pn junction imaging and characterizations using sensitivity enhanced Kelvin probe force microscopy,” *Appl. Phys. Lett.*, vol. 66, no. 25, pp. 3510–3512, Jun. 1995.

[61] E. M. Tennyson, J. L. Garrett, C. Gong, J. A. Frantz, J. D. Myers, R. Y. Bekele, J. S. Sanghera, J. N. Munday, and M. S. Leite, “Assessing local voltage in CIGS solar cells by nanoscale resolved Kelvin Probe Force Microscopy and sub-micron photoluminescence,” *40th IEEE Photovoltaic Specialist Conference (PVSC)*, pp. 0691–0694, 2014.

[62] R. Giridharagopal, P. A. Cox, and D. S. Ginger, “Functional Scanning Probe Imaging of Nanostructured Solar Energy Materials,” *Acc. Chem. Res.*, vol. 49, no. 9, pp. 1769–1776, Sep. 2016.

Chapter 7 –
Conclusions & Perspectives

Contents

7.0 Introduction

In a context of increasing competitiveness of photovoltaic industry, crystalline silicon (c-Si) solar cells are likely to keep the major market share (>80%) in the medium term. Even though, the efficiency of record c-Si solar cells (26.33%) is little by little approaching the Shockley-Queisser limit for single junction solar cells (~30%), several technical improvements are being further considered to increase the efficiency, reduce the cost and improve the reliability of crystalline silicon solar cells. Since these challenges are getting more complex with increasing cell efficiency, advanced characterization techniques are needed to understand precisely the phenomena at stake. Among the features required from advanced characterization techniques, high spatial resolution is a feature of high interest to allow to investigate phenomena at the nano-scale. With electron microscopy, scanning probe microscopy is one of two main microscopy families which enable nano-scale resolution. In the last four decades, scanning probe microscopy techniques have gone from the proof of concept stage to a family of techniques enabling a broad range of measurements at the nano-scale. In particular, AFM electrical extensions have proven to allow several kinds of electrical measurements at the nano-scale.

In this context, this PhD project was designed to answer the following question: “How can AFM electrical extensions help make better crystalline silicon solar cells?”. To do so, we chose to focus on two kinds of AFM electrical extensions that have been very popular lately: Kelvin Probe Force Microscopy (KPFM) and Conducting Probe Atomic Force Microscopy (CP-AFM). In our analysis, we chose to compare these techniques to competing electron microscopy techniques.

In this conclusion chapter, we propose a summary table to outline the take-aways from Chapter 3 to Chapter 6. The weaknesses and strengths of scanning probe microscopies (SPM) (Chapter 3 & 4) represent the lines of the table. The SPM measurements we found valuable to investigate crystalline silicon material properties (Chapter 5) and devices properties (Chapter 6) represent the columns of the table. Then, we synthetize our results by proposing, as a prospective work: an ideal microscopy setup to investigate crystalline silicon solar cells (with no budget constraints).

7.1 Take-away messages

In order to sum up our results, we chose to present our conclusions in a comprehensive table (Table 7.1). The first column of Table 7.1 displays the weaknesses and strengths mentioned respectively in Chapter 3 and Chapter 4. The first line of Table 7.1 displays material measurements and device measurements mentioned respectively in Chapter 5 and Chapter 6. For the weaknesses, the color of each case represents how much a weakness affects the measurements. The color goes from light red (small negative impact) to dark red (strong negative impact). For the strengths, the color of each case represents how much a strength of the scanning probe microscopy (SPM) technique is differentiating compared to electron microscopy (EM) techniques. The color goes from light green (as good as EM) to dark green (uniqueness of this SPM advantage, compared to EM). For both strengths and weaknesses, grey color means that there is no impact on the measurement. The choice of colors comes from our experience, and can, of course, be discussed and challenged. However, we think that it is a good starting point for discussion between microscope experts and solar cell physicists.

This table can be read in two ways: vertically and horizontally. Vertical reading enables to identify which measurements are the most challenging and the most valuable compared to electron microscopy. Horizontal reading enables to determine which weaknesses affect most our measurements and which strengths make our measurements most valuable.

From the vertical reading of weaknesses, we can see that CP-AFM doping measurements are strongly affected by only one weakness: the dependence on topography. The only way to avoid it, in our opinion is to investigate ultra-flat surfaces. CP-AFM is also more affected than KPFM by tip

degradation and tip-induced surface degradation. This is because the contact mode used in CP-AFM is much more intrusive than tapping mode used in KPFM. However, contrary to KPFM, CP-AFM is not affected by thermal noise and stray capacitances which are specific to tapping mode. Besides, CP-AFM measurements are less affected by surface state (e.g. oxidation, band bending) because the strong force used in CP-AFM enables to go through the first layer of the surface. Among KPFM measurements, lifetime measurements are the most challenging because the signal changes are smaller and the quality of the surface investigated can affect measurements. Therefore these measurements are more limited by thermal noise and surface contamination issues than the rest of KPFM measurements. KPFM measurements under illumination are a bit more challenging than measurements under electrical bias, because of the effect of AFM laser that may affect the measurements. However, contrary to measurements under electrical bias, measurements under illumination only need one back contact, therefore they can be more adapted to material investigation when the device is not yet completed.

From the vertical reading of strengths, we can see that all our measurements bring a strong differentiating factor compared to electron microscopy techniques. We believe that this is the reason why these measurements bring additional value for the investigation of solar cells. The strong differentiating factor of doping measurements using CP-AFM is that it is a direct measurement of the resistivity which is a parameter strongly dependent on the doping level. This makes CP-AFM a very powerful technique to investigate doping at the nano-scale. Other SPM and EM techniques can hardly compete with CP-AFM, as was shown in sub-section 5.2.1. Regarding KPFM, lifetime measurements at the nano-scale strongly differentiate from electron microscopy techniques. These measurements strongly benefit from the low charging effects of KPFM and acquisition time and averaging effect of KPFM. Besides, they also take advantage of the possibility to perform measurements under illumination and of the versatility of KPFM techniques to design new measurements. Measurements under illumination also bring strong additional value, given that it is challenging to see the effect of illumination at the nano-scale, because of carrier injection levels. SPM are unique microscopy techniques to investigate the effect of illumination at the nano-scale. Among SPM techniques, KPFM is well adapted because photovoltages measured by KPFM at the nano-scale can be directly compared to the open-circuit voltage of the solar cell measured with a voltmeter. This is the advantage of performing direct electrical measurements. This is also a differentiating advantage for KPFM measurements under electrical bias, where surface potential changes can be directly compared to the value of the applied electrical bias. Compared to EM, KPFM measurements under electrical bias and illumination benefit from the fact that KPFM has a low charging effect. Therefore, several measurements can be performed on the same area while changing the value of either the electrical bias or of the illumination. KPFM strongly benefits from the fact that it is a low intrusiveness technique. This makes it a powerful tool to investigate the influence of external parameters.

From the horizontal reading of weaknesses, we observe that the three most problematic weaknesses are the convolution with topography, stray capacitance and the surface dependence. Therefore, in the ideal setup we imagine and we present in section 7.2, we will pay particular attention to find solutions to limit these weaknesses. Then, tip-induced degradation, thermal noise and the stray illumination of AFM laser can lead some challenges and have also to be considered. Finally, tip degradation and scan speed and sampling area seem to be less important issues to address.

From the horizontal reading of strengths, we show that the fact that SPM performs direct electrical measurements and that they have low charging effects, constitute strong advantages compared to electron microscopy. Acquisition time and averaging effect of KPFM, as well as sensitivity to illumination also constitute unique features for lifetime measurements and measurements under illumination. Finally, spatial resolution and versatility are two helpful features for measurements but do not provide such an important advantage when compared to EM. Table 7.1 enables to take a step back and identify where the efforts should be put in priority. Using this analysis, we will describe our “ideal” microscope setup to investigate silicon solar cells at the nano-scale.

Table 7.1 – Impact of the weaknesses and strengths (described in Chapter 3 and Chapter 4) on the material and devices measurements (described in Chapter 5 and Chapter 6).

Weaknesses / Strengths	Doping at nano-scale (CP-AFM) *(Section 5.2)*	Lifetime at nano-scale (KPFM) *(Section 5.3 & 6.2.3)*	Sensitivity to electrical bias & Extraction of electric field (KPFM) *(Section 6.2.1 & 6.2.2)*	Sensitivity to light intensity and wavelength (KPFM) *(Section 6.3.1 & 6.3.2)*
AFM Laser Induced V_{oc} *(Section 3.1)*				
Tip-induced Degradation *(Section 3.2)*				
Tip Degradation during scans *(Section 3.3)*				
Convolution to topography *(Section 3.4)*				
Stray Cap. *(Section 3.5)*				
Thermal Noise *(Section 3.6)*				
Scan Speed & Size *(Section 3.7)*				
Surface Dep. *(Section 3.8)*				
Spatial Res. *(Section 4.1)*				
Sensitivity to Illumination *(Section 4.2)*				
Low Charging Effects *(Section 4.3)*				
Direct Electrical Measurements *(Section 4.4)*				
Versatility *(Section 4.5)*				
Acquisition Time & Averaging effect *(Section 4.6)*				

Strong negative effect on measurement	Medium negative effect on measurements	Small negative effect on measurements	No Im-pact	Helpul for measurements (SPM = EM)	Advantageous for measurements (SPM > EM)	Uniqueness for measurements (SPM >> EM)

7.2 Perspectives: Our “ideal” microscope to investigate solar cells

Contrary to the competitive world of processing and devices, the world of characterization is collaborative. The more characterization techniques there are, the more understanding of the solar cells there is. Performing the same measurement with different characterization techniques enables to gain confidence on the information obtained and to remove artifacts specific to certain techniques. In this manuscript, we have compared electron, optical and scanning probe microscopy techniques to determine the strengths and weaknesses of each. However, these three techniques can work together to make microscopy measurements of solar cells even more accurate and precise.

Based on this observation, we propose our “ideal” microscopy setup that includes the three kinds of microscopy. As discussed in section 4.5, this setup is composed of two equipments. The first equipment is a versatile microscope that can work under ambient air and controlled atmosphere. It combines optical microscope and scanning probe microscope. It will be called OM/SPM. The second microscope is a high precision microscope working under ultra-high vacuum. It combines electron microscopy and scanning probe microscopy. It will be called EM/SPM.

Both OM/SPM and EM/SPM enable to “see” and “touch” the matter at the nano-scale. The interest of combining these two equipments is that OM/SPM is used to design quickly measurements of interest for different technologies of solar cells. Once the proof of concept measurement is achieved using OM/SPM, the measurement principle can be transferred directly to EM/SPM setup to perform high accuracy measurements. The final goal of this setup is to propose nano-scale electrical measurements customized for a given technology of solar cell and a given problem that has to be addressed. That is why this system needs to be versatile.

In the following, we will detail features of both microscopes, the features that are specific to the OM/SPM and the EM/SPM, and finally the sample holders that enable to perform a broad range of measurements on solar cells using the two setups. This “ideal” microscope setup is based on the previous chapters of this manuscript.

7.2.1 Features of both microscopes

It is clear that using an an AFM system with a laser in the visible range is a source of artifacts and uncertainty for measurements on solar cells (section 3.1). Therefore both KPFM and CP-AFM should have an infrared laser with a wavelength λ>1100 nm. This is already the case for certain commercial AFMs [1].

Regarding the probes used for the measurements, bulk conductive probes have been shown to be interesting because they are more reliable and the tip radius can be smaller enabling better resolution (section 4.1). The material used should be highly conductive to avoid series resistance that can be problematic for CP-AFM measurements on highly conductive samples (sub-section 5.1.3). The material should also ideally be hydrophobic to avoid tip contamination (sub-section 3.3.2). The probes should be long to reduce stray capacitance effects from the cantilever in KPFM measurements (section 3.5). Ideally, these probes should be compatible both with CP-AFM and KPFM to be able to perform both measurements on the same area without changing the tip.

Before performing measurements, the preparation process is key to avoid parasitic surface effects (section 3.8). Therefore, a cleaning process adapted to the solar cell technology should be desgined precisely. In our case, our cleaning process (isopropanol + ethanol) was not good enough to guarantee reproducibility of measurements. Further investigations should be carried out to define ideal cleaning processes to guarantee reproducibility. In any case, performing measurements just after processing the device or cleaving the cross-section gives more confidence in the electrical measurements. Moistering can degrade the electrical properties of the solar cell with time. Therefore, it is key to maintain the samples in dry atmosphere between measurements (e.g. nitrogen boxes). Therefore, in our “ideal” microscope setup, an access to nitrogen should be present. Besides,

chemicals and wet benches used to find the adequate cleaning process should also be close to the microscope room. Besides, the importance of a mirror-like cross-section preparation was highlighted by Scherrer *et al.* [2].We found that micro-cleavage is a quick, low intrusive technique compared to mechanical polishing, even though the throughput was around 50%. Therefore, we propose that a micro-cleavage setup should be present close to our "ideal" microscopes [3]. We have seen that "bevel cross-sections" are useful to increase the resolution of the measurements. Therefore, we believe that a polishing setup to prepare these kinds of cross-section is also valuable for our microscopy setup [4].

Regarding the measurement possibilities, both OM/SPM and EM/SPM should have advanced capabilities for CP-AFM and KPFM measurements. CP-AFM should be equipped with a logarithmic amplifier as for Resiscope and SSRM. However, it should be able to measure currents lower than current CP-AFM and SSRM, in order to be able to perform measurements without scratching the surface, as for current measurements (sub-section 3.2.2). If the setup can measure lower currents, it will require lower contact areas between the tip and the sample to perform measurements. Therefore, a lower force will be applied on the tip and the risk of nano-scratching the surface will decrease. Regarding KPFM, our setups should be able to perform AM-KPFM and FM-KPFM. The lowest voltages should be used on the KPFM tip to avoid tip-induced band bending effects (sub-section 3.2.3). The effects of cross-talk should be minimized to reduce the topographical imprints on the surface potential images (section 3.4), as shown by Barbet *et al.* [5]. Besides, our KPFM measurement process should be time resolved with a time resolution below the microsecond. For this KPFM mode can be used like G-Mode KPFM [6] and should be associated with time resolved EFM and time resolved CP-AFM. These different techniques should enable advanced lifetime investigations at the nano-scale (section 4.6). Finally for both our setups, the solar cell can be contacted when it is on the AFM stage. Therefore, a current voltage J(V) curve can be measured at all times using a voltage source and an ampere meter. Besides, open circuit voltage (V_{oc}) can be measured at all times using a voltmeter. J(V) and V_{oc} can help assess if the solar cell was degraded during measurements (e.g. increase of series or shunt resistances).

Versatility is key to our "ideal" microscope setup. First, inter-communication between OM/SPM and EM/SPM should be user-friendly. Both setups have the same sample holders (for surface and cross-section analysis). These advanced cross-sections can be plugged to an optical fiber and have electrodes to contact the solar cell. Since the same sample holders are used for both setups, it is possible to keep the position on the sample holder while moving the set {sample+sample holder} from an equipment to another. This is very helpful for geo-location and for performing measurements under the same conditions of illumination. Besides, the same software is used for the two equipments and the same area can easily be measured thanks to advanced nano geo-location systems.

Besides, the software uses measurement parameters that are clearly expressed in KPFM and CP-AFM measurement equations, and not intermediate measurement parameters that are hard to understand. Furthermore, the measurement process on our setup would be more versatile than current setups thanks to automatic AFM laser positioning and precise AFM tip positioning. High resolution lateral view of AFM tip and sample would help precise AFM positioning. The positioning of the AFM tip would also be helped by automatic and accurate motion of the AFM plate. This would help perform measurements on a position previously saved. It would also enable to perform measurements at different positions that require withdrawing the tip between measurements. Hence, the microscope operator could define different distant positions and the AFM would scan them automatically without the operator being in the room. Besides, the scan size and speed would be improved (section 4.1) through the use of new kinds of KPFM, called heterodyne KPFM [7]. Other versatile features would help make measurement easier. For instance, the AFM scanner would carry several tips at the same time. By carrying different kinds of tips (KPFM tip, CP-AFM tip, nano-scratching tips), different kinds of measurements could be performed without changing the scanner head. Besides, the scanner head would not be too cumbersome and it would enable topside illumination during measurements. Finally, to investigate the effect of annealing and cooling of the solar cells, the AFM plates of our equipments should be controllable in temperature and incorporate temperature sensors.

After measurements, image processing is key to interpret them. On our "ideal" microscope setup, advanced microscope image processing would be used. For instance, this software would effectively deconvolute the effect of topography on both KPFM and CP-AFM, as some groups have proposed [8]. Besides, this software would enable to remove white thermal noise on KPFM images (section 3.6) and therefore increase the signal-to-noise ratio. Advanced data processing tools based on emerging data science tools would enable to provide insights across large volumes of scanning probe data, as Strelcov *et al.* have shown [9]. Through data processing, nanoscale mapping of key informations such as carrier lifetime can be performed as shown by Fernández Garillo *et al.* [10]. This software would also incorporate a solar cell modeling part and would directly use the inputs of microscope measurements in the solar cell model to understand more precisely the behavior of the solar cell.

7.2.2 Features specific to OM/SPM

The combination of scanning probe microscopy and optical microscopy has already been promoted in the literature [11] for the versatility of the technique. Recent studies have shown that the combination of these two techniques could lead to solving concrete problems [12]. These microscopes combine optical microscopy, laser scanning microscopy and scanning probe microscopy. Our ideal OM/SPM setup would be inspired from these equipments in order to quickly design measurements of interest for different technologies of solar cells. The use of high resolution optical microscopy would help tip positioning and also to provide optical analysis of the surface investigated (color, polarization,…). Besides, 3D topographical images can also be obtained with laser scanning confocal microscopy [13].

The OM/SPM equipment would either be operated in ambient air or in controlled atmosphere. A dry atmosphere is sometimes necessary to avoid tip-induced oxidation (subsection 3.2.1). A first contact mode scan can be performed to remove layers of silicon oxide before measurements. Humidity and temperature sensors should be also included in the measurement room. During the scanning probe microscopy (SPM) measurements, the light of the optical microscope should be turned off to avoid stray illumination phenomena. However, after measurements, optical microscope images would enable to analyze the SPM scanned area to check for any degradation. If the optical microscope is equipped with Raman measurement possibilities, material analysis could be performed on the scanned area and would enable to check for oxide formation for instance.

Because studies are not performed under ultra-high vacuum (UHV), the OM/SPM measurements will be high throughput. However, studies under UHV are much more precise because they have less artifacts. As shown in the summary table of Chapter 3, measurements under UHV enable to reduce tip-induced oxidation (subsection 3.2.1), to reduce tip-induced band bending (subsection 3.2.3), to decrease tip contamination (subsection 3.3.2), to reduce thermal noise by 20 times (section 3.6) and to reduce surface related artifacts (section 3.8). This is a motivation to combine OM/SPM setup with EM/SPM which can achieve more accurate measurements despite the fact that it is less versatile.

7.2.3 Features specific to EM/SPM

The combination of electron microscopy and scanning probe microscopy in a single EM/SPM setup has been introduced in section 6.1 of this manuscript, since KPFM and SEM are complementary techniques to investigate solar cells under electrical bias. Contrary to KPFM, SEM provides fast acquisition and large scale images (> 1 mm). Besides, SEM does not suffer from artifacts of KPFM (Chapter 3) but faces challenges due to a surface modification under the electron beam exposure, mostly attributed to carbon contamination. KPFM enables quantitative, low noise, low intrusiveness images, but it is limited by its scan speed and scan area size. In addition, the KPFM does not require

injection of carriers to perform measurements and hence enables to monitor the effect of illumination at the nano-scale. Therefore, these complementary techniques could be combined in a single setup that would benefit from the advantages of both. These measurements now seem possible since a commercial setup combining SEM and SPM has been very recently available [14].

Here, we develop on the features of our "ideal" EM/SPM setup to investigate crystalline silicon solar cells. Both techniques can operate under ultra-high vacuum which enables more accurate KPFM measurements, as discussed previously.

The electron microscopy part of this setup is thought to enable a wide range of measurements. First, the effect of contamination layers such as carbon, is reduced thanks to the use of energy-filtered scanning electron imaging [15]. This setup enables time resolved SEM measurements to perform dynamic studies in solar cells and to compare these measurements [16] with time resolved KPFM and EFM measurements. The EM/SPM is also equipped with advanced electron microscopy techniques that are coupled to SEM: Energy-Dispersive X-ray spectroscopy (EDX), Electron Beam Induced Current (EBIC), Cathodo-luminescence (CL). EBIC can help provide information about diffusion length and space charge region in the devices. CL can help assess the nature of the doping (n-type or p-type) which is challenging with CP-AFM and KPFM. Besides, if CL is calibrated, it can measure the doping level. Therefore, CL seems to be a complementary technique to CP-AFM. EDX and CL allow to perform chemical analysis at the nano-scale and can help determine if an area was chemically modified by successive SPM scans. After SPM measurements, a quick SEM image of the area scanned with SPM could also help determine if the surface was topographically modified because of the tip, especially for CP-AFM measurements. The tip can also be imaged by SEM before and after SPM measurements to check for any degradation.

In order to apply an electrical bias, microprobes inside the setup should be used. This microprobe system is already used in EBIC setups. In this case, the probing system would enable to apply an electrical bias during EM imaging but also during SPM imaging. Therefore EM and SPM images would be in the exact same conditions of biasing. Constant or modulated frequency electrical biases can be used. Particular attention should be paid to minimize the series resistance in the contacting system. The parasitic contact resistance between the microprobes and the solar cell should be reduced by applying a force strong enough on the microprobes. The constraint of using microprobes to apply an electrical bias is that the quality of the contact brings uncertainty on the measurements. Besides, the contacting step can be time consuming. Therefore, for some kinds of measurements (e.g. cross-section measurements), it is sometimes preferable to apply an electrical bias directly through our customized sample holders, as explained later. In that case, the contacting is done before inserting the sample and the sample holder inside the UHV chamber. Wires are contacted to the sample holder inside the UHV chamber.

In order to illuminate the sample during measurements, an optical fiber would penetrate in the vacuum chamber through an adapted feed through. On the one side of the fiber, different kinds of fiber coupled illumination sources could be used depending on the light parameter investigated (illumination intensity, wavelength, modulation frequency, polarization). The advantage of this setup is that illumination sources can be changed while the AFM tip is still on the sample, which is helpful to perform successive measurements on the same position. On the other side of the fiber, the cannula of the optical fiber is positioned in the sample holder in the position required to illuminate the sample. The position of the cannula is not the same for cross-section measurements where the sample needs to be illuminated horizontally and for surface measurements where the sample needs to be illuminated vertically (either from the top or from the bottom). Ideally, a system enabling the cannula position change on the sample holder inside the UHV chamber would be designed to be able to investigate the influence of the position of the light spot on the electrical measurements on the solar cell.

One of the main challenges of the EM/SPM setup is the versatility. The accuracy of measurements under UHV comes at the expense of operation time. Challenges on the installation time and measurement time need to be addressed to improve the throughput of measurements. The use of

high speed heterodyne AFM/KPFM could be an example to speed up the measurements. The use of scanners with multiple tip holders would enable to reduce time due to tip changing. These are two examples to improve measurements throughput under UHV.

EM/SPM should also be equipped with an in-situ focused ion beam (FIB) milling, as proposed by Saive *et al.* [17], [18]. This technique can be used to mill holes in solar cells and characterize the bare cross-section in-situ. It can also be used to investigate solar cell in depth, by alternatively performing a measurement and milling a layer. It enables 3D-functional imaging. Another advantage of FIB is to be able to repair the probes when they are degraded. This has been advertized by equipment providers that propose a combination of SPM, EM and FIB capabilities [14]. Besides, the possibility of performing in-situ micro-cleavage should be included in our EM/SPM setup. This would prevent from deposition of contaminants at the surface of the cross-section, as it happens under ambient air.

7.3.3 Conclusion

We are convinced that the combination of OM/SPM and EM/SPM enables to achieve versatile and accurate electrical measurements at the nano-scale. The use of well designed surface and cross-section sample holders is key to achieve versatility and inter-exchanges communication between the setups. This combined setup enables to customize measurements for different solar cell technologies. The influence of temperature, electrical bias and illumination can be studied using this setup.

To sum up our analysis, we use a table (Table 7.2) to show how OM/SPM and EM/SPM setups answer to the challenges presented in Chapter 3. We compare it to the regular setup where we took the worst case of Table 7.1.

Table 7.2 shows that OM/SPM and EM/SPM setups show strong improvements compared to the regular setup we used. In particular, the effect of parasitic light from the laser and the tip degradation during scans are largely reduced. The EM/SPM also benefits from low tip-induced degradation, surface dependence and thermal noise because measurements are performed under UHV. This comes at the expense of installation and operation time for measurements. Two points remain challenging for both OM/SPM and EM/SPM: the convolution with topography and the stray capacitance effects. For these points, we find mitigating strategies but no clear suppressing strategies. To avoid the convolution with topography, measurements could be first focused on flat surfaces of solar cells (e.g. cross-section of solar cells, flat part of interdigitated back contact solar cells). Stray capacitance could be deconvoluted by first performing measurements on adapted calibration samples to determine the influence of parasitic capacitances before starting measurements on the sample of interest.

Using these setups, we believe that the measurements shown in Chapter 5 and 6 would be improved and this platform would enable to customize measurements depending on the solar cell technology of interest.

Table 7.2 – Impact of the weaknesses on the three setups: the regular setup used in this Ph.D. project, the OM/SPM setup and the EM/SPM setup.

Weaknesses	Reg. setup	OM/SPM	EM/SPM
AFM Laser Induced V_{oc}		AFM laser in IR	AFM laser in IR
Tip-induced Degradation		• Post-imaging investigation of the scanned area degradation using OM technique. • Reduction of scratching in CP-AFM (larger resistivity acquisition range) • Reduction of oxidation (better control of atmosphere for measurements) • Tip-induced band bending still problematic but lower KPFM can be used to mitigate.	• Post-imaging investigation of the scanned area degradation using EM techniques • Reduction of nano-scratching in CP-AFM (larger resistivity acquisition range) • No tip-induced oxidation (UHV) • Tip-induced band bending is reduced (work under UHV)
Tip Degradation during scans		• Reduction of the degradation of the tip coating by using bulk probes • Reduction of tip contamination by using improved cleaning process + work under appropriate controlled environment + work with hydrophobic probes	• Post-imaging investigation of the tip degradation using EM technique • Reduction of the degradation of the tip coating by using bulk probes + the possibility to repair them in-situ with FIB. • Reduction of tip contamination by improved cleaning process + work under appropriate controlled environment + hydrophobic probes.
Convolution to topography		• Use of advanced topography deconvolution software • In KPFM, use of lift mode to investigate the influence of topography • Reduction of cross-talks in KPFM	• Use of topography deconvolution software • In KPFM, use of lift mode to investigate the influence of topography • Reduction of cross-talks in KPFM • Comparison with electron microscopy measurements to check for effect of topography.
Stray Capacitance		• Use of advanced stray capacitance deconvolution software (with the help of a calibration sample) • Post-imaging data processing to de-convolute capacitance effects • In KPFM, use of lift mode to investigate the influence of topography	• Use of advanced topography deconvolution software (with the help of a calibration sample) • Post-imaging data processing to de-convolute capacitance effects • In KPFM, use of lift mode to investigate the influence of topography
Thermal Noise		• Use of advanced denoising processes in the software to remove thermal noise from the images	• Work under UHV : Noise level ~20x lower than in ambient air • Use of advanced denoising processes in the software to remove thermal noise effects
Scan Speed & Size Installation + Operation time		• Use of high speed AFM/KPFM (heterodyne AFM) • Scan size can be increased over 100µm without decreasing too much the scan speed. However, scan sizes of ~1mm are non realistic for the moment.	• Use of high speed AFM/KPFM (heterodyne AFM) • Scan size can be increased over 100µm without decreasing too much the scan speed. However, scan sizes of ~1mm still challenging • Installation time remains is still a challenge
Surface Dependence		• Adapted cleaning process just before measurements • Measurements + Conservation of samples under controlled atmosphere.	• Cross-section preparation under UHV (cleavage and FIB milling) • Cleaning step just before putting the sample in the UHV chamber to avoid silicon oxide

Strong negative effect	Medium negative effect	Small negative effect	No Impact

REFERENCES

[1] A. G. Temiryazev, S. A. Saunin, V. E. Sizov, and M. P. Temiryazeva, “Magnetic force microscopy study of domain structures in magnetic films,” *Bull. Russ. Acad. Sci. Phys.*, vol. 78, no. 1, pp. 49–52, Feb. 2014.

[2] M. Scherer, R. Saive, D. Daume, M. Kröger, and W. Kowalsky, “Sample preparation for scanning Kelvin probe microscopy studies on cross sections of organic solar cells,” *AIP Adv.*, vol. 3, no. 9, p. 92134, 2013.

[3] C. Smith, K. Kaufman, I. Mazor, E. Chen, and D. Vilenski, “Method and apparatus for cleaving semiconductor wafers,” US5740953 A, 21-Apr-1998.

[4] Y. Chen, Z. Zhang, S.-H. Ko, W.-Y. Hsu, and M. Matsuo, “Methods and apparatus for low cost and high performance polishing tape for substrate bevel and edge polishing in seminconductor manufacturing,” US20080293331 A1, 27-Nov-2008.

[5] S. Barbet, M. Popoff, H. Diesinger, D. Deresmes, D. Théron, and T. Mélin, “Cross-talk artefacts in Kelvin probe force microscopy imaging: A comprehensive study,” *J. Appl. Phys.*, vol. 115, no. 14, p. 144313, Apr. 2014.

[6] L. Collins, A. Belianinov, S. Somnath, B. J. Rodriguez, N. Balke, S. V. Kalinin, and Stephen Jesse, “Multifrequency spectrum analysis using fully digital G Mode-Kelvin probe force microscopy,” *Nanotechnology*, vol. 27, no. 10, p. 105706, 2016.

[7] J. L. Garrett and J. N. Munday, “Fast, high-resolution surface potential measurements in air with heterodyne Kelvin probe force microscopy,” *Nanotechnology*, vol. 27, no. 24, p. 245705, 2016.

[8] T. Machleidt, E. Sparrer, D. Kapusi, and K.-H. Franke, “Deconvolution of Kelvin probe force microscopy measurements—methodology and application,” *Meas. Sci. Technol.*, vol. 20, no. 8, p. 84017, 2009.

[9] E. Strelcov, A. Belianinov, Y.-H. Hsieh, S. Jesse, A. P. Baddorf, Y.-H. Chu, and S. V. Kalinin, “Deep Data Analysis of Conductive Phenomena on Complex Oxide Interfaces: Physics from Data Mining,” *ACS Nano*, vol. 8, no. 6, pp. 6449–6457, Jun. 2014.

[10] P.A. Fernández Garillo, L. Borowik, F. Caffy, R. Demadrille, and B. Grevin, "Photo-Carrier Multi-Dynamical Imaging at the Nanometer Scale in Organic and Inorganic Solar Cells", *ACS Appl. Mater. Interfaces*, Oct. 2016.

[11] S. Moreno Flores and J. L. Toca-Herrera, “The new future of scanning probe microscopy: Combining atomic force microscopy with other surface-sensitive techniques, optical microscopy and fluorescence techniques,” *Nanoscale*, vol. 1, no. 1, p. 40, 2009.

[12] N. A. Geisse, “AFM and combined optical techniques,” *Mater. Today*, vol. 12, no. 7, pp. 40–45, 2009.

[13] B. V. R. Tata and B. Raj, “Confocal laser scanning microscopy: Applications in material science and technology,” *Bull. Mater. Sci.*, vol. 21, no. 4, pp. 263–278.

[14] A. Lewis, A. Komissar, A. Ignatov, O. Fedoroyov, E. Maayan, and D. Yablon, “AFM Integrated with SEM/FIB for Complete 3D Metrology Measurements,” *Microsc. Microanal.*, vol. 20, no. S3, pp. 1112–1113, Aug. 2014.

[15] D. Tsurumi, K. Hamada, and Y. Kawasaki, “Energy-Filtered Secondary-Electron Imaging for Nanoscale Dopant Mapping by Applying a Reverse Bias Voltage,” *Jpn. J. Appl. Phys.*, vol. 51, p. 106503, Oct. 2012.

[16] J. Sun, A. Adhikari, B. S. Shaheen, H. Yang, and O. F. Mohammed, “Mapping Carrier Dynamics on Material Surfaces in Space and Time using Scanning Ultrafast Electron Microscopy,” *J. Phys. Chem. Lett.*, vol. 7, no. 6, pp. 985–994, Mar. 2016.

[17] R. Saive, M. Scherer, C. Mueller, D. Daume, J. Schinke, M. Kroeger, and W. Kowalsky, “Imaging the Electric Potential within Organic Solar Cells,” *Adv. Funct. Mater.*, vol. 23, no. 47, pp. 5854–5860, Dec. 2013.

[18] R. Saive, C. Mueller, J. Schinke, R. Lovrincic, and W. Kowalsky, “Understanding S-shaped current-voltage characteristics of organic solar cells: Direct measurement of potential distributions by scanning Kelvin probe,” *Appl. Phys. Lett.*, vol. 103, no. 24, p. 243303, Dec. 2013.

List of publications

Peer reviewed publications

- P. Narchi, J. Alvarez, P. Chrétien, G. Picardi, R. Cariou, M. Foldyna, P. Prod'homme, J.-P. Kleider, and P. R. i Cabarrocas, "Cross-Sectional Investigations on Epitaxial Silicon Solar Cells by Kelvin and Conducting Probe Atomic Force Microscopy: Effect of Illumination," *Nanoscale Res. Lett.*, vol. 11, no. 1, Feb. 2016.

- P. Narchi, R. Cariou, M. Foldyna, P. Prod'homme, and P. R. i Cabarrocas, "Nanoscale Investigation of Carrier Lifetime on the Cross Section of Epitaxial Silicon Solar Cells Using Kelvin Probe Force Microscopy." Accepted by *IEEE Journal of Photovoltaics.*

- P. Narchi, V. Neplokh, V. Piazza, T. Bearda, F. Bayle, M. Foldyna, C. Toccafondi, P. Prod'homme, M. Tchernycheva, and P. Roca i Cabarrocas, "Surface potential investigation on interdigitated back contact solar cells by scanning electron microscopy and Kelvin probe force microscopy: effect of electrical bias," Submitted to *Sol. Energy Mater. Sol. Cells*

Conference Proceedings

- V. Depauw, I. Abdo, R. Boukhicha, R. Cariou, W. Chen, I. Cosme Bolanos, O. Deparis, He Ding, A. Dmitriev, E. Drouard, O. El Daif, A. Fave, M. Foldyna, E. Garcia-Caurel, B. Heidari, A. Herman, L. Lalouat, K. D. Lee, J. Liu, K.Lodewijk, F. Mandorlo, I. Massiot, A. Mayer, J. Muller, P. Narchi, R. Orobtchouk, G. Picardi, P.Prod'Homme, P. Roca i Cabarrocas, C. Seassal, C. Trompoukis, I. Gordon, J. Poortmans, "*Nanophotonics for Ultra-Thin Crystalline Silicon Photovoltaics: When Photons (Actually) Meet Electrons*," *29th EUPVSEC Proceedings*, vol. 3BO.6.5, pp. 1461-1469, 2014

- P. Narchi, G. Picardi, R. Cariou, M. Foldyna, P. Prod'homme, and P. Roca i Cabarrocas, "Kelvin Probe Force Microscopy Study of Electric Field Homogeneity in Epitaxial Silicon Solar Cells Cross-Section," *31st EU PVSEC Proceedings*, vol. 3BO.6.1, pp. 1026–1029, 2015

- P. Narchi, T. Bearda, M. Foldyna, G. Picardi, P. Prod'homme, and P. Roca i Cabarrocas, "Interdigitated back contact silicon solar cells: diode and resistance investigation at nanoscale using Kelvin Probe Force Microscopy," *43rd IEEE Photovoltaic Specialists Conference (PVSC)*, pp. 3082–3085, 2016

Patent Pending

- P. Narchi and F. Farci, *European Procedure*

International Distinctions

- EUPVSEC Student Award, September 2015, Category: Thin Films

- Siebel Scholarship, September 2016, Category: Energy Science

Résumé

Cette thèse s'intéresse à l'analyse de cellules silicium cristallin à l'échelle nanométrique, à l'aide de techniques de microscopie à sonde locale (SPM). En particulier, nous avons choisi d'analyser les propriétés électriques à l'échelle locale, grâce à deux techniques SPM : la microcopie à sonde de Kelvin (KPFM) et la microscopie à force atomique à sonde conductrice (CP-AFM).

Tout d'abord, nous présentons les forces et faiblesses de ces deux techniques, comparées à la microscopie électronique, qui permet également d'analyser les propriétés électrique à l'échelle nanométrique. Cette comparaison approfondie nous permet d'identifier des mesures où le KPFM et le CP-AFM sont particulièrement adéquat et peuvent apporter de la valeur. Ces mesures sont divisées en deux catégories : les analyses matériaux et les analyses dispositifs.

Ensuite, nous nous focalisons sur les analyses matériaux à l'échelle nanométrique. Nous présentons d'abord des mesures de dopage à l'échelle nanométrique, à l'aide d'une technique avancée de CP-AFM, appelée Resiscope. Nous montrons que cette technique peut détecter des changements de dopage dans la gamme 10^{15} à 10^{20} atomes.cm^{-3}, avec une résolution nanométrique et un bon ratio signal/bruit. Puis, nous présentons des mesures de durée de décroissance sur des wafers silicium cristallin passivés. Les mesures sont réalisées sur la tranche non-passivée des échantillons. Nous montrons que, même si la tranche n'est pas passivée, les durées de décroissance obtenue par KPFM ont une bonne corrélation avec les temps de vie des wafers mesurées par décroissance de la photoconductivité détectée par micro-ondes.

Par la suite, nous nous concentrons sur les analyses dispositif. A l'aide du KPFM, nous analysons deux types de cellules solaires silicium cristallin : les cellules solaires silicium épitaxié (epi-Si) et les cellules solaires hétérojonctions à contact arrière (IBC). En particulier, nous nous focalisons sur l'analyse de dispositifs en condition d'opération. Nous étudions d'abord l'influence de la tension électrique appliquée et nous montrons que les effets de résistance et de diode peuvent être détectés à l'échelle nanométrique. Les mesures de KPFM sont comparées aux mesures de microscopie électronique à balayage (SEM) dans les mêmes conditions, puisque le SEM est aussi sensible au potentiel de surface. Nous montrons que les mesures KPFM sur la tranche de cellules solaires epi-Si peuvent permettre d'étudier les changements de champ électrique avec la tension électrique appliquée. De plus, si la tension électrique est modulée en fréquence, nous montrons que des mesures de temps de vie peuvent être effectuées à l'échelle locale sur la tranche de cellules solaires epi-Si, ce qui peut permettre de détecter les interfaces limitantes. Puis, nous étudions l'influence de l'illumination sur les mesures KPFM et CP-AFM. Nous effectuons des mesures sur la tranche de cellules epi-Si sous différentes valeurs d'intensité et longueurs d'onde d'illumination. Nous montrons une bonne sensibilité des mesures KPFM à l'illumination. Cependant, nous montrons que pour différentes longueurs d'onde, à tension de circuit ouvert fixé, nos mesures ne sont pas corrélées avec les mesures de rendement quantique interne, comme nous le pensions.

Enfin, nous résumons notre travail dans un tableau qui représente les forces et faiblesses des techniques pour les différentes mesures d'intérêt exposées précédemment. A partir de ce tableau, nous imaginons un setup de microscopie « idéal » qui permette d'analyser les cellules solaires de manière fiable, versatile et précise. Pour finir, nous proposons des mesures d'intérêt qui pourraient être réalisées avec ce setup « idéal ».

université PARIS-SACLAY | ÉCOLE DOCTORALE INTERFACES Approches Interdisciplinaires : Fondements, Applications et Innovation

Titre : Etude de cellules solaires en silicium cristallin à l'échelle nanométrique à l'aide de techniques de microscopie à sonde locale.

Mots clés : Microscopie à sonde de Kelvin, Microscopie à force atomique conductrice, Cellules solaires, Silicium cristallin, Caractérisation Avancée, Microscopie Electronique

Résumé : Cette thèse s'intéresse à l'analyse de cellules silicium cristallin à l'échelle nanométrique, grâce à deux techniques de microscopie à sonde locale : la microcopie à sonde de Kelvin (KPFM) et la microscopie à force atomique à sonde conductrice (CP-AFM).

Après une analyse forces/faiblesses de ces deux techniques, nous effectuons des mesures « matériau» et « dispositif». Les mesures « matériau» sont composées des mesures de dopage à l'aide du CP-AFM et de mesures de temps de vie sur wafer passivés à l'aide du KPFM. Les mesures « dispositif» sont réalisées par KPFM sur des cellules en condition d'opération.

Les mesures sous tension électrique sont comparées à des mesures de microscopie électronique à balayage. Elles montrent que le KPFM permet de cartographier des effets de résistance et de diode; ainsi que le temps de vie, à l'aide d'une tension électrique modulée en fréquence. Puis, nous étudions l'effet de l'intensité lumineuse et de la longueur d'onde sur les mesures KPFM.

Enfin, l'analyse de notre tableau de conclusion nous permet d'imaginer un setup de microscopie « idéal » pour effectuer des mesures d'intérêt sur les cellules solaires en silicium cristallin.

Title : Investigation of crystalline silicon solar cells at the nano-scale using scanning probe microscopes

Keywords : Kelvin Probe Force Microscopy, Conducting Probe Atomic Force Microscopy, Solar Cells, Crystalline silicon, Advanced Characterization, Electron Microscopy

Abstract: This thesis focuses on the investigation of crystalline silicon solar cells at the nano-scale using two scanning probe microscopy techniques: Kelvin Probe Force Microscopy (KPFM) and Conducting Probe Atomic Force Microscopy (CP-AFM).

After strengths/weaknesses analysis of both techniques, we perform material and devices investigations. Material investigations include doping measurements using CP-AFM and lifetime measurements on passivated wafers using KPFM. Devices investigations were performed under operating conditions using KPFM.

Measurements under electrical bias are compared to scanning electron microscopy measurements. They show that KPFM enables to map resistance and diode effects at the nano-scale. Lifetime measurements were also highlighted, using modulated frequency electrical bias. Then, the sensitivity of KPFM measurements to illumination intensity and wavelength was studied.

Finally, a summary table is drawn and enables to imagine an "ideal" microscopy setup to for crystalline silicon solar cells investigation. We propose measurements of interest than can be performed using this setup.